Proceedings of the 4th Conference

NMM 2013

Nano & Macro Mechanics

19th September 2013

All contributions in this book have been reviewed. However, the authors take responsibility for the content and for the correctness of their texts, the quality of the tables, graphs and figures. The editors therefore cannot accept responsibility for the final appearance of the manuscripts.

Edited by:

Tomáš Plachý, Pavel Padevět, Pavel Tesárek, Jan Stránský, Ondřej Zobal

Published by:

Department of Mechanics, Faculty of Civil Engineering, Czech Technical University in Prague, Thákurova 7, 166 29 Praha 6

Printed by:

Česká technika - nakladatelství ČVUT, Thákurova 1, 160 41 Praha 6, pages 239, 1st Edition

Acknowledgement:

SVK 08/13/F1

ISBN 978-80-01-05332-4

Table of Contents

COMPARISON OF LINEAR AND NONLINEAR DYNAMIC METHODS OF FEMA356 FOR STEEL MOMENT FRAMES IN NEAR AND FAR FIELD OF FAULTS

Davood ABDOLLAHZADEH[1], Mohsen GERAMI[2],Mohammad MASTALI[3]

***Abstract**: Recently studies showed that near-fault ground motion records exhibit a distinctive long-period, pulse-like time histories, with very high peak velocities. These features in vicinity of active faults caused much of the damages in structures. In this study linear static, linear dynamic and nonlinear dynamic method of FEMA356 have been studied to evaluate special steel moment frame structures under effects of near-fault ground motions. Results showed that linear methods predict demand to capacity ratio of structural elements 47.9% fewer than results presented by nonlinear dynamic procedure for IO performance level but linear methods present 109.38% and 144.41%overestimate results in life safety (LS) and collapse prevent (CP) performance level respectively.*

***Keywords**:Seismic evaluation, Pulse-like motions, Seismic rehabilitation, near and far field earthquakes*

1. INTRODUCTION

Regarding recent progresses in earthquake engineering, researchers found different effects of near and far fault earthquakes. After the earthquakes of Parkfield, California (1966) and Pacoima, San Fernando (1971), the pulse-like motions of near fault was discussed by Bolt (1975) [1]. First time, Studying on structures behavior in near fields of faults was done by Anderson and Bertero (1987) [1] by analyzing of structures behavior under pulse like ground motions after Imperial Valley earthquake (1979) [1]. Although the effects of near fault were distinguished but the importance of it was not understood in the design of civil engineering structures until destructive earthquakes such as Landers, California (1992), Northridge (1994), Kobe, Japan (1995), Chichi, Taiwan (1999) happened [2, 3]. Recent studies in near fault regions showed that forward directivity effects in near field of fault causes high-period pulse-like motions in near field of fault. These pulse-like motions impose high demands of ductility and deflection on structures [7-12]. In near field of faults, the effect of horizontal component that is normal to fault line is more severe than the horizontal component that is parallel to the fault

[1]DavoodAbdollahzadeh, Lecturer, Azad University of Pardis, Pardis, Tehran, Iran, e-mail: davood.abdollahzadeh@gmail.com

[2] Mohsen Gerami, Associated professor, Semnan University, Semnan, Iran, e-mail: mgerami@semnan.ac.ir

[3]Mohammad Mastali, PhD Student, University of Minho, Guimaraes, Portugal, e-mail: Muhammad.mastali@gmail.com

line[6, 7]. Also vertical vibration should be estimated in near field of fault, if it is important for performance of structures [7].Considering that there are a lot of cities located in near field of fault and it is current to use of linear methods by engineers to design and seismic evaluation of structures, in this study linear static procedure (LSP) and linear dynamic procedure (LDP) of FEMA356 in near and far field of fault have been studied. Therefore performance level results of structural members obtained by linear methods and they compared with nonlinear dynamic procedure results by far fault and near fault earthquake records.

2. STRUCTURAL MODELS AND ASSUMPTIONS

2.1. STRUCTURAL SAMMPLES

In this study 5 structural samples that they designed by Iranian Seismic code [16] were used to seismic evaluation. Figure 1 shows structural models and their details in this study. To design and element performance identification, it was assumed that the steel materials are ST37 that its yield point is 235.44 MPa and its elasticity module is 2×105 MPa Also Poisson ratio assumed υ=0.3. Table 1 shows gravity loads that they have applied to structural designing. Figure 2 has been used to plastic hinge modeling of girders and columns based on FEMA356 provisions for nonlinear dynamic analysis. The computer program RAMPERFORM-3DS was used to seismic evaluation of the structures.

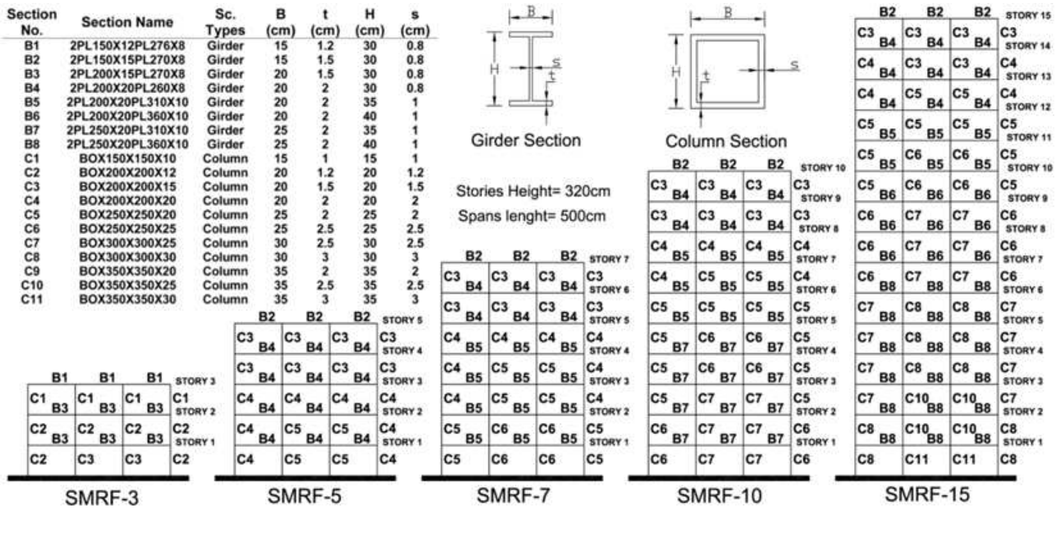

Section No.	Section Name	Sc. Types	B (cm)	t (cm)	H (cm)	s (cm)
B1	2PL150X12PL276X8	Girder	15	1.2	30	0.8
B2	2PL150X15PL270X8	Girder	15	1.5	30	0.8
B3	2PL200X15PL270X8	Girder	20	1.5	30	0.8
B4	2PL200X20PL260X8	Girder	20	2	30	0.8
B5	2PL200X20PL310X10	Girder	20	2	35	1
B6	2PL200X20PL360X10	Girder	20	2	40	1
B7	2PL250X20PL310X10	Girder	25	2	35	1
B8	2PL250X20PL360X10	Girder	25	2	40	1
C1	BOX150X150X10	Column	15	1	15	1
C2	BOX200X200X12	Column	20	1.2	20	1.2
C3	BOX200X200X15	Column	20	1.5	20	1.5
C4	BOX200X200X20	Column	20	2	20	2
C5	BOX250X250X20	Column	25	2	25	2
C6	BOX250X250X25	Column	25	2.5	25	2.5
C7	BOX300X300X25	Column	30	2.5	30	2.5
C8	BOX300X300X30	Column	30	3	30	3
C9	BOX350X350X20	Column	35	2	35	2
C10	BOX350X350X25	Column	35	2.5	35	2.5
C11	BOX350X350X30	Column	35	3	35	3

Fig 1.Structural models in details

Tab 1. Girders dead and live loads (N/m)

Load Type	SMRF3	SMRF5	SMRF7	SMRF10	SMRF15
Girders Dead Load	**24525**	**24525**	**24525**	**24525**	**24525**
Girders Live Load	**9810**	**9810**	**9810**	**9810**	**9810**
Roof Dead Load	**17167.5**	**17167.5**	**20437.5**	**20437.5**	**22072.5**
Roof Live Load	**7357.5**	**7357.5**	**7357.5**	**7357.5**	**7357.5**

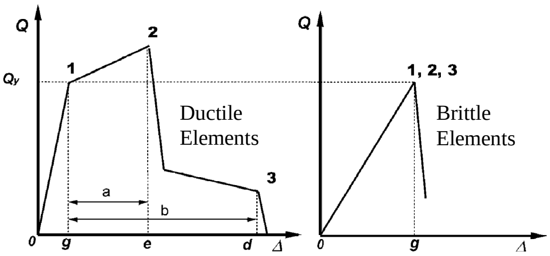

Fig 2. Force versus deformationcurves

2.2. EARTHQUAKES

Based on FEMA356 section (1.6), structures must be evaluated for earthquakes with 10% chances to occur in 50 years of building life.For seismic evaluation of structures 10 near-fault (NF) records and 10 far-fault (FF) records have selected. All records had frequency contents; response spectrum, effective duration and soil type same as assumption construction site. Accelerograms recoded in soil type D based on soil classification in FEMA356 for regions. To study structural samples by linear methods, the 2800 design spectrum, Near Fault (NF) and Far Fault (FF) response spectra were used by linear methods.Figure 3 shows two samples of ground motion records from Chi-Chi, Taiwan earthquake (1999). The near fault and the far fault response spectra obtained from earthquake records showed in Table 2.The 2800 design spectrum, NF and FF response spectra are shown in Figure 4.

Tab 2. Earthquake records

No.	Place of Event	Date	Station	Distance from Fault (km)	No.	Place of Event	Date	Station	Distance from Fault (km)
1	Chi-Chi, Taiwan	1999	CHY065	83.43	11	Denali, Alaska	2002	PumpStation #10	2.74
2	Chi-Chi, Taiwan	1999	TAP095	109.01	12	Bam,Iran	2003	Bam	15>R
3	Loma Prieta	1989	CDMG 58224	72.2	13	Chi-Chi, Taiwan	1999	CHY101	9.96
4	Loma Prieta	1989	CDMG 58472	74.26	14	Chi-Chi, Taiwan	1999	TCU068	0.32
5	Kobe, Japan	1995	HIK	95.72	15	Imperial Valley	1979	CDMG 5158	1.35
6	Loma Prieta	1989	CDMG 58223	58.65	16	Northridge	1994	DWP 74	5.35
7	Manjil, Iran	1990	Qazvin	49.97	17	Silakhor ,Iran	2006	Chalan Choolan	15>R
8	Northridge	1994	CDMG 13122	82.32	18	Kocaeli, Turkey	1999	Yarimca	4.83
9	Tabas, Iran	1978	Ferdows	91.14	19	Zanjiran,Iran	1994	meymand	15>R
10	Kocaeli, Turkey	1999	Bursa Tofas	60.43	20	Kobe, Japan	1995	Takatori	1.47

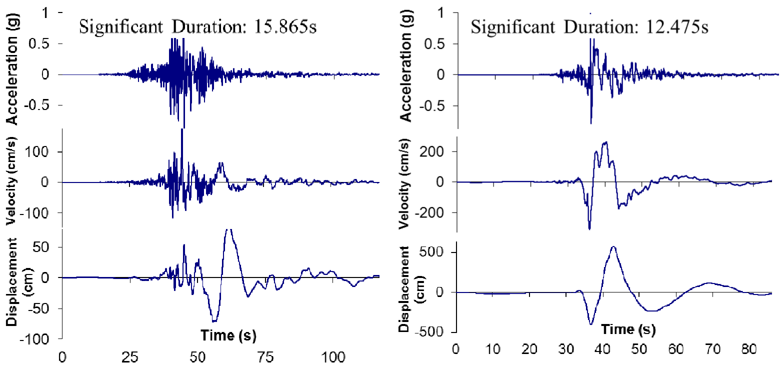

Far Field of Fault *Near Field of Fault*

Fig 3. Two samples of earthquake time histories

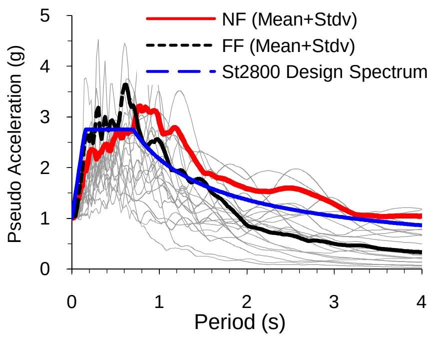

Fig 4. Near fault, Far fault and Standard No.2800 Design spectrum (ξ=5%).

All records are proportionate with site and their peak ground acceleration (PGA) scaled to 0.35g based on seismic hazard map of Tehran in standard No.2800. Based on the source [10] in this study, the near fault records should have specifications of records that they are recorded in less than 15 km of active faults. Hence earthquake records have special characteristics such as 1- All of NF records have forward directivity effects (there are one or two pulse like motion in velocity time history of records). 2-Earthquake records were from earthquakes with Mw>6.5. 3-form two horizontal components of earthquake, one of them that had forward directivity specifications clearly and had more effect on period 1 second in acceleration response spectrum was selected. In Figure 4,it is observed that the near fault (NF) spectrum has more amounts after period of 0.7s than the FF spectrum.

3. COMPARISON OF SEISMIC EVALUATION METHODS

In this section based on FEMA356 provisions the performance levels of the structural members have determined under effect of earthquake records that are shown in Table 2. The structural analyses were done based on FEMA356 to identify the demand to capacity ratio (DCR) of structural elements in three performance levels of Immediate operation (IO), Life Safety (LS) and collapse prevent (CP). In continue results of linear static (LSP), linear dynamic (LDP) and nonlinear dynamic analysis (NDP) methods have been compared. Figures 5 to 16 show average results of demand to capacity ratio of structural members obtained by linear and nonlinear methods in near and far field of faults.

3.1. CONSIDERATION OFMODELS IN IO PERFORMANCE LEVEL

Based on Figures 5 to 8, Study of structural members performance levels in average showed in IO performance level linear methods present DCRs un-conservatively. These methods predict performance levels of structural elements very low in IO level as average result of all data obtained by LSP are 28.55% for girders, 45.74% for columns and 38.36% for whole of structure fewer than the nonlinear dynamic method. Also LDP present performance levels 51.42% for girders, 62% for columns and 57.44% for whole of structure fewer than the NDP in IO performance level. It is considered that if structural members remain in elastic limit of material then results of linear methods are the same forlinear and nonlinear dynamic methods in IO performance level.

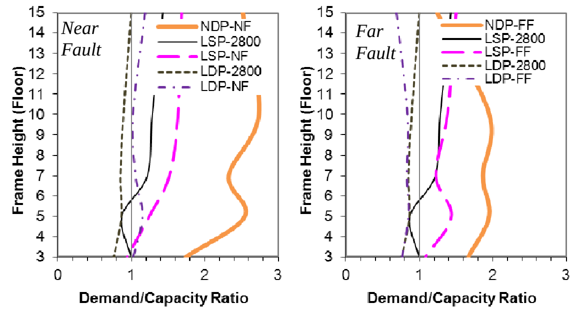

Fig 5. Comparison of linear methods with nonlinear dynamic method in IO performance level for outside girders

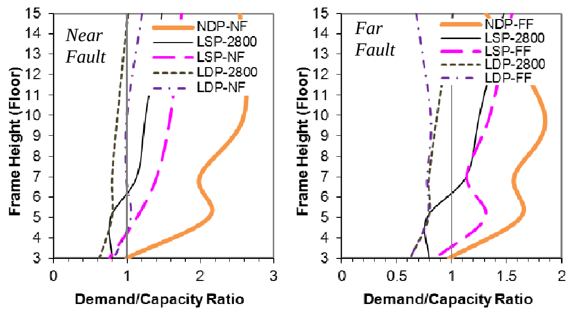

Fig 6. Comparison of linear methods with nonlinear dynamic method in IO performance level for inside girder

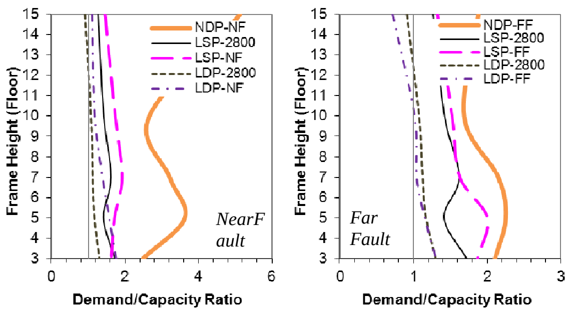

Fig 7. Comparison of linear methods with nonlinear dynamic method in IO performance level for perimeter columns

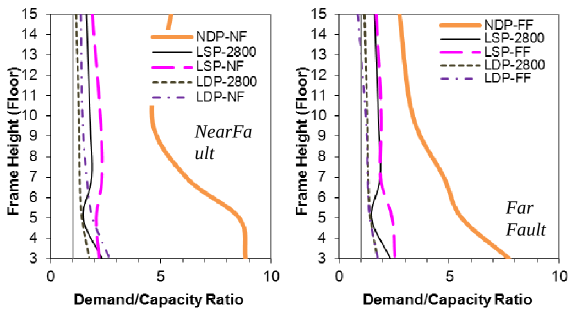

Fig 8. Comparison of linear methods with nonlinear dynamic method in IO performance level for interior columns

3.2. CONSIDERATION OFMODELS IN LSPERFORMANCE LEVEL

According to Figures 9 to 12, consideration of average result of LS performance level for whole of structures showed LSP results for girders are more than the DCRs resulted by NDP. Also performance levels presented by LDP for girders are a little fewer than NDP results in average. Consideration of columns DCRs showed that in average, the linear methods present performance level of members more than the nonlinear dynamic procedure. So that linear static procedure predicts DCRs 43.1% for girders, 235.33% for columns and 152.94% for whole of structure more than NDP. Consideration of Linear dynamic method showed this method presents un-conservative results for girders than nonlinear method about 2.7% in LS performance level. Also this procedure has more conservative results than nonlinear dynamic method for columns for the whole of structures about 117.23% and 65.83% in LS performance level respectively.

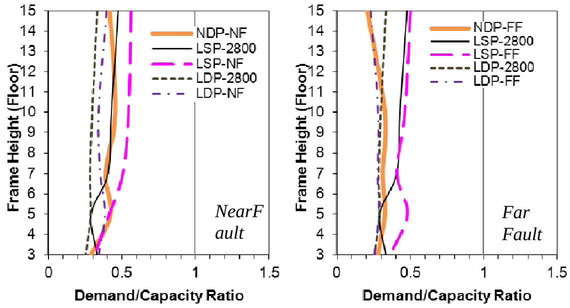

Fig 9. Comparison of linear methods with nonlinear dynamic method in LS performance level for outside girders

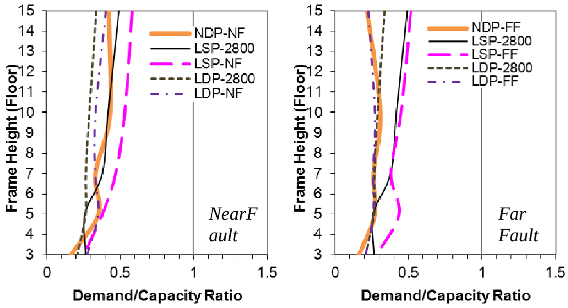

Fig 10. Comparison of linear methods with nonlinear dynamic method in LS performance level for inside girders

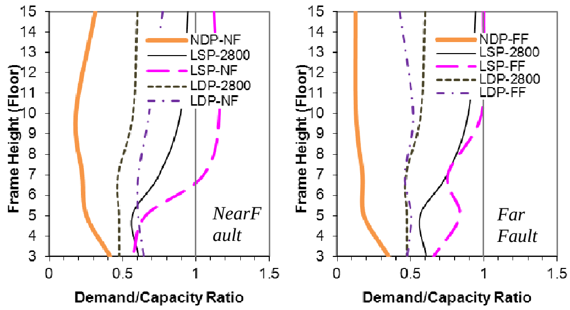

Fig 11. Comparison of linear methods with nonlinear dynamic method in LS performance level for perimeter columns

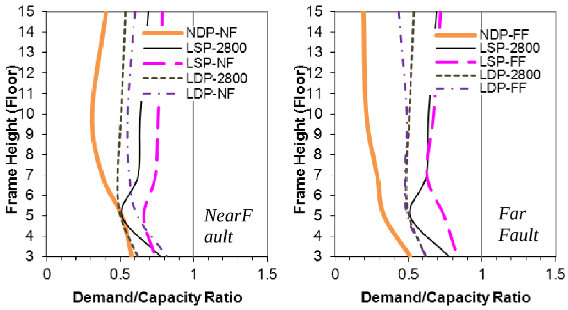

Fig 12. Comparison of linear methods with nonlinear dynamic method in LS performance level for interior columns

3.3. CONSIDERATION OFMODELS IN CPPERFORMANCE LEVEL

Consideration of structural members DCRs in CP performance levels in Figures 13 to 16 illustrated that the linear methods present more conservative results than nonlinear dynamic method in average. So that LSP predicts performance level of structural members 43.78% for girders, 310.43% for columns and 196.46% for all elements more than NDP. Average result of performance level obtained by linear dynamic method showed this method present girders DCRs 2.34% fewer than NDP in CP performance level but its results for columns an whole of structure is 163.39% and 92.36% more than nonlinear dynamic procedure on average respectively.

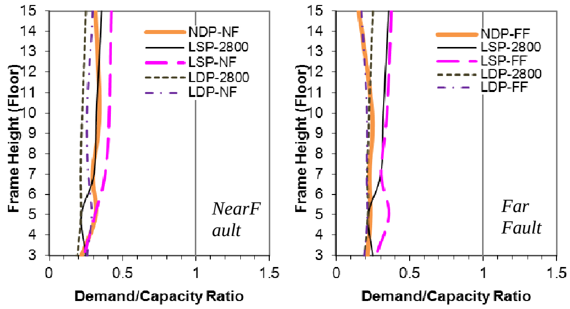

Fig 13. *Comparison of linear methods with nonlinear dynamic method in CP performance level for outside girders*

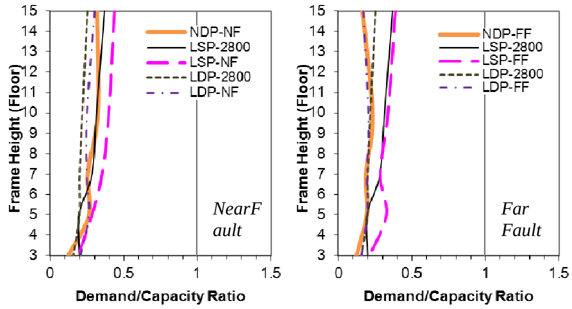

Fig 14. Comparison of linear methods with nonlinear dynamic method in CP performance level for inside girders

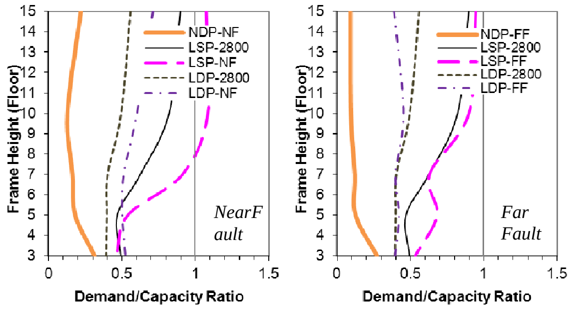

Fig 15. Comparison of linear methods with nonlinear dynamic method in CP performance level for perimeter columns

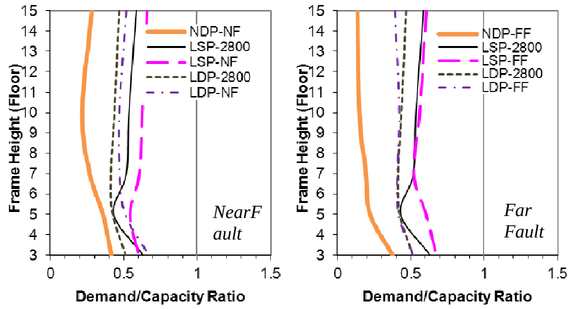

Fig 16. Comparison of linear methods with nonlinear dynamic method in CP performance level for Interior columns

4. CONCLUSION

In this study three methods for seismic evaluation of structures, Static Linear Procedure (LSP), Linear Dynamic Procedure (LDP) and Nonlinear Dynamic Procedure (NDP) have been compared to estimate performance level of steel moment resisting frames in near and far fields of fault. Results showed that:

1-For seismic evaluation of moment resisting steel frames in IO performance level, linear methods predict demand to capacity ratio of structural elements fewer than results presented by nonlinear dynamic procedure related to FEMA356. So that the average of DCRs resulted by linear methods are 47.9% fewer than nonlinear dynamic method.

2-The linear static procedure predict performance level of structural elements more than the nonlinear dynamic procedure conservatively in LS and CP performance levels. But the linear dynamic method presents DCRs for girders fewer than the nonlinear dynamic method for girders in LS and CP performance level. This method predicts girders performance level 2.34% un-conservative than the nonlinear dynamic procedure. So it is advisable that it is better to use average results of both linear method` results (linear static and linear dynamics) for seismic evaluation of girders. Finally average of structural members DCRs showed linear methods present performance level of members 109.38% and 144.41% more than the nonlinear dynamic method respectively.

3-Investigation of girders and columns performance levels resulted by linear methods showed girders DCRs and columns DCRs are not proportional by linear methods. As performance levels resulted by linear static procedure are 43.1% for girders and 235.33% for columns more than nonlinear dynamic procedure. Also it was observed that linear methods present perimeter columns DCRs more than interior column `s DCRs. also perimeter columns DCRs to interior column `s DCRs ratio in IO, LS, and CP performance levelfor the linear static procedure is 1.68, 2.07 and 2.18 andfor the linear dynamic procedure is 1.74,1.67 and 1.66.

4-Comparison of results in near and far field of fault showed that to evaluation of structures located in regions with forward directivity effects, it is important to use site specific response spectrum or near fault design spectra provided by codes because results obtained by this study showed average results of performance levels for structural members are 16.44% based on the linear static procedure and 19.35% based on the linear dynamic procedure related to the 2800 design spectrum is fewer than results obtained for near fault earthquake records.

5. REFERENCES

[1] BOLT,B.A. Seismic input motions for nonlinear structural analysis.*ISET journal of earthquake technology*. 2004, **41**(2), 223-232. ISSN 0972-0405.

[2] CHOI, I.K. et al. Shaking table test of steel frame structures subjected to scenario earthquakes. *Journal of the Nuclear Engineering and Technology*. 2005, **37**(2), 191-200.ISSN 1738-5733.

[3] GALAL, K. and GHOBARAH,A. Effect of near-fault earthquakes on North American nuclear design spectra. *Nuclear Engineering and Design*.2006. **236**(18), 1928-1936.ISSN 0029-5493.

[4] BOZORGNIA,Y. and BERTERO V. V. *Earthquake Engineering: From Engineering Seismology to Performance-Based Engineering*. NewYork: CRC Press, 2004, pp. 138-211.ISBN 0-8493-1439-9.

[5] NAEIM,F. *THE SEISMIC DESIGN HANDBOOK*. 2nd ed.New York: Kluwer Academic Publishers, 2001, pp.33-34.ISBN 0-412-07891-0.

[6] STEWART, J. P. et al. *Ground Motion Evaluation Procedures for Performance-Based Design*. California:Pacific Earthquake Engineering Research Center(PEER), University of California,Berkeley, 2001. Report No. 2001/09.

[7] ALAVI,B. and KRAWINKLER,H. *Effects of near-fault ground motions on frame structures*. California: The John A. Blume Earthquake Engineering Center, Stanford University,2001. Report No. 138.

[8] MENUN, C. and FU, Q. An analytical model for near-fault ground motions and the response of SDOF systems. In:*Seventh US National Conference on Earthquake Engineering*. Massachusetts:

Mira Digital Publishing, 2002.ISBN 0-943198-09-7. [online]. [cited 2002-07-25]Available from:http://peer.berkeley.edu/research/peertestbeds/Cct/Menun%20and%20Fu%202002.pdf

[9] SU,F. et al. Characteristics of ground motion response spectra from recent large earthquakes and their comparison with IEEE standard 693. In:*100th anniversary earthquake conference commemorating the 1906 San Francisco*. Oakland: EERI, 2006, pp. 18-29. ISBN-10: 1932884254

[10] SAIIDI, M. and SOMERVILLE, P. *Bridge seismic analysis procedure to address near-fault effects*. Nevada: Nevada University (Reno), 2005. Research report of Caltrans Project.

[11] GERAMI, A. et al. behavior of structures in near field of faults.In:*4th National congress on Civil Engineering*. Tehran: Tehran University. 2008. (In Persian). [online]. [cited 2008-05-06] Availabale from:http://www.civilica.com/Paper-NCCE04-NCCE04_593.html

[12] MORTEZAEI, A. et al. Effectiveness of modified pushover analysis procedure for the estimation of seismic demands of buildings subjected to near-fault earthquakes having forward directivity. *The structural design of tall and special buildings*. 2011, **20**(6), 679-699. ISSN 1541-7808

[13] GERAMI,M. and ABDOLLAHZADEH, D. Estimation of Forward Directivity Effect on Design Spectra in Near Field of Fault. *Journal of Basic and Applied Scientific Research*. **2**(9), 8670-8686, 2012. ISSN 2090-4304

[14] Uniform Building Code. UBC97. International Conference of Building Officials, California:Whittier, 1997.ISBN-13 978-1884590870

[15] The Federal Emergency Management Agency. *PRESTANDARD AND COMMENTARY FOR THE SEISMIC REHABILITATION OF BUILDINGS*. Washington: FEMA, 2000.
Available from: http://www.fema.gov/media-library/assets/documents/757#

[16] Building and Housing Research Center. *IRANIAN CODE OF PRACTICE FOR SEISMIC* RESISTANT *DESIGN OF BUILDINGS* (Standard No. 2800). 3rd ed. Tehran:BHRC Publication,2007.ISBN: 978-964-9903-41-5. Available from:
http://www.apadanabana.com/uploads/news7_En_iranian%20cod%20of%20practice%20for%20seismic%20resistant%20design%20of%20buildins.pdf

PROGRAMMING AND SIMULATION OF THE MACHINING OF THE WORM GEAR 3D MODEL FOR FEM ANALYSIS

Ing. Cossi Alindé Hugues AHOSSY[1]

Abstract: *The manufacturing of the exact geometry of the worm gear toothing is a complicated issue since the flank surface of the worm gear tooth is a curved surface explicitly indefinable [5]. The accurate geometry of the toothing can be obtained by running the manufacturing simulation application written in Auto Lisp. However, the obtained 3D model shows a flank surface of the tooth which consists of several small surfaces irregularly positioned and sized. To facilitate the FEM analysis using this 3D model is necessary to clean the obtained tooth groove and the flank surfaces. This work deals with the machining of the accurate 3D tooth profile and the reshaping of the 3D model of the worm gear without impacting the accuracy of the obtained geometry.*

Keywords: *Worm, worm gear, gear toothing, machining simulation, flank surface.*

1. INTRODUCTION

A worm drive (Fig. 1) is a gear arrangement in which a worm, which is a gear in the form of a screw, meshes with a worm gear. The worm and gear drive is the simplest way to obtain a large speed reduction with high torque in a compact space.

The worm and gear set is a kinematical and force relation between cylindrical shafts of skew axes at the location of their shortest secants. The angle of their axes is usually 90°. A worm and gear set is in fact a helical cylindrical gear set where the number of teeth of the driving gear, called worm, is one, two or three, rarely more. The driven component is called the worm gear or gear wheel.

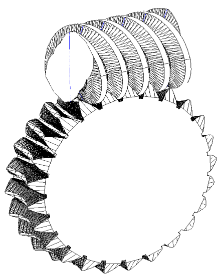

Fig. 1 CAD model of the worm gear set

[1]Ing. Cossi Alindé Hugues AHOSSY, Dept. of Designing and Machine Components, Czech Technical University, Prague, Czech Republic, CossiAlindeHugues.Ahossy@fs.cvut.cz

2. OBJECTIVES

In spite of the number of investigations devoted to worm and gear set research and analysis, they still remain to be developed. We still need to find out the best manufacturing approach capable of predicting the effects of manufacturing method in gear geometry, contact and bending stresses, stiffness and transmission errors. The geometry of the worm and gear set is a complicated issue. So far, none of the CAD systems contain appropriate tools that would allow the generation of an accurately shaped gear toothing by simply inserting predefined parameters. The aim of this work is to find out methods suitable for modelling the accurate 3D model of gear tooth for the strength analysis by using the Finite Element Method (FEM) on a personal computer.

3. THE WORM TOOTHING DEFINITION

The worm, which has a profile composed of segments in the section cut with the plane perpendicular to the helical generatrix curve at the center is called general worm. The flank surface of the spline is generated by a helical motion of a straight line skew to the axis of the worm. The exact profile of the thread groove with straight flank can only be generated by a turning operation. In the practice, the ordinary worm is machined by a side and face cutter or a hobbler, so that the tool's rotation axis is skew to the worm axis [1].

The described technology means the machining of the worm thread groove with a conical tool witch's axis is skew to the machined worm axis [2]. The inclination is equal to the climbing angle. It is also common to use the so called shank-type gear shaper cutter for worms with bigger dimensions. This cutter is a conical tool with axis perpendicular to the axis of the machined worm.

4. THE WORM GEAR TOOTHING DEFINITION

The flank surface of the worm thread groove is a helical surface generated by a helical motion of a straight line secant to the axis of the worm. This does not apply to worm gear since a simple helical motion of a straight line cannot define its profile. This particularity makes the manufacturing of the exact geometry of the worm gear difficult. The flank surface is an arbitrary curved surface (Fig. 2).

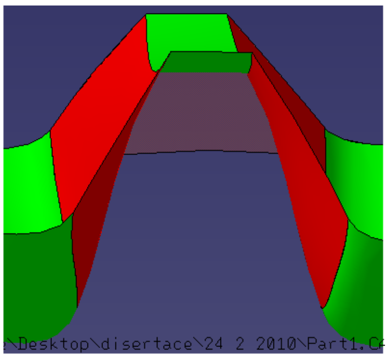

Fig. 2 Flank curved surface

4.1 ANALITICAL DEFINITION OF THE GEOMETRY

One of the possible methods of generating the exact profile of the worm gear toothing is the analytic definition of the toothing. The coordinate of the evolving points and the transition curve can be calculated by a repetitive computing of parametric equations of the evolvement with suitable step of the generatrix. The result of this analytical method could be effective but it is very complicated due to the amount of mathematical equations to solve.

4.2 DIRECT MODELING IN CAD SYSTEMS

The direct generation of the shape in 3D CAD systems could be the best way to prepare the 3D models for using in software which will perform the computer aided engineering analysis. But 3D CAD systems work in such a way that they use elementary curves and geometry such as segments, spirals, circle, ellipse, etc. and with the combination of operations such as rotation, revolution, sweep, extrude, and Boolean operations, they can generate most of shapes. But for the special case of worm gear, the tooth flank is a curved surface which cannot be exactly defined by any combination of the listed operations, unless we simplify the teeth geometry and substitute some of its part with known elementary geometries. But the obtained result will not provide the exact profile of the gear toothing so this approach doesn't meet the goal of our investigations.

4.3 MATHEMATICAL SIMULATION OF THE GEAR MACHINING

The mathematical simulation of the machining is another possible method but it needs to determine all the coordinates of all points defining the tooth flank shape. This procedure generates the same difficulties as the above mentioned method and is not suitable for obtaining the exact geometry of the worm gear.

4.4 CUTTING THE WORM GEAR WITH A TOOL IDENTICAL TO THE WORM

The sought accurate geometry means a shape of the worm gear which can perfectly conjugate with no misalignment at the contact surface. Such an accurate geometry of the worm gear is obtained when the tool used to cut the gear has the same shape as the worm (Fig. 3). The defined technology means the subtraction of a half thread of the worm from the gear blank.

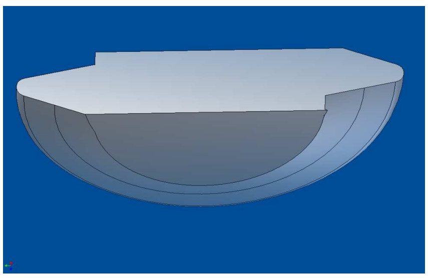

Fig. 3 Tool used to cut the groove

By removing the half thread volume of the worm from the gear blank, the imprint of the worm is left on the blank and this creates the groove which matches perfectly with the worm. After removing two times the thread and creating two adjacent grooves, the remaining part between the grooves represents one tooth. By removing regularly Z time the half thread from the gear blank, we obtain a Z tooth worm gear. To perform the operation, the worm as a tool and the gear blank must be correctly positioned in operating position and both must be actuated by a well-defined motion.

It is also necessary to increase the head diameter of the worm as the tool by the functional clearance Ca (Fig. 4) [2].

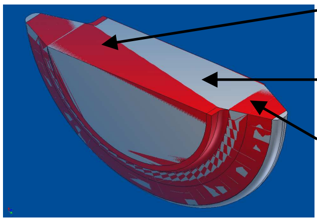

Fig. 4 The worm and the tool shape comparison

5. PROGRAMMING OF THE MACHINING SIMULATION

The goal of this work is to generate an accurate 3D model by simulating the manufacturing by removing the half part of the worm from the gear blank [2]. To achieve this, it is necessary to write generating program to perform the Boolean operation of subtracting the tool from the blank. The possible environments to use are Math Lab or Auto LISP.

For this work, the Auto LISP was chosen because the 3D model generated after launching the program can be directly converted into known formats such as STP, SAT, IGES, … and edited for other uses. Auto LISP is a dialect of Lisp programming language built specifically for use with the full version of AutoCAD and its derivatives.

Auto LISP is a small, dynamically scoped, dynamically typed LISP dialect with garbage collection, immutable list structure and settable symbols, lacking in such regular LISP features as macro system, records definition facilities, arrays, functions with variable number of arguments or let bindings. Auto LISP code can interact with the user through Auto cad's graphical editor by use of primitive functions that allow user to pick points, choose objects on screen, input numbers and other data.

After setting the geometrical characteristics, both components are positioned at the beginning of the operation so that the tool axis is skew to the wheel blank axis and is progressively subtracted from the blank [4].

The blank rotates around its axis while the tool has a translation motion. The center to center distance is set to a = 230.907 mm and that ensures having the head circle of the worm tangent to the root diameter of the worm gear. Below, there are the main functions in the written program:

“defun prime” define the program file called “prime”, ‘(setq MODUL 10.0 D2 361.814 ZUBU 36)’ sets the module, the pitch diameter and the number of gear teeth. ‘(setq BOD1 (list X 0.0 0.0))’ defines the start position in local coordinate systems which is 110 mm from the gear axis (Fig. 5).

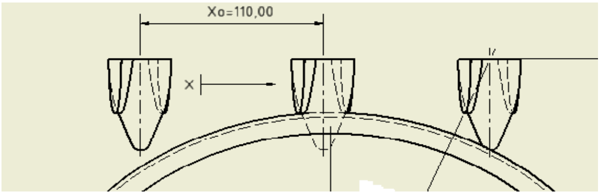

Fig. 5 Relative tool and blank position

As a result after running the program, AutoCAD creates an imprint on the gear blank which represents the groove between two teeth (Fig. 6). This groove mashes exactly with the worm and will conjugate perfectly with it in functional position.

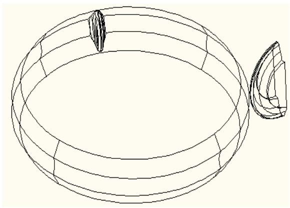

Fig. 6 Tool’s imprint on the blank

6. MODELING OF THE WHOLE 3D GEOMETRY OF THE GEAR WHEEL

To obtain the final 3D model of the worm gear we just have to make Z time the circular pattern of the groove. But as the objective of our investigations on the worm gear is to prepare an accurate 3D model for strength analysis purpose by using the finite element method on a classic personal computer, we still have an important piece of work to do on the surface of the generated groove before patterning it. As it is shown on Fig. 7, the surface of the obtained groove is not smooth.

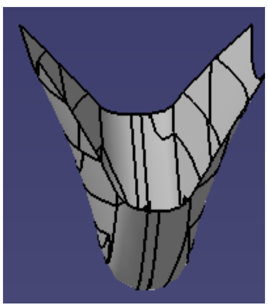

Fig. 7 Isolated groove surface

Auto Lisp created the shape of the groove identical to the worm as it is demanded and realized the Boolean operation of subtraction of the worm from the blank without caring about the quality and the regularity of the surface. The surface is generated by several lines and curves arbitrary positioned to get the demanded shape. When applying a zoom on the areas where the surface curves meet cross we find out that not only the groove surface is made of multiple non-regular small surfaces with arbitrary curves but we can see that some parts of the surface are opened. If we generate the whole gear 3D model with this structure of the groove, it will be impossible to make meshing of the model for strength analysis using the finite element method. The FEM software will display inconsistence error messages or in the best case the meshing and the calculation of such a model will be possible only with a computer with very high memory.

So we need to reshape the groove surface and clean it in order to obtain a much smoother groove surface composed of wide elementary surfaces perfectly connected in line intersections. The goal of this correction is to reduce the number of elementary surfaces to the minimum and at the same time to conserve the form and the dimension of the groove surface.

First of all the, the lines defining the elementary surfaces were brought out and their connection and relative position was studied.

The next step is numbering (Fig. 8) of different vertexes and the reconstitution of the lateral curved surfaces with new curves and lines which lie in the same curved surface as the previous curves.

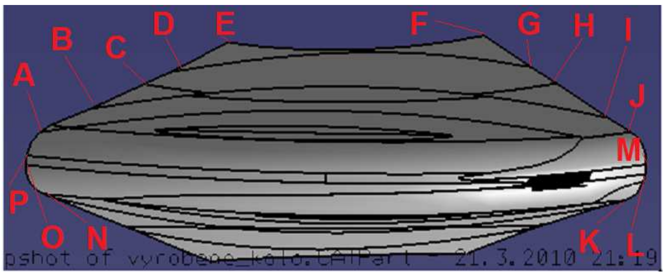

Fig. 8 Flank surface substitution process

The more new surfaces we have, the more the new surface matches with the initial one. During this operation it is not possible to replace the whole initial surface with the new regenerated surface with 100% accuracy. But the errors can be led to the root of the groove, where there is a functional clearance between the worm and the gear according to the gearing definition.

The substitution of the initial groove with a 5 surfaces groove is shown on Fig. 9. The yellow part is the original shape obtained by the manufacturing simulation with Auto Lisp, the grey part is the

Corrected tooth flank made by regular surfaces. There is a geometrical error of 0.001mm on the tooth flank whereas the groove root shows a 0.2mm. The 0.001mm error is acceptable for the flank surface and the 0.2mm error on the groove is negligible comparing the clearance of Ca=2.2mm

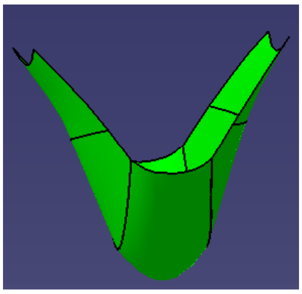

Fig. 9.1 New 5 surfaces groove

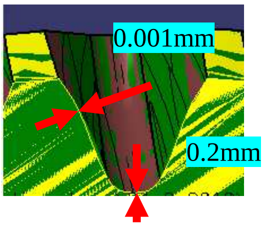

Fig. 9.2 Comparison of the 5 surfaces groove with the initial groove

The whole 3D model of a cleaned worm gear is then obtained by subtracting from the wheel blank a circular pattern made of the groove.

This corrected 3D model is converted by a simple ‘save as’ to the relevant type of file SAT or IGS or CATpart and can be used for a strength analysis using the finite element method which are representations used to perform the computer aided engineering analysis, they are complementary to the computer aided design which is mainly graphical representation of product. The principle of the FEM leads in meshing (Fig. 10) of the geometry supposed to be calculated. A polygon mesh is often used and it is a collection of vertices, edges and faces that define the shape of a polyhedral object in 3D computer graphics and solid modeling.

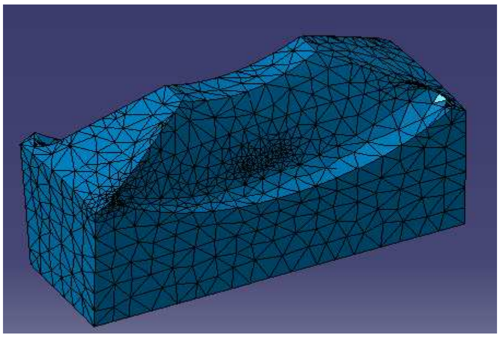

Fig. 10 Polygon mesh applied on the 3D model for FEM analysis

The faces usually consist of triangles, quadrilaterals or other simple convex polygons, since this simplifies rendering. The remodeling of the gear tooth flank surfaces allows the meshing of the 3D model (Fig. 10) and more, this surface reshaping is suitable for localization of the contact surface between the worm and the worm gear for force application.

7. CONCLUSION

The 3D geometry of worm gear generated by running the simulation program of the gear machining written in Auto Lisp is very accurate [3]. This method is, indeed, the most appropriate to achieve the required accuracy of the gear toothing. The other methods like the direct generation of the toothing of the gear in CAD systems require a simplification of the shape of the gear. The mathematical definition or the mathematical simulation of the machining are very complicated due to the amount of mathematical equations to solve and the necessity to determinate all the coordinates of all the points defining the tooth shape.

However, the 3D model obtained by running the manufacturing simulation program in Auto Lisp presents a rough tooth flank surface (Fig. 7) which might not be suitable for strength analysis purposes. The flank surface can be cleaned manually or automatically without impact on the shape accuracy [2]. The local errors on the shape can be led to the groove surface where there is a functional clearance (Fig. 4) between the worm and the worm gear.

ACKNOWLEDGEMENTS

The research described in the paper was supervised by doc. Ing. Jan Bečka, CSc, FME CTU in Prague.

REFERENCES

[1] AHOSSY C. A. H. *Computer analysis of worm and gear meshing*. MATTAR Praha 2008 PART 1, pp. 217- 219. ISBN 978-80-903421-9-4.

[2] AHOSSY C. A. H. Analysis of the worm and gear manufacturing. In: *KCMS 2008 CTP Engineering 49. Mezinárodní konference částí a mechanismů strojů*, pp. 9. ISBN 978-80-7043-718-6.

[3] AHOSSY C. A. H. Computer analysis of worm and gear meshing. In: *Sudentská Tvůrčí Činnost. Konference STC 2008* ČVUT PRAHA Fakulta Strojní.

[4] BEČKA J. *Modelování a Výpočty Ozubených Kol na PC* Praha 2003 – vydavatelství ČVUT

[5] G. SABATIER, F. RAGUSA, H. ANTZ. *Manuel de Construction Mécanique* 2e edition, DUNOD, PARIS, 2006-2009 ISBN 978-2-10-052354-2

[6] ŠVEC, V. *Části a Mechanismy Strojů: Mechanické Převody*. Praha: Vydavatelství ČVUT, 2003. ISBN 80-01-01934-9

EVOLUTION OF THE CEMENT PASTE CREEP WITH ADDITION OF THE 50 % OF A FLY ASH

Petr BITTNAR[1], Pavel PADEVĚT[2]

***Abstract**: The cement paste forms the basis of a concrete composite. This paper is focused on the analysis of the creep of cement paste with fly ash based on experimental measurements. Measurement results of creep-dried and water saturated pastes are presented. The ratio of cement to fly ash of 1:1 was used for the production of the mixture. Experimental measurements were carried out on material age of 4 months*

***Keywords**: Cement paste, Fly Ash, Creep, Shrinkage.*

1. INTRODUCTION

The coal-fired power plants produce many tons of fly ash in the world. A fly ash is generated as the secondary product by burning a brown coal in the lignite power plants. The generated quantity of the fly ash is between 10 % and 30 % of the original volume of a burned coal. Grain size fly ash from power plants is between 1 and 1000 microns [1]. Density of an ash from power plants is between 750 and 950 kg/m^3. From the perspective of chemistry, the fly ash is inert material; the main component is SiO_2 and Al_2O_3 and CaO and SO_4. Conventional fly-ash contains up to 80 % glass phase, as the main component. The fly ash is a suitable building material for their inert behavior. One possibility of processing of fly ash is its use in concrete or in cement paste.

2. MATERIAL FOR CREEP TEST AND ITS REALIZATION

The experiments were executed by using the cement paste [2] with addition of a fly ash. The components of cement paste were: Portland cement CEM I 42.5 R (according to European Standard), fly ash and water [3]. The cylindrical specimens were prepared from components and concreted into the plastic cylindrical moulds. The prism specimens were realized into the steel moulds. These are suitable for preparation the specimens tested in compression. Water/cement ratio of the prepared cement paste was 0.4. 40 % water from weight of solid parts was used for cement paste design. The weight ratio between cement and fly ash was 1:1.

[1] Ing. Petr Bittnar, Department of Mechanics, Faculty of Civil Engineering, Czech Technical University in Prague, petr.bittnar@fsv.cvut.cz

[2] Ing. Pavel Padevět, Ph.D., Department of Mechanics, Faculty of Civil Engineering, Czech Technical University in Prague, pavel.padevet@fsv.cvut.cz

The specimens were taken out from moulds one day after production. The prepared material for testing was placed into the water basin.

The specimens were cut shorted on the length 70 mm before testing. A diameter of prepared cylinders was 10 mm. Six specimens were prepared for the experiments. The first two specimens were determined for a measurement of creep in drying condition. Other two specimens were used for a measurement of shrinkage. The last two specimens were used for a measurement of creep in water saturated condition. The prism specimens were used for testing the material properties of the cement paste. From the original length of 100 mm was created two blocks with a length of 50mm. The compression test was carried out until failure of the specimens. The modulus of elasticity was measured together with the compression test [4]. Figure 2 shows edges of extensometer for measuring the strain. The specimens were placed in a water basin for five months.

Fig. 1 The test arrangements of creep – detail of measuring units.

The age of the tested specimens was 120 days. The measurement of creep was realized in the lever mechanisms [5]. The total number of specimens was six of which two specimens were tested on shrinkage only. The applied load on a specimen achieved the size 697N. This force was unchangeable during the process of a measurement. In Figure 1 there are shown loading frames. The load is equal to the distance and size of weight from the center of rotation of the mechanism. All specimens were covered in the foil to guarantee condition of the humidity. The specimens were loaded by plumbs after their placing in the lever mechanisms.

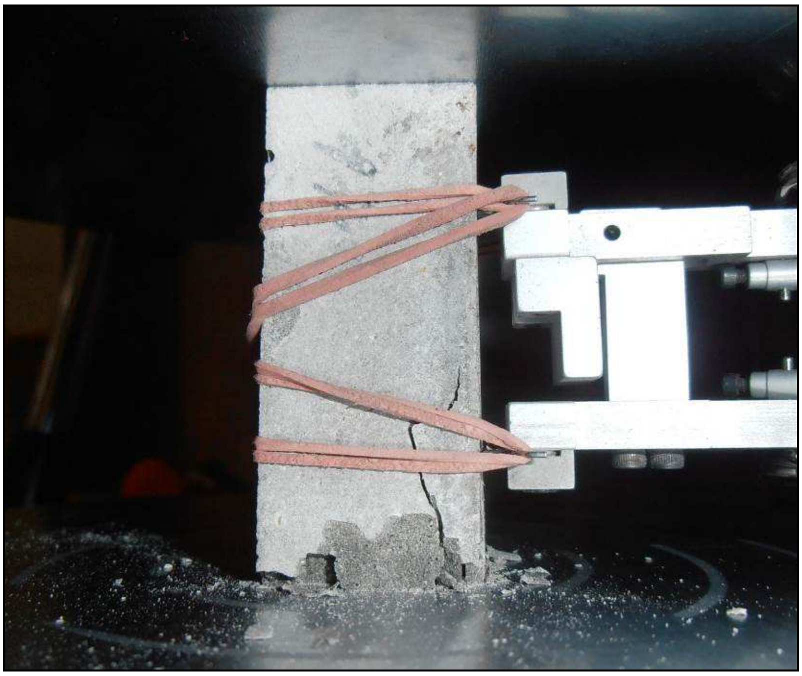

Fig. 2 The specimen from a cement paste in the compression test.

Test time of creep is selected usually 30 days. The specimens that are loaded by plumbs are unloaded before the end of the test. Measurement of shrinkage takes place throughout the test without load. The ambient temperature during the test is maintained at 20 °C [6].

In this case, the tests were carried out at 4 with water saturated and 4 dried solids. Measuring strain sensor length was 25 mm, which corresponds to the half length of the body [7]. The cement paste with a fly ash is a fine-grained material. For this reason, it is not necessary testing of voluminous specimens. Cross-sectional areas of the prisms were 20 x 20 mm. The dried specimens were placed in a drying oven and heated to the temperature 24 hours before testing in compression. The strain was measured by the strain gauge and from adequate strength the modulus of elasticity was calculated.

3. RESULTS

The figures 3 and 4 display stress-strain diagrams with 2 moisture situations. The average compressive strength of dried solids was 58.07 MPa. On the contrary, the average strength of the saturated cement paste was lower 43.2 MPa. In both cases, it is evident very good agreement between the results of the working diagrams of individual test samples. The working diagrams have a similar trend also in the descending branches. After reaching the ultimate strength, a rapid decrease in strength occurs in both cases. The deformation increases during slow loss of strength in the continued part of working diagrams.

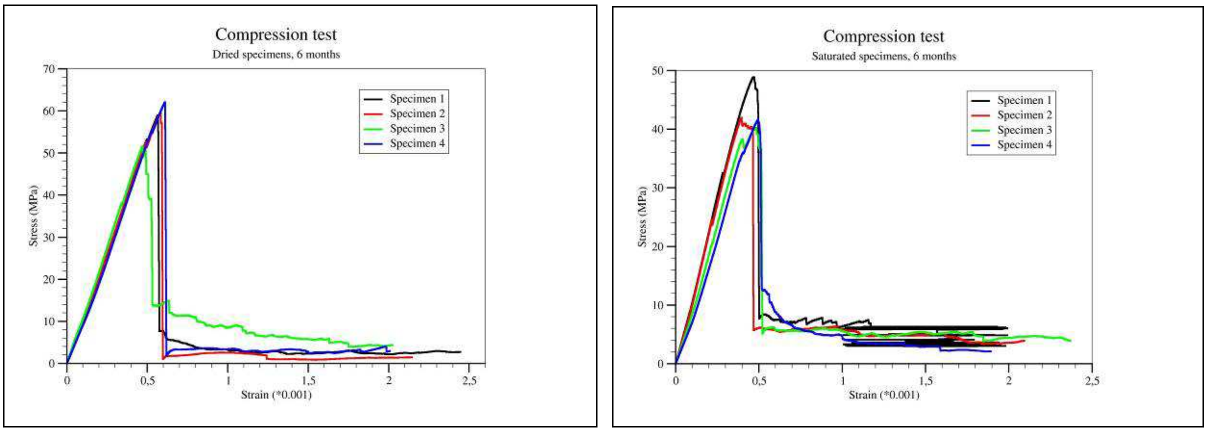

Fig.4 Stress-strain diagrams for the dried (left) and saturated (right) cement pastes.

The results of material properties are summarized in Table 1. The difference between the two humidity conditions is shown in Table 1.

Tab. 1 Compression strength, modulus of elasticity and volumetric weight of cement paste with fly ash in water saturated and dried conditions.

Conditions	Dried	Saturated
Compression strength (MPa)	58.07	43.20
Standard deviation (MPa)	4.502	3.868
Modulus of elasticity (GPa)	13.654	14.573
Standard deviation (GPa)	1.822	2.598
Volumetric weight (kg/m^3)	1439	1778

Figures 5 and 6 display results calculated with shrinkage one of the specimens. Between the graphs there are some small differences caused by the differences between the curves of creep specimens. Principally, the creep of a cement paste is calculated as the difference between the creep and shrinkage, which occurs on the body. Basic creep is calculated from the creep of the dried specimens. The length of testing was 31 days. In the Figure 6 is possible see unloading after finishing of the test.

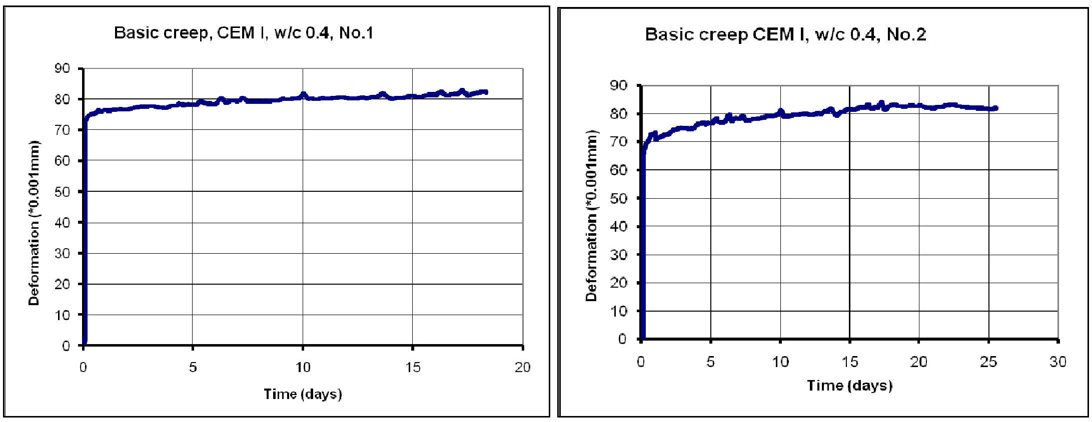

Fig. 5 Basic creep of cement paste with fly ash – water dried specimens.

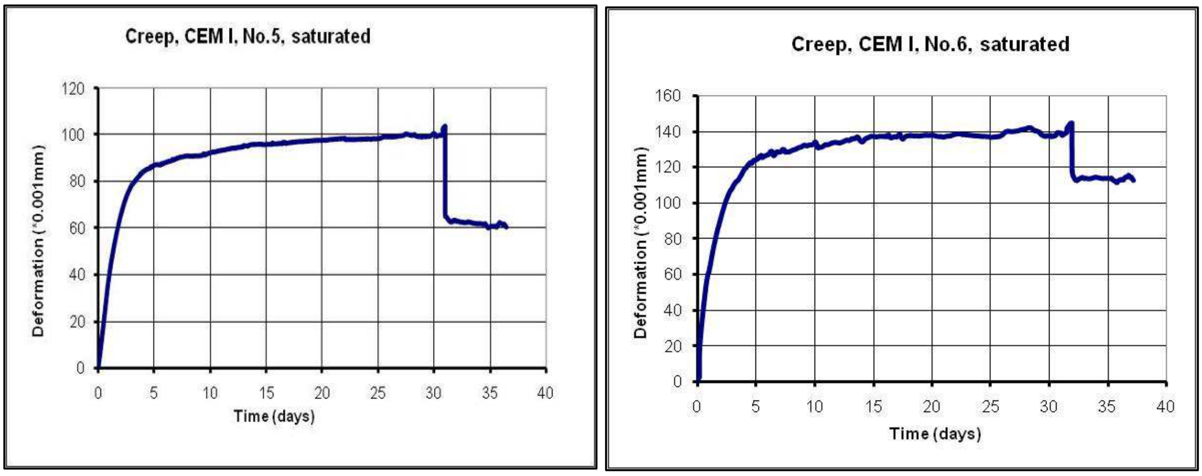

Fig. 6 Creep of cement paste with fly ash – water saturated specimens.

4. CONCLUSION

The size of the basic creep for a cement paste is 13 microns after the period of 20 days. The increase in deformations is continuous during the entire testing period. Measurement of the creep of dried specimens was carried out for 18 and 25 days.

The creep of the saturated cement paste has a completely different progress compared with the dried cement paste. The specimen deformations are enlarging during the first three days after the initial loading. Then this rapid growth trend slows and deformation has been slow. Rapid growth of the strain in the first days reaches of 80 microns for three days. The deformation reaches the size of 20 microns in the slower phase of its increasing. This takes almost 25 days.

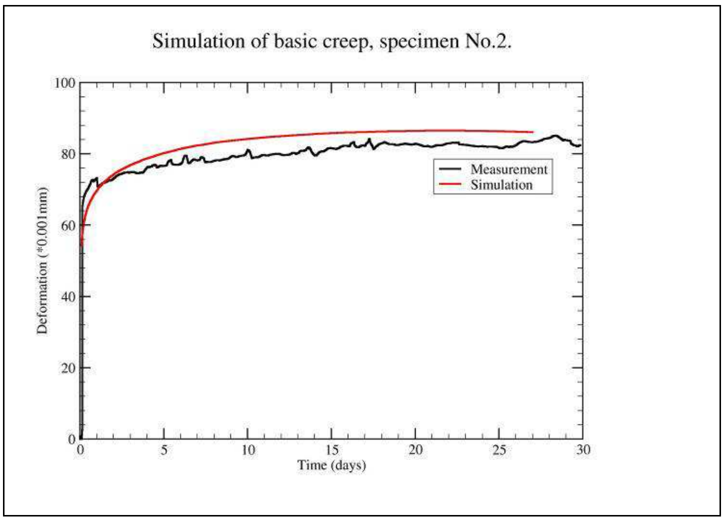

Fig. 7 Simulation of basic creep for the specimen 2.

In Figure 7, it is compared simulation of a creep evaluation by the B3 [8] model with measured data. Coefficients q_1 to q_4 are used for describing the red curve by the model B3 [9].

ACKNOWLEDGEMENT

This work has been supported by a project of the Faculty of Civil Engineering, Czech Technical University in Prague (SGS project No. 12/1117/OHK1/2T/11).

REFERENCES

[1] *Information about secondary energy products*. [online] [cited 2013-08-15] Avaible from: http://www.cez.cz/cs/odpovedna-firma/zivotni-prostredi/programy-snizovani-zateze-zp/vyuziti-vedlejsich-produktu-uhelnych-elektraren.html

[2] NEVILLE, A. M. *Properties of Concrete*, John Wiley & Sons, 1997. 844 p. ISBN 0-470-23527-6.

[3] ZOBAL, O. and PADEVĚT, P. Compressive strength and the tensile strength in bending after 28 days, *Proceedings of the Conference Nano and Macro Mechanics 2011*, Prague, pp.130-134. ISBN 978-80-01-04892-4.

[4] PADEVĚT, P. and ZOBAL, O. Change of Material Properties of the Cement Paste CEM I, *Proceedings of the 48th International Scientific Conference on Experimental Stress Analysis,* Velké Losiny, May – June 2010, pp. 307-310, ISBN 978-80-244-2533-7.

[5] PADEVĚT, P. and BITTNAR, P. Measuring of Creep of Cement Paste Specimen, *Proceedings of the 2nd WSEAS International Conference on Applied Mathematics, Simulation, Modeling (ASM'09),* Athens, Greece, 2009, pp. 33-39. ISBN 978-960-474-147-2.

[6] POLÁK, M. and PLACHÝ, T. Long-Time Monitoring of Thermal Action on a Prestressed Concrete Bridge Structure, in *Proceedings of the 48th International Scientific Conference on Experimental Stress Analysis* ,Velké Losiny, May – June 2010, pp. 369-376, ISBN 978-80-244-2533-7.

[7] VAN MIER, G. M. *Fracture Processes of Concrete* CRC Press (1997). 448p. ISBN 0-8493-9123-7.

[8] *OOFEM project home page*. [online] [cited 2013-08-15] Avaible from: http://www.oofem.org.

[9] BAŽANT, Z. P. and BAWEJA, S. Creep and Shrinkage Prediction Model for Analysis and Design of Concrete Structure – Model B3, *Materials and Structures,* **28**, pp. 357-365, 1995.

USING OPEN-MP IN OOFEM

Michal BOŠANSKÝ[1], Bořek PATZÁK[2]

Abstract: *We aim to speed-up the computation time of our free finite element code with object oriented architecture (OOFEM) for solving mechanical, transport and fluid mechanics problems. We use OpenMP, which is an Application Program Interface (API) for multi-platform shared-memory parallel programming in C/C++ and Fortran. We use a set of compiler directives, library routines and environment variables that influence the run-time behaviour of our program. We show that by parallelizing the task into several subtasks the computation time can be significantly reduced.*

Keywords: *OpenMP, finite element code, parallel programming*

1. INTRODUCTION

The aim of this work is to speed-up computation time in OOFEM software [1]. OOFEM is free finite element code with object oriented architecture for solving mechanical, transport and fluid mechanics problems. It is an efficient and robust tool for FEM (Finite Element Method) computations. We use OpenMP API [2] to create parallel sections from the sequential OOFEM C++ code.

The OpenMP API was developed to enable portable shared-memory parallel programming. It is widely used for the parallelization of applications in many disciplines. More specifically, in this work, the effect of parallelization vector assembly oparations is evaluated.

This paper is organized as follows. We briefly introduce OpenMP API and its constructs in Section 2. Our results are shown and discussed in Section 3. Finally, we conclude the paper in Section 4.

2. OpenMP

OpenMP is a programming interface that supports multi-platform shared memory multiprocessing programming in C, C++, and Fortran, on most processor architectures and operating systems. It consists of a set of compiler directives, library routines, and environment variables that influence run-time behavior.

[1] Ing. Michal Bošanský, Department of Mechanics, Faculty of Civil Engineering, CTU in Prague; michal.bosansky@fsv.cvut.cz

[2] prof. Dr. Ing. Bořek Patzák, Department of Mechanics, Faculty of Civil Engineering, CTU in Prague; Borek.Patzak@fsv.cvut.cz

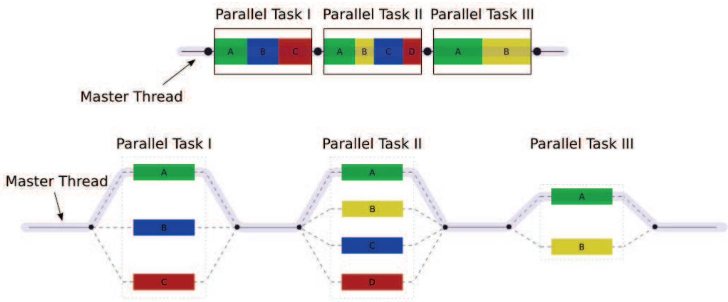

Fig. 1 An illustration of multithreading, where the master thread forks off a number of threads which execute blocks of code in parallel. Adapted from en.wikipedia.

A thread is a runtime entity that is able to independently execute a flow of instructions. If multiple threads collaborate to execute a program, they will share the resources of the corresponding process. The individual threads need just a few resources of their own. Threads running simultaneously on multiple processors or cores may work concurrently to execute a parallel program. Multithreaded program (illustration of which is shown in Fig. 1) can be executed in various ways, some of which permit interactions between threads. OpenMP supports programming model which is called fork-join. The program starts as a single thread of execution, just like a sequential program. The initial thread is the thread that executes this code. Parallel construct is encountered by a thread while it is executing the program, it creates a team of threads (fork), becomes the master of the team, and collaborates with the other members of the team enclosed by the construct to execute the code dynamically. At the end of the construct, only the original thread, or master of the team, continues, all others terminate (join).

Using OpenMP, enable us to create teams of threads, specify distribution of work among the threads, declare types of variables (shared and private), synchronize threads and other features.

When creating teams of threads, one has to specify the parallel region by using a parallel directive before the code that is to be executed in parallel, at the end we use an end parallel directive. Additional information can be supplied along with the parallel directive. This is mostly used to enable threads to have private copies of some data for the duration of the parallel region and to initialize that data. Synchronization implicit barrier is at the end of the parallel region. No thread can process until all other threads have finished their portion of the work. Then the program execution continues with the threads that previously existed. One can control the number of threads that execute a parallel region.

3. RESULTS AND DISCUSSION

In this work, the focus is on parallelization of vector assembly operator and its evaluation. Nodal forces vector is assembled in for-cycle which execution can be made faster by creating a parallel section by splitting the loop and assign the work to individual threads. Sequential code has been modified using parallel clauses creating parallel sections in sequential code. Different threads and related variables are not mutually independent and therefore choice of correct parallel construction is important. Three different parallel constructions were used. The first construction (see Algorithm 1) uses two different types of variables (private and shared). The second construction (see Algorithm 2) utilises thread synchronisation using critical sections, which is a part of a code that is being executed by a single thread thereby avoiding mistakes which occur when two (or more) different threads access variable that is being computed. The third construction (see Algorithm 3) (described as low level parallel programming) utilises locks (sometimes also called semaphores) again ensuring correct synchronisation between threads. Simple locks which lock and unlock thread only once during its execution were used.

Tab. 1 Vector assembly runtimes using two, four, six and eight threads in different constructs

	Number of threads				
	1	2	4	6	8
Sequential construct	5.14 s	-	-	-	-
Parallel for-loop construct	-	3.24 s	1.88 s	1.51 s	1.23 s
Critical sections	-	3.24 s	1.74 s	1.46 s	1.21 s
Simple locks	-	3.24 s	1.74 s	1.46 s	1.21 s

Tab. 2 Vector assembly speed up times using two, four, six and eight threads in different constructs

	Number of threads			
	2	4	6	8
Parallel for-loop construct	1.90 s	3.26 s	1.51 s	3.91 s
Critical sections	1.90 s	3.40 s	3.68 s	3.93 s
Simple locks	1.90 s	3.40 s	3.68 s	3.93 s

The number of parallel threads depends on hardware that is being used for computation. In our case, we have used eight core processor, meaning maximum of eight threads could run simultaneously effectively. Vector assembly durations using two, four, six and eight threads are given in Tab. 1 and speed up times in Tab. 2. It can be observed that time needed for this calculation is reduced significantly as number of threads gets bigger. Anyway are the gain of the speed up time and number of used threads not proportional. The more threads are used the less is the gain of the speed up time. This fact is caused by the maintenance of increased number of threads and and by the using of critical sections and simple locks. Nevertheless is clear that numerical calculations of mechanic problems can be made significantly faster using OpenMP platform – when hardware is used more effectively.

Algorithm 1: Parallel Construction - for-loop Construct

$omp\_set\_num\_threads(number\_of\_threads)$;

 # pragma omp parallel for shared(...) private(...)

for $number\_of\_nodal\_points$ **do**
  assembly of a vector of nodal forces

for $number\_of\_nodal\_points$ **do**
  operations on the vector of nodal forces

Algorithm 2: Parallel Construction - Critical Sections

```
omp_set_num_threads(number_of_threads);
# pragma omp parallel for private(...)
for number_of_nodal_points do
    assembly of a vector of nodal forces
# pragma omp critical
for number_of_nodal_points do
    operations on the vector of nodal forces
```

Algorithm 3: Parallel Construction - Simple Locks

```
omp_init_lock(&my_lock);
# pragma omp parallel
{
# pragma omp parallel for
for condition do
    omp_set_lock(&my_lock);
    # pragma omp parallel for
    for condition do
        –
    omp_unset_lock(&my_lock);
omp_destroy_lock(&my_lock);
```

4. CONCLUSION

In the presented work, we use a set of compiler directives, library routines and environment variables of OpenMP that speed-up the run-time of our OOFEM program. We show that by parallelizing tasks into several subtasks the computation time can be significantly reduced. In future work, we plan to speed-up computation time in our OOFEM software even further by parallelizing corresponding sections of the code using OpenMP.

ACKNOWLEDGEMENT

The financial support of this research by the Czech Technical University in Prague (SGS project No. SGS13/034/OHK1/1T/11) is gratefully acknowledged.

REFERENCES

[1] B. PATZÁK. *OOFEM project home page*, In: http://www.oofem.org [online], 2002-05-01 [cited 2013-06-15]. Available from: http://www.oofem.org/en/documentation/manual.html

[2] B. CHAPMAN, G. JOST and R. V. D. PAS, foreword D. J. KUCK. *Using OpenMP - portable shared memory parallel programming* The MIT press, Cambridge Massachusetts, London, England: 2008 MIT. ISBN-13: 978-0-262-53302-7.

[3] B. STROUSTRUP. *The C++ programming language Third edition.* Murray Hill, New Jersey: 1997 by AT T. ISBN 0-201 885954-4.

BIOMECHANICAL ANALYSIS OF CONSOLIDATION AND OSSIFICATION PROCESSES OF THE BONE REGENERATE DURING LONG BONES LENGTHENING BY DISTRACTION OSTEOGENESIS METHOD

František DENK[1], Miroslav PETRTÝL[2], Radek MYSLIVEC[3], Ivo MAŘÍK[4]

Abstract*: Elongation of long bones is currently the most often performed by distraction osteogenesis method. After osteotomy of the diaphysis and bone fragments stabilization by external fixator the formed callus in interfragmental gap is sequentially stretching during the treatment process of gradual extension. Continuous optimization of the treatment plan during active elongation and neutral fixation can make a key contribution to the quality of bone tissue formation and consolidation, the appearance of a full bone, and significantly treatment time reduction. To optimize the treatment plan parameters the biomechanical study of bone regenerate behavior was prepared according to various criteria in characteristic stages of its consolidation and ossification.*

Keywords*: elongation, distraction osteogenesis, biomechanical processes, bone regenerate ossification, interfragmental tissue*

1. INTRODUCTION

Presented study involves the partial results of biomechanical analysis of the genesis, consolidation and ossification processes of interfragmental tissue according to several criteria in case of long bones lengthening by distraction osteogenesis method. Extension of the diaphyses in children and adolescents is achieved by planar osteotomy followed by gradual mutual distraction of the opposite

[1] Ing. arch. et Ing. František Denk; Laboratory of Biomechanics and Biomaterial engineering, Department of mechanics, Faculty of Civil Engineering, CTU in Prague; Thákurova 7, 160 00, Prague, Czech republic; frantisek.denk@fsv.cvut.cz

[2] Prof. Ing. Miroslav Petrtýl, DrSc.; Laboratory of Biomechanics and Biomaterial engineering, Department of mechanics, Faculty of Civil Engineering, CTU in Prague; Thákurova 7, 160 00, Prague, Czech republic; petrtyl@fsv.cvut.cz

[3] MUDr. Radek Myslivec; ON Příbram, a.s.; U nemocnice 84, 261 01, Příbram, Czech republic; r.myslivec@seznam.cz

[4] Doc. MUDr. Ivo Mařík, CSc.; Ambulant Centre for Defects of Locomotor Apparatus; Olšanská 7, 130 00, Prague, Czech republic; ambul_centrum@volny.cz

vital bone fragments. Controlled stress and strain changes initiated by external effects, which very effectively regulate the rate of healing and formation of new bone tissue support structures simultaneously with adequate development of elastic and viscoelastic properties, are very important for the development of quality interfragmental tissue [1].

Within presented study an evaluation of detailed radiographic analysis of the bone regenerate development is performed in a group of patients during periods of active elongation and neutral fixation. Interim results are combined with theoretical numerical simulations of homogeneous and inhomogeneous volume development of callus in various stages of new bone tissue formation process.

2. RADIOGRAPHIC ANALYSIS OF BONE REGENERATE

Radiographic analysis of the bone regenerate development during the elongation and consolidation process evaluates a total of 26 tibia and 11 femurs of 14 elongated patients with achondroplasia (the age range 6-16 years, 10 men and 4 women) and total of 14 tibia and 3 femurs of 12 elongated patients with unilateral hypoplasia (the age range 2-23 years, 4 men and 8 women) [2].

2.1 EVALUATION OF DATA SET

The average final prolongation in patients with achondroplasia was 72.8 mm on tibia and 78.7 mm on femur and in patients with unilateral hypoplasia 62.5 mm on tibia and 68.0 mm on femur. A comprehensive assessment involves determining of the callus geometric criteria CDR (Callus Diameter Ratio), i.e. the criterion of the mutual proportion of the narrowest part of callus to the osteotomy level on the tibia or femur in radiographic 2D projection, with regard to the prediction of the bone regenerate collapse possibility after fixation extraction based on extensive statistical evaluation of data sets [3]. Cases of the average CDR criteria achieved values of less than 85% mostly lead to the deformation or collapse of the bone regenerate. In evaluating set the deformation or collapse of the callus was detected in all cases at 5 tibia and 2 femurs with CDR < 85% in patiens with achondroplasia (19% of all patients), and at 6 tibia and 2 femurs with CDR < 85% of patients with unilateral hypoplasia the callus collapse occurred in cases of 5 tibia and 1 femur (total of 35% of patients). In other cases, with CDR criteria values > 85%, there has been a successful genesis of new bone tissue without any complications.

2.2 ANALYSIS OF CALLUS DEVELOPMENT DURING TREATMENT

Specific case of successful extension of the left tibia in the patient without achondroplasia (woman, 6 years) with a total treatment time of 200 days was chosen for detailed radiographic analysis of the running of interfragmental tissue formation and ossification during the active elongation and neutral fixation period (Fig. 1).

Radiographic evaluation of the callus development process from the elongation beginning is carried out by the treatment program analysis with corresponding detailed review of 2D projection images at different stages of treatment (Fig. 2, 3) [4]. The evaluation includes the monitoring of overall regenerate shape, detailed morphology and structure at characteristic stages of regeneration.

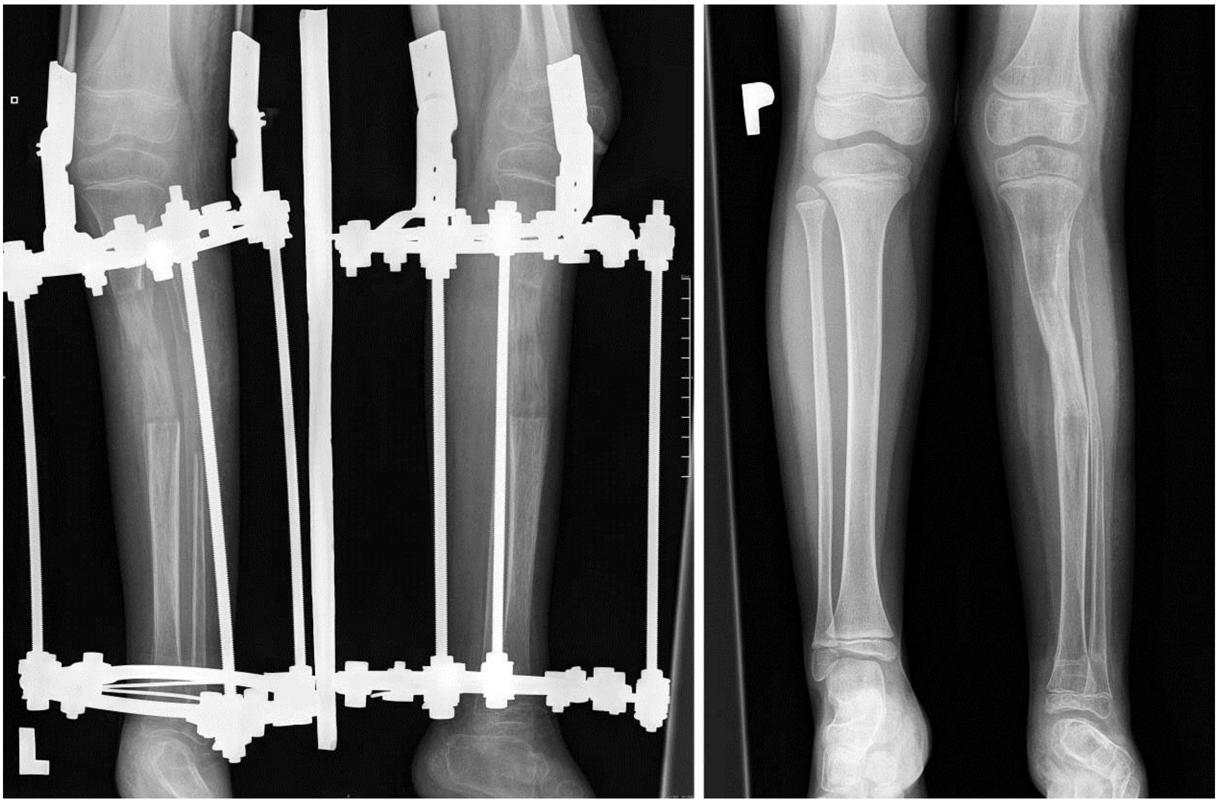

Fig. 1. 65 mm extension of the left tibia using the Ilizarov apparatus, left: tibia 3 months after osteotomy, 1 month after the end of elongation, left limb, A/P and L projection, right: tibia 6 months after osteotomy, 1 month after extraction of external fixation, both limbs, A/P projection

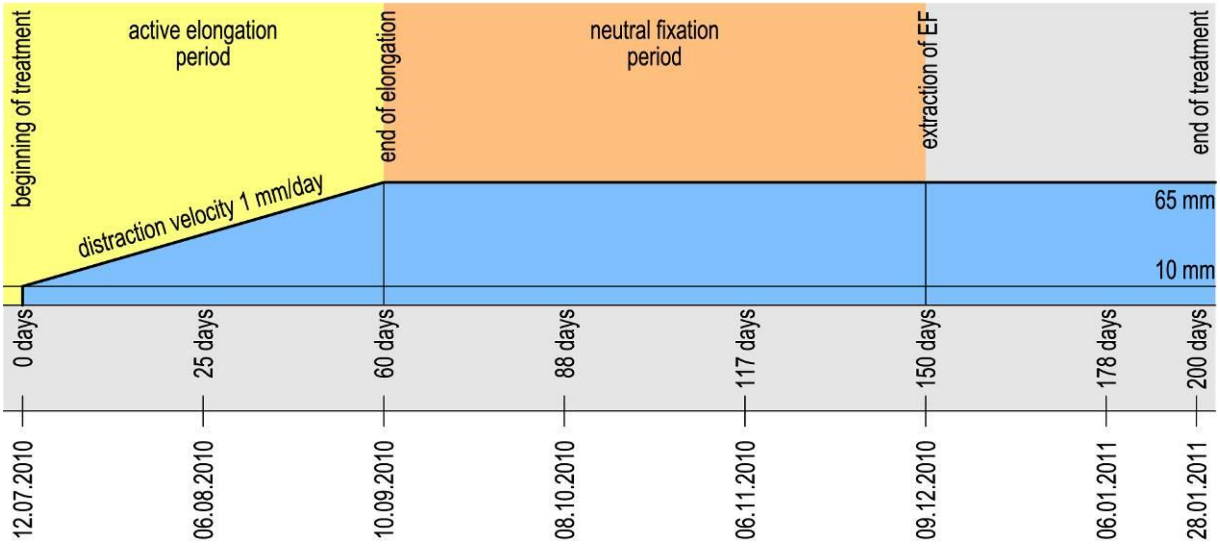

Fig. 2. Analysis of the treatment program

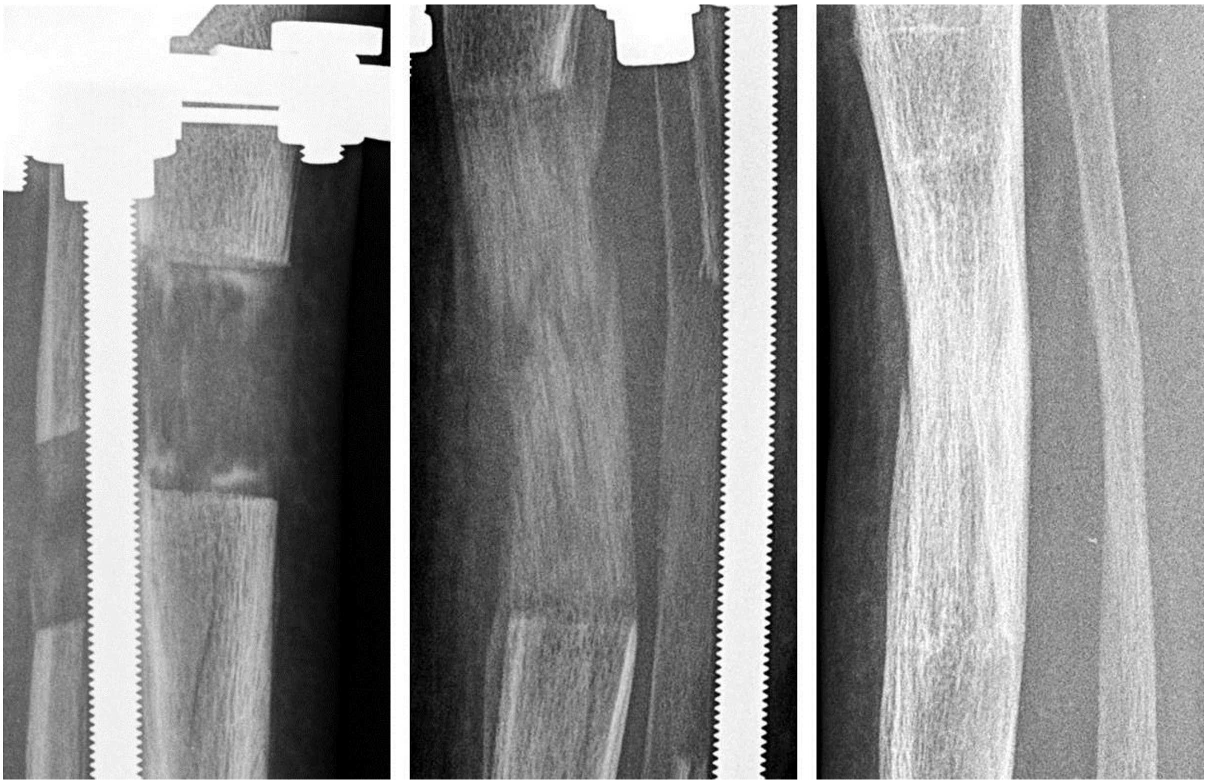

Fig. 3. Detail of interfragmental tissue formation, from left side: callus after 25 days, 88 days and 200 days from the beginning of treatment

3. NUMERICAL VERIFICATION OF INTERFRAGMENTAL TISSUE FORMATION

Numerical part of biomechanical study of bone callus genesis includes the simulation of new bone tissue formation in interfragmental space at individual stages of treatment program. The analysis is prepared in relation with the part of radiographic evaluation of a 65 mm tibia extension particular case for a detailed 3D analysis of individual characteristic bone tissue formation sub-stages during healing process, especially in the period of active elongation.

Computational process is executed using a 3D FEM model in ANSYS APDL environment. In this work, an alternative solution is made by a single iteration step, which corresponds approximately to the time around 30-th day of treatment process (active elongation period). Distribution of hydrostatic and deviatoric components of stress fields in the sagittal section under the tensile deformation load of vital bone fragments (represented by 10 mm value of the mutual movement) is the basis for the evaluation of volume and internal callus tissue structure temporal changes (Fig. 4).

The secondary objective of the numerical verifications is analysis of the bone regenerate behavior and redistribution of stress and strain states according to the change of external interfragmental tissue borders. The study takes into account the initial shape of the callus formed immediately after osteotomy and without depending on external biomechanical influences, and the shape changes initiated by biomechanical processes during extension, consolidation and ossification processes.

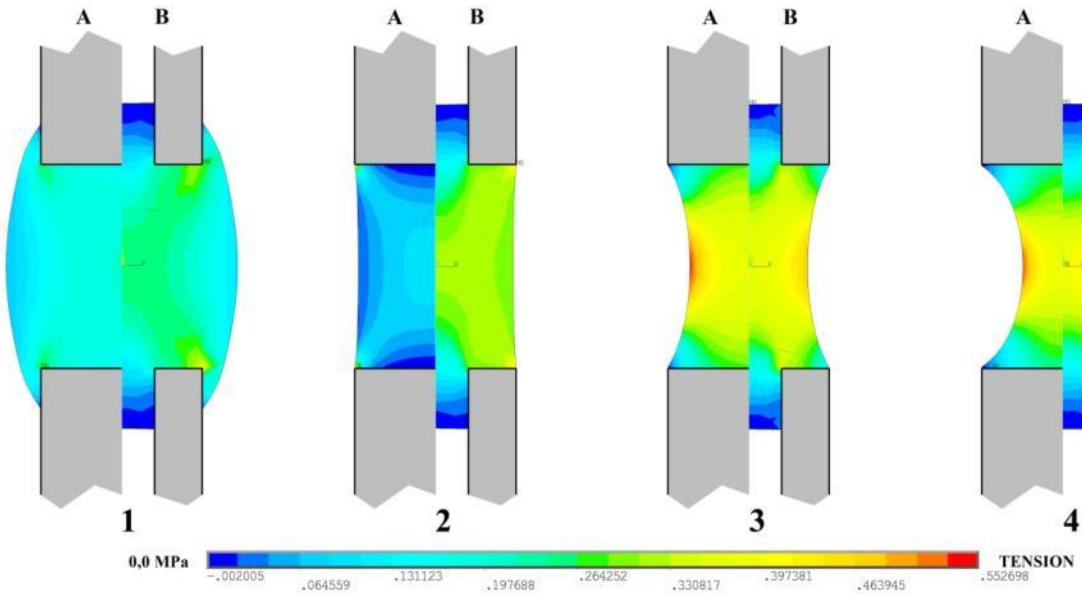

Fig. 4. Sagittal section of callus, distribution of principal stress $\boldsymbol{\sigma_1}$ (MPa), fragments without (A) and with (B) intramedullar canal, with characteristic (1) hypertrophic, (2) cylindrical, (3) concave, hypotrophic, (4) central, very hypotrophic shape of callus

4. CONCLUSION

The results of performed analyzes can be recapitulated into the following interim conclusions, which will be, in solving of other phases of prediction problem of bone regenerate biomechanical properties during long bones elongation, the subject of further detailed verifications:

(1) The radiographic and numerical analyzes of the development of the bone regenerate external geometry shows that the shape changes of borders occurs as a result of temporal changes of stress-strain states and material properties of intefragmental tissue throughout the treatment period. While immediately after osteotomy the callus can be generally characterized mostly as a hypertrophic, during the following phases in medial zone the loss of incurred granulated tissue occurs. The relatively rapid volume reduction is also evident in periosteal localities of callus near the bone shaft fragments. Simultaneously we can say that the interfragmental tissue can be approximately till 30-th day of treatment characterized as a homogeneous and isotropic (with elasticity modulus of approximately E = 1,0 MPa), corresponding to the advanced stage of granulation tissue with the beginning of fibrotisation (phase 1 of the active elongation period). The second phase of active extension period is typical by an inhomogeneous development of highly oriented fibrous tissue with the early local consolidation (ossification). In the neutral fixation period the volume re-expansion can conversely occurs, especially in medial zone of regenerate, as a result of very intensive consolidation and ossification of interfragmental tissue (due to increase of stress values and decrement of deformations). Within inhomogeneous development of callus tissue is in volume also apparent the regulation of tissue

structure organization to genetically predetermined shape of diaphysis, including the restoration of intramedullary canal. Radiographic evaluation of entire data set also confirmed that the improving of the bone regenerate geometry occurs in the following approximately 6 months after external fixator extraction, this phenomenon is called the peripheral lateral drift corticalis.

(2) Decrease of callus tissue toward the longitudinal axis of the diaphysis is characterized as **Hypotrophic drift (HD)**. Loss of the granulated tissue in the medial zone of callus is a consequence of the dominant tensile stress effect during extension process (Fig. 5).

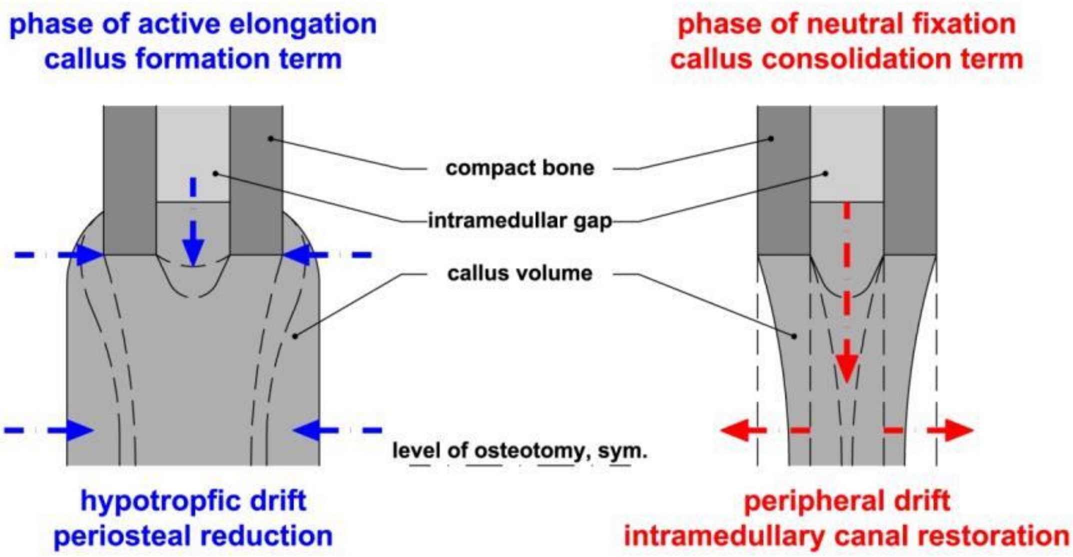

Fig. 5. Schematic sagittal section of the proximal half of the callus, the consequences of hypotrophic and peripheral drift on bone regenerate

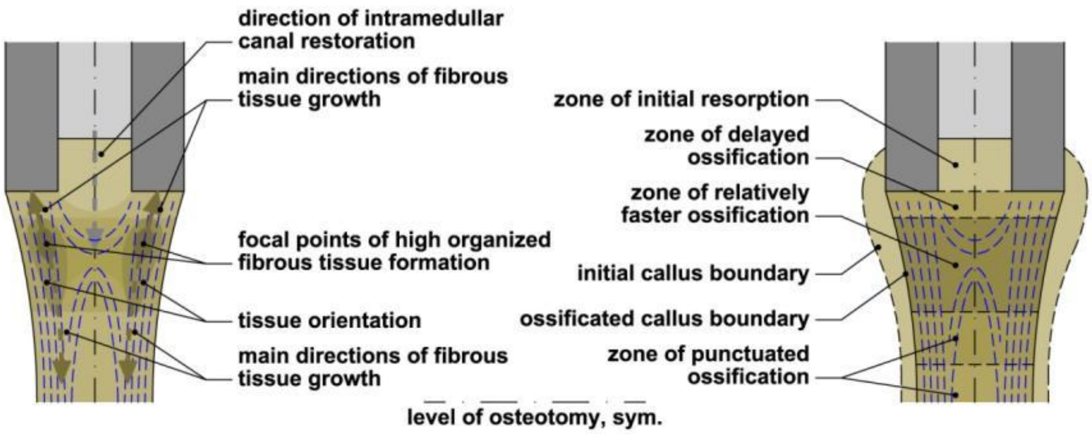

Fig. 6. Schematic sagittal section of the proximal half of the callus, left: kinetics of fibrous tissue formation, right: division of the section into the zones of inhomogeneous ossification

(3) The increase of the ossified tissue volume in the medial zone of callus away from the longitudinal axis of the diaphysis is called **Peripheral drift (PD)**. Positive hypertrophy of the bone regenerate takes place only in case of hypotrophic callus during consolidation and ossification processes (Fig. 5).

(4) Depending on the stress-strain states analysis and radiographic classification the proximal half of the callus can be divided into zones with different development of interfragmental tissue, sites with dominant production of organized tissue structures and with prediction of their expansion directions (Fig. 6). During the gradual elongation of the diaphysis, respectively, in the course of the mutual distraction of bone fragments the characteristic phenotypes of tissue structures, i.e. the sites with dominant representation of mutually different cell populations and of the various degrees of intramembranous ossification are formed in the regenerated space of callus. These in-time metabolic (biochemical) different zones are continuously interconnected. With regard to the production of tissue phenotypes in different parts of the bone regenerate volume the proximal half (at 4-th up to 6-th week after osteotomy) can be horizontally divided into three main zones:

- **Zone of punctuated ossification (ZPO)**, mostly represented by the highly organized fibrous structure. The locality is from the biomechanical point of view characterized by greatest changes of the strain in axial direction of the diaphysis, especially in the surface layers of the callus medial zone.
- **Zone of delayed ossification (ZDO)**, i.e. the locality of callus with less advanced osteogenesis due to the greatest changes of the stress state during the running of consolidation processes. The zone is in the immediate vicinity of the bone fragment surface of the diaphysis and is characterized by a vast presence of fibroblast and osteoblast populations, but without the production of osteoid.
- **Zone of relatively faster ossification (ZFO)** is locality of the most advanced osteogenesis, which is caused by comparatively time-stable distribution of stress and strain throughout the cross-section creating suitable conditions for the acceleration of intramembranous ossification and osteoid formation.

(5) The foregoing evaluation and assessment of the callus development running within the bones lengthening process forms the basis for preparing the detailed analysis of the bone regenerate behavior (formation, consolidation and ossification) throughout the treatment period and subsequently for creating an effective tool for classification and coordinated optimization of treatment program in connection with the application of new, electronically controlled, extension apparatus [5].

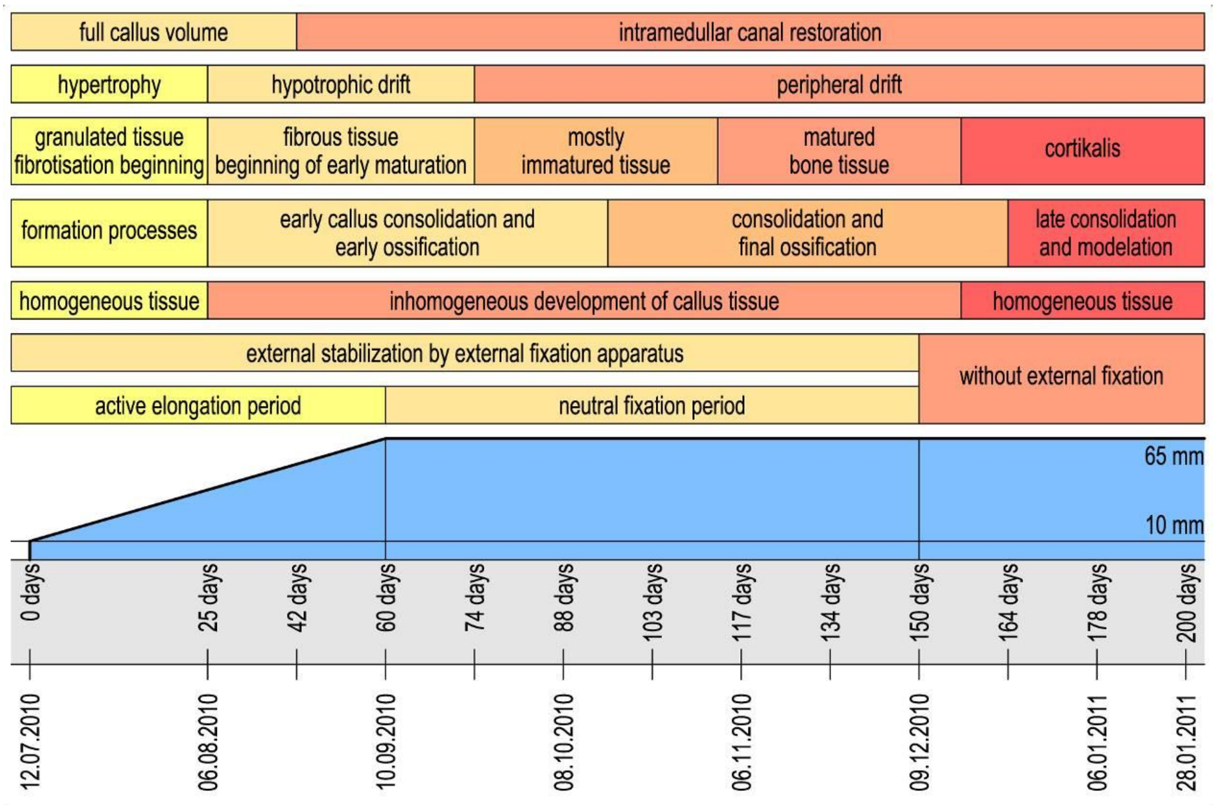

Fig. 7. Detailed analysis of the bone regenerate development during treatment period according to various criteria

ACKNOWLEDGEMENT

The financial support of this experiment by the Faculty of Civil Engineering, Czech Technical University in Prague (SGS project No. SGS12/117/OHK1/2T/11) is gratefully acknowledged.

REFERENCES

[1] MAŘÍK, I., MYSLIVEC, R., DENK, F., et.al. Bone regenerate at the long bones lengthening by Ilizarov, *Pohybové ústrojí*, 2013, **20**, 20-21. ISSN 1212-4575.

[2] MYSLIVEC, R., DENK, F., PETRÁŠOVÁ, Š., et.al. Prediction of biomechanical properties of regenerate of bone by lengthening of femur and tibia, *Pohybové ústrojí*, 2013, **20**, 21-22, ISSN 1212-4575.

[3] MAMADA, K., NAKAMURA, K., MATSUSHITA, T., et.al. The diameter of callus in leg lengthening, 28 tibial lengthening in 14 patients with achondroplasia, *Acta Orthop Scand* 1998, **69**(3), 306-310, ISSN 0001-6470

[4] LI, R., SALEH, M., YANG, L., COULTON, L. Radiographic classification of osteogenesis during bone distraction, *Journal of Orthopaedic Research* 2006, **24**, 339-347, ISSN 1554-527X

[5] LERACH, A., VÍTEK, T., PETRTÝL, M., LÍSAL, J., MAŘÍK, I., DENK, F. External monolateral fixator, *The utility design, Office of industrial property*, 24421, 2012-10-15, 2012

EXPERIMENTAL INVESTIGATION OF CONCRETE SPECIMENS FATIGUE PERFORMANCE UNDER SEVERE ENVIRONMENT

Jakub GÖRINGER[1], Marek FOGLAR[2]

Abstract:*Due to the research in concrete materials modern concrete structures could be and are more slender. For structures subjected to cyclic loadings it means higher stress ranges and thus higher probability of fatigue failure. These types of structures are often located in places with severe environment (bridges, crane tracks in chemical plants etc.). The paper presents an experimental research focused on the coupled damage of these structures. Damage due to cyclic loading interacts with damage due to aggressive environment.*

Keywords:*Concrete, Fatigue, Aggressive environment, Deflections*

1. INTRODUCTION

Nowadays concrete is one of the most widely used building materials for different kinds of structures. Along with the improvement of its properties, particularly its strength is possible to design slender and light structural elements. These modern structures exhibit higher stress concentration and also in the case of cyclically loaded structures higher stress ranges against the dead loads. Hence higher vulnerability to fatigue failure can be assumed. Many common structures are exposed to cyclic loading e.g. bridges and crane tracks. Both of these structures are often located in aggressive environment (de-icing salts for road maintenance, chemical plants).

Fatigue can be defined as a process of permanent progressive changes in the structure of material subjected to cyclic loading. Fatigue is divided by the number of cycles during the life-time to low-cycle fatigue (up to 1,000 cycles), high-cycle fatigue (up to 10,000,000 cycles) and nowadays super-high cycle fatigue (up to $5x10^8$ cycles). The influence of fatigue on changes in material structure and their descriptions have been studied by many authors [1-8]. Approach set out in [1-3] is based on usage of experimentally obtained stress-strain diagrams of concrete subjected to cyclic loading. These approaches are easy to use in common practice or for simple implementation into the FEM

[1]Ing. Jakub Göringer, Faculty of Civil Engineering, Czech Technical University in Prague, jakub.goringer@fsv.cvut.cz

[2]Ing. MarekFoglar, Ph.D., Faculty of Civil Engineering, Czech Technical University in Prague, marek.foglar@fsv.cvut.cz

solvers.Their disadvantage is the inability to capture the complex behavior of concrete under cyclic loading. More sophisticated approaches are based on continuum damage mechanics. From this group, one type is models based on usage of bounding surfaces[4, 5]. The bounding surface models are defined for example in [10]. The second type of mentioned approaches [6-9] is damage and damage-plasticity models.

It is appropriate to mention the analytical models based on experiments. The influence of changes in the material caused by cyclic loading on the deflections of concrete samples, or structures was developed by Holmen [11]. This approach was further extended by Foglar [12].

The influence of aggressive environment can be divided into two types of deterioration mechanism, mechanical –agents contained in aggressive environment crystallize in the pores of the material and cause pore pressures and consequently lead to the formation and propagation of cracks in the material matrix, chemical – the material is exposed e.g. to acid solution which reacts with concrete components and successively weakens composition of the binder. The phenomenon of chemical deterioration has been extensively investigated with regard to the effect of acid rain on concrete structures in [13-17]. The influence on the properties of concrete for various concentrations of acids was investigated in [18, 19]. All mentioned researches investigated the influence of aggressive environment for commonly used mechanical material properties – compressive strength, flexural strength and modulus of elasticity; in [18] the influence on increase of porosity was examined. Concrete mix design influence on resistance to aggressive environment was investigated by Girardi et al. [20].

Based on the mentioned researches it is clear that both areas of material damage (fatigue caused by cyclic loading, deterioration due to the aggressive environment) arewidely explored. However, the interaction of these two adverse effects has not yet been properly quantified.

2. METHODOLOGY

2.1. AGGRESSIVE ENVIRONMENT AND ITS DEFINITION

Due to the necessity to use approaches given in standards for common practice it is appropriate to define aggressive environments according to the current standards. In Europe, set of EN standards provides definition of aggressive environment for concrete structures in EN 206-1 [21] as can be seen in Tab. 1.

Tab. 1 Exposure classes for chemical attack according to EN 206-1 [21]

Chemical properties	XA1	XA2	XA3
Aggressiveness	Weak	Medium	Strong
pH	5.5 - 6.5	4.5 - 5.5	4.0 - 4.5

In the EN set for design of concrete structures is not further differentiated to which type of acidic solution the structure is exposed. From the viewpoint of conventional chemical aggression the solutions from EN 206-1 are weak. The value of pH 4.0 corresponds to concentration of H^+ ions, which cause the acidity of solution, $c_{H+}=10^{-4}$mol/dm^3. For better understanding it is worth mentioning that the juice of oranges or apples has a pH around 3.5. With regard to the cementitious materials, which pH is around 12, the environment prescribed in EN standards is very aggressive.

In developed experimental program is considered in relation to EN 206-1 with an aggressive environment consisting of hydrochloric acid (*HCl*) solution of pH 4.0.

2.2. CHEMICAL DETERIORATION OF CONCRETE

Together with the chemical composition of material the rate of chemical deterioration of concrete is primarily affected by the concentration of H^+ ions, the pH value as mentioned in the previous section and demonstrated experimentally in [13, 19]. As a main deteriorative reaction which weakens the composition of binder, the neutralization defined in equation (1)can be assumed. The dissolution of ferrite or aluminate hydrates occurs at lower values of pH and in a lesser extent than the dissolution of calcium hydroxide (*$Ca(OH)_2$*). This assumption will be experimentally verified.

$$2HCl + Ca\left(OH\right)_2 \Rightarrow CaCl_2 + 2H_2O \tag{1}$$

With the depletion of calcium hydroxide from the concrete surface layers it can be assumed that the rate of deterioration of the concrete ceases to be primarily dependent on the solution pH and that it will switch to the diffusion phenomenon that is mainly influenced by the concrete diffusivity. Scheme of expected chemical processes is shown in Fig. 1.

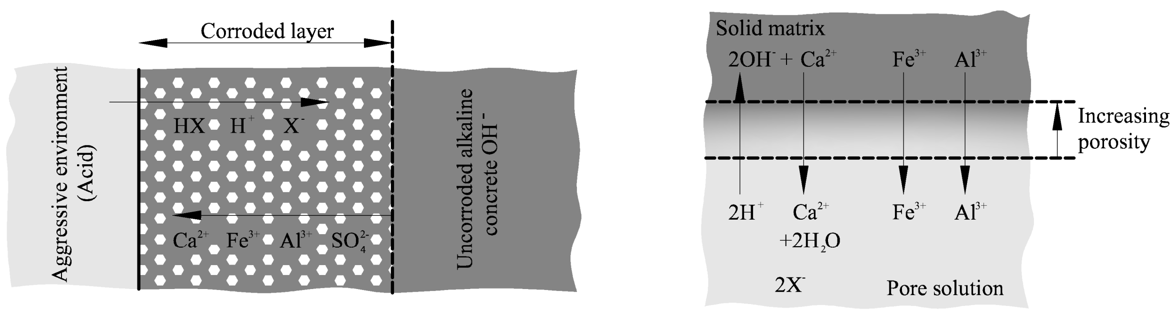

Fig. 1 Scheme of chemical deterioration processes [22]

2.3. PROBLEM FORMULATION

Assume that the major effect on the strength of the concrete has a content of calcium hydroxide (*CaO*) in the cement, which during the hydration process changes to hydration products. When using the known concrete mix design it is possible to determine the initial concentration of Ca^{2+} ions and thus determine the maximum capacity for neutralization from the amount of cement and its content of calcium hydroxide [22].

To determine the kinetics of reaction it is appropriate to use the rate equation, which in the case of neutralization according to equation (1) has the following form:

$$-\frac{dc_{Ca}}{dt} = k_{Ca} c_{H}^{\alpha} c_{Ca}^{\beta} \tag{2}$$

wherec_{Ca} = concentration of calcium in reaction, c_H = concentration of H^+ions, k_{Ca} = rate constant.

With the experimental measurements it is possible to determine the reaction order $\alpha + \beta$ which classify the reaction and rate constant. In the case, that the proposed mechanism is correct and corresponds to the experimental data set, it is possible to use the relation established in equation (2) for further calculations e.g. loss of calcium. Due to heterogeneity of concrete and uncertain input data it is appropriate to determine the kinetics of reaction using additive properties, for example the change of pH over time.

Due to the low solution concentrations the calculation of rate of calcium dissolution using the change of pH value over time can be subjected to big uncertainty. In this case it is possible to verify the calculations with mass spectrometry and determine the concentration of components (*Ca*, *Fe, Al*) in aggressive solution.

If we return to the assumption that the total amount of *CaO* in mixture affects the compressive strength of concrete it is possible to develop the relationship between time loss of Ca^{2+} ions from the material matrix due to aggressive environment and decrease of compressive strength. The result of the chemical deterioration process is primarily from this viewpoint the reduction of compressive strength. By increasing the porosity of the matrix due to the deterioration it is possible to expect reduction in other material properties – modulus of elasticity, tensile strength, flexural strength, as presented in [13-19].

For a description of fatigue deterioration the compressive strength is used in all previously mentioned approaches for modeling fatigue damage. Prerequisite for coupled deterioration due to aggressive environment and fatigue caused by cyclic loading is to combine reduction of compressive strength of both damage components. The principle of interaction of both types of damage can be seen in Fig. 2.

To develop and verify an approach to describe the interaction of fatigue and material deterioration authors are currently considering three possible approaches based on fatigue damage behavior. The first possible approach is an extension of stress-strain diagram of concrete subjected to cyclic loading [1-3]. The second approach is based on [4] with a usage of continuum damage mechanics. For common practice the analytical approach based on [11, 12] appears to be the most usable.

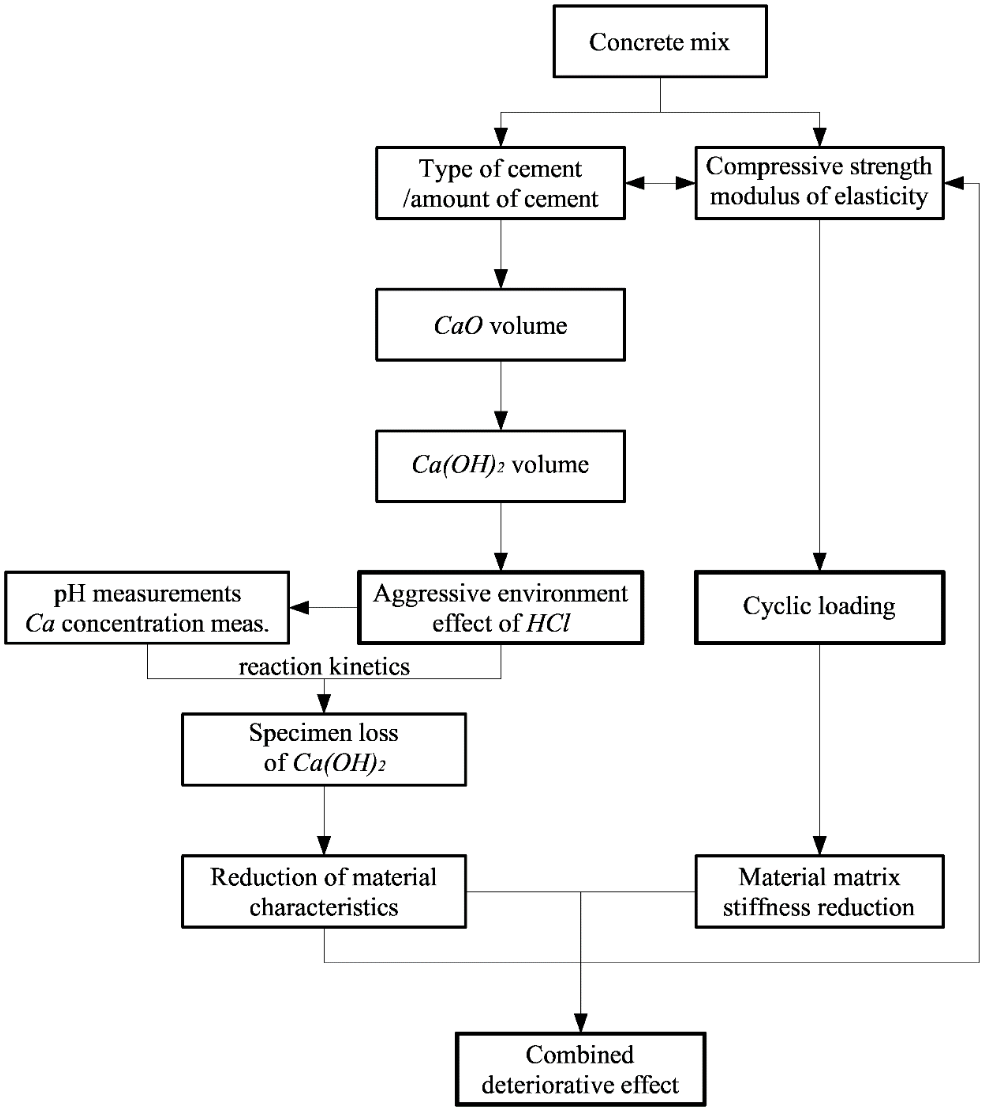

Fig. 2 Principle of interaction of damage components due to fatigue and material deterioration

3. EXPERIMENTAL PROGRAM

3.1. CONCRETE SPECIMENS

For the proposed long-term experimental program reinforced concrete specimens were designed. The strength class of concrete C25/30-X0 with low grade of resistance against the influence of environment was intentionally chosen to increase the effect of the aggressive environment. Three types of specimens will be made; beams with dimensions of 300×150×1300 mm for cyclic loading, three beams for each cyclic beam with dimensions of 100×100×400 mm for determining the modulus of elasticity, flexural and compressive strength, and one cube per set with dimensions of 150×150×150 mm for preset of modulus of elasticity experiment. All these specimen sets will be stored in dry or aggressive environment proposed in section 1.1.

The specimens for cyclic loading were designed as over-reinforced (6Ø16 grade B500 reinforcing steel), thus a failure by compressive-zone crushing should occur and the fatigue failure of concrete can be assumed.

3.2. LAYOUT OF THE FATIGUE TESTING

The arrangement of the cyclic loading is the four-point bending with span length 1000 mm and overhangs of the length of 150 mm. This testing layout has been chosen for its several advantages which are discussed later in the section 2.3. Experiments will be conducted in laboratories of Faculty of Civil Engineering, CTU in Prague.

3.3. MATERIAL MODEL POINT

Two basic types of testing layout were compared. For evaluation of the crack propagation and determination of fracture energy or fracture toughness (material properties that are commonly investigated in relation to fatigue of materials), the three-point bending layout with notch is usually chosen.

From the perspective of the structural analysis, bending cracks are crucial for acceleration of the deteriorative effects of the aggressive environment. Material point in the presented experiment is therefore a zone subjected to pure bending (decomposed to tension) without the influence of shear. According to this approach, the four-point bending layout corresponds to the mentioned assumptions. The localization zone between the loading forces is exposed to pure bending. Due to the absence of a notch it can be assumed that the concentration of maximal normal stresses occurs at the point of maximal material deterioration. This corresponds to the behavior of common structures and therefore it is used in the experimental program. The above described principle is illustrated in Fig. 2.

The purpose of the experimental program is to create an analytical tool usable for a common practice, not a sophisticated material model for advanced 2D / 3D-FEM simulations.

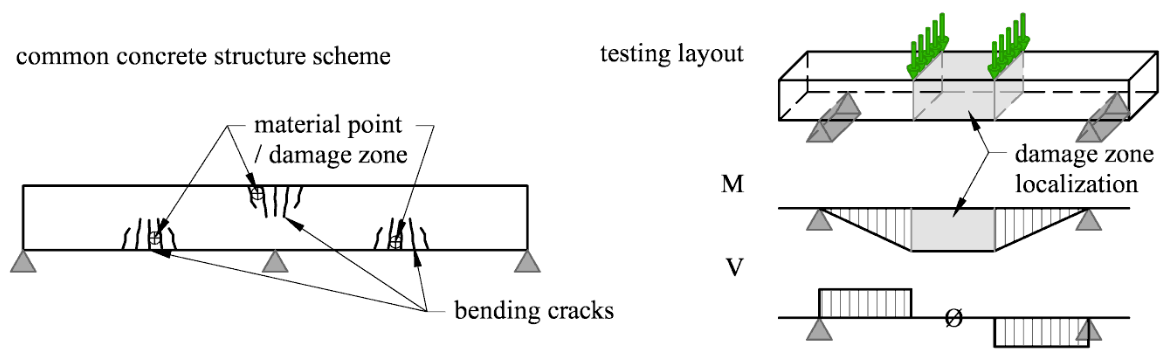

Fig. 4 Four-point bending arrangement and localization zone principle

3.4. DEFLECTION MEASUREMENTS

Two types of deflection measurements will be performed within fatigue testing. The first type – static deflection measurement which took place each hour of the cyclic loading (circa 18000 load cycles). The second type - dynamic deflection measurement which will be carried out during the fatigue testing at least once between two static deflection measurements.

4. CONCLUSION

This paper described starting long-term experimental program focused on interaction between aggressive environment and cyclic loading. Firstly the paper presents review of approaches used to describe the behavior of fatigue damage due to cyclic loading and some experimental programs focused on material deterioration due to aggressive environment, mostly acidic environment. It continues with the proposition of new approach to describe the coupled problem of both types of deterioration which will be based on forthcoming experimental program.

ACKNOWLEDGEMENT

The financial support of this experiment by the Faculty of Civil Engineering, Czech Technical University in Prague (SGS project No. 13/035/OHK1/1T/11) and Czech Science Foundation (project No. 13-30441S) is gratefully acknowledged.

REFERENCES

[1] MARTÍNEZ-RUEDA, J. and ELNASHAI, A. Confined concrete model under cyclic load. In: *Materials and Structures*. 1997, **30**, 139-147. ISSN 0025-5432.

[2] BAHN, B. and HSU C. Stress-strain behavior of concrete under cyclic loading. In: *ACI Materials Journal*. 1998, **95**(2), 178-193. ISSN 0889-325X.

[3] SINHA, B., GERSTLE, K. and TULIN, L. Stress-strain relations for concrete under cyclic loading. In: *ACI Journal Proceedings*. 1964, **61**(2), 195-210.

[4] ABU-LEBDEH, T. *Plasticity-damage bounding surface model for concrete under cyclic-multiaxial loading.* Louisiana, 1993. Doctoral thesis. Louisiana State University.

[5] YANG, B., DAFALIAS, Y. and HERRMAN, L. A bounding surface plasticity model for concrete. In: *Journal of Engineering Mechanics*. 1985, **111**(3), 359-380. ISSN 0733-9399.

[6] MAEKAWA, K., OKAMURA, H. and PIMANMAS, A. *Nonlinear mechanics of reinforced concrete.* London: Spon Press, 2003. 721p.

[7] PAPA, E. and TALIERCO, A. Anisotropic damage model for the multiaxial static and fatigue behavior of plain concrete. In: *Engineering Fracture Mechanics*. 1996, **55**(2),163-179. ISSN 0013-7944.

[8] ALLICHE, A. Damage model for fatigue loading of concrete. In: *International Journal of Fatigue*. 2004, **26**(9), 915-921. ISSN 0142-1123.

[9] GRASSL, P. and REMPLING, R. A damage-plasticity interface approach to the meso-scale modelling of concrete subjected to cyclic compressive loading. In: *Engineering Fracture Mechanics*. 2008, **75**(16), 4804-4818. ISSN 0013-7944.

[10] CHEN, W. and HAN, D. *Plasticity for Structural Engineers*.New York: Springer-Verlag, 1988. 606 p. ISBN 978-1-4612-8380-5

[11] HOLMEN, J. Fatigue of concrete by constant and variable amplitude loading. In: *NTH Bulletin*. 1979, **79**(1), 71-110.

[12] FOGLAR, M. The strain development in concrete under cyclic loading. In: *Proceedings of the 5th international conference of bridge maintenance, safety and management*. Philadephia: Balkema, 2010, pp. 3185-89. ISBN 978-0-415-87786-2.

[13] FAN, Y., HU, Z. and ZHANG, Y. Deterioration of compressive property of concrete under simulated acid rain environment. In: *Construction and Building Materials.* 2010, **24**(10), 1975-83. ISSN 0950-0618

[14] KONG, H. and ORBISON, J. Concrete deterioration due to acid precipitation. In: *ACI Materials Journal*. 1987, **24**(2), 110-116. ISSN 0889-325X

[15] CHEN, M., WANG, K. and XIE, L. Deterioration mechanism of cementitious materials under acid rain attack. In: *Engineering Failure Analysis*. 2013, **27**, 272-285. ISSN 1350-6307.

[16] XIE, S., QI, L. and ZHOU, D. Investigation of the effects of acid rain on the deterioration of cement concrete using accelerated tests established in laboratory. In: *Atmospheric Environment.* 2004, **38**(27), 4457-66. ISSN 1352-2310.

[17] OKOCHI, H. et al. Deterioration of concrete structures by acid deposition – an assessment of the role of rainwater on deterioration by laboratory and field exposure experiments using mortar specimens. In: *Atmospheric Environment*. 2000, **34**(18), 2937-45. ISSN 1352-2310.

[18] FAN, Y., LUAN, H. and ZHANG, S. Multiscale investigation of porosity characteristics in concrete exposed to acidic environment. In: *Int. Journal of Corrosion.* 2012. ISSN 1687-9325.

[19] HUANG, P., BAO, Y. and YAO, Y. Influence of HCl corrosion on the mechanical properties of concrete. In: *Cement and Concrete Research.* 2005, **35**(3), 584-589. ISSN 0008-8846.

[20] GIRARDI, F., VAONA, W. and MAGGIO, R. Resistance of different types of concretes to cyclic sulfuric acid and sodium sulfate attack. In: *Cement & Concrete Composites.* 2010, **32**(8), 595-602. ISSN 0958-9465.

[21] ČSN EN 206-1. *Beton – Část 1: Specifikace, vlastnosti, výroba a shoda*. Praha: Český normalizační institut, 2001.

[22] BEDDOE, R. and DORNER, H. Modelling acid attack on concrete: Part I. The essential mechanism. In: *Cement and Concrete Research*. 2005, **35**(12), 2333-39. ISSN 0008-8846.

[23] DORNER, H. and BEDDOE, R. Prognosis of concrete corrosion due to acid attack. In: *9th Int. Conf. on Durability of Building Materials*. Brisbane: CSIRO, 2002. ISBN 978-0-643-06827-8.

POLYNOMIAL CHAOS-BASED QUANTIFICATION OF UNCERTAINTY IN DESCRIPTION OF GROUNDWATER FLOW THROUGH RANDOM MATERIALS

Jan HAVELKA[1], **Jan SÝKORA**[2], **Anna KUČEROVÁ**[3]

Abstract: *The prediction of groundwater flow is strongly influenced by the soil permeability generally varying within the space. Determination of the spatial distribution of the permeability is, however, unfeasible and thus the relevant uncertainties should be taken into account. One possibility is to describe the soil permeability by a random field. The present contribution is devoted to propagation of these uncertainties in permeability into probabilistic description of groundwater flow. The attention is paid the acceleration of the propagation using a polynomial chaos-based approximation of groundwater flow.*

Keywords: *uncertainty propagation, stochastic modelling, polynomial regression, stochastic collocation, groundwater flow*

1. INTRODUCTION

This paper is focused on the modeling of uncertainties in material properties and investigates the influence of such uncertainties on groundwater flow, described by a steady-state diffusion equation. As a simple example, consider the following (deterministic) elliptic partial differential equation (PDE) for the hydraulic head $u(x)$:

$$-\nabla \cdot (\kappa(x)\nabla u(x)) = f(x), \qquad x \in D, \tag{1}$$

$$u(x) = g(x), \qquad x \in \partial D, \tag{2}$$

where $\kappa(x)$ is the soil permeability (hydraulic conductivity), $f(x)$ is a given source or sink inside the region D ($D \subset \mathbb{R}^2$) and $g(x)$ are prescribed flows and hydraulic heads on the boundary ∂D.

[1] Bc. Jan Havelka, Faculty of Civil Engineering, Department of Mechanics, Czech Technical University in Prague, jan.havelka.1@fsv.cvut.cz

[2] Ing. Jan Sýkora, PhD., Faculty of Civil Engineering, Department of Mechanics, Czech Technical University in Prague, jan.sykora.1@fsv.cvut.cz

[3] Ing. Anna Kučerová, PhD., Faculty of Civil Engineering, Department of Mechanics, Czech Technical University in Prague, anicka@cml.fsv.cvut.cz

Consider now a system involving material variability. If the input parameter is defined as a random field, the system would be governed by a set of stochastic partial differential equations (SPDE) and the corresponding responses would also be random vectors of nodal displacements, see [1, 2]. Let us formulate this for the soil permeability $\kappa(x)$. A random model is obtained by defining $\kappa(x)$ for each $x \in D$ as a random variable $\kappa(x) : \mathit{\Omega} \to \mathbb{R}$ on a suitable probability space $(\mathit{\Omega}, \mathscr{S}, \mathbb{P})$. As a consequence, $\kappa : D \times \mathit{\Omega} \to \mathbb{R}$ is a random field, where any elementary event $\omega \in \Omega$ gives a realization $\kappa(\cdot, \omega) : D \to \mathbb{R}$ of the soil permeability. Alternatively, $\kappa(x, \omega)$ can be seen as a collection of real-valued random variables indexed by $x \in D$, see [1, 3, 4]. Introduction of random system parameters into Eqs. (1) and (2) we obtain the stochastic partial differential equation:

$$-\nabla \cdot (\kappa(x,\omega)\nabla u(x,\omega)) = f(x,\omega), \qquad x \in D, \tag{3}$$

$$u(x,\omega) = g(x,\omega), \qquad x \in \partial D. \tag{4}$$

In order to solve this stochastic partial differential equation and obtain the approximate responses of the system, Monte Carlo (MC) method is usually used. The effort of performing Monte Carlo simulations is high, and hence alternative techniques have been developed, such as the spectral stochastic finite element method (SSFEM). The interested reader is referred to [1, 5, 6] for further information.

2. DISCRETIZATION OF RANDOM FIELDS

Assuming the random field $\kappa(x, \omega)$ to be Gaussian, it is defined by its mean

$$\mu_\kappa(x) = \mathbb{E}[\kappa(x,\omega)] = \int_{\mathit{\Omega}} \kappa(x,\omega)\, \mathbb{P}(\mathrm{d}\omega) \tag{5}$$

and its covariance

$$\begin{aligned} C_\kappa(x,x') &= \mathbb{E}[(\kappa(x,\omega) - \mu_\kappa(x))(\kappa(x',\omega) - \mu_\kappa(x'))] \\ &= \int_{\mathit{\Omega}} (\kappa(x,\omega) - \mu_\kappa(x))(\kappa(x',\omega) - \mu_\kappa(x'))\, \mathbb{P}(\mathrm{d}\omega)\,. \end{aligned} \tag{6}$$

In a computational setting, the random field and the numerical model must be discretized. The most common approach for achieving this is the Karhunen-Loéve expansion (KLE), see [4]. KLE is an extremely useful tool for the concise representation of the stochastic processes. Based on the spectral decomposition of covariance function $C_\kappa(x, x')$ and the orthogonality of eigenfunctions ψ_i, the random field $\kappa(x, \omega)$ can be written as

$$q(x,\omega) = \mu_\kappa(x) + \sum_{i=0}^{\infty} \sqrt{\varsigma_i}\xi_i(\omega)\psi_i(x), \tag{7}$$

where $\boldsymbol{\xi}(\omega) = (\ldots, \xi_i(\omega), \ldots)^{\mathrm{T}}$ is a set of uncorrelated random variables of zero mean and unit variance. The spatial KLE functions $\psi_i(\boldsymbol{x})$ are the eigenfunctions of the Fredholm integral equation with the covariance function as the integral kernel:

$$\int_D C_\kappa(x, x')\psi_i(x)\mathrm{d}x' = \varsigma_i \psi_i(x)\,, \tag{8}$$

where ς_i are positive eigenvalues ordered in a descending order.

Since the covariance is symmetric and positive definite, it can be expanded in the series

$$C_\kappa(x, x') = \sum_{i=1}^{\infty} \varsigma_i \psi_i(x)\psi_i(x')\,. \tag{9}$$

However, computing the eigenfunctions analytically is usually not feasible. Therefore, one discretizes the covariance spatially according to chosen grid points (usually corresponding to a finite element mesh). The resulting covariance matrix $\mathbf{C}_\kappa$ is again symmetric and positive definite and Eq. (8) becomes symmetric matrix eigenvalue problem, see [1], where the eigenfunctions $\psi_i(x)$ are replaced by eigenvectors $\boldsymbol{\psi}_i$. The eigenvalue problem is usually solved by a Krylov subspace method with a sparse matrix approximation. For large eigenvalue problems, [7] proposes the efficient low-rank and data sparse hierarchical matrix techniques.

For practical implementation, the series (7) and (9) are truncated after M terms, yielding the approximations

$$\hat{\boldsymbol{\kappa}}(\omega) \approx \mu_\kappa + \sum_{i=1}^{M} \sqrt{\varsigma_i}\xi_i(\omega)\boldsymbol{\psi}_i\,, \tag{10}$$

$$\hat{\mathbf{C}}_\kappa \approx \sum_{i=1}^{M} \varsigma_i \boldsymbol{\psi}_i^{\mathrm{T}} \cdot \boldsymbol{\psi}_i\,. \tag{11}$$

Such spatial semi-discretization is optimal in the sense that the mean square error resulting from a truncation after the M-th term is minimized.

2.1. NUMERICAL STUDY

This section supports through numerical study the proposed methodology. In doing so we consider geometry together with the initial and loading conditions displayed in Fig. 1. 2-D domain was discretized by an FE mesh into 1195 nodes and 2228 triangular elements.

It is clear from the preceding text that the implementation of the Karhunen-Loève expansion requires knowing the covariance function of the process being expanded. We assume the normalized exponential

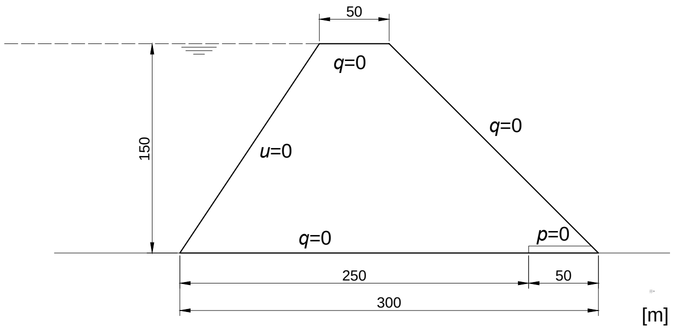

Fig. 1 2-D domain with boundary conditions

covariance kernel described by following formula:

$$C_\kappa = \exp\left(-\left|\frac{x-x'}{l_x}\right| - \left|\frac{y-y'}{l_y}\right|\right), \tag{12}$$

where $l_x = 5$ [m] and $l_y = 3$ [m] are covariance lengths. In practise, the correlation lengths can be determined by the image analysis of a given material [8]. Several interesting results have been derived within the scope of the calculation of KLE. Associated eigenvectors are collected in Figs. 2(a)-(d) and Figs. 3(a)-(b) shows a comparison of an arbitrary realization of hydraulic field $\kappa(x)$ computed using all 1195 eigenmodes and its approximation $\hat{\kappa}(x)$ computed using only the first 100 eigenmodes.

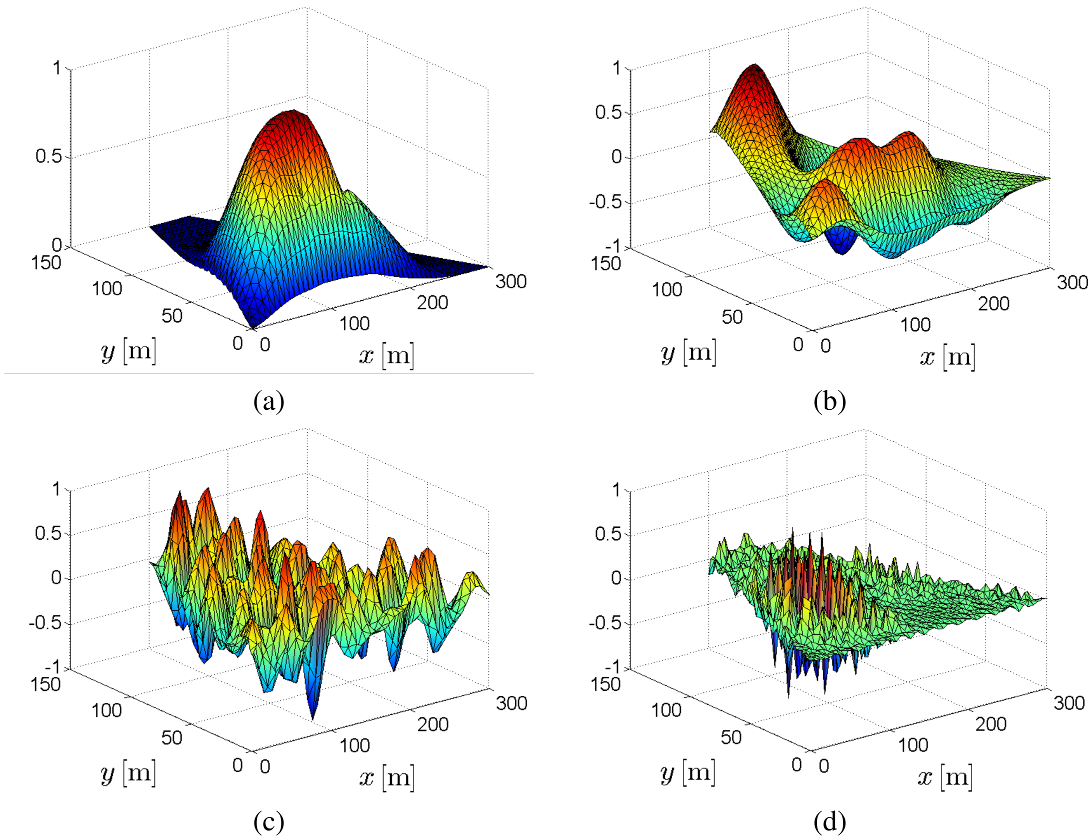

Fig. 2 Examples of eigenvectors ψ_i, (a) $i = 1$, (b) $i = 10$, (c) $i = 100$, (d) $i = 1195$

In order to choose an appropriate number of eigenmodes, a relative pointwise error of input fields averaged over all finite elements and over independent random realizations was computed. A similar

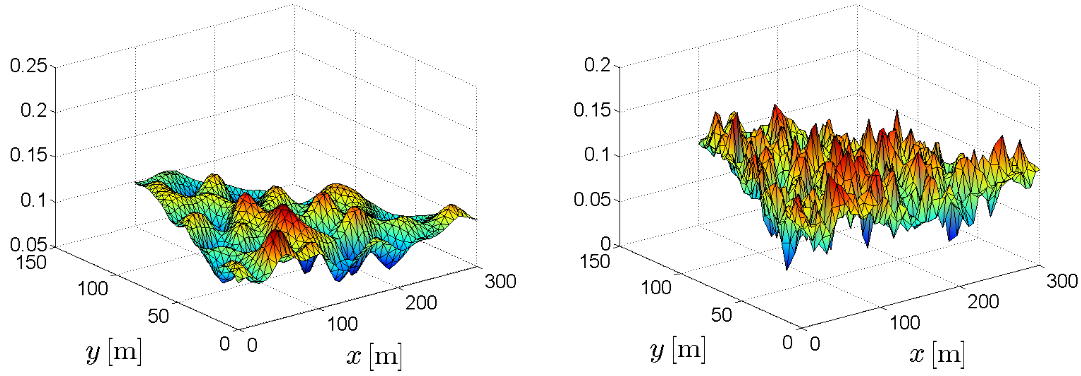

(a) (b)

Fig. 3 The hydraulic conductivity field computed using, (a) only the first 100 eigenmodes, (b) all 1195 eigenmodes

error can be also computed in terms of response fields. These errors as a function of the number of eigenmodes M involved in the description of input fields are depicted in Fig. 4. It can be seen again that the error in description of input fields is decreasing slowly, while the error in the response fields descends much faster due to the smoothing effect of the numerical model.

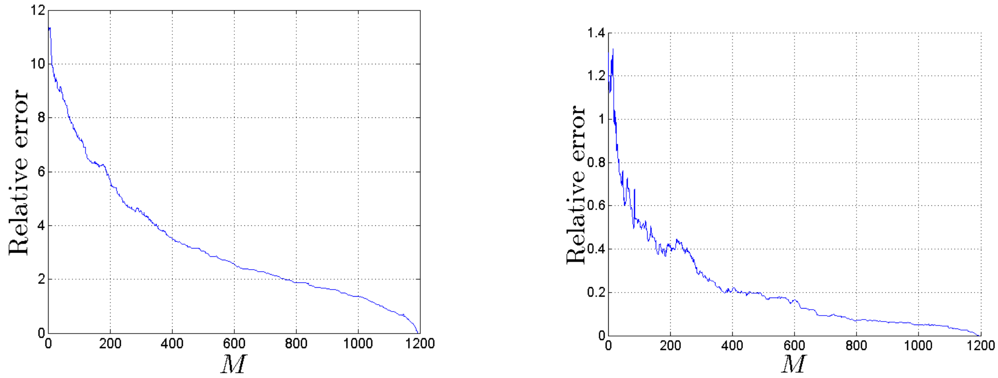

(a) (b)

Fig. 4 Relative mean point-wise error [%], (a) of the input hydraulic conductivity field and (b) of the overall responses induced by KLE approximation based on M eigenmodes

3. SURROGATE MODEL

While the KLE can be efficiently applied to reduce the number of random variables, construction of a surrogate of the computational model can be used for a significant acceleration of each sample evaluation. Here we employ the stochastic collocation method [9] to construct the surrogate model based on polynomial chaos expansion (PCE).

According to Eq. (10), all model parameters are described by M independent standard Gaussian RVs $\boldsymbol{\xi}(\omega) = (\xi_1(\omega), \ldots, \xi_M(\omega))^{\mathrm{T}}$. Hence, the discretised model response $\boldsymbol{u}(\boldsymbol{\xi}(\omega)) = (\ldots, u_i(\boldsymbol{\xi}(\omega)), \ldots)^{\mathrm{T}}$ is a random vector which can be expressed in terms of the same RVs $\boldsymbol{\xi}(\omega)$. Since $\boldsymbol{\xi}(\omega)$ are independent standard Gaussian RVs, Wiener's PCE based on multivariate Hermite polynomials—orthogonal in the

Gaussian measure—$\{H_\alpha(\boldsymbol{\xi}(\omega))\}_{\alpha\in\mathcal{J}}$ is the most suitable choice for the approximation $\tilde{\boldsymbol{u}}(\boldsymbol{\xi}(\omega))$ of the model response $\boldsymbol{u}(\boldsymbol{\xi}(\omega))$ [10], and it can be written as

$$\tilde{\boldsymbol{u}}(\boldsymbol{\xi}(\omega)) = \sum_{\alpha\in\mathcal{J}} \boldsymbol{u}_\alpha H_\alpha(\boldsymbol{\xi}(\omega)), \tag{13}$$

where $\boldsymbol{u}_\alpha$ is a vector of PC coefficients and the index set $\mathcal{J} \subset \mathbb{N}_0^{(\mathbb{N})}$ is a finite set of non-negative integer sequences with only finitely many non-zero terms, i.e. multi-indices, with cardinality $|\mathcal{J}| = R$.

3.1. STOCHASTIC COLLOCATION

Stochastic collocation method is based on an explicit expression of the PC coefficients:

$$u_{\alpha,i} = \int u_i(\boldsymbol{\xi}) H_\alpha(\boldsymbol{\xi})\, \mathrm{d}\mathbb{P}(\boldsymbol{\xi})\,, \tag{14}$$

which can be solved numerically using an appropriate integration rule (quadrature) on $\mathbb{R}^{n_\xi}$. Equation *(14)* then becomes

$$u_{\alpha,i} = \sum_{j=1}^{N} u_i(\boldsymbol{\xi}_j) H_\alpha(\boldsymbol{\xi}_j) w_j\,, \tag{15}$$

where $\boldsymbol{\xi}_j$ stands for an integration node, w_j is a corresponding weight and N is the number of quadrature points. Here we employ versions of the Smolyak quadrature rule, in particular quadratures with the Gaussian rules as basis for normal distribution and nested Kronrod-Patterson quadrature rules see [11].

The quality of a PC-based surrogate model depends on the number M of eigenmodes involved in KLE describing the fields of material properties as well as on the degree of polynomials P used in the expansion Eq. *(13)*[4]. Figure 5 shows the error estimate $\varepsilon(\boldsymbol{u})$ computed for different numbers of eigenmodes M and for the polynomial order $P = 2, 3, 4$. Here, the response fields $\boldsymbol{u}^a$ are computed by the FEM based on one realization of the KLE of the parameter fields (further shortly called FE simulations) and the response fields $\boldsymbol{u}^b$ are obtained by evaluation of the constructed PCE in the same sample point. The solid lines represent the error induced by PC approximation and the KL approximation of the parameter fields.

[4] We assume the full PC expansion, where number of polynomials R is fully determined by the degree of polynomials P and number of eigenmodes M according to the well-known relation $R = (M + P)!/(M!P!)$.

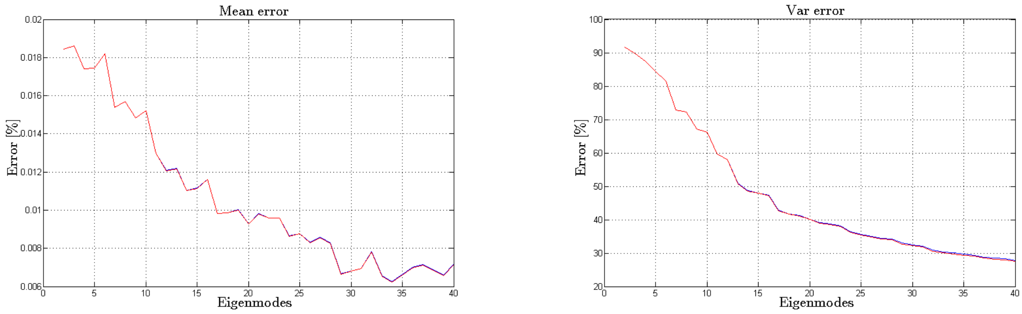

(a) (b)

Fig. 5 Errors in approximation of the the hydraulic head induced by PCE and KLE as a function of number of eigenmodes, (a) mean, (b) variance.

4. CONCLUSION

This paper presents the stochastic numerical study of groundwater flow in random media under steady-state conditions. For a sake of simplicity, the random fields representing the heterogenity of porous media are assumed to be Gaussian.

The surrogate model based on the stochastic collocation and the polynomial chaos expansion is introduced as a promising alternative to the very computationally exhaustive Monte Carlo technique.

ACKNOWLEDGEMENTS

This outcome has been achieved with the financial support of the Czech Science Foundation, project No. 105/11/0411 and 105/12/1146.

REFERENCES

[1] KEESE, A. and MATTHIES, H.G. Hierarchical parallelisation for the solution of stochastic finite element equations. *Computers and Structures*, 2005, **83**, 1033–1047, ISSN 0045-7949.

[2] KUČEROVÁ, A. and SÝKORA, J. Uncertainty updating in the description of coupled heat and moisture transport in heterogeneous materials. *Journal of Computational and Applied Mathematics*, 2013, **219(13)**, 7252–7261, ISSN 0096-3003.

[3] KEESE, A. *Numerical Solution of Systems with Stochastic Uncertainties.*, 2004, PhD thesis, TU Braunschweig.

[4] EIRMANN, M., ERNST, O.G. and ULLMANN, E. Computational aspects of the stochastic finite element method. *Computing and Visualization in Science*, 2008, **10**, 3–15, ISSN 1432-9360, 1433-0369.

[5] KUČEROVÁ, A., SÝKORA, J., ROSIĆ, B. and MATTHIES, H.G. Acceleration of uncertainty updating in the description of transport processes in heterogeneous materials. *Journal of Computational and Applied Mathematics*, 2012, **236(18)**, 4862–4872, Available from: http://arxiv.org/abs/1110.2049.

[6] CHEN, N.Z. and SOARES, C.G. Spectral stochastic finite element analysis for laminated composite plates. *Computer Methods in Applied Mechanics and Engineering*, 2008, **197**, 4830–4839, ISSN 0045-7825.

[7] KHOROMSKIJ, B.N. and LITVINENKO, A. Data sparse computation of the Karhunen-Loéve expansion. *Proceedings of International Conference on Numerical Analysis and Applied Mathematics 2008*, 2008, **1048**, pp. 311–314, ISSN 0094243X.

[8] LOMBARDO, M., ZEMAN, J., ŠEJNOHA, M. and FALSONE, G. Stochastic modeling of chaotic masonry via mesostructural characterization. *International Journal for Multiscale Computational Engineering*, 2010, **7**, pp. 171–185, Available from: http://arxiv.org/abs/0811.0972.

[9] BABUSKA, I., NOBILE, F. and TEMPONE, R. A Stochastic Collocation Method for Elliptic Partial Differential Equations with Random Input Data. *SIAM Journal on Numerical Analysis*, 2007, **45(3)**, 1005–1034, ISSN 0036-1445, 1095-7200.

[10] XIU, D. and KARNIADAKIS, G. E. The Wiener–Askey Polynomial Chaos for Stochastic Differential Equations. *SIAM Journal on Scientific Computing*, 2002, **24(2)**, pp. 619–644, ISSN 1064-8275.

[11] HEISS, F. and WINSCHEL, V. Likelihood approximation by numerical integration on sparse grids. *Journal of Econometrics*, 2008, **144(1)**, pp. 62–80, ISSN 0304-4076.

DEFICIENCIES OF THE MICROPRESTRESS-SOLIDIFICATION THEORY

Petr HAVLÁSEK[1], **Milan JIRÁSEK**[2]

Abstract: *The microprestress-solidification theory is a widely used material model for concrete creep and shrinkage. It describes these phenomena at the material point level and is capable of capturing the effects of variable humidity and temperature. However, it turns out that this model has several essential deficiencies, which are presented and analyzed in this contribution.*

Keywords: *Creep, shrinkage, concrete, numerical modeling, microprestress, solidification*

1. INTRODUCTION

The microprestress-solidification theory (MPS) [1], [2] is a widely used material model for concrete creep and shrinkage. Up till now, the first paper on the MPS has been cited in Scopus 105× and the second one (extension for temperature effects) 40×. Despite of its popularity and recognition, this model suffers from several essential deficiencies which are presented in this paper.

2. DESCRIPTION OF THE MATERIAL MODEL

The MPS model does not use the "average cross-sectional" approach exploited by many other models for concrete creep and shrinkage (B3/3.1/4, ACI 209, GL2000, *fib*), but instead works at the "material point" level. This allows for a more accurate and realistic description of the stress distribution in the concrete member.

The complete constitutive model can be represented by the rheological scheme shown in Fig. 1. It consists of (i) a non-aging elastic spring, representing instantaneous elastic deformation, (ii) a solidifying Kelvin chain, representing short-term creep, (iii) an aging dashpot representing long-term creep, (iv) a shrinkage unit, representing volume changes due to drying, (v) a unit representing thermal expansion, and (vi) a unit representing cracking. All these units are connected in series, and thus the total strain is the sum of the individual contributions, while the stress transmitted by all units is the same.

[1] Ing. Petr Havlásek, Department of Mechanics, Faculty of Civil Engineering, Czech Technical University in Prague, petr.havlasek@fsv.cvut.cz

[2] Prof. Ing. Milan Jirásek, DrSc., Department of Mechanics, Faculty of Civil Engineering, Czech Technical University in Prague, milan.jirasek@fsv.cvut.cz

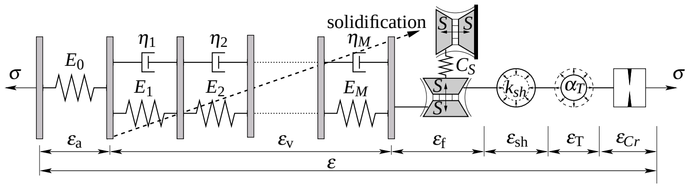

Fig. 1 Rheological scheme of the complete hygro-thermo-mechanical model

Further description of the material model can be found in [1], [2]).

The material model was implemented into the finite element package OOFEM [3, 4, 5], which was used to run all numerical computations. All examples have been run as a staggered problem, with the moisture transport analysis preceding the mechanical analysis.

3. EXPERIMENTS OF BRYANT AND VADHANAVIKKIT (1987)

3.1. EXPERIMENTAL SETUP

Reference [6] presents shrinkage and creep data of prismatic and "slab" specimens. Effects of the specimen size, shape and age at loading on creep and shrinkage have been examined. All specimens were made of the same concrete mixture composed from: 390 kg/m^3 of ordinary Portland cement, 183 kg/m^3 of water (w/c = 0.47), 1667 kg/m^3 of coarse aggregates, and 318 kg/m^3 of sand (a/c = 5.09). The concrete mixture contained no additives. The 28-day compressive strength determined on 150 $\times$ 300 mm cylinders was 50.1 MPa, and the modulus of elasticity 29.8 GPa.

The mold was removed after two days and the specimens were moved to the controlled environment room with relative humidity $h_{\text{env}} = 95\%$, which was dropped to $h_{\text{env}} = 60\%$ after 6 days. The temperature was kept throughout the experiment at 20°C. Creep specimens were loaded by external or internal bars causing a compressive stress of 7 MPa.

All faces of the companion sealed specimens, 4 faces of the "slab" specimens, and 2 parallel faces of the prismatic specimens were sealed with a 0.035 mm thick aluminum foil. The sealing had failed after approximately 300 days. This failure had a significant impact on sealed specimens (failure is accompanied by sudden increase in creep rate and shrinkage) but only a partial effect on slab segments which had by the time of sealing failure already partially dried out. All sealed specimens had the size of 150$\times$150$\times$600 mm, drying specimens (prismatic and wall) D$\times$D$\times$4D with D = 100, 150, 200, 300 or 400 mm.

Experimental results for basic creep are shown in Fig. 2, shrinkage in Fig. 3, and creep of drying specimens in Figs. 4 and 5.

3.2. NUMERICAL SIMULATIONS

First, it was essential to determine parameters q_1–q_4 controlling the basic creep. The first estimate was based on the empirical formulae of the B3 model which use the value of the compressive strength and concrete mixture. However, this prediction overestimates the effect of aging and also gives a too low viscoelastic compliance (see Fig. 2a). In order to get an acceptable agreement with the experimental data it was necessary to modify parameters q_1–q_3 while parameter q_4 controlling long-time creep was kept at its original value (see Fig. 2b for the improved fit; predicted and adjusted values of parameters q_1–q_4 are listed in Table 1).

Next, it was necessary to fit 4 parameters of the Bažant-Najjar moisture transport model [7], one shrinkage parameter, one drying creep parameter, and finally 2 parameters controlling cracking.

It has been found that the exact values of the cracking parameters (tensile strength and fracture energy) do not matter (if they are within a reasonable range characteristic of the given concrete class). What significantly matters is whether or not cracking is assumed – see Fig. 6 for comparison. If cracking is neglected, the shrinkage deformation grows faster and reaches a higher final value. On the other hand the compliance is higher if cracking is assumed; the reason is that the compliance is computed as a difference of the total and shrinkage strains divided by the compressive stress. Therefore a smaller value of the shrinkage strain is subtracted from the total strain and this results in a higher compliance.

Since no information on humidity profiles or water loss were available, the only option how to determine parameters of the Bažant-Najjar model was to exploit the assumption of the MPS theory postulating the proportionality of the humidity change and shrinkage strain at the material point level. The approximate values of parameters can be then obtained inversely by fitting experimentally measured shrinkage curves. A trial-and-error procedure was used to calibrate these values and k_{Sh} on shrinkage data of a 150 mm thick slab (thick black line in Fig. 3a). The remaining gray curves show (except the last data point in 200 mm, 300 mm and 400 mm series) that with these parameters the agreement with the rest of experimental data is excellent. Still reasonable is the fit of shrinkage data of prismatic specimens – see Fig. 3b. The measured value of shrinkage at the age of 2000 days of larger specimens is lower than modeled. (An approximate value of μ_S can be used in this set of simulations, because shrinkage development is not sensitive to that value. Parameter μ_S replaces the product $c_0 c_1 q_4$.)

Finally the remaining parameter μ_S controlling the magnitude of the drying creep was calibrated to give the best possible agreement with the experimental measurements on a 150 mm thick drying slab (gray long-dashed line in Fig. 4a). It seems that the "final" value of the drying creep is captured correctly, even though the drying creep seems to be significantly delayed; this delay is in the remaining cases even more pronounced. However, the time delay of the drying creep is not the biggest disadvantage. What is striking is that the final value of the drying creep is incorrectly scaled with specimen size. The smaller the specimen size the smaller is the final value of the drying creep, which contradicts experimental observations – see Figs. 4a and b. To show this behavior in more detail, the basic creep has been subtracted from the total compliance and the resulting drying creep and cracking strain are plotted in Fig. 7. In this figure the red curve corresponds to the smallest specimen size and the blue one to the biggest.

Creep of partially predried slabs and prisms is shown in Fig. 5. In the first case (drying slabs, Fig. 5a), the magnitude of the drying creep seems to be captured correctly. In the latter case (drying prisms, Fig. 5b) the drying creep is underestimated (approx 1/2 - 2/3 of the correct value). Naturally–in both cases the more predried the specimen, the smaller the time delay between experimental and numerically obtained values.

All values of parameters are summarized in Tables 1 and 2.

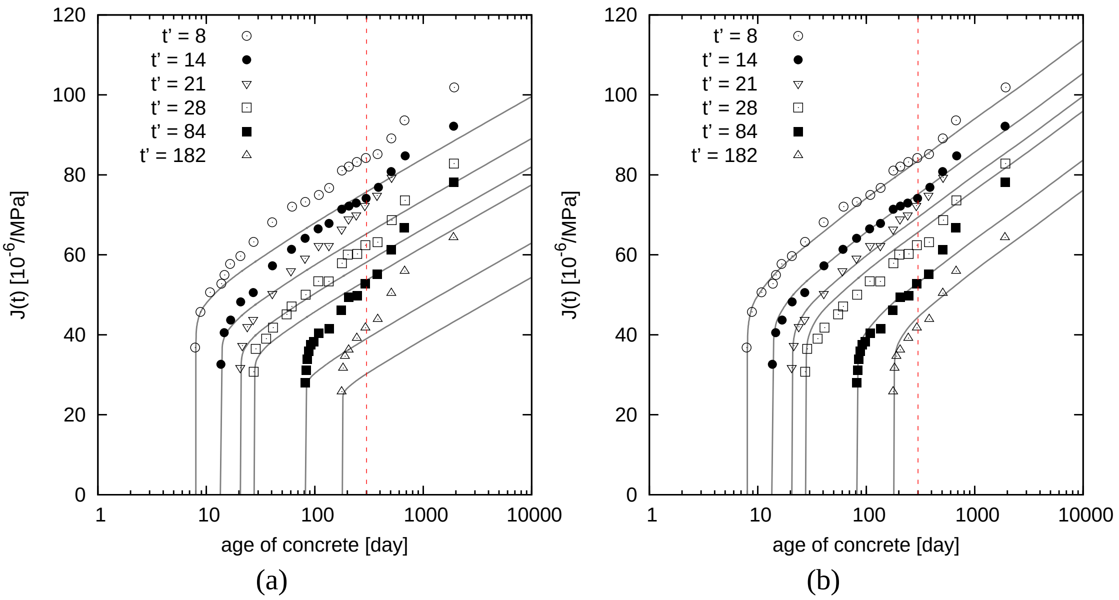

Fig. 2 Time development of basic creep for different times at loading t' with a) parameters predicted from concrete composition, b) optimized set of parameters; dashed line indicates the approximate time of sealing failure (experimental data from [6])

Tab. 1 Values of parameters – structural analysis

	basic creep				MPS		fracture	
	q_1 MPa^{-1}	q_2 MPa^{-1}	q_3 MPa^{-1}	q_4 MPa^{-1}	μ_S MPa^{-1}day^{-1}	k$_{Sh}$ –	f_t MPa	G_F N/m
Bryant	9×10^{-6}	75×10^{-6}	28×10^{-6}	6.5×10^{-6}	5×10^{-6}	0.00195	2	100
predict.	18×10^{-6}	108×10^{-6}	1.5×10^{-6}	6.5×10^{-6}				
Keeton	14×10^{-6}	200×10^{-6}	4×10^{-6}	8×10^{-6}	3×10^{-6}	0.0022	2	100
cyclic h	9×10^{-6}	75×10^{-6}	28×10^{-6}	6.5×10^{-6}	5×10^{-6}	0.002	2	100

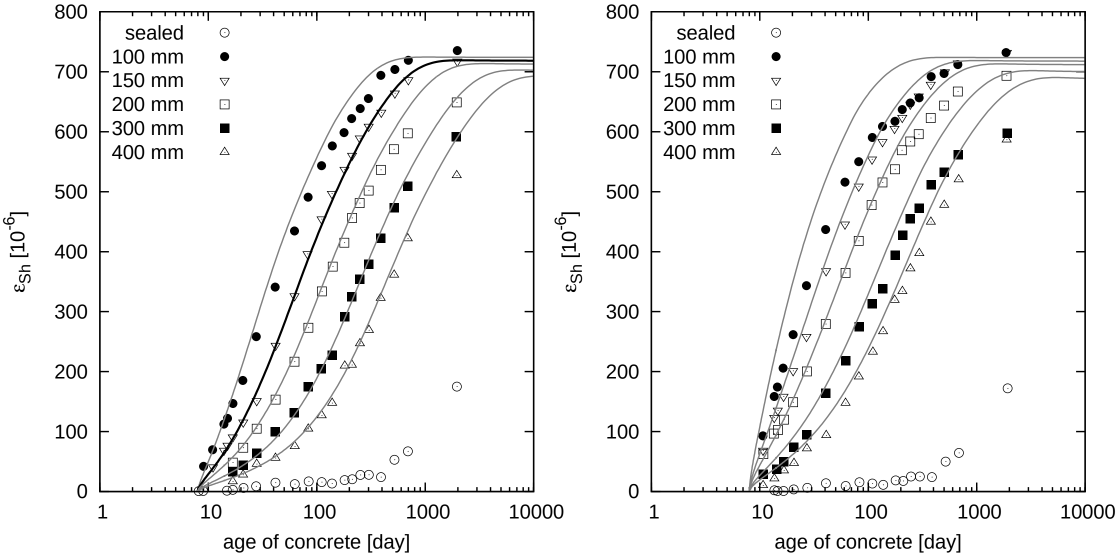

(a) (b)

Fig. 3 Time development of shrinkage strains measured on a) slabs and b) prisms, $t_0 = 8$ days; lines correspond to the results of FE simulations, points are experimental measurements [6]

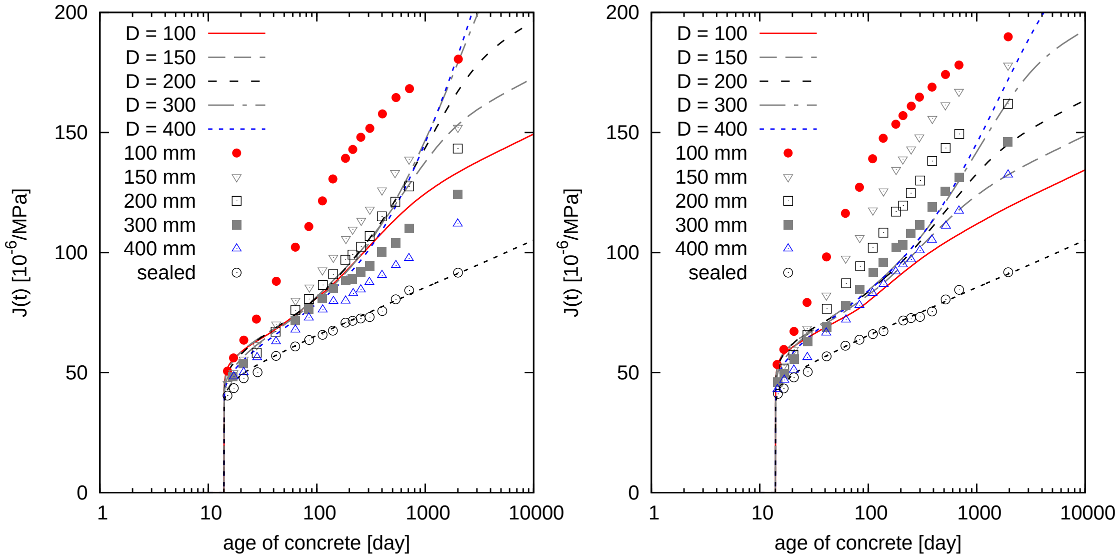

(a) (b)

Fig. 4 Compliance of drying a) slabs and b) prisms of various thicknesses, $t_0 = 8$ days, $t' = 14$ days, lines correspond to the results of FE simulations, points are experimental measurements [6]

4. EXPERIMENTS OF KEETON (1965)

4.1. EXPERIMENTAL SETUP

The technical report [8] presents shrinkage and creep data measured on cylindrical specimens of three different sizes and stored at different levels of relative humidity.

The specimens were removed from the steel mold after one day; then the specimens were cured for 7

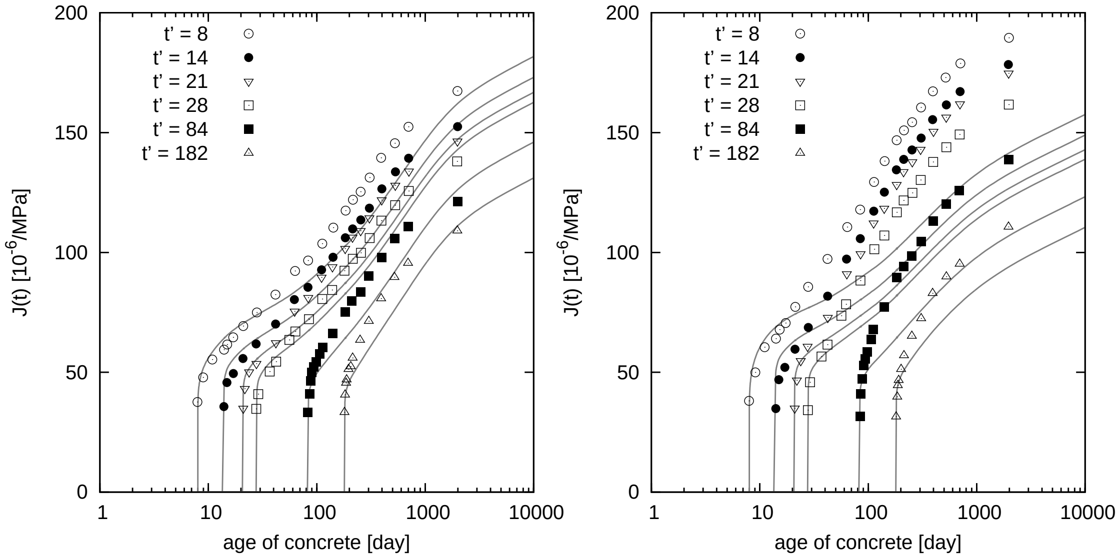

(a) (b)

Fig. 5 Compliance of drying a) slabs 150 mm thick and b) prisms 150×150 mm loaded at different ages t', for $t_0 = 8$ days, lines correspond to the results of FE simulations, points are experimental measurements [6]

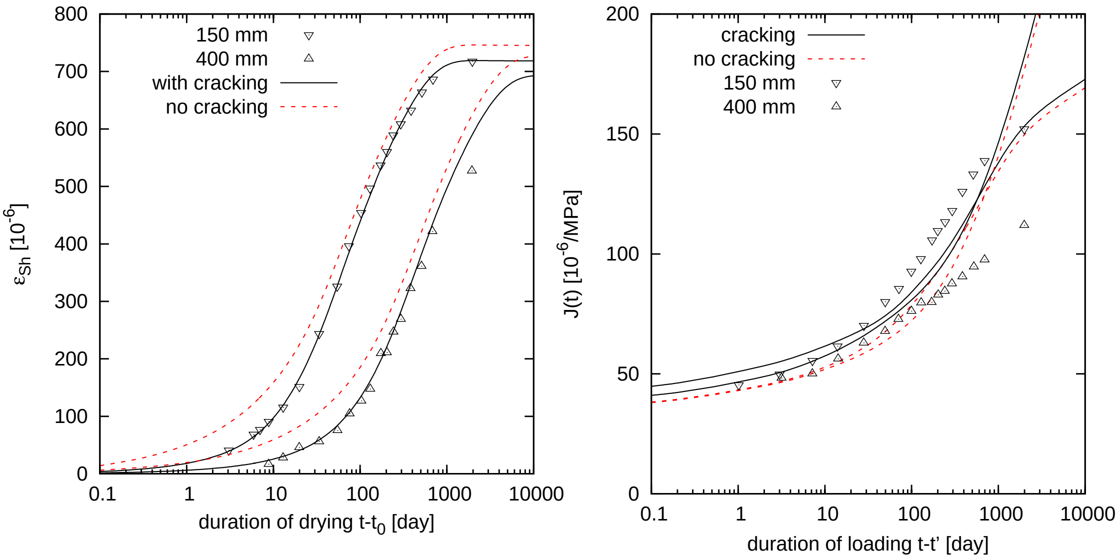

(a) (b)

Fig. 6 Comparison of results of FE simulations of drying slabs with/without cracking: a) shrinkage, b) compliance, $t_0 = 8$ days, $t' = 14$ days

days at 100% relative humidity. The height of each cylinder was 3× its diameter. Strain measurements were made in the central portion of the specimens.

The exact concrete composition is somewhat unclear. The specified cement content was 452.4 kg/m^3, aggregate content 1689.9 kg/m^3 and water content 206.95 kg/m^3, which corresponds to $w/c \approx 0.46$, but the report specifies this ratio to be 0.32. After 28 days of curing at $h_{\mathrm{env}} = 100\%$, the compressive strength was 45.16 MPa and Young's modulus 27.23 GPa.

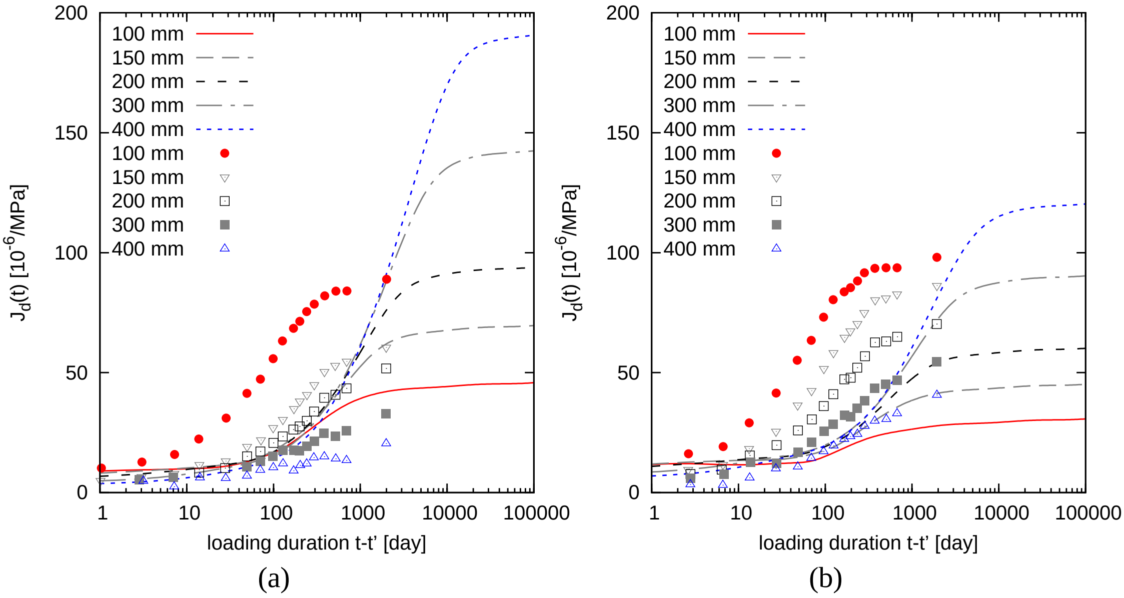

Fig. 7 Drying component of compliance of a) slabs and b) prisms, $t_0 = 8$ days, $t' = 14$ days, lines correspond to the results of FE simulations, points are experimental measurements [6]

Tab. 2 Values of parameters – transport analysis

	Bazant - Najjar			
	C_1	α_0	h_C	n
	m^2/day	–	–	–
Bryant	40×10^{-6}	0.18	0.75	10
Keeton	60×10^{-6}	0.04	0.8	6
cyclic h	40×10^{-6}	0.18	0.75	10

4.2. NUMERICAL SIMULATIONS

A similar procedure as in Section 3.2 was applied also in the case of Keeton's data. Parameters of the Bažant-Najjar transport model and the shrinkage coefficient k_{Sh} were calibrated to match experimental data measured on 4-in diameter cylinder exposed to drying at 50% relative humidity (middle line in Fig. 8b). Shrinkage at $h_{\mathrm{env}} = 50\%$ of 3-in (Fig. 8a) and 6-in (Fig. 8c) cylinders is also captured correctly, but in all cases shrinkage at lower relative humidity ($h_{\mathrm{env}} = 20\%$) is overestimated and shrinkage at higher relative humidity ($h_{\mathrm{env}} = 75\%$) is underestimated.

All parameters are summarized in Tables 1 and 2.

5. RESPONSE TO CYCLIC HUMIDITY

In the majority of concrete structures, concrete is subjected to changes in relative humidity and temperature. Due to the relatively low moisture diffusivity, daily changes in r.h. affect only a very thin surface layer, while annual cycles can penetrate deeper. Not only concrete exposed to ambient conditions, but also laboratory specimens undergo humidity and temperature fluctuations, although these

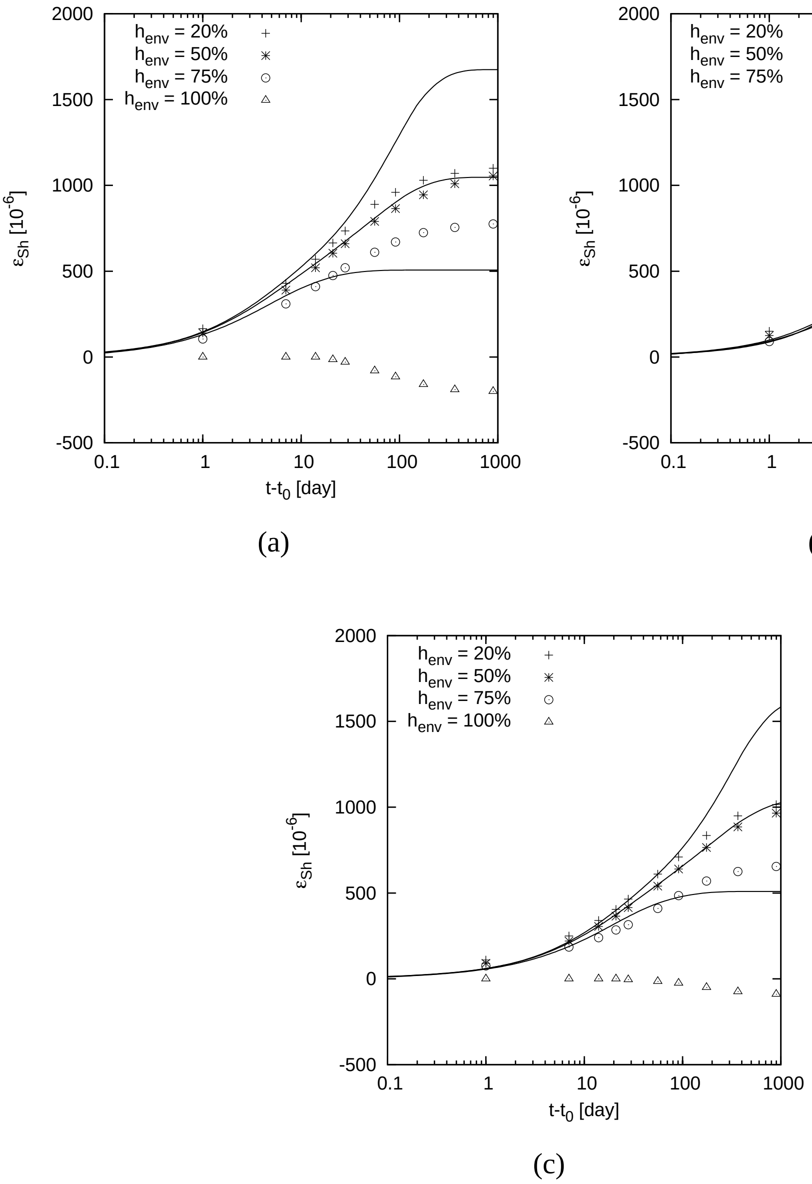

Fig. 8 Time development of shrinkage strains of concrete cylinders exposed to different relative humidities, $t_0 = 8$ days, a) D = 3 in, b) D = 4 in, c) D = 6 in; lines correspond to the results of FE simulations, points are experimental measurements [8]

changes are smaller. Even when the specimen is placed in a climate chamber, the r.h. and temperature inevitably oscillate (e.g. in [9] the relative humidity was 50 ± 4 % and temperature 23 ± 1.7 °C).

For these reasons, the material model describing creep and shrinkage should give similar results for constant r.h. and temperature as well as for slightly fluctuating/cyclic conditions. Sudden changes should of course lead to an increase in creep rate, but the effect of further cycling should be damped (see e.g. experimental results in [10] or [11]).

Fig. 9 shows shrinkage and compliance response of 100 mm thick wall to cyclic relative humidity as modeled by the MPS theory. The curing time was 7 days, the initial humidity was 95% and the amplitude 2.5%. Prescribed cyclic humidity with period T applied at the boundary was described by the cosine function (with mean 92.5%). Material parameters are almost idential to those from Section 3.2 and are summarized in Tables 1 and 2. In Fig. 9, the curve with $T = 0$ corresponds to prescribed humidity starting from 95% linearly decreasing to 92.5% within 0.25 day and then kept constant. This figure shows that although the magnitude of the prescribed relative humidity was very small, the increase in creep deformation is substantial, reaching almost 1.5× the compliance without cycles after one year of loading.

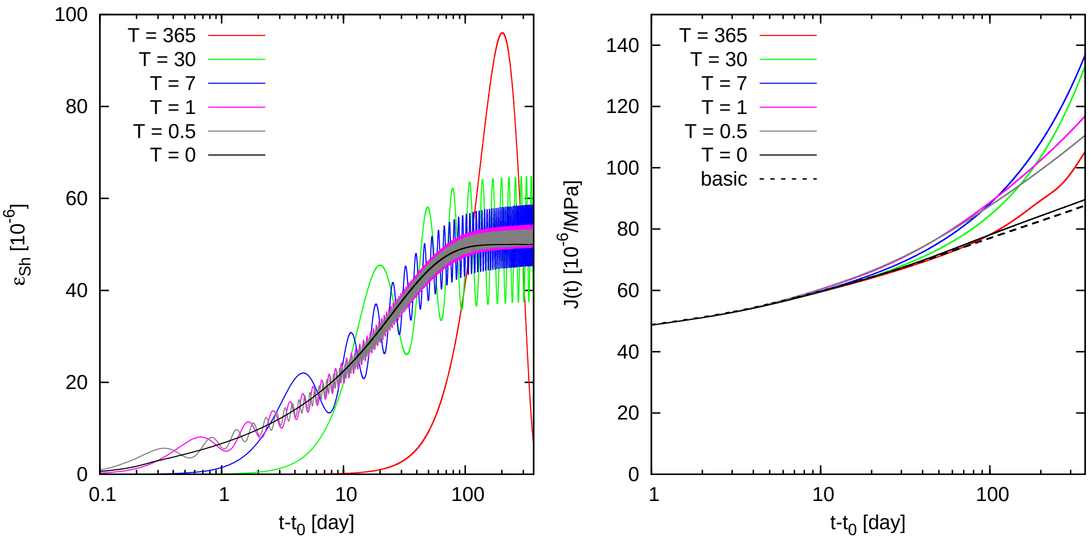

(a) (b)

Fig. 9 Response to cyclic humidity of period T prescribed at the boundary of a wall with thickness 100 mm, $t_0 = 7$ days: a) shrinkage, b) compliance

6. CONCLUSIONS

The originally proposed microprestress-solidification theory has been found unsuitable for modeling of drying creep and shrinkage under general conditions. The main deficiencies are summarized with decreasing order of importance. A modified version of the MPS theory, which could at least partially eliminate these deficiencies, is currently under development.

- The modeled drying creep is too delayed behind experiments. Experiments reported in [6], [8], [12] and many other papers indicate that shrinkage and drying creep occur simultaneously.
- The drying creep as modeled by the MPS theory conctradicts the experiments. Using MPS, the drying creep of large specimens is several times bigger than for small specimens [12].
- Drying creep is strongly influenced even by small fluctuations in relative humidity. Not only the amplitude, but also the frequency of these fluctuations matters.
- A linear relationship between humidity and shrinkage rates seems to be too simplistic, shrinkage

at different levels of relative humidity is not captured correctly, e.g. [8].

- The current model does not take into account swelling, e.g. [8].
- If the shrinkage development is calibrated on small specimens, then the prediction on large members tends to be overestimated [6], [12].
- The material model does not provide enough parameters to fully calibrate the shrinkage and drying creep behavior (only one parameter for each affecting the magnitude).

ACKNOWLEDGEMENT

The financial support provided by grant SGS13/034/OHK1/1T/11 received from the Czech Technical University in Prague is gratefully acknowledged.

REFERENCES

[1] BAŽANT, Z.P., HAUGGAARD, A.B. and ULM, F. Microprestress-solidif. theory for concrete creep. I: Aging and drying effects. *J. of Eng. Mech.* 1997, **123**(11), 1188–1194. ISSN 0733-9399.

[2] BAŽANT, Z.P., CEDOLIN, L. and CUSATIS, G. Temperature effect on concrete creep modeled by microprestress-solidification theory. *J. of Eng. Mech.* 2004, **130**(6), 691–699. ISSN 0733-9399.

[3] *OOFEM home page* [online]. [cited 2013-06-21]. Available from: http://www.oofem.org

[4] PATZÁK, B. and BITTNAR, Z. Design of object oriented finite element code. *Advances in Engineering Software* 2001, **32**(10-11), 759–767. ISSN 0965-9978.

[5] PATZÁK, B., RYPL, D. and BITTNAR, Z. Parallel explicit finite element dynamics with nonlocal constitutive models. *Computers Structures* 2001, **79**(26-28), 2287-2297. ISSN 0045-7949.

[6] BRYANT, A.H. and VADHANAVIKKIT, C. Creep, Shrinkage-size, and Age at Loading Effects *ACI Materials Journal* 1987, **84**(2), 117–123. ISSN 0889-325X.

[7] BAŽANT, Z.P. and NAJJAR, L.J. Nonlinear water diffusion in nonsaturated concrete. *Materials and Structures.* 1972, **5**(1), 3–20. ISSN 1359-5997.

[8] KEETON *Study of Creep in Concrete, Phase 1 (I-beam)* U. S. Naval Civil Engineering Laboratory, Port Hueneme, California, 1965.

[9] AGUILAR, C.P. *Estudio del comportamiento y desarrollo de una metodologia de prediccion de la retraccion hidraulica de hormigones* Santiago de Chile, 2005. Ph.D. Thesis. Pontificia Universidad Catolica de Chile. Escuela de Ingenieria.

[10] PICKETT, G. The effect of change in moisture-content on the creep of concrete under a sustained load. *Journal of the ACI* 1942, **38**, 333–355. ISSN 0002-8061.

[11] FAHMI, H.M., POLIVKA, M. and BRESLER, B. *Time-dependent behavior of concrete under sustained load and cyclic temperature* Report no. UC SESM 72-6, Structural Engineering Laboratory, University of California, Berkeley, April 1972.

[12] HANSEN, T.C. and MATTOCK A.H. Influence of Size and Shape of Member on the Shrinkage and Creep of Concrete *Journal of the ACI* 1966, **62**(2), 267–290. ISSN 0002-8061.

PREPARATION AND PROPERTIES OF ALKALI ACTIVATED FLY ASH FOAM

Petr HLAVÁČEK[1], **Vít ŠMILAUER**[2]

Abstract: *This work aims at description of foams based on alkali activated fly ash. The foam is produced from alkali activated fly ash paste by powder alumina which reacts with the alkalies from the activation solution. Hydrogen is released during this reaction and creates a closed-pore structure. The amount of liquid activation solution and powder alumina has been optimized considering proper pore distribution and prescribed bulk density of the foam. Compressive strength, flexural strength, thermal conductivity and capacity and residual strength after fire-resistance test were measured and compared with traditional porous building materials.*

Keywords: *Alkali activation, fly ash, foam, compressive strength, fire-resistance*

1. INTRODUCTION

The main objective of this work is to prepare the alkali activated fly ash foam (AFAF) and determine its material properties. The mixture composition has been optimized considering pore distribution and bulk density. The compressive strength, flexural strength, thermal conductivity and capacity and residual strength after exposure to high temperature were determined and compared with traditional porous building materials.

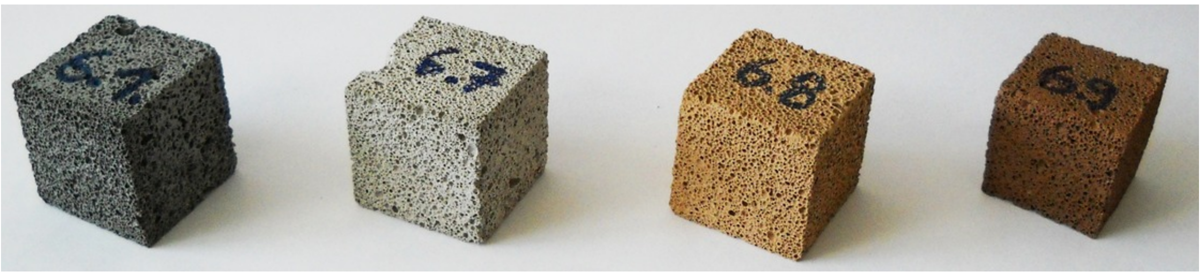

Fig. 1 Alkali-activated fly ash foam, samples after fire-resistance test (reference, 500 °C, 800 °C, 1100 °C).

The world annual production of fly ashes (FA) is estimated to be 600 million tons [1]. The current

[1] Ing. Petr Hlaváček, Department of Mechanics, Faculty of Civil Engineering, CTU in Prague, petr.hlavacek@fsv.cvut.cz

[2] Doc. Ing. Vít Šmilauer, Ph.D., Department of Mechanics, Faculty of Civil Engineering, CTU in Prague, vit.smilauer@fsv.cvut.cz

production of FA in the Czech Republic is about 6 million tons per year [3] (the thermal power plants release about 80 g of FA per production of 1 MWh of electric power). It is estimated that only 20-30% of FA is secondarily used, the rest is stored on landfills/lagoons which present due to the risk of air and ground water pollution the biggest ecological problem in the Czech Republic nowadays. Due to those facts a suitable utilization of FA is searched. Previous research testified that fly ash can enter the process of alkali-activation. The long term tests proved the stability of alkali activated fly ash [2]. The alkali-activated fly ash paste can be intermixed with powder alumina. Hydrogen is released during this reaction and the closed-pore structure is created. Figure 1 shows 20x20x20 mm^3 AFAF cubes after fire-resistance test.

2. MATERIALS AND METHODS

The fly ash class F from Opatovice brown coal power station, Czech Republic (Blaine 210 m^2/kg) was used as the source material for alkali activation. The chemical composition is given in the Table 1. Powder alumina (Al) from Albo Schlenk Inc., Bojkovice, Czech Republic, product type 76013 (D50 35 μm) was used as the foaming agent.

Tab. 1 Chemical composition of fly ash (wt %).

	SiO_2	Al_2O_3	Fe_2O_3	CaO	K_2O	TiO_2
Fly ash	51.9	32.8	6.3	2.7	2.12	1.89

Fig. 2 Manufacturing of alkali activated fly ash foam.

The reaction between powder alumina and alkalies is very fast, in our case there is about 15 seconds for stirring and casting. Due to this fact were the fly ash and powder alumina thoroughly mixed together in dry state and liquid activation solution was added subsequently. The hand stirring took place directly in the mold. Any different workflow led to improper pore distribution. The foaming runs for about 1-2 minutes. The forms with foam were left in ambient conditions for two hours and followingly given to oven for 12 hours by 80 °C. Figure 2 shows the foam manufacturing.

The compositon of the gel was taken from previous research on the fly ash [4, 5, 6]. The amount of powder alumina was roughly estimated from known cement-based foam concrete recipes. Fine tuning of the composition was done iteratively. The final compositions of the mixes is given in the Table 2, the pore structure corresponding to those compositions is shown in the Picture 3. The composition AFAF 5

Tab. 2 Composition of alkali activated fly ash foam mixes. Mass needed to fill up one mold (approximately 0.1 liter). Measured bulk density of matured foam in dry state is given in right column.

Foam Mixture	FA [g]	liquid/solid [-]	NaOH [g]	water glass [g]	Al [g]	bulk density [kg/m^3]
AFAF 1	50	0.37	2.8	15.7	0.030	751
AFAF 2	50	0.38	2.9	16.1	0.030	778
AFAF 3	50	0.39	3.0	16.5	0.030	772
AFAF 4	50	0.37	2.8	15.7	0.045	700
AFAF 5	50	0.38	2.9	16.1	0.045	671
AFAF 6	50	0.39	3.0	16.5	0.045	626
AFAF 7	50	0.37	2.8	15.7	0.060	574
AFAF 8	50	0.38	2.9	16.1	0.060	521
AFAF 9	50	0.39	3.0	16.5	0.060	422

was chosen for all further experiments due to its pore size. The compressive strength was measured on cubes 20×20×20 mm^3, flexural strength on beams 40×40×160 mm^3 which were cutted from larger pieces of matured foam. Thermal conductivity and capacity was determined on cylindrical specimens 70 mm in diameter and 20 mm thick. The fire resistance (or resistance to high temperatures) was studied on cubes 20×20×20 mm^3. The mass and volumetric changes after exposure to high temperature were measured and compressive strength was obtained.

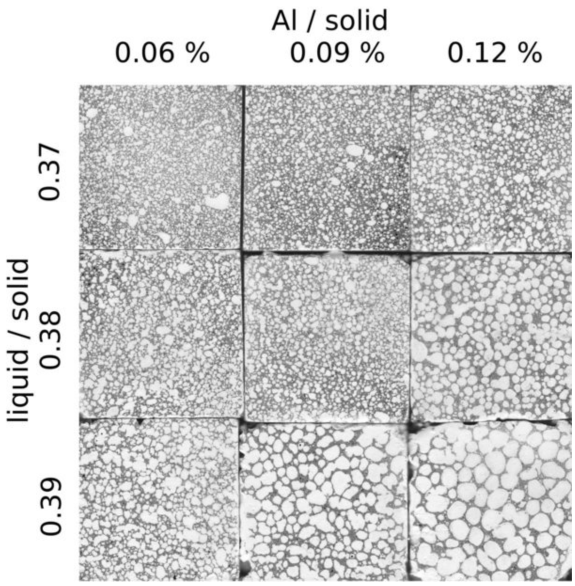

Fig. 3 Effect of amount of the activation solution and powder alumina to the pore distribution. Pores fulfilled with acrylic sealant for better contrast of the image.

3. RESULTS AND DISCUSSION

Figure 3 shows the AFAF pore structure for different mix compositions. The pore structure is very sensitive to the viscosity of the mix. For example, when the liquid/solid ratio reaches 0.40, the foam will be unstable due to clustering of the pores. On the other hand for liquid/solid ratio below 0.37 is the mixture to dense to be foamed by powder alumina.

Table 3 gives the measured bulk density, compressive strength, flexural strength and thermal conductivity and capacity on AFAF. The reference material for comparison is commercially available traditional porous material XELLA Ytong P6-650.

Tab. 3 Comparison of measured data on AFAF with reference material Xella Ytong P6-650, data from Xella Ytong technical documentation [7]. In case of AFAF the value represents an average of at least four measurements.

	Bulk density [kg/m^3]	Compressive strength [MPa]	Flexural strength [MPa]	Thermal conductivity [W/m·K]	Thermal capacity [J/kg·K]
AFAF	671	6.0	1.0	0.145	1089
Ytong P6-650	650	6.5	≤ 0.5	0.170	1000

Figure 5 shows the change of volume/mass/color of AFAF after fire-resistance test. The mass loss of 9.3% presents the amount water, which was added to mixture in the alkaline solution. Almost all water was evaporated already at 800 °C and no mass change occured after heating to 1100 °C. On the other hand the biggest shrinkage/deformation increment appeared between 800 °C and 1100 °C which is related to the gel sintering. The compressive strength and elasticity evolution is depicted in Figure 4. The increase of compressive strength and elasticity for samples loaded by 1100 °C can be explained by the gel sintering and increase of the bulk density.

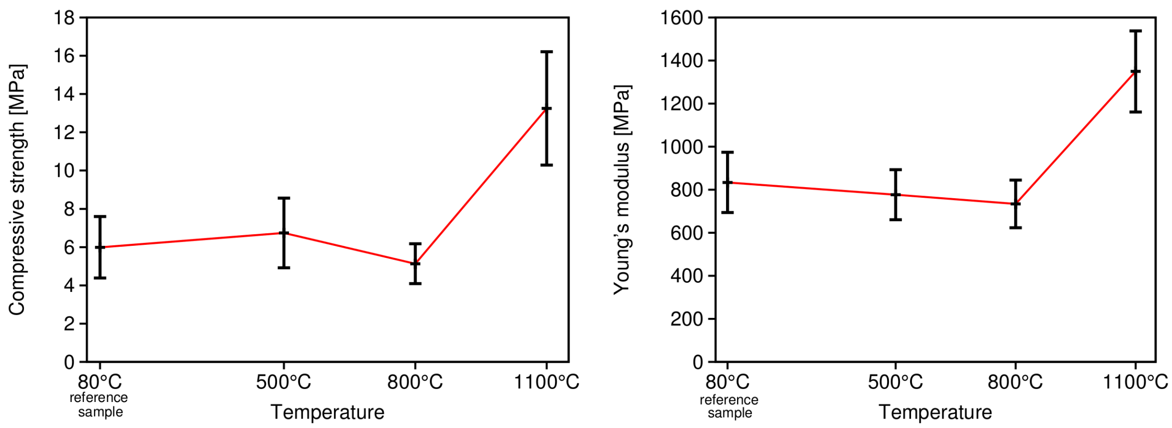

Fig. 4 Compressive strength and elasticity evolution of AFAF samples after fire-resistance test. Average and standard deviation from three measurements each.

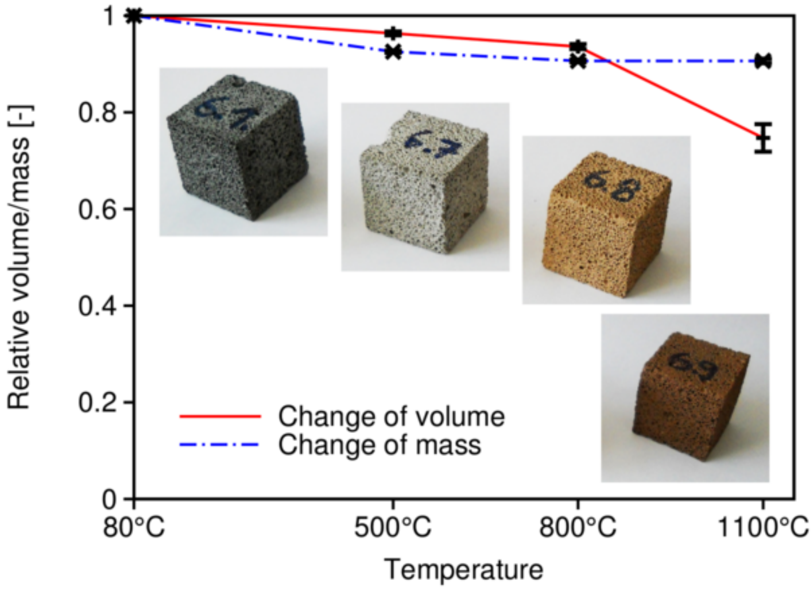

Fig. 5 Relative change of mass and volume of fly ash foam after fire-resistance test. Average and standard deviation from three measurements each.

4. CONCLUSION

The foam based on alkali activated fly ash (AFAF) was produced. The powder alumina was used as the foaming agent. The effect of amount of liquid activation solution and powder alumina was studied. The viscosity of the initial mix was found as the crucial factor for the foam stability.

The fire-resistance of the AFAF was testified. Mass loss, volume change, compressive strength and elasticity was obtained. It was found that almost all mass loss occures below 500 °C. On the other hand the biggest volume change take place between 800 °C and 1100 °C which is related to sintering of the gel.

The mechanical and thermal properties of the AFAF were compared with the traditional porous building material XELLA Ytong P6-650. No significant difference was observed in the mechanical properties, on the other hand the AFAF shows 15% lower thermal conductivity against Ytong. The main advantage of the alkali activated fly ash foam to Ytong and other similar materials lies in the absence of energy-intensive autoclave-treatment during production.

The long term properties of the AFAF and its resistance to aggresive environment will be studied in future work.

ACKNOWLEDGEMENT

Authors gratefully acknowledge the financial support from the Czech Technical University Foundation under grant No. SGS12/116/OHK1/2T/11.

REFERENCES

[1] AHMARUZZAMAN, M. A review on the utilization of fly ash, *Progress in Energy and Combustion Science.* 2010, **36**(3), 327-363. ISSN: 0360-1285.

[2] WALLAH, S.E. and RANGAN, B.V. *Low-calcium Fly Ash-based Geopolymer Concrete: Long Term Properties*, Research Report GC 2, Perth, Australia, 2006.

[3] CEZ web page. *CEZ web page* [online, 2013]. [cited 2013-07-12] Available from: http://www.cez.cz.

[4] ŠMILAUER, V., ŠKVÁRA, F., NĚMEČEK, J., KOPECKÝ, L. and HLAVÁČEK, P. Application of Micromechanics on Alkali-activated Materials, *Advances in Science and Technology.* 2010, **69**, 75-85. ISSN 1662-0356.

[5] ŠMILAUER, V., HLAVÁČEK, P., ŠKVÁRA, F., ŠULC, R., KOPECKÝ, L. and NĚMEČEK, J. Micromechanical multiscale model for alkali activation of fly ash and metakaolin, *Journal of Materials Science.* 2011, **46**(20), 6545-6555. ISSN 0022-2461.

[6] ŠKVÁRA, F., ŠMILAUER, V., HLAVÁČEK, P., KOPECKÝ, L. and CÍLOVÁ, Z. A weak alkali bond in (N, K)–A–S–H gels: Evidence from leaching and modeling, *Ceramics - Silikáty.* 2012, **56**(4), 374-382. ISSN 0862-5468.

[7] Xella Ytong web page. *Xella Ytong web page* [online, 2013]. [cited 2013-07-12] Available from: http://www.ytong.cz.

ON CONSISTENT HYPOELASTIC MODELS

Martin HORÁK[1]

Abstract: *Hypoelasticity is an extension of small strain elasticity to large strains. We show how to derive objective stress rate from hyperelastic relation. However, hypoelastic law defining by stress rate derived from hyperelasticity is only an approximation of hyperelastic behaviour. Finally, we show how to construct hypoelastic model which can be derived from strain energy function.*

Keywords: *hypoelasticty,work conjugacy, objective rates*

1. INTRODUCTION

In this paper we explore hypoelastic material laws. Hypoelasticity is a generalization of linear elasticity. In contrast to hyperelasticity, hypoelasticity doesn't rely on postulating of strain energy density. The hypoelastic constitutive law is written in a rate form

$$\overset{\triangle}{\boldsymbol{\tau}} = \mathbb{D} : \boldsymbol{d} \tag{1}$$

where $\triangle$ denotes some objective rate, $\mathbb{D}$ is the elastic stiffness tensor, $\boldsymbol{d}$ is the strain rate tensor, and $\boldsymbol{\tau}$ is the Kirchhoff stress. The hypoelasticity has been very widely used for ad-hoc extension of a small strain plasticity models into large strain regime. Lots of attention was paid to explore how to choose an appropriate objective stress rate. It was shown in [1] that not every objective rate leads to correct expression of second order work. Moreover, in [2] it was proved that some rates does not define an elastic material, i.e. these models dissipate energy within a closed deformation cycle. Here we explore hypoelastic models derived from hyperelasticity, derive appropriate objective rate and compare them with rates obtained in [1] from the expression of second order work. Finally we show how to construct hypoelastic models consistent with hyperelaticity.

[1] Ing. Martin HORÁK, Department of Mechanics, Faculty of Civil Engineerig, Czech Technical University in Prague, martin.horak@fsv.cvut.cz

2. STRAIN MEASURES

2.1. LAGRANGIAN STRAIN MEASURES

A family of strain measures derived from the right Cauchy-Green deformation tensor was introduced in [4], [5]. These generalized strain measures are defined as

$$\boldsymbol{E}^{(m)} = \begin{cases} \dfrac{1}{2m}\left(\boldsymbol{C}^m - \boldsymbol{I}\right), & \text{if } m \neq 0 \\ \\ \dfrac{1}{2}\ln \boldsymbol{C}, & \text{if } m = 0 \end{cases} \tag{2}$$

where $\boldsymbol{I}$ is the second-order unit tensor. In the special cases when m = 0 and m = 0.5 we obtain the so-called Hencky (logarithmic) and Biot tensor, while for m = 1 we obtain the Green-Lagrange strain tensor. Recall that the Cauchy-Green deformation tensor is defined as

$$\boldsymbol{C} = \boldsymbol{F}^T\boldsymbol{F} \tag{3}$$

and its spectral decomposition is

$$\boldsymbol{C} = \sum_{a=1}^{3} \lambda_a \boldsymbol{N}^a \otimes \boldsymbol{N}^a \tag{4}$$

where $\boldsymbol{F}$ is the deformation gradient, λ_a are the eigenvalues of the right Cauchy-Green deformation tensor, $\boldsymbol{N}^a$ are the corresponding eigenvectors, or so-called Lagrangian triad. Equation (6) can be rewritten as

$$\boldsymbol{E}^{(m)} = \begin{cases} \dfrac{1}{2m}\displaystyle\sum_{a=1}^{3}(\lambda_a^m - 1)\boldsymbol{M}^a, & \text{if } m \neq 0 \\ \\ \dfrac{1}{2}\displaystyle\sum_{a=1}^{3}\ln \lambda_a \boldsymbol{M}^a, & \text{if } m = 0 \end{cases} \tag{5}$$

where $\boldsymbol{M}^a = \boldsymbol{N}^a \otimes \boldsymbol{N}^a$

2.2. EULERIAN STRAIN MEASURES

Similarly to the Lagrangian Seth - Hill strain measures described in previous section one can derived Eulerian strain measures from the left Cauchy-Green deformation. These generalized strain measures are defined as

$$\boldsymbol{e}^{(m)} = \begin{cases} \dfrac{1}{2m}\left(\boldsymbol{b}^m - \boldsymbol{I}\right), & \text{if } m \neq 0 \\ \\ \dfrac{1}{2}\ln \boldsymbol{b}, & \text{if } m = 0 \end{cases} \tag{6}$$

The left Cauchy-Green deformation tensor is defined as

$$\boldsymbol{b} = \boldsymbol{F}\boldsymbol{F}^T \tag{7}$$

and its spectral decomposition is

$$\boldsymbol{b} = \sum_{a=1}^{3} \lambda_a \boldsymbol{n}^a \otimes \boldsymbol{n}^a \tag{8}$$

where λ_a are again the eigenvalues of the left Cauchy-Green deformation tensor, $\boldsymbol{n}^a$ are the corresponding eigenvectors, or so-called Eulerian triad. The eigenvectors of $\boldsymbol{C}$ and $\boldsymbol{b}$ are related by expression

$$\boldsymbol{n}^a = \boldsymbol{R}\boldsymbol{N}^a \tag{9}$$

where $\boldsymbol{R}$ is the rotation tensor obtained from polar decomposition of the deformation gradient. Equation (6) can be rewritten as

$$\boldsymbol{e}^{(m)} = \begin{cases} \dfrac{1}{2m} \displaystyle\sum_{a=1}^{3} (\lambda_a^m - 1)\boldsymbol{m}^a, & \text{if } m \neq 0 \\[2em] \dfrac{1}{2} \displaystyle\sum_{a=1}^{3} \ln \lambda_a \boldsymbol{m}^a, & \text{if } m = 0 \end{cases} \tag{10}$$

where $\boldsymbol{m}^a = \boldsymbol{n}^a \otimes \boldsymbol{n}^a$

2.3. RATE OF DEFORMATION

We start by definition of the spatial velocity gradient

$$\boldsymbol{\nabla v} = \boldsymbol{l} = \frac{\partial \boldsymbol{F}}{\partial t} \boldsymbol{F}^{-1} \tag{11}$$

Symmetric part of velocity gradient is called spatial rate of deformation

$$\boldsymbol{d} = \frac{1}{2} \left[\boldsymbol{l} + \boldsymbol{l}^T \right] \tag{12}$$

Skew-symmetric part of velocity gradient is called the spin or vorticity tensor

$$\boldsymbol{w} = \frac{1}{2} \left[\boldsymbol{l} - \boldsymbol{l}^T \right] \tag{13}$$

Writing the rate of deformation tensor in Eulerian and Lagrangian triad

$$\boldsymbol{d} = \sum_{i=1,j=1}^{3} d_{ij}\boldsymbol{n}^i \otimes \boldsymbol{n}^j \qquad \boldsymbol{D} = \sum_{i=1,j=1}^{3} D_{ij}\boldsymbol{N}^i \otimes \boldsymbol{N}^j \tag{14}$$

where we defined rotated rate of the deformation tensor by expression

$$\boldsymbol{D} = \boldsymbol{R}^T \boldsymbol{d} \boldsymbol{R} \tag{15}$$

The expression between Lagrangian strains and rotated rate of deformation can be expressed as

$$\dot{E}_{ij} = \begin{cases} \lambda_i^m D_{ij}, & \text{if } i = j \\ \\ \dfrac{\lambda_j^m - \lambda_i^m}{\lambda_j^2 - \lambda_i^2} 2\lambda_i\lambda_j D_{ij}, & \text{if } i \neq j \quad and \quad \lambda_i \neq \lambda_j \end{cases} \tag{16}$$

where no summation is applied over repeated indices.

3. OBJECTIVITY AND OBJECTIVE RATES

The principle of material frame-indifference postulates that all variables for which constitutive relations are required must be objective tensors. It is well known that Kirchhoff stress tensor is an objective tensor, i.e. under rigid body rotation $\boldsymbol{Q}$, Kirchhoff stress transforms as

$$\boldsymbol{\tau}^* = \boldsymbol{Q}^T \cdot \boldsymbol{\tau} \cdot \boldsymbol{Q} \tag{17}$$

However, material time derivative of the Kirchhoff stress tensor is not an objective tensor, i.e. material time derivative of the Kirchhoff stress tensor does not transform like a second order tensor.

$$\dot{\overline{\boldsymbol{\tau}^*}} = \dot{\boldsymbol{Q}}^T \boldsymbol{\tau} \boldsymbol{Q} + \boldsymbol{Q}^T \dot{\boldsymbol{\tau}} \boldsymbol{Q} + \boldsymbol{Q}^T \boldsymbol{\tau} \dot{\boldsymbol{Q}} \tag{18}$$

Therefore introduction of an objective time derivative is necessary. Here we introduce only so-called corotational rates

$$\overset{\circ}{\boldsymbol{\tau}} = \dot{\boldsymbol{\tau}} + \boldsymbol{\tau} \cdot \boldsymbol{\omega} + \boldsymbol{\omega}^T \cdot \boldsymbol{\tau} \tag{19}$$

where $\boldsymbol{\omega}$ is a skew - symmetric tensor. For example the Green - Naghdi rate is obtained for $\boldsymbol{\omega} = \dot{\boldsymbol{R}}\boldsymbol{R}^T$ and the Jaumann for $\boldsymbol{\omega} = \boldsymbol{w}$

4. HYPOELASTICITY

A hypoelasticity is a generalization of linear elasticity to finite strains by rewriting stress-strain law in a rate form

$$\overset{\triangle}{\boldsymbol{\tau}} = \mathbb{D} : \boldsymbol{d} \tag{20}$$

where $\mathbb{D}$ is isotropic and constant stiffness tensor and $\triangle$ is again some objective rate. However, not all objective rates provides correct expression for the second order work. Due to this fact, a class of objective rates was proposed in [1]

$$\hat{\boldsymbol{\tau}}^{(m)} = \dot{\boldsymbol{\tau}} - \boldsymbol{l}\boldsymbol{\tau} - \boldsymbol{\tau}\boldsymbol{l}^T + \left(1 - \frac{m}{2}\right)(\boldsymbol{\tau}\boldsymbol{d} + \boldsymbol{d}\boldsymbol{\tau}) \tag{21}$$

associated with an approximation of the Seth-Hill tensors $\boldsymbol{E}^{(m)}$.

5. HYPERELASTICITY IN A RATE FORM

Hyperelastic constitutive law can derive from strain energy density W

$$\dot{\boldsymbol{T}}^{(m)} = \frac{\partial W}{\partial \boldsymbol{E}^{(m)}} \tag{22}$$

Rate form of hyperelasticity is obtained simply by time differentiating of equation 22

$$\dot{\boldsymbol{T}}^{(m)} = \mathbb{D}^{(m)} : \dot{\boldsymbol{E}}^{(m)} \tag{23}$$

where $\mathbb{D}^{(m)} = \dfrac{\partial^2 W}{\partial \boldsymbol{E}^{(m)} \partial \boldsymbol{E}^{(m)}}$ and the stress $\boldsymbol{T}^{(m)}$ and strain $\boldsymbol{E}^{(m)}$ are work conjugated pair. Our effort now is to transform equation 23 to spatial description. We start with case $m = 1$. In this case $\boldsymbol{T}^{(1)}$ is the Second Piola-Kirchhoff stress and $\boldsymbol{E}^{(1)}$ is the Green-Lagrangean strain. We utilize the well know formula

$$\boldsymbol{T}^{(1)} = \boldsymbol{F}^{-1}\boldsymbol{\tau}\boldsymbol{F}^{-T} \tag{24}$$

along with the relation

$$\dot{\boldsymbol{E}}^{(1)} = \boldsymbol{F}^T\boldsymbol{d}\boldsymbol{F} \tag{25}$$

Substituting equations 24 and 25 into equation 23 we arrive at

$$\boldsymbol{F}^{-1}\boldsymbol{\tau}\boldsymbol{F}^{-T} = \mathbb{D} : \boldsymbol{F}^T\boldsymbol{d}\boldsymbol{F} \tag{26}$$

After some algebra we obtain

$$\overset{\triangle}{\boldsymbol{\tau}}_{Ol} = \mathbb{C} : \boldsymbol{d} \tag{27}$$

where

$$\mathbb{C}_{ijkl} = JF_{im}F_{jn}F_{ko}F_{Flp}\mathbb{D}_{mnop} \tag{28}$$

and $\overset{\triangle}{\boldsymbol{\tau}} = \dot{\boldsymbol{\tau}} - \boldsymbol{l}\boldsymbol{\tau} - \boldsymbol{\tau}\boldsymbol{l}$ is so called Oldroyd rate. This result is consistent with the rate consistent with the second order work expression (21) . Using the same procedure we can derive the consistent objective rate for logarithmic strain. We start form the rate equation

$$\dot{\boldsymbol{T}}^{(0)} = \mathbb{D}^{(0)} : \dot{\boldsymbol{E}}^{(0)} \tag{29}$$

Where we denoted $\mathbb{D}^{(0)} = \frac{\partial^2 W^{(0)}}{\boldsymbol{E}^{(0)}\boldsymbol{E}^{(0)}}$ For isotropic elastic material, stress conjugated to logarithmic strain can be expressed as

$$\boldsymbol{T}^{(0)} = \boldsymbol{R}^T\boldsymbol{\tau}\boldsymbol{R} \tag{30}$$

and its rate

$$\dot{\boldsymbol{T}}^{(0)} = \dot{\boldsymbol{R}}^T\boldsymbol{\tau}\boldsymbol{R} + \boldsymbol{R}^T\dot{\boldsymbol{\tau}}\boldsymbol{R} + \boldsymbol{R}^T\boldsymbol{\tau}\dot{\boldsymbol{R}} \tag{31}$$

Substituting equations (31) and (16) into (29) leads to

$$\overset{\circ}{\boldsymbol{\tau}}_{GN} = \mathbb{C} : \boldsymbol{d} \tag{32}$$

in the equation above $\overset{\circ}{\boldsymbol{\tau}}_{GN}$ is the Green-Naghdi rate of Kirchhoff stress and

$$\mathbb{C}_{ijkl} = \begin{cases} \hat{D}_{ijkl}, & \text{if } k = l \\ \\ 2\hat{D}_{ijkl}\frac{\ln\lambda_l - \ln\lambda_k}{\lambda_l^2 - \lambda_k^2}\lambda_k\lambda_l, & \text{if } k = l \end{cases} \tag{33}$$

where $\hat{D}_{ijkl} = R_{im}R_{jn}R_{ko}R_{lp}D_{ijkl}$ and $\mathbb{C}$ is the spatial logarithmic stiffness. For isotropic material $\hat{\mathbb{D}}_{ijkl} = \mathbb{D}_{ijkl}$

This results differs from consistent rate obtained from equation (21). From equation (33) and (28) follows that hyperelatic spatial stiffness tensors are not constant nor isotropic even for isotropic elastic material, thus constructing of hypoelastic material models from hypoelastic framework is only an approximation of a hyperelastic model.

6. HYPOELASTIC MODELS CONSISTENT WITH HYPERELASTICITY

To define work conjugacy for Eulerian tensors is not so simple as for Lagrangean tensors, because unlike the Lagrangian strains, Eulerian strain $\dot{\boldsymbol{e}}$ are not objective tensors. The work conjugacy can be extended to the Eulerian objects by defining conjugacy in terms of objective rates. The Cauchy stress tensor $\boldsymbol{\sigma}$ is work-conjugated to a strain tensor $\boldsymbol{e}^{(m)}$ if they fulfill

$$\dot{w} = \boldsymbol{\tau} : \overset{\diamond}{\boldsymbol{e}}^{(m)} \tag{34}$$

where w is rate of work per unit reference volume and $\diamond$ is a objective rate such that $\overset{\diamond}{\boldsymbol{e}}^{(m)} = \boldsymbol{d}$ There are many possibilities how to define strain tensor and its objective rate which are conjugated to Kirchhoff stress. Here we show two examples:

- $m = -1$

$$\dot{\boldsymbol{e}}^{(-1)} = -\frac{1}{2}\left(\dot{\boldsymbol{F}}^{-T}\boldsymbol{F}^{-1} + \boldsymbol{F}^{-T}\dot{\boldsymbol{F}}^{-1}\right) = \boldsymbol{d} - \boldsymbol{l}^T\boldsymbol{e}^{(-1)} - \boldsymbol{e}^{(-1)}\boldsymbol{l} \tag{35}$$

$$\dot{\boldsymbol{e}}^{(-1)} + \boldsymbol{l}^T\boldsymbol{e}^{(-1)} + \boldsymbol{e}^{(-1)}\boldsymbol{l} = \boldsymbol{d} \tag{36}$$

- $m = 1$

$$\dot{\boldsymbol{e}}^{(1)} = \frac{1}{2}\left(\dot{\boldsymbol{F}}\boldsymbol{F}^T + \boldsymbol{F}\dot{\boldsymbol{F}}^T\right) = \frac{1}{2}\left(\boldsymbol{l}\boldsymbol{F}\boldsymbol{F}^T + \boldsymbol{F}\boldsymbol{F}^T\boldsymbol{l}^T\right) = \boldsymbol{d} + \boldsymbol{l}\boldsymbol{e}^{(1)} + \boldsymbol{e}^{(1)}\boldsymbol{l}^T \tag{37}$$

$$\dot{\boldsymbol{e}}^{(1)} - \boldsymbol{l}\boldsymbol{e}^{(1)} - \boldsymbol{e}^{(1)}\boldsymbol{l}^T = \boldsymbol{d} \tag{38}$$

Hypoelastic models formulated using the $\diamond$ rate are hyperelastic.

$$\overset{\diamond}{\boldsymbol{\sigma}} = \mathbb{D} : \boldsymbol{d} = \mathbb{D} : \overset{\diamond}{\boldsymbol{e}}^{(m)} \tag{39}$$

after integration of this equation we arrive at a hyperelastic stress-strain relation

$$\boldsymbol{\sigma} = \mathbb{D} : \boldsymbol{e}^{(m)} \tag{40}$$

which can be derived from quadratic strain energy density

$$W = \frac{1}{2}\boldsymbol{e}^{(m)} : \mathbb{D} : \boldsymbol{e}^{(m)} \tag{41}$$

7. CONCLUSION

The hypoelastic constitutive models with stress rates derived from hyperelasticity were investigated and compared with rates derived from second order work expression. Finally, hypoelastic law consistent with hyperelasticity were derived. Further research will focus on extension of plasticity into large strain range using hypoelastic formulation.

ACKNOWLEDGEMENT

The financial support of this research by the Czech Technical University in Prague (SGS project No. SGS13/034/OHK1/1T/11) is gratefully acknowledged.

REFERENCES

[1] BAŽANT, Z.P. A correlation study of incremental deformations and stability of continuous bodies. *Journal of Applied Mechanics.* 1971, **38**, 919-928. ISSN 0021-8936.

[2] SIMO, J.C. and PISTER, K.S. Remarks on rate constitutive equations for finite deformation problems: computational implications. *Computer Methods in Applied Mechanics and Engineering.* 1984, **46**(2), 201–215. ISSN 0045-7825.

[3] PERIC, D. On consistent stress rates in solid mechanics: Computational implications. *International Journal for Numerical Methods in Engineering.* 1992, **33**(4), 799–817. ISSN 1097-0207.

[4] SETH, B.R. Generalized Strain Measure with Application to Physical Problems. In: *Second-Order Effects in Elasticity, Plasticity and Fluid Dynamics.* Oxford: Pergamon Press, 1964, pp. 162-172. ISBN 978-0080110844

[5] HILL, R. On Constitutive Inequalities for Simple Materials. *Journal of the Mechanics and Physics of Solids.* 1968, **16**, 229-242. ISSN 0022-5096.

MEMBRANE STRUCTURES – DYNAMIC RELAXATION

Miloš HÜTTNER[1], Jiří MÁCA[2]

***Abstract**: The purpose of this paper is to describe the basic idea of the analysis of membrane structures and compare the efficiency of calculation using dynamic relaxation. Nine different methods of dynamic relaxation are applied to five simple examples. Methods with viscous damping and methods with kinetic damping are used.*

***Keywords**: membrane structure, dynamic relaxation, nonlinear analysis, triangular element*

1. INTRODUCTION

The load analysis of membrane structures is geometrically nonlinear problems. Several methods exist to solve these structures, the most common methods are: dynamic relaxation, force density method and finite element method. Two different procedures of dynamic relaxation method (DRM) will be used in this study – methods with viscous damping [1] and with kinetic damping (KD) [2].

1.1. IDEALIZATION

The surface of membrane structure is discretized into a system of joints and triangle membrane elements. The edges of the triangle form the connection between the joints and they are called links. The joints can be supported or unsupported. The equilibrium position unsupported nodes loaded of the nodal load is iteratively searched during load analysis. There are considered large displacements of the structure and small deformation of elements.

2. MEMBRANE ELEMENT

For a membrane structures the natural stiffness element can be used for calculation of internal forces. The original formulation of the natural stiffness element is credited to Argyris [3] but the formulation here follows the work of Barnes [4] and Topping [5]. For the formulation of the natural stiffness element a triangular element is considered. This element has only in-plane stiffness so the element formulation is with respect to displacements in the local coordinate directions. Using equations of equilibrium, it is possible to convert the surface stress within the element into forces along the sides of the triangle. General application of this element is described for example in [5].

---

[1] Ing. Miloš Hüttner, Department of Mechanics, Czech Technical University in Prague - Faculty of Civil Engineering, Thákurova 7; 166 29, Prague 6 - Dejvice; CZ, e-mail: milos.huttner@fsv.cvut.cz

[2] Prof. Ing. Jiří Máca, CSc.: Department of Mechanics, Czech Technical University in Prague - Faculty of Civil Engineering, Thákurova 7; 166 29, Prague 6 - Dejvice; CZ, e-mail: maca@fsv.cvut.cz

In this case the idealization of a typical element is as shown in Fig. 1 where the local coordinate system is conveniently chosen such a way that the x' axis coincides with the first side. The stresses in the element with respect to x' a y' directions, with $\sigma_{z'}$ equal to zero, are the standard plane stress formulation for an isotropic material [6].

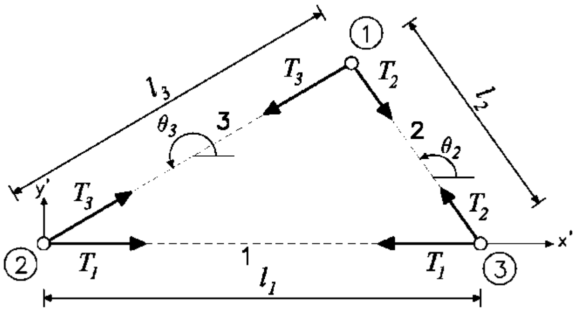

Fig. 1 Triangular element

The initial forces T_1, T_2 and T_3 of sides 1, 2 and 3 are defined for membrane element as:

$$\begin{pmatrix} T_1 \\ T_2 \\ T_3 \end{pmatrix} = Ad \begin{bmatrix} 1/l_1^0 & 0 & 0 \\ 0 & 1/l_2^0 & 0 \\ 0 & 0 & 1/l_3^0 \end{bmatrix} \begin{bmatrix} 1 & \dfrac{a_3c_2 - a_2c_3}{Q} & \dfrac{a_2b_3 - a_3b_2}{Q} \\ 0 & \dfrac{c_3}{Q} & -\dfrac{b_3}{Q} \\ 0 & -\dfrac{c_2}{Q} & \dfrac{b_2}{Q} \end{bmatrix} \begin{bmatrix} \sigma_{x'} \\ \sigma_{y'} \\ \tau_{xy'} \end{bmatrix}, \tag{1}$$

and

$$\begin{pmatrix} \sigma_{x'} \\ \sigma_{y'} \\ \tau_{xy'} \end{pmatrix} = \begin{bmatrix} \dfrac{E}{(1-\nu^2)} & \dfrac{\nu E}{(1-\nu^2)} & 0 \\ \dfrac{\nu E}{(1-\nu^2)} & \dfrac{E}{(1-\nu^2)} & 0 \\ 0 & 0 & \dfrac{E}{2(1+\nu)} \end{bmatrix} \begin{bmatrix} \dfrac{1}{l_1} & 0 & 0 \\ \dfrac{a_3c_2 - a_2c_3}{Ql_2} & \dfrac{c_3}{Ql_2} & -\dfrac{c_2}{Ql_2} \\ \dfrac{a_2b_3 - a_3b_2}{Ql_3} & -\dfrac{b_3}{Ql_3} & \dfrac{b_2}{Ql_3} \end{bmatrix} \begin{bmatrix} \Delta l_1 \\ \Delta l_2 \\ \Delta l_3 \end{bmatrix} \tag{2}$$

where A is the area of the element, d is the thickness of the membrane, E is the Young's modulus of elasticity and ν is the Poisson's ratio. Further l_i^0 is the length of the side i of the unloaded element, l_i is the current length of the side i, Δl_i is the elongation of the side i, $a_i = \cos^2\theta_i$, $b_i = \sin^2\theta_i$, $c_i = \sin\theta_i \cos\theta_i$ and θ_i is the inclination of the side i to the local x' axis. And $Q = b_2c_3 - b_3c_2$.

The direct stiffness S_1, S_2 and S_3 of sides 1, 2 and 3 are defined for membrane element as:

$$S_i = \frac{EAd}{\left(l_i^0\right)^2} \tag{3}$$

3. DYNAMIC RELAXATION

The theory of this method was first described by Day [1]. This theory was further developed and its detailed overview can be found in Barnes [4], Topping [5] or Lewis [7]. Practical examples of the application can be seen in [8, 9, 10].

3.1. PRINCIPLE

The basic unknowns form nodal velocity, which are calculated from nodal displacements. The discretization from timeline with time step Δt will be performed. During the step Δt a linear change of velocity is assumed. Acceleration during the step Δt is thus considered to be constant. By substituting the above assumptions the velocity for joint i in direction j (x, y and z) can be expressed in a new time point $t + \Delta t/2$ thus:

$$v_{ij}^{(t+\Delta t/2)} = v_{ij}^{(t-\Delta t/2)} \frac{M_{ij} / \Delta t - C_{ij} / 2}{M_{ij} / \Delta t + C_{ij} / 2} + \frac{R_{ij}^{t}}{M_{ij} / \Delta t + C_{ij} / 2}, \tag{4}$$

where R_{ij}^{t} is residual force (i.e. out of balance) at joint i in the direction j and at time t.

M_{ij} is the fictitious mass at joint i in the direction j.

C_{ij} is the viscous damping factor for joint i in the direction j.

$v_{ij}^{t+\Delta t/2}$ is velocity at joint i in the direction j and at time $t + \Delta t/2$.

Current coordinate x (and similarly for y and z) of the joint i at the time point $t + \Delta t$ can then be expressed as follows:

$$x_i^{(t+\Delta t)} = \Delta t \cdot v_{ix}^{(t+\Delta t/2)}. \tag{5}$$

From the imbalance (between external and internal forces) in node i one can calculate the residual force for the corresponding node in time t.

$$R_{ij}^{t} = P_{ij} - \sum_{k} T_{jk}^{t}, \tag{6}$$

where P_{ij} is the external load at joint i in the direction j.

T_{jk}^{t} is the tension force in the direction j of the link k entering into joint i at time t. The force T_k is possible for each link of membrane to be calculated from equation (1). Note – if the $\Sigma(T_{jk}^{t}) < 0$, so $\Sigma(T_{jk}^{t}) = 0$.

It is also possible at each time point to calculate the kinetic energy U_k throughout the structures.

3.2. SCHEMAS

Nine different schemes DRM will be used in this paper. Schemes A-B are based on the theory of viscous damping [1]. Schemes C-E are based on the theory of kinetic damping (KD) with a peak in the middle of the time step [5] and schemes F-H are based on the theory of KD with parabolic approximation [7].

Scheme A

Discretized mass M is chosen in this schema the same for each node and all directions.

$$M = \frac{\Delta t^2}{2}\left(\max S_{ij}\right) = \frac{\Delta t^2}{2}\left[\max\left(\sum_k S_{jk}\right)\right] \tag{7}$$

where S_{jk} is the direct stiffness in the direction j of the link k entering into joint i and it is possible for each link of membrane to be calculated from equation (3).

Viscous damping coefficient C for the whole structure is calculated using the theory of critical damping [5]:

$$C = \max C_i = \max\left(2\sqrt{S_i \cdot M_i}\right) = \sqrt{8}\,\frac{M}{\Delta t} \tag{8}$$

*Scheme A**

Fictitious values (M and C) for the whole structure are optimized (based on repeated calculations) so that the number of iterations is minimized.

Scheme B

Fictitious values M_i and C_i are calculated for each joint i separately and $M_i = \max(S_i)\Delta t^2/2$; $S_i = \max(S_{ix}, S_{iy}, S_{iz})$.

Scheme C

This scheme is based on the theory of KD with a peak in the middle of the time step. The mass for whole structure is calculated from equation (7).

Scheme D

This scheme is similar to the scheme C, but fictitious values M_i and C_i are calculated for each joint i separately and $M_i = \max(S_i)\Delta t^2/2$; $S_i = \max(S_{ix}, S_{iy}, S_{iz})$.

Scheme E

This scheme is similar to Scheme D but masses M_i are recalculated after each restart of the kinetic energy.

Scheme F, G and H

These schemes are similar to Scheme C (respectively D and E) but it used the theory of KD with parabolic approximation.

4. EXAMPLES

The chosen methods are applied to five simple constructions. The initial geometry (no internal stress) is evident from individual figures. The parameters of membranes are always E = 20 MPa, d = 1 mm and ν = 0.3. The time step is chosen Δt = 1 s in all calculations. The calculation is terminated when the residual forces in all joints are less than 0.003 kN.

4.1. EXAMPLE 1

It is a structure with 6 nodes (of which 2 are unsupported) interconnected with 4 membrane elements. This structure is shown in Fig. 2. The load P_{iz} = 3 kN acts on both unsupported joints.

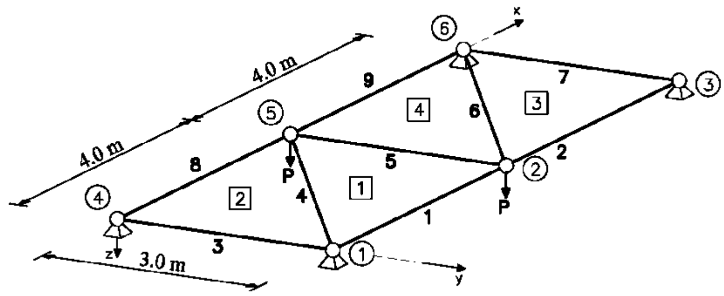

Fig. 2 Topology and initial geometry of Example 1

4.2. EXAMPLE 2

It is a structure with 10 nodes (of which 6 are unsupported) interconnected with 8 membrane elements. This structure is shown in Fig. 3. The load P_{iz} = 1.5 kN acts in all unsupported joints.

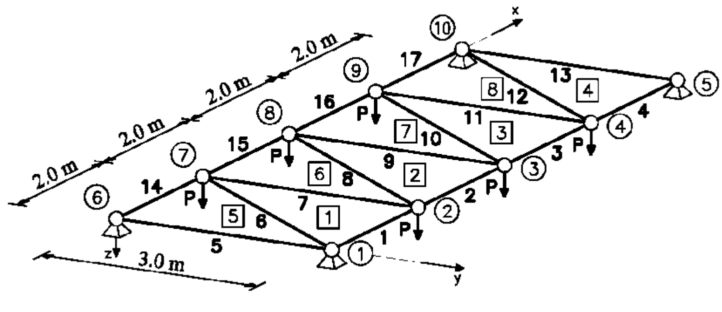

Fig. 3 Topology and initial geometry of Example 2

4.3. EXAMPLE 3

It is a structure with 8 nodes (of which 4 are unsupported) interconnected with 8 membrane elements. This structure is shown in Fig. 4. The load P = 1.5 kN.

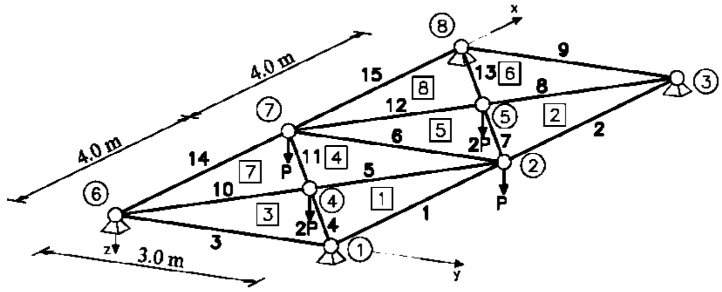

Fig. 4 Topology and initial geometry of Example 3

4.4. EXAMPLE 4

It is a structure with 15 nodes (of which 11 are unsupported) interconnected with 16 membrane elements. This structure is shown in Fig. 5. The load P = 0.75 kN.

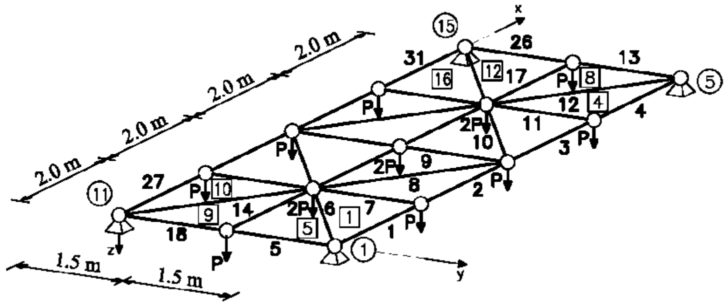

Fig. 5 Topology and initial geometry of Example 4

4.5. EXAMPLE 5

It is a structure with 45 nodes (of which 41 are unsupported) interconnected with 64 membrane elements. This structure is shown in Fig. 6. The load P_{iz} = 0.375 kN for joints 11-17, 20-26, 29-35 and P_{iz} = 0.1875 kN for all other unsupported joints.

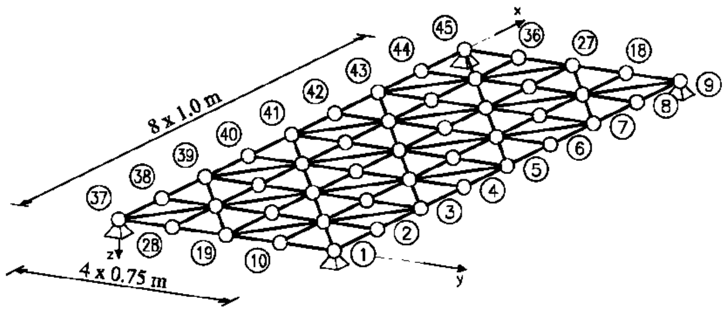

Fig. 6 Topology and initial geometry of Example 5

5. CONCLUSION

Summary of results is shown in Tab 1. (number of iterations) respectively Tab. 2 (time of solution).

Tab. 1 Summary of values - number of iterations

Schema	A	A*	B	C	D	E	F	G	H
Example 1	139	26	139	36	36	57	37	37	45
Example 2	232	33	239	39	39	55	41	41	68
Example 3	435	44	-	50	-	68	40	40	66
Example 4	935	72	482	104	62	112	101	64	101
Example 5	2878	148	1825	304	-	-	362	-	-

Tab. 2 Summary of values - time of solution (CPU in seconds)

Schema	A	A*	B	C	D	E	F	G	H
Example 1	0.39	0.10	0.37	0.11	0.10	0.21	0.12	0.13	0.15
Example 2	1.28	0.18	1.28	0.20	0.21	0.33	0.25	0.24	0.39
Example 3	2.30	0.23	-	0.42	-	0.41	0.23	0.25	0.43
Example 4	9.32	0.69	5.05	1.00	0.84	1.32	1.17	0.70	1.22
Example 5	111.8	6.00	70.83	12.09	-	-	15.72	-	-

Overall ranking methods, sorted by the number of errors (sum of all examples), the total number of iterations and the total CPU time, is shown in Tab. 3.

The method A * seems to the most effective. The method is practically unusable (need several repeated calculated). However, the method A * shows the potential of method A. If the choice of fictitious parameters occurs to develop, the viscous damping method can be more efficient than the method with kinetic damping. Furthermore, it appears that they are more stable methods that use the same mass for the whole structure than methods that use different masses for each joint.

Tab. 3 Outline of schemes

Total number	A*	C	F	A	G	H	E	B	D
Errors	0	0	0	0	1	1	1	1	2
Iteration	323	533	581	4619	182	280	292	2685	137
CPU time	7.20	13.82	17.49	125.1	1.32	2.19	2.27	77.53	1.15

ACKNOWLEDGEMENT

The results presented in this paper are outputs of the research project "P105/11/1529 - Cable - membrane structures analyses" supported by Czech Science Foundation and project "SGS13/034/OHK1/1T/11 - Advanced algorithms for numerical simulations in civil engineering" supported by the Faculty of Civil Engineering, Czech Technical University in Prague.

REFERENCES

[1] DAY, A. S. An introduction to dynamic relaxation. *The Engineer*. January 1965, 218-221, ISSN 0013-8029.

[2] CUNDALL, P. A. Explicit finite-difference methods in geomechanics. In: *Proceedings E.F. conf. numerical methods in geomechanics.* Blacksburg, June 1976, pp 132-150.

[3] ARGYRIS, J. H. Recent Advances in Matrix Methods of Structural Analysis. *Progress in Aeronautical Sciences*. Pergamon Press, London, 1964, **4**. ISSN 0376-0421

[4] BARNES, M. R. Form and stress engineering of tension structures. *Structural Engineering Review*, 1994, **6** (3-4), 175-202. ISSN 0952-5807.

[5] TOPPING, B.H.V. and IVÁNYI, P. *Computer Aided Design of Cable Membrane Structures*. Kippen, Saxe-Coburg Publications, 2008. 233 p. ISBN 978-1-874672-11-1.

[6] ZIENKIEWICZ, O., TAYLOR, R., *The finite element method – volume 1 the basis.* Butterworth-Heinemann, Oxford, England 2000. 125 p. ISBN 0-7506-5049-4.

[7] LEWIS, W. J. *Tension structures: from and behaviour*. London: Thomas Telford, 2003. 201 p. ISBN 0-7277-3236-6.

[8] HÜTTNER, M. *Analýza lanoplachtové konstrukce.* Praha 2012. Diploma Thesis. ČVUT v Praze. Fakulta stavební.

[9] HÜTTNER, M., MÁCA J., Cable structures - numerical analysis. In: *Proceedings of the 3rd conference: NMM 2012 Nano & Macro mechanics*. Praha: ČVUT, 2012, pp 81-88. ISBN 978-80-01-05097-2.

[10] REZAIEE-PAJAND, M., SARAFRAZI, S. R., REZAIEE, H., Efficiency of dynamic relaxation methods in nonlinear analysis of truss and frame structures. *Computers and Structures*. 2012. (112-113), 295-310. ISSN 0045-7949.

MODELLING OF BLAST WAVE PROPAGATION WITHIN CONTAINED SPACE OFA RAILWAY STATION BUILDING

RadekHÁJEK[1]

Abstract*:This paper is focused mainly on computer modelling and understanding of blast wave dynamics in interaction with the solid building. The effect of atmospheric overpressure on human body is also studied. The paper includes validation of FEM analysis results in comparison to experimental data and empiric values. Pressure wave reflections inside a confined space are studied. Multiple arrangements of concrete barriers are then proposed for faster energy dissipation and effective reduction of the damage and injuries caused by the explosion.*

Keywords*:explosion, pressure wave, FEM analysis, barriers against the pressure wave spreading*

1. INTRODUCTION

Due to the rise of the threat of terrorist attack, the research in the area of explosive loads of structures, especially public buildings, has received considerable attention in recent years. Buildings like railway stations, airports, embassies etc. ought to be designed to ensure as much safety of people inside as theoretically possible [1].

The primary requirement for any such building is to withstand the explosion without collapse of any of its crucial structural parts. Another requirement is to reduce the amount of potentially harmful fragments of interior equipment, e.g. window glass shards, pieces of metal or wood furniture etc.

With the development of computer hardware and software, it is possible to perform numerical analysis of explosion itself, its range and more importantly the behaviour of surrounding air and objects within range of the explosion [2].

2. EFFECTS OF EXPLOSION

The nature of loading generated by an explosion is propagation of a pressure wave, which is essentially an area of compressed air, which is moved from centre of the explosion at significant speed. The pressure wave velocity normally exceeds the speed of sound [3]. This means that it will travel even through large spaces within milliseconds.

[1]Ing.RadekHájek, Department of Concrete and Masonry Structures, Faculty of Civil Engineering, CTU in Prague, radek.hajek@fsv.cvut.cz

2.1. BLAST LOADING ON STRUCTURES

At the front of a blast wave the area of highly increased atmospheric pressure is formed. The wave also has enough kinetic energy to carry some debris or free objects along thus causing even more damage. It can be compared to very strong wind loading. Behind the blast wave, a low pressure area is formed causing some small objects, e.g. shards, to return back. This effect usually causes little damage compared to the initial blast wave and is often neglected.

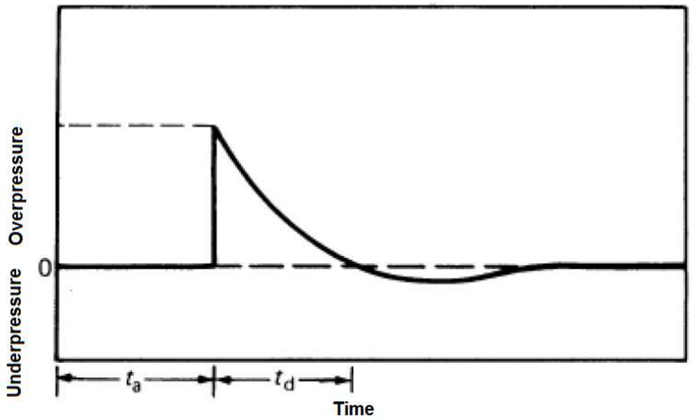

Fig. 1 Idealized shape of the air shock wave [4]

2.2. BLAST INJURIES

Propagation velocity and peak overpressure depends on many factors, e.g. size and chemical composition of the charge or reflections from rigid elements. The pressure wave generated inside a building is much more devastating than a wave generated in the open space explosion.

The human body can withstand relatively massive overpressure. Tab. 1 shows multiple types of overpressure injuries together with the overpressure values for each injury and the probability of their occurrence among people within range of an explosion.

Tab. 1 Overpressure effects on human body[5]

Peak overpressure Δp [kPa]	**Impact on the human body**
16.5	Eardrums damage at 1% affected
19.3	Eardrums damage at 10% affected
34.5	Eardrums damage at 50% affected
43.4	Lungs damage threshold
100.0	Fatal injuries at 1% affected
120.7	Fatal injuries at 10% affected
141.3	Fatal injuries at 50% affected
175.8	Fatal injuries at 90% affected
200.0	Fatal injuries at 99% affected

3. FEM ANALYSIS

To analyse the propagation of a blast wave within a large contained space e.g. railway station building, an elementary computer model was created. Simulation was performed with software suite for explicit dynamics called LS-DYNA. The use of ALE elements allows generation of two independent element meshes, one for air and explosive, and the other for building model. The method of interaction between those two meshes is defined.

Some rigid barriers were also added to the model to study reflections and channelling of the pressure wave. The goal was to try to determine the most favourable position of barriers which increases the speed of blast wave dissipation. Multiple calculations with changes in position of the explosive charge and barriers were conducted.

3.1. GEOMETRY

With focus on typical arrangement of interior of a railway station building (Fig. 2) a simplified FEM model was developed. The dimensions of the model are 50 m x 20 m x 15 m. Boundaries of modelled area were set to emulate the realistic behaviour of such building. Walls and floor reflect incoming shock wave and ceiling is set to allow the blast wave to travel through - as equivalent of fragile glass windows as seen in Fig. 2.

Although an explosion can occur due to any number of reasons, this paper is focused solely at detonation of a high explosive, which produces overpressure waves travelling at supersonic velocity.

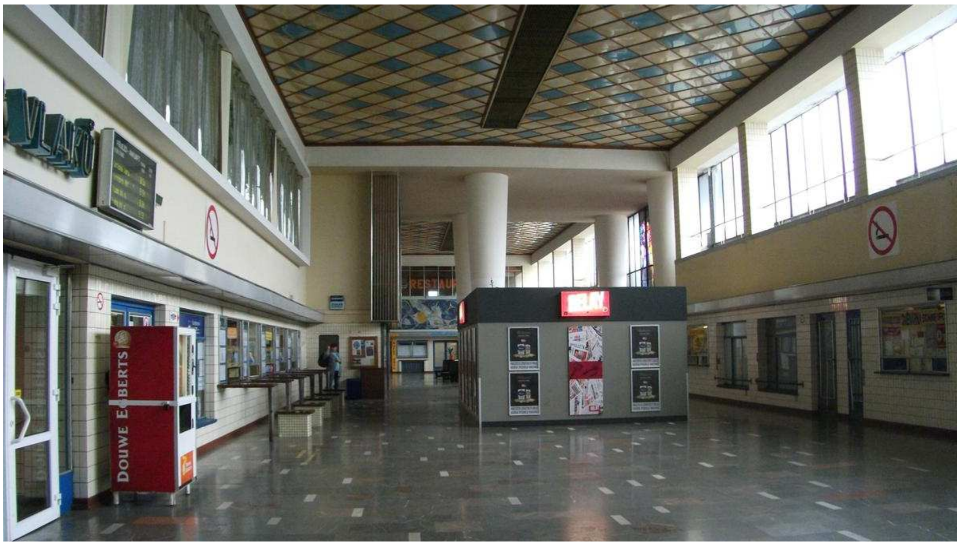

Fig. 2Interior of a typical railway station (Cheb, Czech Republic)

Because of the nature of terroristic attack, it isn’t possible to determine exactly position of the explosive. On the other hand it can be assumed that the explosive will be detonated in the most crowded areas. With this in mind, series of calculations were performed for variable positions of the explosive. Even various heights above the floor were examined (Fig. 3).

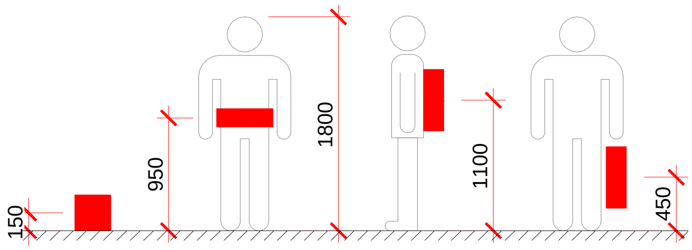

Fig. 3Position of explosive charge above the floor

3.2. MATERIAL MODELLING

Because the aim at this stage of research is to simulate the behaviour of blast wave and its reflections, material of the building and barriers was simplified. Those structures were modelled with RIGID elements (no deformation, no damage).Air and explosive are modelled using 3D solid ALE (Arbitrary Lagrangian-Eulerian) finite elements.For air a material model 009-NULL in combination with ideal gas equation of state (1) was defined.

$$P = (C_4 + C_5\mu)e_{ipv0} = (\gamma - 1)\frac{\rho}{\rho_0}e_{ipv0} \qquad (1)$$

where $C_4 + C_5 = \gamma - 1 = 0{,}4$ and initial energy per reference volume e_{ipv0} is definedfor standard atmospheric pressure $P_0 = 101{,}3\,\mathrm{kPa}$with a formula $e_{ipv0} = P_0 v_0 / (\gamma - 1)$, where $v_0 = 1{,}0$.

To characterize the high explosivethe widely usedJones-Wilkins-Lee equation of state of TNT (2) was embedded. Parameters of JWL EOS can be widely found in literature [2, 6, 7, 8, 9].

$$p = A\left(1 - \frac{\omega}{R_1}\frac{\rho}{\rho_0}\right)e^{-R_1\frac{\rho_0}{\rho}} + B\left(1 - \frac{\omega}{R_2}\frac{\rho}{\rho_0}\right)e^{-R_2\frac{\rho_0}{\rho}} + \omega E\frac{\rho}{\rho_0} \qquad (2)$$

Because of wide range of possible values defined in literature it turned out to be difficult to add concrete values to EOS parameters. Because of this it was decided to perform a verification task that would determine the most accurate EOS for use in future research and FEM models.

3.3. RESULTS VERIFICATION

Results obtained from FEM analyses were compared to empirical equations and to results from physical experiment conducted in 2010 by Foglar and Kovář[10]. Experimental results were proven accurate enough when compared to empirical equations [10].

Considering the actual arrangement of the experiment (Fig. 4), according FEM model was created and the explosion calculated for multiple sets of JWL EOS parameters. As predicted, results of FEM analysis vary considerably depending on the EOS parameters.

Fig. 4Blast experiment layout

Fig. 5 shows comparison of FEM, experimental and empirical results (peak overpressure). Best agreement between all three types of results was achieved with set of parameters named EOS V, which was declared accurate enough to be used in future calculations.

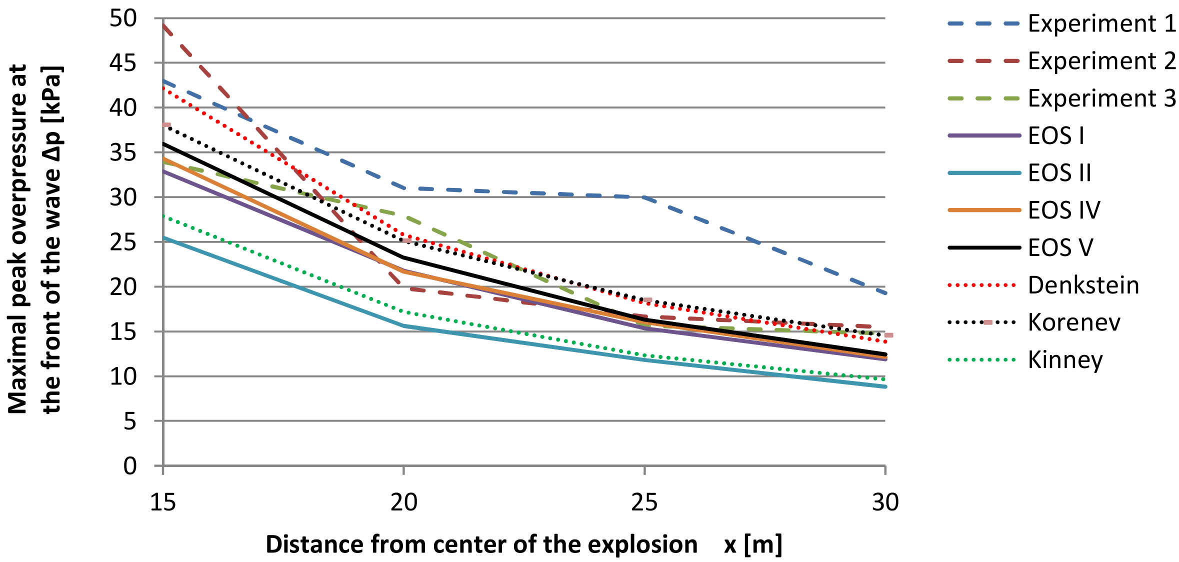

Fig. 5Comparison of FEM (continuous), empirical (dotted) and experimental (dashed) results

4. BLAST BARRIERS OPTIMIZATION

When designing a public building any possible means of protection against an accidental load should be considered. Rigid barriers are proposed to divide large open space to multiple sections. Effects of position and size of barriers were studied.

4.1. BARRIERS ARRANGEMENT

To reduce damage and number of injuries it is essential to reduce range of the explosion, i.e. the peak overpressure and number of flying fragments in areas behind proposed barriers. Because of close proximity of epicentre of the explosion, those areas in front of barriers cannot be successfully protected from both the overpressure and debris.

As mentioned before, barriers should be arranged to effectively divide large open space so the overpressure wave after an explosion is mostly confined to only one section. On top of that they also must allow free passage of people from one section to another.

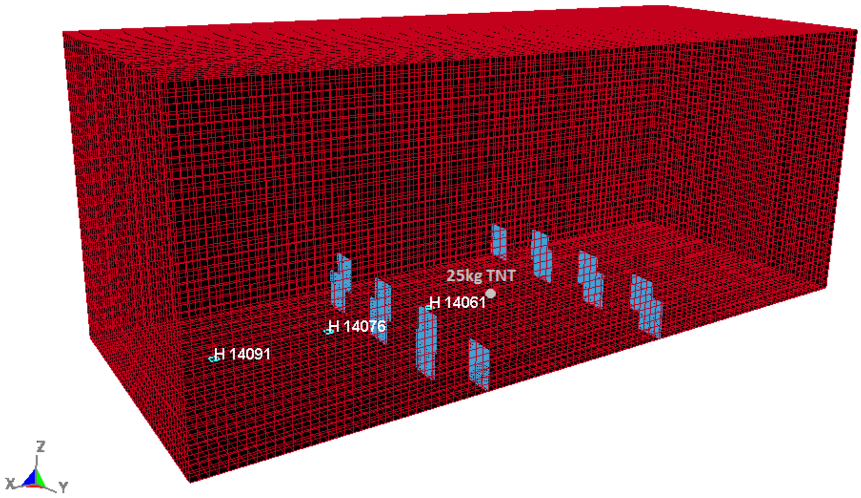

Fig. 6Example of afull scale FEM model for barriers optimization

It was proven that proposed arrangement of rigid barriers can effectively reduce the peak overpressure at the front of blast wave. This is possibly caused by disruption of the air flow in area between barriers. Comparison of free and disrupted blast wave is shown at Fig. 7.

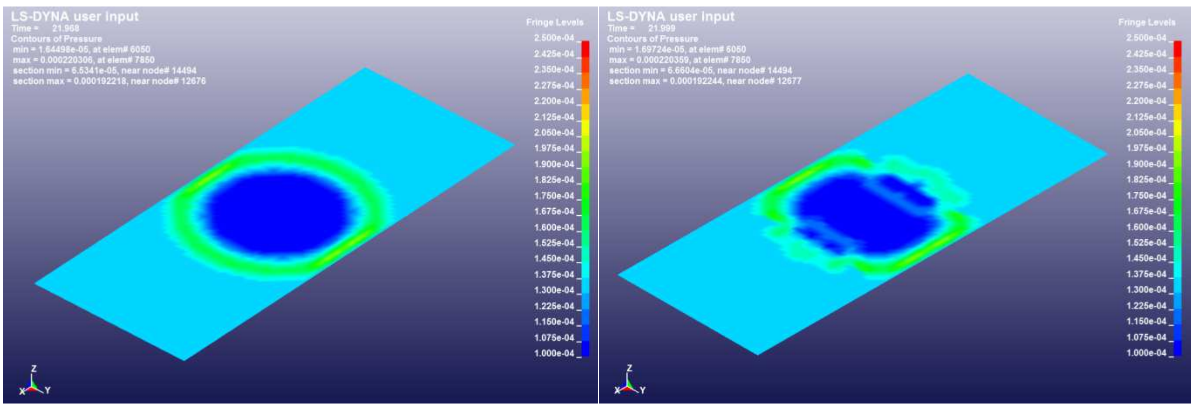

Fig. 7Contours of atmospheric pressure at t=20 ms (without barriers and with barriers)

4.2. DAMAGE REDUCTION EFFICIENCY

To eliminate faults resulting from relatively coarse finite element mesh a small scale FEM model was created (Fig. 8) to study the blast wave propagation through the barriers in more detail. Some determinative results are summarized in Tab. 2.

For finer finite element mesh the results were even more optimistic proving reduction of the injury causing peak overpressure by up to 45%. According to Tab. 1 obtained peak values indicate that in the area behind blast barriers, the probability of a serious injury is almost eliminated.

Tab. 2Peak overpressure obtained from small scale FEM model

Model	Value	Monitored position (Fig. 8)				
		A	B	C	D	E
1 m wide barriers	Overpressure [KPa]	42.4	20.7	30.2	20.1	20.5
	Elapsed time [ms]	12.5	17.5	17.0	23.0	21.0
2 m wide barriers	Overpressure [KPa]	35.3	13.8	20.8	12.4	11.2
	Elapsed time [ms]	16.0	22.5	19.0	26.0	24.0
No barriers	Overpressure [KPa]	72.6	44.6	49.2	33.3	35.2
	Elapsed time [ms]	12.0	17.0	16.5	21.5	21.0

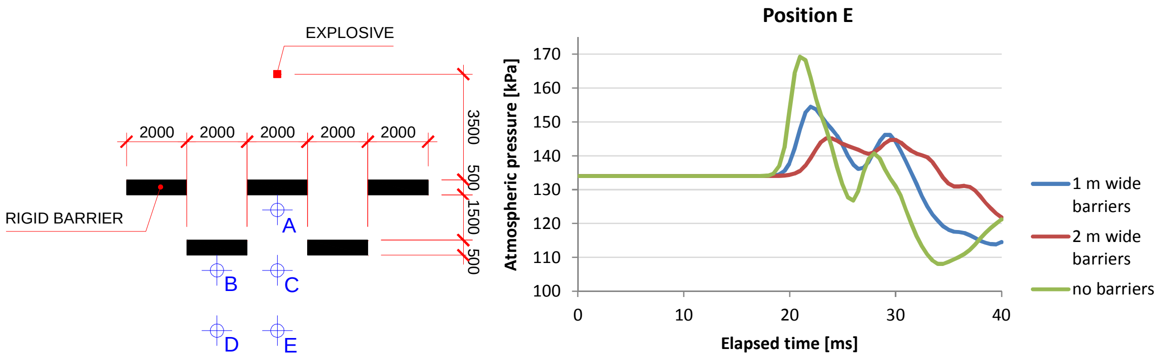

Fig. 8Layout of small scale FEM model [mm] and overpressure history

5. CONCLUSIONS

This paper represents an introduction to the modelling of blast wave behaviour inside a public building and possibilities to ensure safety of people and stability of the building itself. With the rapid development in computer software and hardware a large scale numerical analysis can be performed on available computer equipment. Preliminary results show that it is possible to change the behaviour of blast wave and reduce its destructive potential. For the future research it is crucial to prove the accuracy of obtained results by comparison with experimental data and, if needed, to calibrate the computer model. Definition of JWL equation of state for TNT explosive requires more attention. Also more barrier types, positions and dimensions should be investigated.

ACKNOWLEDGEMENT

The financial support of the CTU grant no. SGS13/035/OHK1/1T/11, Ministry of the Interior of the Czech Republic project no. VG20132015114 and the Czech Republic Grant Agency project no.13-30441S is kindly acknowledged.

REFERENCES

[1] ZHOU, X. Q. and HAO, H. Prediction of airblast loads on structures behind a protective barrier. *International Journal of Impact Engineering*, **35** (5), May 2008, 363-375. ISSN 0734-743X.

[2] HUANG, Y. and WILLFORD, M. R. Validation of LS-DYNA® MMALE with Blast Experiments. In: *12th International LS-DYNA Users Conference*. Detroit, USA, 3 - 5 June 2012.

[3] HENRYCH, Josef. *Dynamikavýbuchu a jejíužití*. Praha : Academia – nakladatelství ČAV. 1973. 412 s.

[4] MAKOVIČKA, D. and JANOVSKÝ, B.: *Příručkaprotivýbuchovéochranystaveb (Handbookof antiexplosion protection of structures)*, Českátechnika – nakladatelství ČVUT v Praze, 2008, ISBN 978-80-01-04090-4.

[5] WELLS, Geoff L. *Major hazards and their management*. London : Institution of Chemical Engineers. 1997. 305 p. ISBN 9780852953686.

[6] TABATABAEI, Zahra S. and VOLZ, Jeffery S. A comparison between Three Different Blast methods in LS-DYNA: LBE, MM-ALE, Coupling of LBE and MM-ALE. In: *12th International LS-DYNA Users Conference*. Detroit, USA, 3 - 5 June 2012.

[7] ZUKAS, Jonas A and WALTERS, William P. *Explosive Effects and Applications*. New York : Springer-Verlag GmbH. 1997. 460 p. ISBN 9780387982014.

[8] ARRIGONI M. et al. Numerical simulation of air blast waves. In: *2011 European Hyperworks Technology Conference*, Bonn, Germany, 7 – 9 November 2011.

[9] TOUSSAINT, G. and DUROCHER R. Finite Element Simulation using SPH Particles as Loading on Typical Light Armoured Vehicles. In: *10th International LS-DYNA Users Conference*, Dearborn, MI, USA, 8 - 10 June 2008. ISBN 0-9778540-4-3.

[10] FOGLAR, M. and KOVÁŘ, M. Conclusions from experimental testing of blast resistance of FRC and RC bridge decks, *International Journal of Impact Engineering*, **59**, 18-28. ISSN 0734-743X.

EFFICIENT METHODS FOR UNCERTAINTY QUANTIFICATION

Eliška JANOUCHOVÁ[1], Anna KUČEROVÁ[2], Jan SÝKORA[3]

Abstract: *An extensive development of efficient methods for stochastic modelling enabled uncertainty propagation through complex models. In this contribution, we present a review and comparison of several approaches such as stochastic Galerkin method, stochastic collocation method or polynomial regression based on Latin Hypercube Sampling.*

Keywords: *Stochastic modelling, polynomial chaos expansion, uncertainty propagation, reliability analysis*

1. INTRODUCTION

Reliability analysis and modelling of structures in general need to take into account all the relevant information as well as the uncertainties in the environmental conditions, loading or structural properties. Thanks to the growth of powerful computing technology, recently developed procedures in the field of stochastic mechanics have become applicable to realistic engineering systems. Stochastic finite element methods (SFEM) [1, 2] is a powerful tool extending the classical deterministic finite element method (FEM) to the stochastic framework involving finite elements whose properties are random [3].

In this contribution we concentrate on SFEM based on polynomial chaos expansion (PCE) used for approximation of the model response in the stochastic space. Uncertainty in the model output can be then quantified using Monte Carlo method employed for sampling model parameters and evaluating the PCE instead of full numerical model. The efficiency of SFEM thus depends on computational requirements of the PCE construction and its consequent accuracy. There are several methods for construction of PCE-based approximation of a model response: linear regression [4], stochastic collocation methods [5, 6] and stochastic Galerkin method [7, 8]. The aim of this paper is to compare these methods in terms of computational requirements and accuracy on a simple illustrative example of a frame structure.

[1] Bc. Eliška Janouchová, Department of Mechanics, Faculty of Civil Engineering, Czech Technical University in Prague, eliska.janouchova@fsv.cvut.cz

[2] Ing. Anna Kučerová, Ph.D., Department of Mechanics, Faculty of Civil Engineering, Czech Technical University in Prague, anicka@cml.fsv.cvut.cz

[3] Ing. Jan Sýkora, Ph.D., Department of Mechanics, Faculty of Civil Engineering, Czech Technical University in Prague, jan.sykora.1@fsv.cvut.cz

2. MOTIVATION

In order to demonstrate a performance of the methods on an engineering structure, we have chosen a simple frame presented in [9].The geometry and load distribution of the frame are shown in Fig. 1.

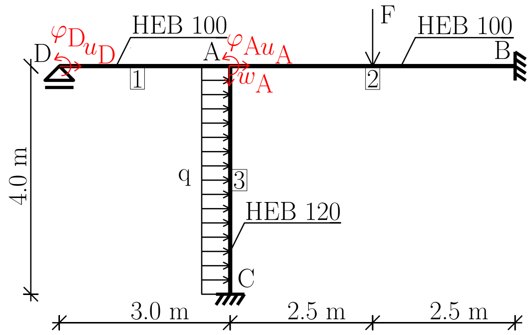

Fig. 1 Scheme of a frame structure.

Tab. 1 Material data, geometrical data and loading and variations.

Data	Nominal value	Variable	Histogram
Yield stress	$f_{y,\mu} = 235\text{GPa}$	$f_{y,\sigma}$	Fy235A
Moment of inertia	$I_1 = 449.5\ \text{cm}^4$	$I_{\sigma 1}$	N1-05
Cross-sectional area	$A_1 = 26.04\ \text{cm}^2$		
Moment of inertia	$I_2 = 449.5\ \text{cm}^4$	$I_{\sigma 2}$	N1-05
Cross-sectional area	$A_1 = 26.04\ \text{cm}^2$		
Moment of inertia	$I_3 = 864.4\ \text{cm}^4$	$I_{\sigma 3}$	N1-05
Cross-sectional area	$A_3 = 34.01\ \text{cm}^2$		
Elastic section modulus	$W_3 = 144.1\ \text{cm}^3$		
Lengths	$l_1 = 3, l_2 = 5, l_3 = 4$ m	l_σ	N1-01
Dead load	$D_1 = 11$ kN/m	$D_{\sigma 1}$	DEAD2
Short-lasting load	$S_1 = 9$ kN/m	$S_{\sigma 1}$	SHORT1
Long-lasting load	$L_1 = 5.5$ kN/m	$L_{\sigma 1}$	LONG1
Dead load	$D_2 = 3.5$ kN	$D_{\sigma 2}$	DEAD2
Short-lasting load	$S_2 = 2.2$ kN	$S_{\sigma 2}$	SHORT1
Long-lasting load	$L_2 = 1.7$ kN	$L_{\sigma 2}$	LONG1

Material of the frame is steel with Young's modulus $E = 210\text{GPa}$ and uncertain yield stress f_y obtained by the product of the nominal value $f_{y,\mu}$ and uncertain variation $f_{y,\sigma}$ defined by a prescribed histogram Fy235A (see Fig. 2). Also the geometrical parameters of particular beams are considered as uncertain and defined as products of the corresponding nominal values and variations given in [9] and listed in Tab. 1. Particular histograms are also depicted in Fig. 2.

The prescribed loading are linear combinations of dead load, long-lasting load and short-lasting load given as $q = D_1 D_{\sigma 1} + S_1 S_{\sigma 1} + L_1 L_{\sigma 1}$ [kN/m] and $F = D_2 D_{\sigma 2} + S_2 S_{\sigma 2} + L_2 L_{\sigma 2}$ [kN], where particular loads are statistically independent and described by random variables with extreme values and variations defined by histograms given in Tab. 1 and depicted in Fig. 2.

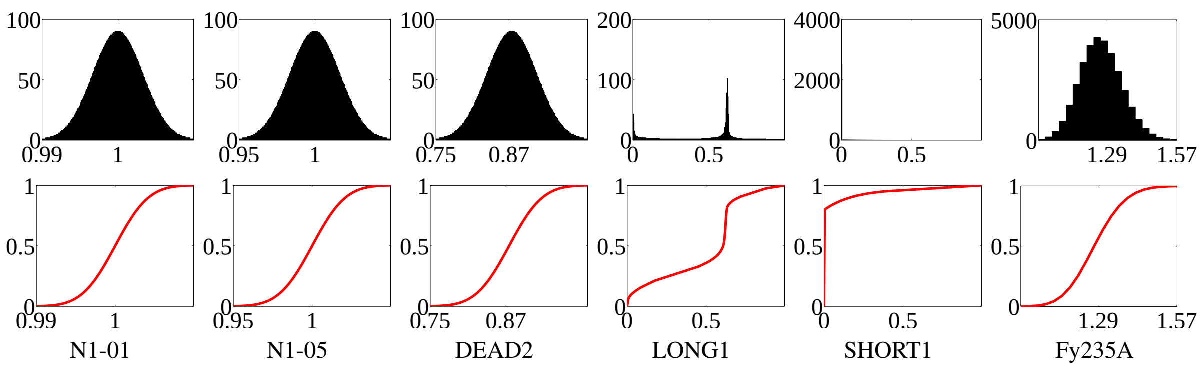

Fig. 2 Histograms of uncertain parameters and corresponding cumulative density functions.

Since instability of the column in the frame is not caused by buckling pressure in view of the fact that the axial force in the column does not achieve critical intensity, the column has only one failure mode. The maximal internal forces will appear in the column at support C and can be computed from the displacements of the joint A. The unknown displacements $\boldsymbol{r}$ can be for linear elastic behaviour considered here computed by the finite element method or displacement method. We start directly with the latter one from discretised form of equilibrium equations:

$$\mathbf{K}\boldsymbol{r} = \boldsymbol{f}\,, \tag{1}$$

which – after applying the boundary conditions – is a system of 5 linear equations for unknown displacements $\boldsymbol{r} = (u_{\mathrm{D}}, \varphi_{\mathrm{D}}, u_{\mathrm{A}}, w_{\mathrm{A}}, \varphi_{\mathrm{A}})$.

Safety margin M of the column is the difference between the yield stress f_y and stress produced by external load σ. Failure F occurs when σ exceeds f_y. Probability of failure $\Pr(F)$ is then estimated as the number of failures divided by the total number of executed simulations.

3. POLYNOMIAL CHAOS EXPANSION

In order to accelerate the sampling procedure in uncertainty propagation process, the evaluations of a numerical model including solutions of Eq. 1 can be replaced by evaluations of a model surrogate. In particular, we search for an approximation of the response $\boldsymbol{r}$ by polynomial chaos expansion (PCE) [1, 2]. PCE can be used to approximate the response with respect to probability distribution of the random variables. The convergence of the approximation error with the increasing number of polynomial terms is optimal in case of orthogonal polynomials of a special type corresponding to the probability distribution of the underlying variables [10]. For example, Hermite polynomials are associated with the Gaussian distribution, Legendre polynomials with the uniform distribution and so on.

In the considered example all the random variables are listed in Tab. 1. Let us simplify the notation and denote them as m_i, $\boldsymbol{m} = (\ldots, m_i, \ldots)^{\mathrm{T}} = (I_{\sigma 1}, I_{\sigma 2}, I_{\sigma 3}, l_\sigma, D_{\sigma 1}, S_{\sigma 1}, L_{\sigma 1}, D_{\sigma 2}, S_{\sigma 2}, L_{\sigma 2})^{\mathrm{T}}$. Since none of these variables has a continuous probability density function (PDF), but their distribution is described by histograms, we introduce new standard random variables $\boldsymbol{\xi} = (\ldots, \xi_i, \ldots)^{\mathrm{T}}$ with a continuous PDF. The variables m_i can be then expressed by non-smooth transformation functions t_{jk} of variables ξ_i according to the given histogram j and type k of the ξ_i distribution, i.e. $m_i = t_{jk}(\xi_i)$. Particular examples of transformation functions will be discussed in Section 4.

Once we have expressed the model variables $\boldsymbol{m}$ as functions of standard variables $\boldsymbol{\xi}$, also the model response becomes a function of these variables. This function can be thus approximated by the PCE of a type corresponding to the type of $\boldsymbol{\xi}$ distribution, i.e.

$$\tilde{\boldsymbol{r}}(\boldsymbol{\xi}) = \sum_{\alpha} \boldsymbol{\beta}_\alpha \psi_\alpha(\boldsymbol{\xi}), \tag{2}$$

where $\boldsymbol{\beta}_\alpha$ is a vector of PC coefficients $\beta_{\alpha,i}$ corresponding to a particular component of system response r_i. $\psi_\alpha(\boldsymbol{\xi})$ are multivariate polynomials. The expansion *(2)* is usually truncated to the limited number of terms n_β, which is very often related to the number of random variables n_ξ and to the maximal degree of polynomials n_p according to the relation $n_\beta = \frac{(n_\mathrm{p}+n_\xi)!}{n_\mathrm{p}! n_\xi!}$.

3.1. LINEAR REGRESSION

A very general method of computing PC coefficients in Eq. *(2)* is a well-known linear regression [4]. The application is based on the three following steps: (i) preparation of data $\boldsymbol{\Xi} \in \mathbb{R}^{n_\xi \times n_\mathrm{d}}$ which are obtained as n_d samples of parameter vector $\boldsymbol{\xi}_i$ (ii) evaluation of the model for samples $\boldsymbol{\xi}_i$ resulting in response samples $\boldsymbol{r}_i$ organised into the matrix $\mathbf{R} \in \mathbb{R}^{n_\mathrm{r} \times n_\mathrm{d}}$, where n_r is a number of response components and (iii) computation of PC coefficients $\boldsymbol{\beta}_\alpha$ organised into the matrix $\mathbf{B} \in \mathbb{R}^{n_\mathrm{r} \times n_\beta}$ using e.g. the ordinary least square method.

In this work samples are obtained by Latin hypercube sampling (LHS) considering the prescribed probability distribution [11]. Each computation of a response sample $\boldsymbol{r}_i$ then includes the evaluation of the transformations and the evaluation of the model *(1)*. The computation of the PC coefficients $\mathbf{B}$ starts by evaluation of all the polynomial terms ψ_α for all the samples $\boldsymbol{\xi}_i$ and saving them in the matrix $\mathbf{Z} \in \mathbb{R}^{n_\mathrm{d} \times n_\beta}$. The ordinary least square method then leads to $\mathbf{Z}^\mathrm{T}\mathbf{Z}\mathbf{B}^\mathrm{T} = \mathbf{Z}^\mathrm{T}\mathbf{R}^\mathrm{T}$ which is n_r independent systems of n_β linear equations.

3.2. STOCHASTIC COLLOCATION

Stochastic collocation method is based on an explicit expression $\beta_{\alpha,i} = \int r_i(\boldsymbol{\xi})\psi_\alpha(\boldsymbol{\xi})\,\mathrm{d}\mathbb{P}(\boldsymbol{\xi})$, which can be solved numerically using an appropriate integration rule (quadrature) on $\mathbb{R}^{n_\xi}$. The expression then becomes $\beta_{\alpha,i} = \sum_{j=1}^{n_\mathrm{d}} r_i(\boldsymbol{\xi}_j)\psi_\alpha(\boldsymbol{\xi}_j)w_j$, where $\boldsymbol{\xi}_j$ stands for an integration node and w_j is a corresponding weight. Here we employ versions of the Smolyak quadrature rule, in particular quadratures with the Gaussian rules (GQN) and nested Kronrod-Patterson quadrature rules (KPN), see [12].

It is clear that the stochastic collocation method is similar to linear regression, because in both cases the most computational effort is needed for evaluation of a set of model simulations. The principal difference can be seen in sample generation, where stochastic collocation method uses a preoptimised sparse grids while the linear regression is based on stochastic LHS.

3.3. STOCHASTIC GALERKIN METHOD

Stochastic Galerkin method is principally different to the previous ones, which are based on a set of independent model simulations. Stochastic Galerkin method is an intrusive method, i.e. it requires reformulation of the governing equations of the model *(1)*. To this purpose, we rewrite Equation *(2)* using matrix notation $\tilde{\boldsymbol{r}}(\xi) = (\mathbf{I} \otimes \boldsymbol{\psi}(\boldsymbol{\xi}))\boldsymbol{\beta}$, where $\mathbf{I} \in \mathbb{R}^{n_\mathrm{r} \times n_\mathrm{r}}$ is the unity matrix, $\otimes$ is the Kronecker product, $\boldsymbol{\psi}(\boldsymbol{\xi})$ is a n_β-dimensional vector of polynomials and $\boldsymbol{\beta}$ is a $(n_\beta \cdot n_\mathrm{r})$-dimensional vector of PC coefficients organised here as $\boldsymbol{\beta} = (\ldots, \boldsymbol{\beta}_i, \ldots)^\mathrm{T}$, where $\boldsymbol{\beta}_i$ consists of PC coefficients corresponding to i-th response component. Substituting the model response $\boldsymbol{r}$ by its PC approximation $\tilde{\boldsymbol{r}}$ and applying Galerkin conditions, we obtain $\int \boldsymbol{\psi}(\boldsymbol{\xi}) \otimes \mathbf{K}(\boldsymbol{\xi}) \otimes \boldsymbol{\psi}^\mathrm{T}(\boldsymbol{\xi})\,\mathrm{d}\mathbb{P}(\boldsymbol{\xi}) \cdot \boldsymbol{\beta} = \int \boldsymbol{\psi}(\boldsymbol{\xi}) \otimes \boldsymbol{f}(\boldsymbol{\xi})\,\mathrm{d}\mathbb{P}(\boldsymbol{\xi})$, which is a linear system of $(n_\beta \cdot n_\mathrm{r})$ equations. The integration can be done numerically or analytically. The analytical solution is available e.g. when all terms in the stiffness matrix and in the loading vector are polynomials with respect to $\boldsymbol{\xi}$. In such a case, the method is called *fully intrusive*. In our particular example, we can multiply the governing Equation *(1)* by l_σ^3 so as to obtain polynomials in terms of model parameters $\boldsymbol{m}$. However, we will not obtain polynomials in terms of $\boldsymbol{\xi}$ due to non-smooth transformations. Hence, in such a case, a numerical integration leading to *semi-intrusive* Galerkin method is inevitable. Here we use again Smolyak integration rule, in particular GQN [12].

4. RESULTS

The goal of the presented work is to compare the described methods for approximating the model response and accelerating the Monte Carlo (MC) sampling performed for estimation of probability distribution of safety margin M and probability of structural failure. In this numerical study two variants of model response are considered, the first one is directly safety margin, in the second case the model response is displacement vector and safety margin is calculated from its approximation.

Tab. 2 Time requirements and errors in predicting safety margin in case of **prescribed histograms** *for model parameters* $\boldsymbol{m}$*.*

Model response:		**Safety margin**				**Displacement vector**			
Method	p	n_d	Time [s]	$\Pr(F)$	ε_M [%]	n_d	Time [s]	$\Pr(F)$	ε_M [%]
MC	–	10^7	23825	$735 \cdot 10^{-7}$	–	10^7	22352	$735 \cdot 10^{-7}$	–
LHS	1	23	32	$7 \cdot 10^{-7}$	4.2024	19	217	$282 \cdot 10^{-7}$	1.3289
	2	243	164	$1580 \cdot 10^{-7}$	2.6572	163	896	$617 \cdot 10^{-7}$	0.6323
	3	1607	757	$15678 \cdot 10^{-7}$	2.1177	871	2746	$1795 \cdot 10^{-7}$	0.4434
	4	7789	2702	$13842 \cdot 10^{-7}$	1.7934	3481	11021	$1830 \cdot 10^{-7}$	0.3740
KPN	1	23	31	$10 \cdot 10^{-7}$	4.3112	19	250	$172 \cdot 10^{-7}$	0.8836
	2	243	164	$4910 \cdot 10^{-7}$	3.1118	163	896	$947 \cdot 10^{-7}$	0.6350
	3	1607	760	$11272 \cdot 10^{-7}$	2.9822	871	2776	$1327 \cdot 10^{-7}$	0.5904
	4	7789	2701	$8352 \cdot 10^{-7}$	3.4264	3481	8770	$1114 \cdot 10^{-7}$	0.6519
GQN	1	23	31	$0 \cdot 10^{-7}$	3.5143	19	214	$42 \cdot 10^{-7}$	0.7086
	2	265	164	$505 \cdot 10^{-7}$	9.7539	181	703	$382 \cdot 10^{-7}$	1.7807
	3	2069	764	$71942 \cdot 10^{-7}$	6.9817	1177	2795	$6179 \cdot 10^{-7}$	1.2896
	4	12453	2713	$322860 \cdot 10^{-7}$	15.7367	5965	11143	$9332 \cdot 10^{-7}$	2.7486
GM	1					–	194	$42 \cdot 10^{-7}$	0.6911
	2					–	868	$395 \cdot 10^{-7}$	1.7709
	3					–	2766	$6201 \cdot 10^{-7}$	1.2705
	4					–	12539	$9167 \cdot 10^{-7}$	2.7066

We assume $\boldsymbol{\xi}$ as standard Gaussian variables and thus we employ Hermite polynomials for model surrogate. The reference estimation of probability distribution of safety margin M is obtained by MC sampling with 10^7 samples. Tab. 2 shows the required computational time and relative errors in predictions for linear regression, stochastic collocation method and semi-intrusive Galerkin method for four polynomial degrees p. The relative errors in the prediction of safety margin are obtained as $\varepsilon_M = \frac{1}{n}\sum_{i=1}^{n} \frac{|M_\mathrm{PCE} - M_\mathrm{MC}|}{\max(M_\mathrm{MC}) - \min(M_\mathrm{MC})} \cdot 100$, where M_MC stands for the safety margin estimated by the MC method and M_PCE stands for the safety margin obtained using a chosen surrogate.

The results show relatively good predictions of safety margin, but the prediction of failure probability is unsatisfactory for all the examined methods. Significant difference in prediction of M for particular variants of model response is caused by the different number of random variables involved in the approximated response. While the displacement vector depends only on ten random variables, safety margin is influenced also by the uncertain yield stress f_y.

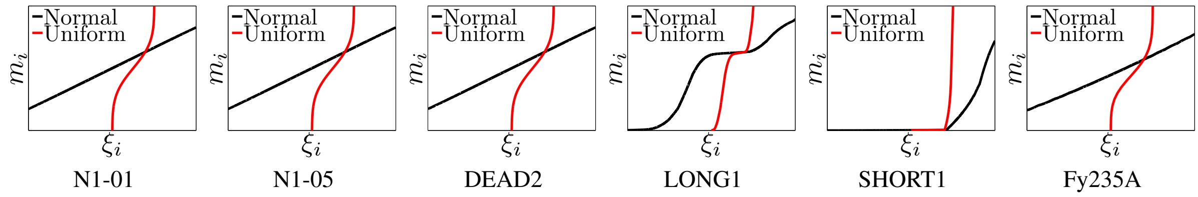

Fig. 3 Transformation relations for prescribed histograms.

The reason for these unsatisfactory results is probably highly nonlinear transformation for parameters with prescribed histograms LONG1 and SHORT1, as shown in Fig. 3. In order to test this assumption, we have replaced these two prescribed histograms by the new ones more close to normal distribution, see Fig. 4. New errors in predicting safety margin are listed in Tab. 3.

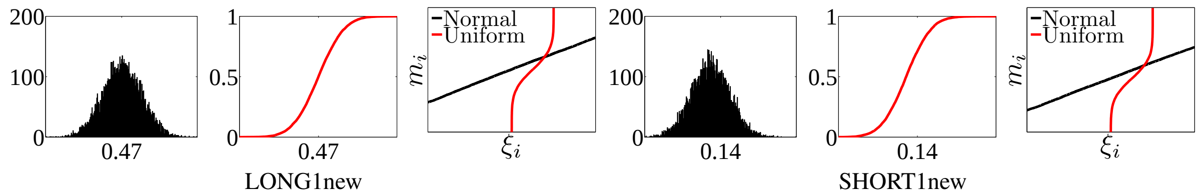

Fig. 4 New histograms of model parameters with corresponding cumulative density functions and transformation relations.

Tab. 3 Time requirements and errors in predicting safety margin in case of **new histograms** *for model parameters* $\boldsymbol{m}$.

Model response:		**Safety margin**				**Displacement vector**			
Method	p	n_{d}	Time [s]	$\Pr(F)$	ε_M [%]	n_{d}	Time [s]	$\Pr(F)$	ε_M [%]
MC	–	10^7	23833	$5 \cdot 10^{-7}$	–	10^7	22027	$5 \cdot 10^{-7}$	–
LHS	1	23	32	$9 \cdot 10^{-7}$	0.2855	19	216	$5 \cdot 10^{-7}$	0.0320
	2	243	165	$6 \cdot 10^{-7}$	0.0798	163	743	$5 \cdot 10^{-7}$	0.0142
	3	1607	753	$3 \cdot 10^{-7}$	0.0826	871	2787	$5 \cdot 10^{-7}$	0.0143
	4	7789	2701	$15 \cdot 10^{-7}$	0.2003	3481	8762	$5 \cdot 10^{-7}$	0.0275
KPN	1	23	31	$10 \cdot 10^{-7}$	0.2592	19	216	$5 \cdot 10^{-7}$	0.0202
	2	243	164	$6 \cdot 10^{-7}$	0.0821	163	719	$5 \cdot 10^{-7}$	0.0132
	3	1607	758	$1 \cdot 10^{-7}$	0.1663	871	2876	$5 \cdot 10^{-7}$	0.0241
	4	7789	2786	$8 \cdot 10^{-7}$	0.1299	3481	9561	$5 \cdot 10^{-7}$	0.0220
GQN	1	23	31	$10 \cdot 10^{-7}$	0.2407	19	237	$5 \cdot 10^{-7}$	0.0212
	2	265	164	$6 \cdot 10^{-7}$	0.1466	181	895	$5 \cdot 10^{-7}$	0.0235
	3	2069	763	$1 \cdot 10^{-7}$	0.1981	1177	2865	$5 \cdot 10^{-7}$	0.0339
	4	12453	2714	$2 \cdot 10^{-7}$	0.2944	5965	9332	$5 \cdot 10^{-7}$	0.0348
GM	1					–	194	$5 \cdot 10^{-7}$	0.0502
	2					–	871	$5 \cdot 10^{-7}$	0.0392
	3					–	2780	$5 \cdot 10^{-7}$	0.0537
	4					–	12448	$5 \cdot 10^{-7}$	0.0543

One can see that the replacement of the two histograms led to a significant improvement of the results achieved by all the methods. We can also notice that the GQN-based collocation provides the worst results in the case of response equal to M, in the second case Galerkin method gives the worst prediction. Behaviour of these two methods is very similar due to numeric integration in Galerkin method based on GQN rule.

In order to investigate the performance of fully intrusive stochastic Galerkin method, we have changed the prescribed distributions for model parameters once more. This time, we assume all the parameters to be normally distributed with the original values of mean and standard deviation. In such a case, the transformation becomes the 1$^{\text{st}}$ order polynomial and hence, analytical integration is available. The errors in prediction of safety margin are shown in Tab. 4.

Tab. 4 Time requirements and errors in predicting safety margin in case of **normal distribution** *for model parameters* $\boldsymbol{m}$.

Model response:		**Safety margin**				**Displacement vector**			
Method	p	n_{d}	Time [s]	$\Pr(F)$	ε_M [%]	n_{d}	Time [s]	$\Pr(F)$	ε_M [%]
MC	–	10^7	3819	$12 \cdot 10^{-7}$	–	10^7	3773	$12 \cdot 10^{-7}$	–
LHS	1	23	32	$12 \cdot 10^{-7}$	0.1139	19	181	$12 \cdot 10^{-7}$	0.0249
	2	243	179	$12 \cdot 10^{-7}$	0.0021	163	704	$12 \cdot 10^{-7}$	$2.50 \cdot 10^{-4}$
	3	1607	802	$12 \cdot 10^{-7}$	$4.17 \cdot 10^{-5}$	871	2823	$12 \cdot 10^{-7}$	$3.05 \cdot 10^{-6}$
	4	7789	2987	$12 \cdot 10^{-7}$	$1.35 \cdot 10^{-6}$	3481	9139	$12 \cdot 10^{-7}$	$4.88 \cdot 10^{-8}$
KPN	1	23	38	$12 \cdot 10^{-7}$	0.0742	19	181	$12 \cdot 10^{-7}$	0.0134
	2	243	214	$12 \cdot 10^{-7}$	0.0013	163	746	$12 \cdot 10^{-7}$	$1.49 \cdot 10^{-4}$
	3	1607	875	$12 \cdot 10^{-7}$	$3.32 \cdot 10^{-5}$	871	2851	$12 \cdot 10^{-7}$	$2.21 \cdot 10^{-6}$
	4	7789	2997	$12 \cdot 10^{-7}$	$1.00 \cdot 10^{-6}$	3481	9401	$12 \cdot 10^{-7}$	$4.08 \cdot 10^{-8}$
GQN	1	23	31	$12 \cdot 10^{-7}$	0.0742	19	182	$12 \cdot 10^{-7}$	0.0134
	2	265	212	$12 \cdot 10^{-7}$	0.0013	181	697	$12 \cdot 10^{-7}$	$1.49 \cdot 10^{-4}$
	3	2069	848	$12 \cdot 10^{-7}$	$3.32 \cdot 10^{-5}$	1177	2836	$12 \cdot 10^{-7}$	$2.21 \cdot 10^{-6}$
	4	12453	2796	$12 \cdot 10^{-7}$	$9.98 \cdot 10^{-6}$	5965	9233	$12 \cdot 10^{-7}$	$4.08 \cdot 10^{-8}$
GM	1					–	157	$12 \cdot 10^{-7}$	0.0135
	2					–	644	$12 \cdot 10^{-7}$	0.0014
	3					–	2698	$12 \cdot 10^{-7}$	0.0013
	4					–	8729	$12 \cdot 10^{-7}$	0.0013

The results proof that the $M - \boldsymbol{\xi}$ relation is now linear and thus the 1$^{\text{st}}$ order polynomials are sufficient for an excellent surrogate and the differences among the particular methods are here negligible in terms of accuracy as well as the time requirements.

5. CONCLUSION

This contribution presents comparison of several numerical methods for construction of a polynomial chaos-based surrogate of a numerical model under the assumption of random model parameters. The investigated methods are stochastic Galerkin method, stochastic collocation method and polynomial regression based on Latin Hypercube Sampling. The quality of obtained surrogates in terms of accuracy and the time requirements are demonstrated within the comparison with the traditional Monte Carlo method on a simple illustrative example of a frame structure.

ACKNOWLEDGEMENT

This outcome has been achieved with the financial support of the Czech Science Foundation, projects No. 105/11/0411 and 105/12/1146, and Grant Agency of the Czech Technical University in Prague, grant No. SGS OHK1-042/13.

REFERENCES

[1] MATTHIES, H. G. Uncertainty quantification with stochastic finite elements. In Erwin Stein, René de Borst, and Thomas J. R. Hughes, editors, *Encyclopaedia of Computational Mechanics*. John Wiley & Sons, Chichester, 2007. Available from: doi:10.1002/0470091355.ecm071.

[2] STEFANOU, G. The stochastic finite element method: Past, present and future. *Computer Methods in Applied Mechanics and Engineering* 2009, **198**(9-12), pp. 1031-1051. ISSN 0045-7825.

[3] GHANEM, R. G. and SPANOS, P. D. *Stochastic finite elements: A spectral approach*, Springer-Verlag New York, Inc., 1991. ISBN 978-1-4612-7795-8.

[4] BLATMAN, G. and SUDRET, B. An adaptive algorithm to build up sparse polynomial chaos expansions for stochastic finite element analysis. *Probabilistic Engineering Mechanics* 2010, **25**(2), pp. 183-197. ISSN 0266-8920.

[5] BABUSKA, I. and NOBILE F. and TEMPONE, R. A Stochastic Collocation Method for Elliptic Partial Differential Equations with Random Input Data. *SIAM Journal on Numerical Analysis* 2007, **45**(3), pp. 1005-1034. ISSN 0036-1429.

[6] XIU, D. Fast Numerical Methods for Stochastic Computations: A Review. *Communications in Computational Physics* 2009, **5**(2-4), pp. 242-272.

[7] BABUSKA, I. and TEMPONE, R. and ZOURARIS, G. E. Galerkin Finite Element Approximations of Stochastic Elliptic Partial Differential Equations. *SIAM Journal on Numerical Analysis* 2004, **42**(2), pp. 800-825. ISSN 0036-1429.

[8] MATTHIES, H. G. and KEESE, A. Galerkin methods for linear and nonlinear elliptic stochastic partial differential equations. *Computer Methods in Applied Mechanics and Engineering* 2005, **194**(12-16), pp. 1295–1331. ISSN 0045-7825.

[9] MAREK, P. and BROZZETTI, J. and GUŠTAR, M. and TIKALSKY, P. editors. *Probabilistic assessment of structures using Monte Carlo simulation*, Institute of Theoretical and Applied Mechanics, Academy of Sciences of the Czech Republic, Prague, 2003. ISBN 9788086246192.

[10] XIU, D. and KARNIADAKIS, G. E. The Wiener–Askey Polynomial Chaos for Stochastic Differential Equations. *SIAM Journal on Scientific Computing* 2002, **24**(2). ISSN 1064-8275.

[11] JANOUCHOVÁ, E. and KUČEROVÁ, A. Competitive Comparison of Optimal Designs of Experiments for Sampling-based Sensitivity Analysis. *Computers & Structures*, 2013, **124**, pp. 47-60. ISSN 0045-7949.

[12] HEISS, F. and WINSCHEL, V. Likelihood approximation by numerical integration on sparse grids. *Journal of Econometrics* 2008, **144**(1), pp. 62-80. ISSN 0304-4076.

TRUCK IMPACT DAMAGE OF THE BRIDGE PIER ACCORDING TO THE DIFFERENT TYPES OF REINFORCEMENT ARRANGEMENT

Pavel JIŘÍČEK[1]

***Abstract**: This paper compares possibilities of reinforcement arrangement in bridge piers and its influence on damage of the pier caused by truck impact. The vehicle impact at the bridge pier is modeled with the use of ANSYS Autodyn. Nonlinear material model with damage and strain-rate effect is used for concrete.*

***Keywords**: reinforced concrete, RHT concrete model, impact*

1. INTRODUCTION

Traffic intensity increase leads to higher risk of traffic accidents. In 2010 and 2011 about 1250 accidents involving bridges and tunnels happened in the Czech Republic. Heavy trucks (above 30t) hitting the bridge substructure can lead into progressive collapse of the bridge superstructure thus causing severe fatalities, therefore this loading case should be considered especially at the motorways.

The impact forces described in EN 1991-1-7 (Appendix C) give more accurate values to real vehicle impact. These forces come up to 2MN and give inaccurate values trough design process. Reinforcement arrangement significantly affects damage of the pier.

The bridge pier truck impact is considered according to EN 1991-1-7 (vehicle - 30tonnes; 90kph). Four options of reinforcement arrangement are compared and evaluated within the paper.

2. CONSIDERED IMPACT LOADING

Previous research [1] focused on full scale model of truck impact considering real vehicle geometry was very time consuming. It has shown similarities between real vehicle impact and approach prescribed in [2] to obtain impact forces. Due to these circumstances, complex vehicle model was replaced with simplified object consisting of one block formed with simple linear material model. Stiffness of substitute material is chosen according to current design standard [2] and its value is 300 kN/m. Unlike the current design standards, the height of the impacting face of the block was enlarged from 0.5 m to 1.0 m.

[1] Ing. Pavel Jiříček, Faculty of Civil Engineering, Czech Technical University in Prague, pavel.jiricek@fsv.cvut.cz

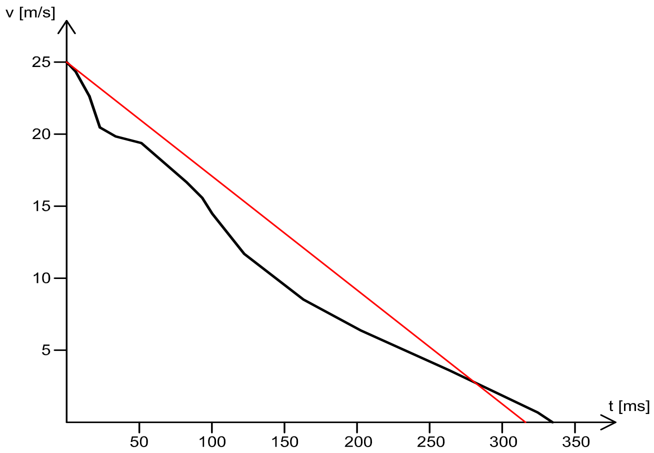

Fig. 1 Schematic diagram of the bridge pier truck impact velocity/time dependence. Black line – numerical simulation; Red line – EN 1991-1-7 Appendix C [2]

3. ANALYZED BRIDGE PIER

The dimensions of the bridge pier are 1000 x 4800 x 6700 mm (width x length x height), concrete class C30/37. The deflections at the bottom and at the head of pier are restricted. For illustration see Fig. 2.

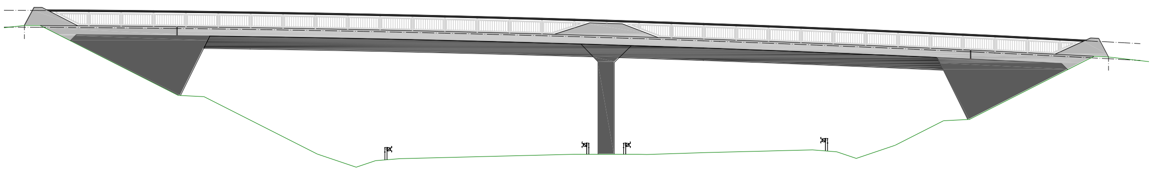

Fig. 2 View of the assessed bridge

The material of the bridge pier was chosen to describe its behavior when subjected to the vehicle impact; the two main aspects are:

- Damage of the material when subjected to ultimate loading

- Increase of the strength (both tensile and compressive) depending on the speed of loading (dynamic increase factor)

According to previous research [1] material model of pier remains identical. Due to requirements listed above, one of RHT (see Fig 3) concrete models, which is the part of ANSYS Autodyn material library, was used. The material model RHT is developed for evaluation of behavior of quasi – brittle materials under high velocity loading. There are many existing and published RHT model input data ([3]; [4]), the data provided by [5] are used for this modeling.

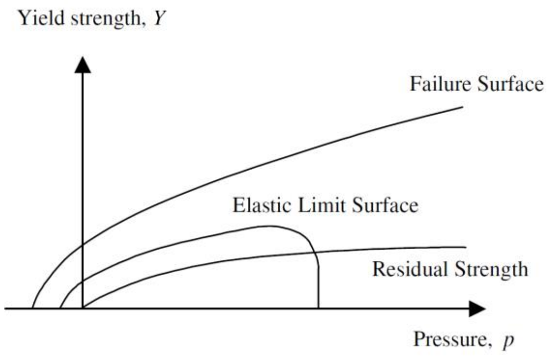

Fig. 3 RHT model used for concrete; based on Riedel [6]

3.1. REINFORCEMENT TYPES OF THE PIER

For reinforcement bars material model of common structural steel with yield stress 500 MPa was chosen. Reinforcement is formed by longitudinal bars Ø20/200mm and shear reinforcement (bars Ø10 each 300mm; Fig 4).

- The pier without reinforcement
- The pier with vertical reinforcement in one layer
- The pier with vertical and shear reinforcement in one layer
- The pier with vertical and shear reinforcement in two layers

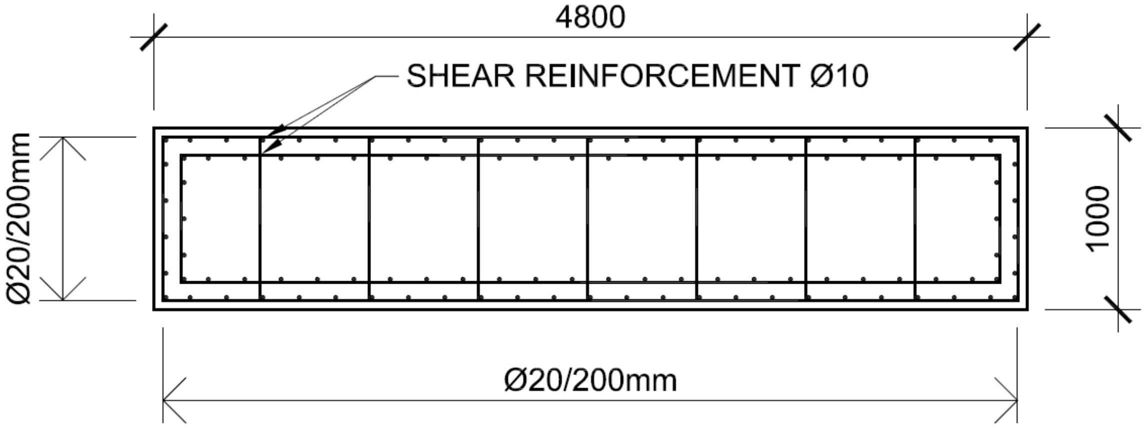

Fig. 4 Vertical and shear reinforcement in two layers (cross-section)

The pier without reinforcement has only comparative purpose, reinforcement in one layer is closer to surface than the second layer and reinforcement in two layers is arranged according to German design standards [7].

4. RESULTS OF THE NUMERICAL MODELING

Reinforcement arrangement significantly affects damage of the pier, see Fig 5. It is obvious that pier without any reinforcement is damaged the most; only plain concrete deals with the impact of the vehicle. As mentioned before, it has only comparative purpose, therefore the area of eroded concrete will be considered as 100% (Fig. 5a).

It is obvious that fully anchored longitudinal bending reinforcement transmits some impact force and therefore enlarges impact area in the height of the pier. The volume of the eroded concrete is about 85 % compared to the pier without reinforcement (Fig. 5b). It has to be mentioned that this type of reinforcement is not actually used in real designs (similar to plain concrete).

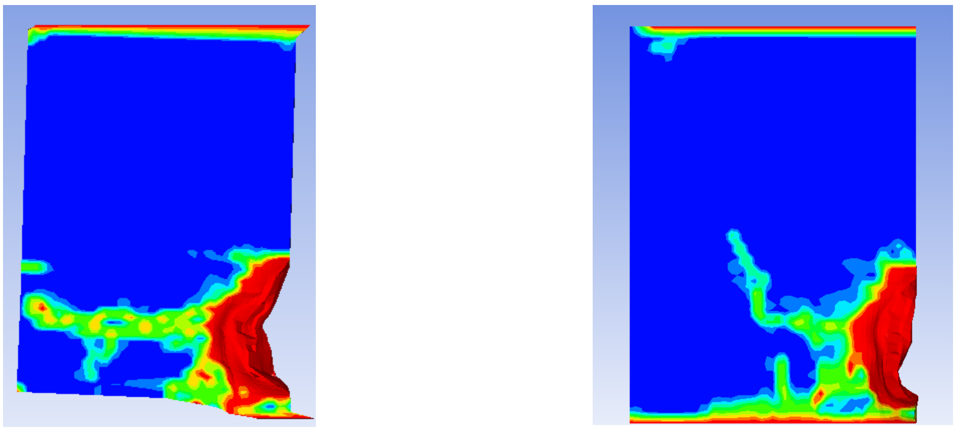

a – The pier without reinforcement *b – The pier with vertical reinforcement*

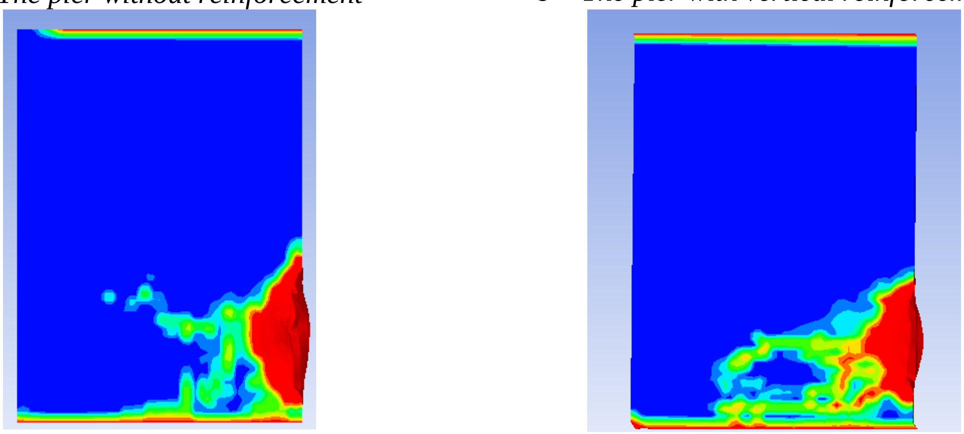

c – The pier with vertical and shear reinforcement *d – The pier with longitudinal and shear reinforcement in two layers*

Fig. 5 The damage of the pier according to different types of reinforcement arrangement

As seen at Fig. 5c, the damage of the pier is significantly reduced (according to plain concrete). Shear reinforcement confines concrete within vertical bars and therefore reduces the volume of eroded concrete. Reduction of the depth of concrete spalling is a positive phenomenon, larger area of cross-section of the pier is resisting the vertical loading. The volume of the eroded concrete is about 60% compared to the pier without reinforcement.

As the last option, the reinforcement according to German design standards [7] was considered. Main idea of placing reinforcement in two layers is localization of concrete spalling in the area of the first layer of reinforcement. This assumption was confirmed and damage within the second layer of vertical bars remains mainly uneroded. The volume of eroded concrete is about 40% compared to the pier without reinforcement. Further reduction can be achieved by adding PP fibers in the concrete mix [8]. The effect of fibers on the impact resistance of concrete will be studied in the on-going research.

Last but not least, size of dynamic increase factor (DIF) was evaluated. Through modelling process the area of uneroded concrete with compressive stress above ultimate concrete strength was observed. This phenomenon is known as dynamic increase factor and described as increase of the strength (both tensile and compressive) depending on the speed of loading [9]. As seen at Fig. 6 strain rate depending on vehicle impact is about 3.6 -/s. This value is determined from linear deceleration (Fig. 1) and from change of the strain in the impact area.

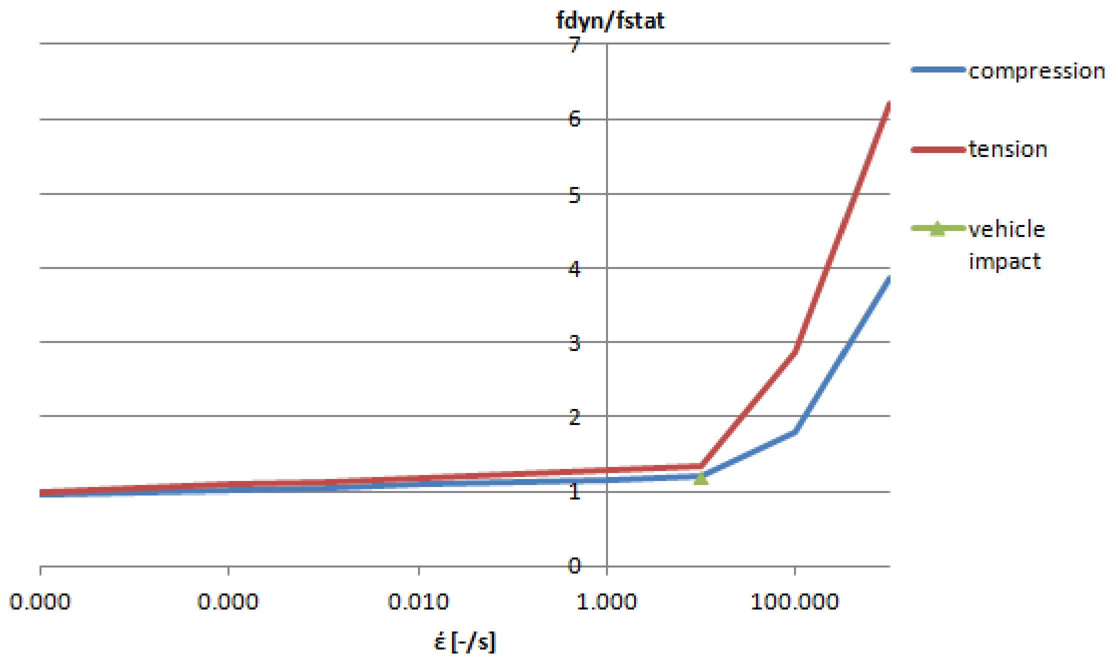

Fig. 6 Dynamic increase factor according to [9]

Main curves determining the increase of concrete compressive strength are prescribed in [9] by simple equations:

$$f_{c,imp,k} / f_{cm} = \left(\dot{\varepsilon}_c / \dot{\varepsilon}_{c0}\right)^{0.014} \quad for\ \dot{\varepsilon}_c \leq 30\, s^{-1} \tag{1}$$

$$f_{c,imp,k} / f_{cm} = 0.012\left(\dot{\varepsilon}_c / \dot{\varepsilon}_{c0}\right)^{1/3} \quad for\ \dot{\varepsilon}_c \geq 30\, s^{-1} \tag{2}$$

where f_{cm} is the mean value of compressive strength and reference value $\dot{\varepsilon}_{c0} = 30 \cdot 10^{-6}\ s^{-1}$.

5. CONCLUSION

The four types of pier reinforcement were evaluated in this paper. It's obvious that fully anchored longitudinal bending reinforcement transmits some impact force and therefore enlarges impact area in comparison to the plain concrete. The shear reinforcement confines the concrete surrounded by the longitudinal bars and limits the erosion of concrete. In case of placing reinforcement in two layers, the main damage and erosion of concrete takes place in the area of the first layer. The concrete behind the second layer remains mainly uneroded. In general, the increase of reinforcement area in the spot of the impact enhances the resistance of the pier to impact loading.

ACKNOWLEDGEMENT

The financial support of CTU grant 13/035/OHK1/1T/11, the Ministry of Interior of the Czech Republic project VG20132015114 and Czech Science Foundation project No. 13-30441S are kindly acknowledged.

REFERENCES

[1] JIŘÍČEK, P. and FOGLAR, M. Concrete Bridge Pier Subjected to Truck Impact. In: *Proceedings of the 3rd conference Nano and Macro Mechanics NMM 2012.* Praha: České vysoké učení technické v Praze, Fakulta stavební, 2012, pp. 103-110. ISBN 978-80-01-05097-2.

[2] ČSN EN 1991-1-7. *Zatížení konstrukcí, Obecná zatížení – Mimořádná zatížení.* Praha:ÚNMZ, 2007.

[3] REMPLING, R. *Concrete Wall Subjected to Fragments Impacts.* Göteborg 2004. Master's Thesis. Chalmers University of Technology, Department of Structural Engineering and Mechanics, Concrete structures.

[4] BRANNON, R. and LEELAVANICHKUL, S. Survey of Four Damage Models for Concrete. In: *Sandia Report.* Albuquerque & Livermore: 2009.

[5] LEPPÄNEN, J. *Numerical Simulation of Projectile Penetration in Concrete.* Göteborg 2003. Chalmers University of Technology, Department of Structural Engineering and Mechanics, Concrete structures.

[6] RIEDEL, W. *Beto unter dynamischen Lasten Meso und Makromechanische Modelle und ihre Parameter.* Freiburg 2000. Ernst – Mach Institut der Bundeswehr München, Institut Kurzzeitdynamik.

[7] DIN - Fachbericht102. *Betonbrücken*. Deutsches Institut für Normung, 2009.

[8] FOGLAR, M. and KOVAR, M. Conclusions from Experimental Testing of Blast Resistance of FRG and RC Bridge Decks. *International Journal of Impact Engineering,* 2013, 59, pp. 18-28. ISSN 0734-743X.

[9] CEB-FIP Model Code 2010, 2010. Comité Euro-International du Béton.

EFFECTS OF CONCRETE COUPLED BEAM ON BEHAVIOR OF CONCRETE CORE WALL SYSTEM IN STEEL BUILDINGS IN NEAR AND FAR FAULT

M. A. KAFI[1], M. MASTALI[2],Z. ABDOLLAHNEJAD[3]

Abstract:*One of the most important notes in high rise buildings is using a resistance system to stand againstapplied lateral loads. One of these passive resistance systems is the dual system. Concrete core wall system in steel buildings is proposed as a dual system which is commonly used against applied lateral loads in high rise buildings. Core wall system is used as two kinds: (a) open core; (b) semi-open core. In this paper, effects of concrete coupled beams in open and semi-open core wall systems were investigated in both near and far fault. In this direction, a 15-story steel building with concrete core wall system was analyzed by using ETABS 9.5.V software. Time HistoryAnalysis in near and far fault of Kobe earthquake showed that concrete coupled beams caused to reduce story rotation in plan and core rotation in height in near and far fault. In addition, these beams caused to increase of base shear and entered energy to structure, which these criteria had higher value in near field in compare to far field.*

Keywords:*concrete coupled beams, near and far fault, open and semi-open core wall, steel building.*

1. INTRODUCTION

Paying attention to the development of cities and increasing of population and limiting of the areas for making buildings, cause the increase of the height of buildings [1]. One of the most important points in high raised buildings is the resistance systems of these buildings against lateral loads such as: earthquake, wind, etc. Furthermore, building codes suggest using Dual systems in high raised buildings. Concrete core wall system in steel buildings is one of these systems. In this study, this kind of resistance system has been used as the second resistance system in a steel 15- stories building. Nowadays, the different effects of near and far fault earthquake on responses of structures are

[1]Mohammad Ali KAfi, Assistant Professor, Department of Civil Engineering, Semnan University, mkafi@semnan.ac.ir

[2]Mohammad Mastali, PhD student , Department of Civil Engineering, Minho University, Muhammad.mastali@gmail.com

[3]Zahra Abdollahnejad, PhD student, Department of Civil Engineering, Minho University, tolumahvash@gmail.com

obviously considered [2]. In this direction, linear dynamic analysis has been used for investigating of near and far fault effects on concrete core wall system in steel buildings and all results have been obtained by using ETABS software.

2. DYNAMIC ANALYSIS

Exist of limitation in Static Analysis methods and develop of calculator equipment caused to move of Scientifics in direction of more exact methods. These methods had to be considered plastic deformation, nonlinear effects of structures and some dynamic characters of structure such as: natural frequency, effect of oscillation modes and damping,…. [3]. In this direction, some methods such as: nonlinear statically and dynamically methods (Pushover and Time History Analysis) have been suggested by Scientifics [3]. Each of this method has some power and weak points which can improve and cover problems of Static Analysis, so using these methods are obligated in special zones for analyzing of structures [4]. Correct performance and nonlinear analysis of structural systems are the best way for knowing of dynamic response of structures which include: yielding mechanism, internal forces and required deformation [5]. Hence, Time History Analysis has been used in this study for evaluating near and far fault effects on this type ofa structure.

3. CHARACTERIZATION OF NEAR AND FAR FAULT RECORDES

Differences of near and far fault records are natural phenomenon. Area of 15 kilometers of every fault is assumed near fault. In the near fault, earthquakes dependent to three things: 1) rupture mechanism; 2) direction of rupture spread; 3) permanent displacements due to fault slip. These parameters cause two effects: 1) rupture direction; 2) fling step. Rupture directivity include: 1) forward directivity; 2) backward directivity [2]. Effects of forward directivity cause horizontal oscillation of earth in perpendicular direction of fault, which bring horizontal impacts and these impacts, have higher amplitudes as compared with impacts of parallel of fault. Effects of forward directivity will be increased with decrease of angle between site and fault, and increase of rupture area of between site and fault. These pulses cause to increase of inelastic displacement needs in structures, so that structures have high displacements and responses in near fault. Study of near fault records showed which characters of these records include: 1) short duration; 2) single or multi special pulses with high amplitudes and medium up to high period [2&7].

4. CASE STUDY

In this paper, a steel 15 – stories building with concrete open and semi-open core wall systems has been studied by using ETABS software. The structure was considered that is located in Tehran and shear velocity wave of soil and height of each story were considered is 275m/s and 3.3m, respectively. Specifications of material and plan of structure have been shown in Tab. 1 and Fig. 1.

Tab. 1.Material properties

Beam depth	500 mm
Specific gravity of concrete	2403 kg/m3
Poisson's ratio	0.17
Wall thickness	300 mm
Pressure strength of concrete	fc=24.525 MPa
Yielding resistance of steel	fy=392.4 MPa
Elastic modulus of steel	E=250 GPa

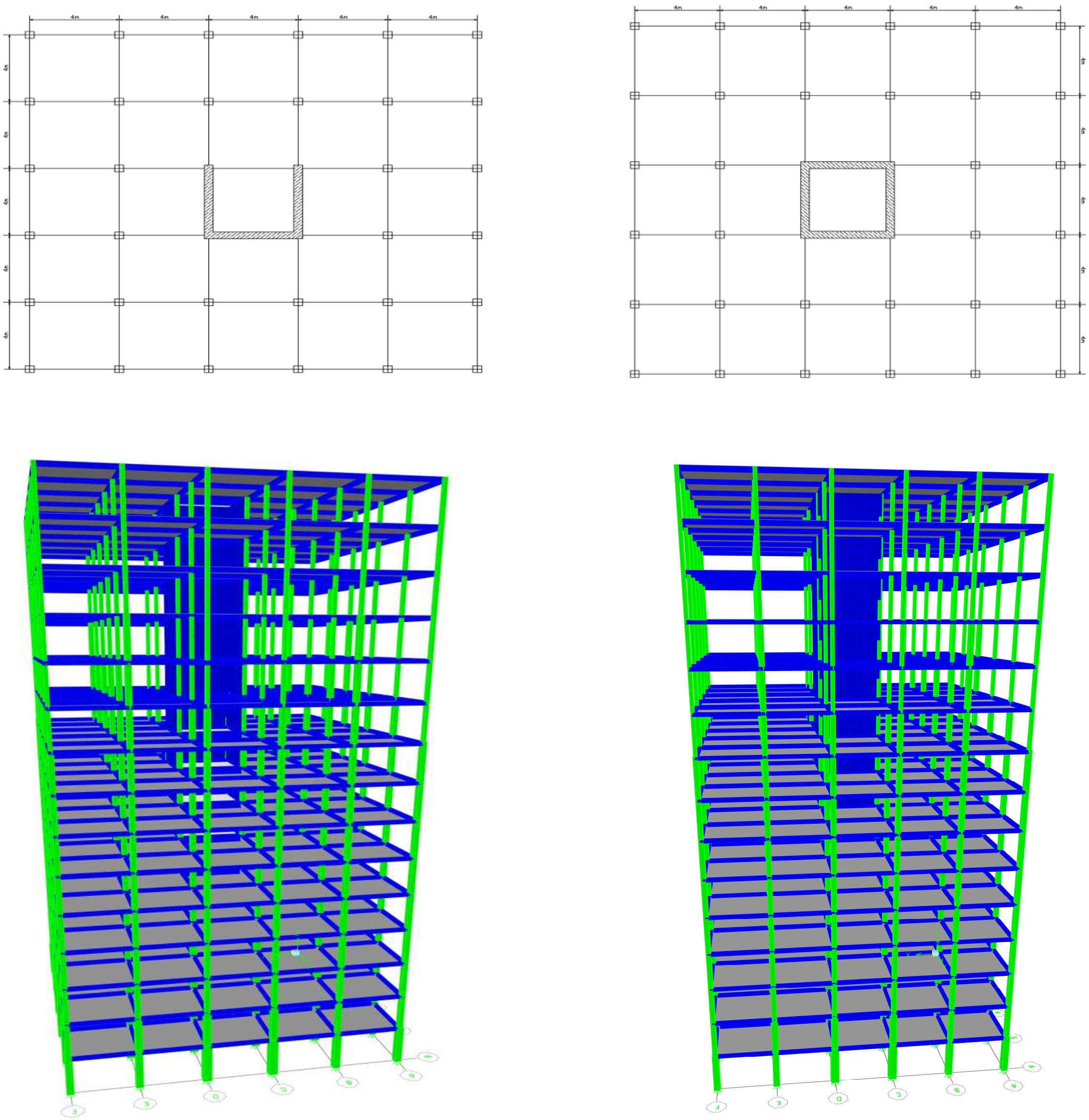

MODEL 2 MODEL 1

Fig. 1 Plan and three dimension of structure

Tab. 2 Properties of Models

	Second Resistance System	First Resistance System
1	Concrete Semi-open core wall system	Steel moment resistance frame
2	Concrete open core wall system	Steel moment resistance frame

- Assumptions of modeling:

1. Effect of P-Δ has been withdrawn.
2. Behavior factor for study case was assumed R=8 [8].
3. Small eccentricity in column and beam joints was withdrawn.
4. Slabs are considered completely rigid. On the other hand, there is no non-planar deformation.

The frame with 15 stories was analyzed by near and far faults record of Kobe earthquake. PGA of this earthquake in near and far fault are 0.61g and 0.14g, respectively. The Kobe records in both near and far faults are indicated in Fig. 2.

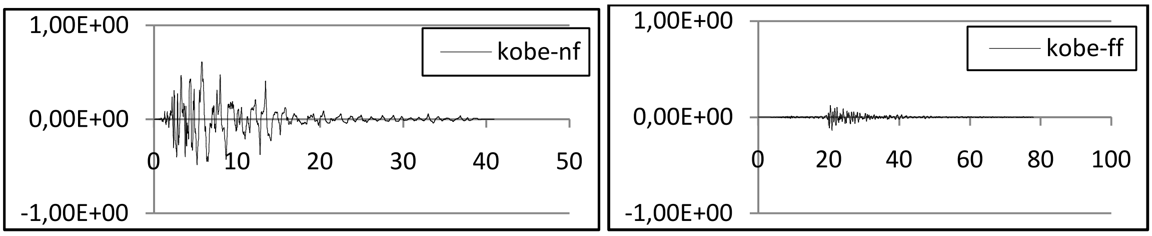

a) b)

Fig. 2 Records of Kobe earthquake: a) Near Field; b) Far Field.

5. RESULTS

Fig. 3 is illustrated positive effects of beams in reduction of maximum displacement in model 1 compare to model 2 amounts to 8.86% in near fault which this effect is more in three last stories.

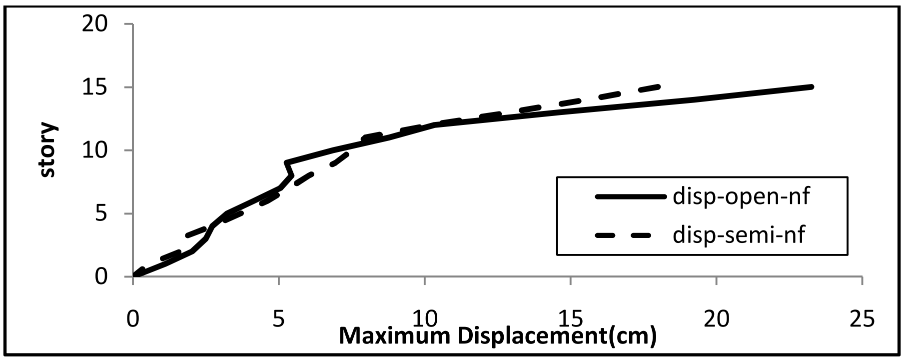

Fig.3 Maximum Displacement of Models 1&2 in Near Field

Fig. 4 is shown the ineffectiveness of these beams in Model 1 so that these beams caused to increase of maximum displacements in Model 2 in far fault amounts to 57.11 which were observed in throughout of structure height and it maybe was related to low PGA value. This study showed that steel moment resistance absorbs more earthquake energy to dissipate in compare to core wall system if PGA value is small. Higher weight in Model 1 compare to Model 2 leads to be observed more earthquake effects in Model 1.Therefore, the maximum displacements in Model 1 had higher valuein compare to Model 2. By increasing of PGA value, percentage of absorbing of earthquake energy in core wall system was increased and this phenomenon was also observed in near field in Fig. 3 in 20% last of structure height.

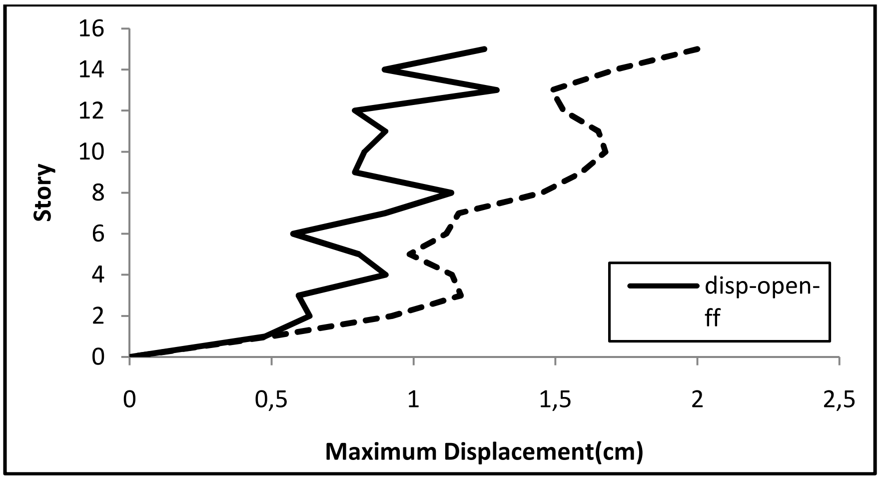

Fig. 4 Maximum displacement of Model 1&2 in Far Field

Figures 5 and 6 were indicated positive effects of beams in reduction of rotation stories in throughout of structure height in both fields, so that these reductions in near and far fault are 40.93% and 27.59%, respectively. In addition, these beams caused to increase of torsional stiffness of these structures and subsequently caused to increase of rotation stories in Model 2 in compare to Model 1. The maximum and minimum beam effects on increasing of torsional stiffness was observed in 0.33 and 0.47 up to 0.67 structure height in Kobe near field earthquake, respectively.

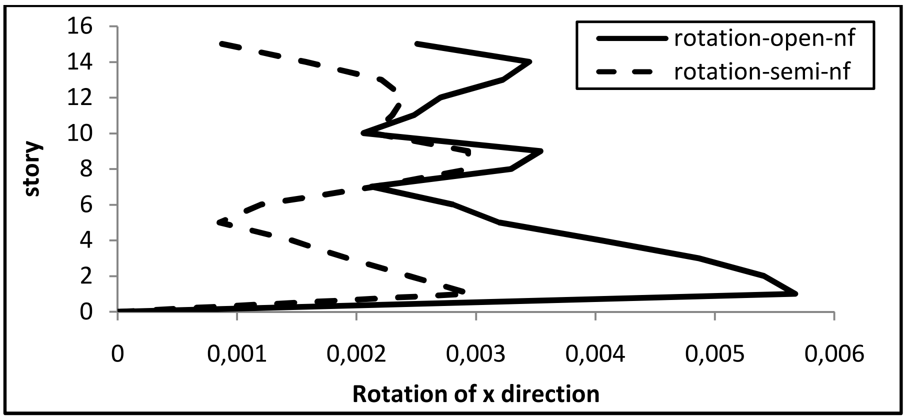

Fig. 5 Rotation of Stories in X plan in Near Fault

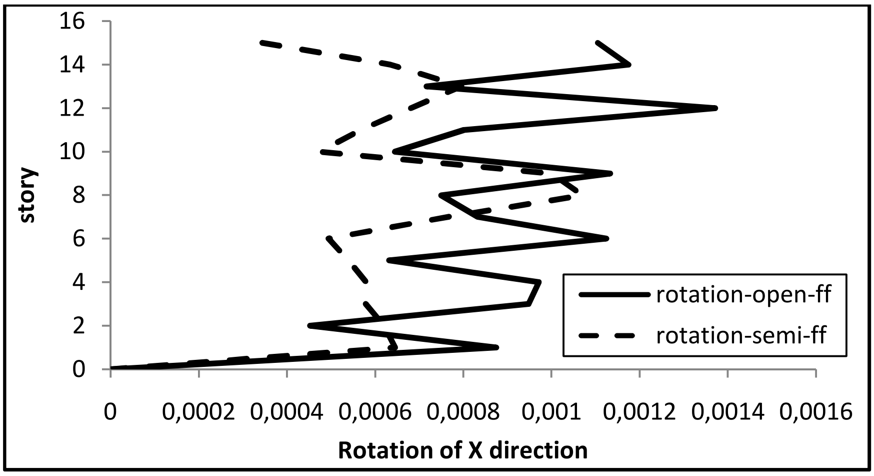

Fig. 6 Rotation of Stories in X plan in Far Fault

Furthermore, in Figures 7 and 8 have been showed positive effect of these beams in reduction of core rotation in structure height, so that these reductions in near and far fault have reached to amounts 64.96% and 9.58%, respectively. As Fig. 7 has shown core rotation in Model 1 is less than Model 2 in throughout of structure height in near fault but in far fault, coupled beams in the first Model in 0.33 last height of structure have positive effect in reduction of core rotation. Whereas, in 0.33 middle height of structure concrete coupled beams are ineffective in reduction of core rotation.

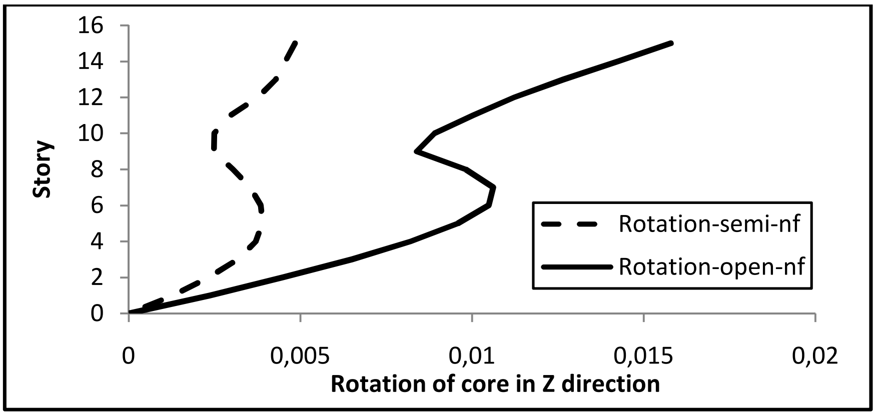

Fig.7 CoreRotation in StructureHeight in NearFault

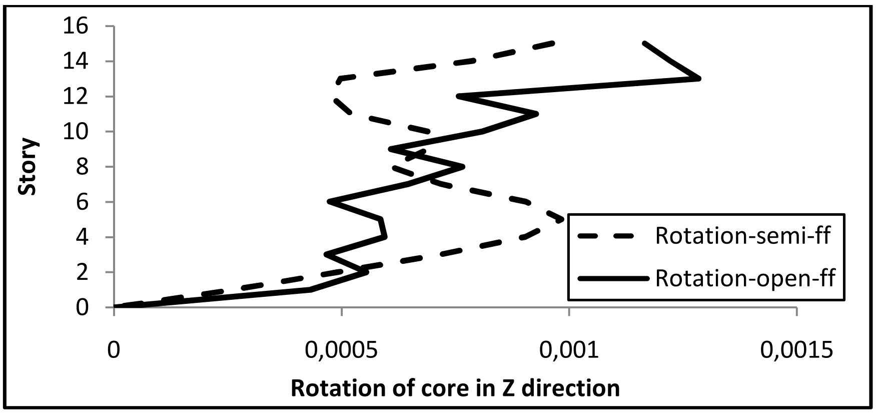

Fig. 8 Core Rotation in Structure Height in Far Fault

In Fig.9 is illustrated that coupled beams caused to increase of base shear value. In far fault, base shear value in model 1 was higher than Model 2 to amounts 66.48% while this amount was measured 51.03% in the near field.

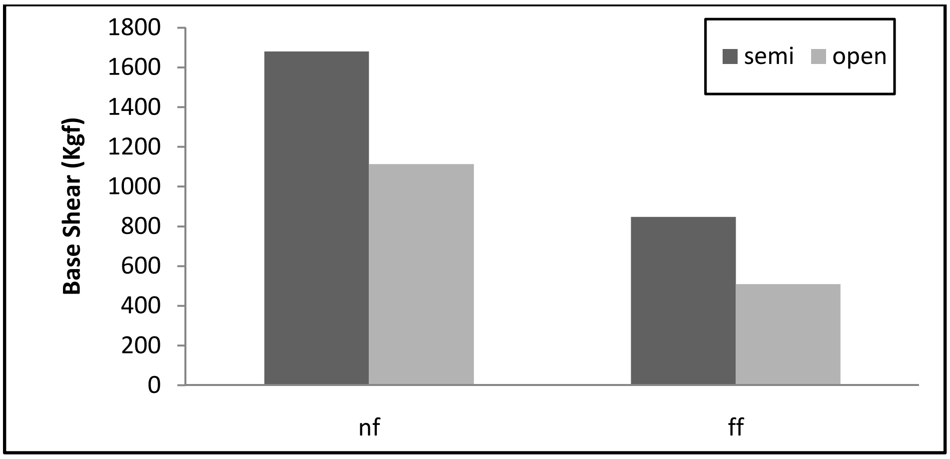

Fig. 9 Base shear values in Near and Far Field

Fig.10 is shown entered energy to structure during of earthquake. In near and far fault, amounts of entered energy to structure in model 1 was more than model 2, to 2.55% and 25.13%, respectively.

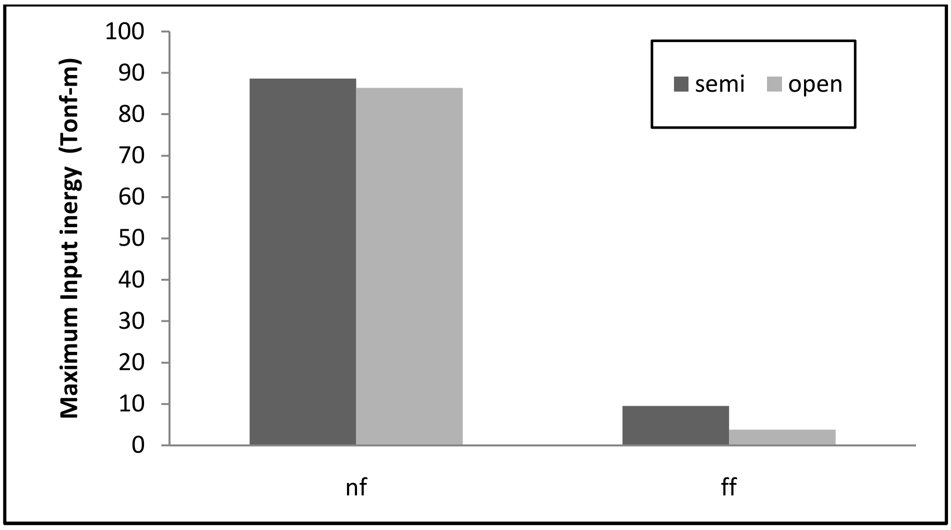

Fig. 10 Values of entered energy to structure in Near and Far Field

6. CONCLUSION

Time History Analysis on concrete coupled beams in steel buildings showed that these beams cause the reduction of maximum displacement in near fault, but these beams are ineffective in far fault. Furthermore, in both fields, these beams caused the reduction of rotation stories in plan, core rotation in height whilethe base shear and entered energy were increased in structure. According toobtained analytical results in both fields, there is a direct relation between PGA value and effect of concrete coupled beams in decreasing the maximum displacements in structure height.

REFERENCES

[1] STANFORD SMITH B., COULL A. *Tall building structures: analysis and design*, Wiley: New York, 1991, ISBN-13: 978-0471512370.

[2] ABDOLLAHZADEH, D. *Consideration of special steel moment resisting frame rehabilitation criteria under near fault earthquakes effects*, 2008, Thesis of M.Sc., Semnanuniversity, Iran.

[3] VALA MANESH, V., ESTEKANCHI, H., VAFA, A.,Evaluation of endurance time method with statically analysis in two Dimensional frames, *Journal of Sharif*, 2006, **35**, 17-26, ISSN: 1026-3098.

[4] SEAOC, Recommended lateral force requirements and commentary, *Structural Engineers Association of California-Seismology Committee*, 1999.

[5] MOEHLE, J.P.Performance-based seismic design of tall building in the U.S., In:*The 14th world conference on earthquake engineering*, 2008, October 12-17, Bejing, China.

[6] MORTEZAI, A., ROUNAGH, H.R., KHEYRODDIN, A.,Seismic evaluation of FRP strengthened RC buildings subjected to near-fault ground motion having flip step,*Journal of Composite Structure*, 2010, **92**, 1200-1211, ISSN: 0263-8223.

[7] BUILDING AND HOUSE RESEARCH CENTER,Iranian code of practice for seismic resistant design of buildings,*Standard No.2800 3th Edition*, 2006, Tehran, Iran.

NANOINDETATION AND MECHANICAL PROPERTIES OF HUMAN TOOTH ROOT DENTIN

Alice KAPKOVÁ[1], Aleš JÍRA[2],Jiří NĚMEČEK[3]

Abstract*:Knowledge of the mechanical properties of hard dental tissues is important for understanding broad spectrum dental procedures, from the design to the selection of dental methods. The behavior of dental tissues has long beendescribed in the literature as well asby individual authors, and has been especially dedicated to all fundamental components of teeth,butless research has been carried out pertaining to themicromechanical properties of dentin and bone cement in the root of the tooth. This work deals with the micro-structure and nanoindentationof tooth root dentintaking into account the micromechanical properties of the wall of the tooth.The detailed knowledge of the properties of the intraosseous partof the tooth allows us to optimize the design of current dental implants in the next stage.*

Keywords*: tooth root, dentin, dental cement, nanoindentation, micromechanical properties*

1. INTRODUCTION

It is obvious that comprehensive knowledge of the tooth at the macro and micro level, its mechanical properties and the behavior under different loading conditions is necessary for the proper applicationof various dental procedures.An experimental analysis of tooth properties was presented, e.g., in [1-2]where all parts of teeth were studied. Nevertheless, the essential part ofthis work is focused on the tooth crown, and its dental enamel and dentin (remove „in her part“). For our needs, aimed at the design of new dental implants, it is necessary to focus on the intraosseous part of the tooth and its root.In recentyears, thanks to new methods and procedures,there has been an increase in reported values , which are, for the most part, determined by the quality of the different teeth of individual people.

[1]MDDr. etIng. Alice Kapková,CzechTechnicalUniversity in Prague, Faculty of Civil Engineering, alice.kapkova@fsv.cvut.cz

[2]Ing.AlešJíra, Ph.D., CzechTechnicalUniversity in Prague, Faculty of Civil Engineering, jira@fsv.cvut.cz

[3]Doc. Ing. JiříNěmeček, Ph.D., CzechTechnicalUniversity in Prague, Faculty of Civil Engineering, jiri.nemecek@fsv.cvut.cz

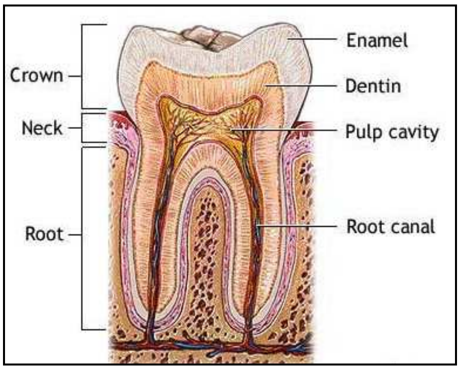

Fig. 1 Medial-frontal incision of tooth [3]

1.1. TOOTH STRUCTURE

Human teeth consist of four basic components: enamel, dentin, cement and pulp. Dentin forms the largest part of the tooth which covers enamel on the crown and cement on the root. Inside the tooth is pulp. The subject of our work will be solely devoted to the root of the tooth.

1.2. DENTINUM

Dentin is a hard connective tissue that forms a major part of the tooth and is also the most mineralized tissue in a human tooth. For this reason knowledge of the mechanical properties is important for the prognosis of dental caries and production of dental implants whose mechanical properties (remove „is“) will approach the properties of tooth dentin.
Dentin varies from light yellow in the deciduous dentition to yellow in the permanent dentition and partlygives color to the tooth, because it shines through the translucent enamel.It is harder than bone, but is not as hard as enamel, anddue to the organic matrix and tubulum it is more elastic than the enamel. Dentin has a lower mineral content than the enamel, thus causing higher radiolucency.It consists mainly of inorganic substances hydroxyapatite - 50% of the volume, organic substances: collagen I - 30% by volume (fibersup to 50-100 nm in diameter which are randomly oriented in a plane perpendicular to the direction of the dentine) and the balance water - 20% by volume. [4]Dentinal tubules, which number 12 000-75 000, arefound on a 1 mm^2 area and cause the formation of the characteristic radial annealing dentin on the tooth.The tubules are in the form of an S-Curl: the first bend convexity is directed to the apex of the tooth root and is located closer to the pulp, the second bend convexity is reversed to the crown, and is closer to the outer surface of the dentin. The headroom of the dentinal tubules betweenthe pulp r and the dentin reaches 2-4 micron and incrementally narrows towards their current branching at thedentino-enamel junction (or dentino-cementum junction) interface. Between adjacent tubules anastomoses frequently occur[5].

Mechanical properties of human dentin are reviewed within the last 50 years.The results in this area are very disparate, so it is often necessary to re-analyze previous studies and re-examine the structure of dentin and its mechanical properties. According to literature,the Young modulus is between 20 and 25 GPa, tensile strengthis stated as 41 MPa andcompressive strength is 275 MPa. [4]

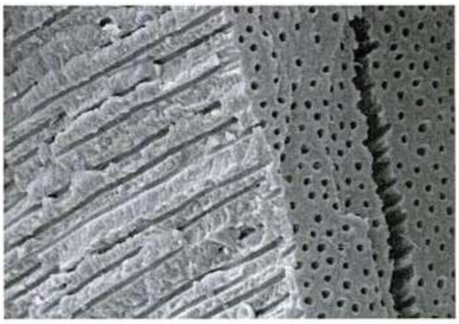

Fig. 2 Electron microscopic view of dentinal tubules [1]

1.3. CEMENTUM

Dental cement is a thin, calcified layer, which covers the dentin of the root.It belongs to the pendant apparatus of the tooth, because it is involved in the anchoringof the tooth in the dental alveol. Cement has various strengths on different tooth surfaces.The strongest layer is located on the root apex,especially on the interradicular area (50-200 um, sometimes may exceed up to 600 microns).The thinnest layer of cement is located in the neck part (10-15 um). Cement is gradually created during the human lifetime.

Physical properties:cementum is light yellow and has a matte surface,and is softer than the dentin. The permeability varies with the age and type of cementum. Cellular cement is permeable, much more so compared to dentin.

Chemical properties:cementum consists of inorganic components (65%), organic components (23%) and water (12%). The main inorganic component is hydroxyapatite.

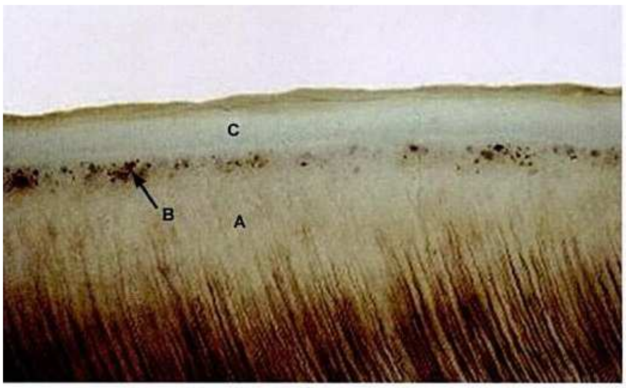

Fig 3.Acellularcementum: A - dentin, B – Tomes‘ granular layer, C – Primary cementum [1]

2. METHODOLOGY

For the determination of micromechanical properties ananoindented premolar tooth, extracted for orthodontic reasons, was used. The specimen was preparedbyvertical assemblage in epoxy resin andsectioned with a frontal cut. It was then polished to the required quality of a perfect surface and evaluated in the device of CSM Instruments.

2.1. DETERMINATION OF ELASTIC MODULUS

Nanoindentation experiments were performed using instrumental hardness TTX / NHT by CSM Instrumentsprovided by Berkov's element. Indentationswere created in the cement and dentin. Indentations were made in the form of 4x31 matrices in one row and 20x4 and 27x4 in second row. (Fig. 4.5) The first indentation is near the cementum, followed by indentation against the dentin over the cement-dentin junction, with an offset distance of 0.04 mm between each one.

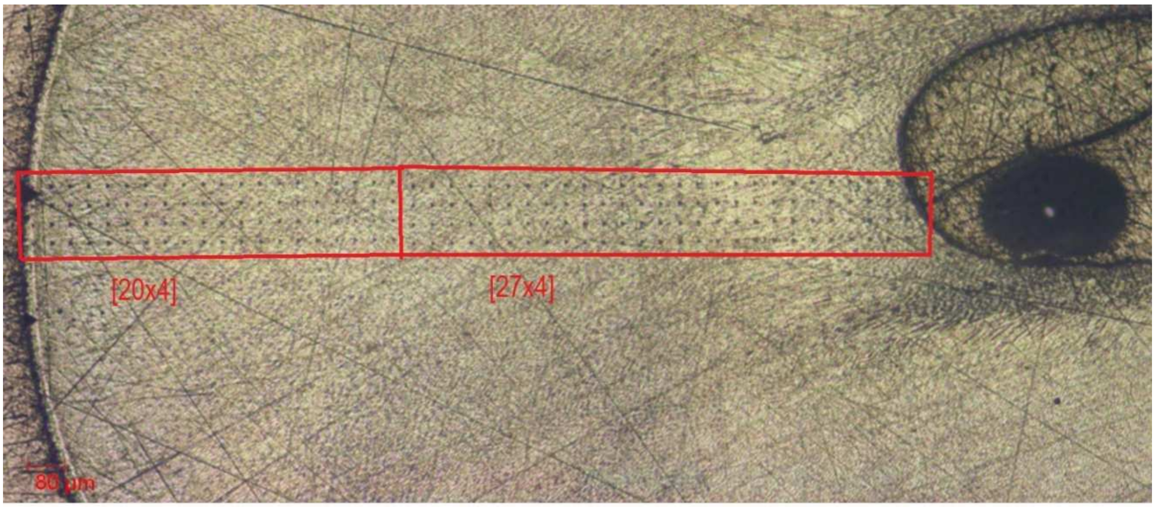

Fig. 4 Disto-mesial matrix indent - from the outer edge of the tooth to the core

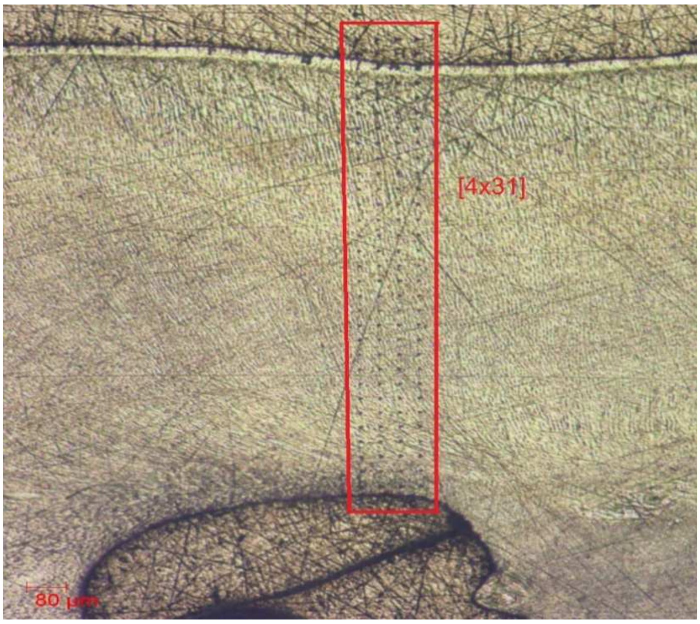

Fig. 5 Vestibulo-oral Indent matrix - from the outer edge of the tooth to its core

Indentation took place by controlled forcewith a maximum size of 30 mN, where the loading rate was 360 mN/min followed by a 10 s pause, during which the indenter maintains a constant load (maximum force of 30 mN) and unloaded again at a speed of 360 mN/min. The depth of injection at full load is evident from the map and its course corresponds with the process of modulus of elasticity of the wall thickness of the tooth (Fig. 6)

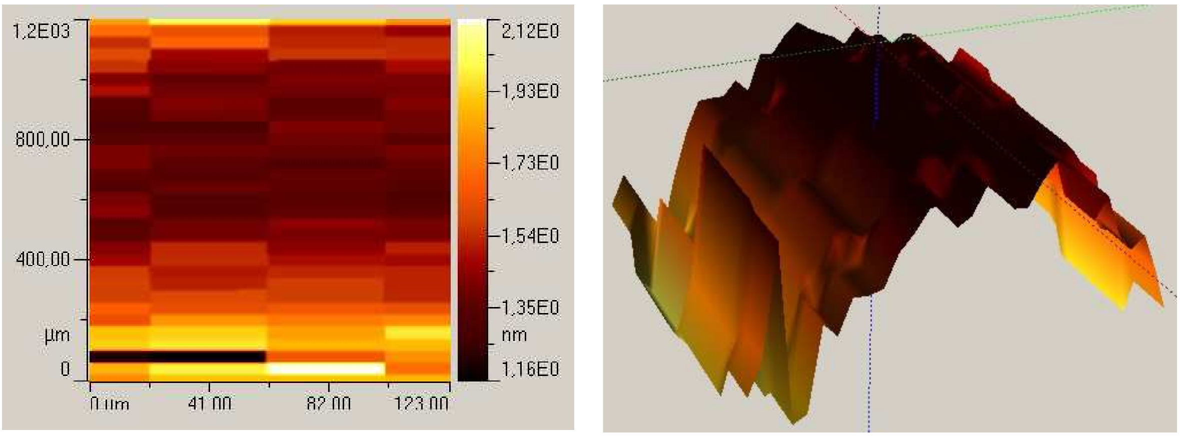

Fig. 6 The depth of the tooth injection in the wall –vestibulo-oral matrix (left vestibulo-oral axis - the distance of the core to the outer edge of the tooth, the right vestibulo-oral axis - the legend depth of injection, disto-mesial axis - the disto-mesial mutual distance columns indents)

2.2. CYCLIC LOADING

Cyclic loading causes damage to the material with each load cycle, so every time it operates with slightly altered properties. In order to verify whether the tooth dentin is subject to material fatigue, cyclic loading has been carried out in the middle of the wall dentin. Cyclic loading was carried out withinfive cycles, and its progress is showngraphically inFig. 7

First load: 10 mN
Unload to: 5 mN
Max load: 50 mN
Loading rate: 120 mN/min
Unloading rate: 120 mN/min
Pause: 10 s

The position in the center of the wall dentin was chosen for cyclic measuring because of the gradual changes in the modulus of elasticity so that the modulus of elasticity of the indentation matrix would ideally be constant. As seen in Fig. 7,a stable behavior of the dentin of the tooth root from the perspective of low cycle fatigue is apparent. Additionally, no significant difference is measured in the values of modulus of elasticity, E.

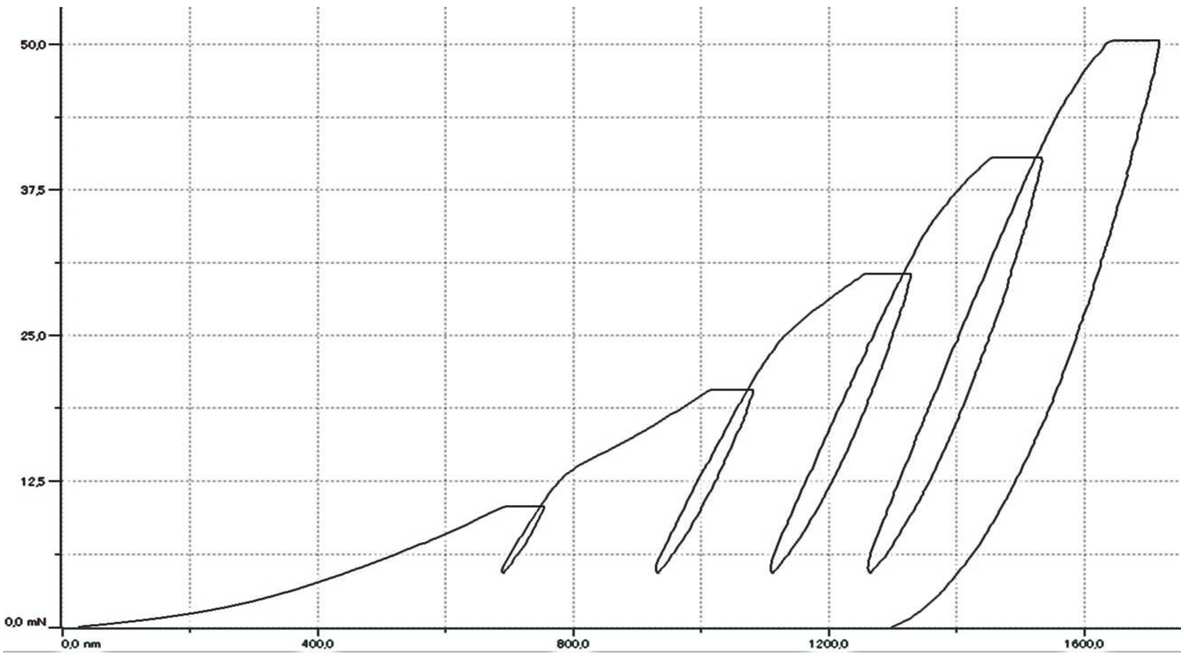

Fig. 7 – Load displacement diagram (disto-mesial axis)

3. CONCLUSION

From the results of the measurements the value of Young's modulus of the tooth root was found.The lowest values occur at the edge of tooth in the area of the cementum and cement-dentin junction and near the root canal. The highest values are found in the middle of this area.

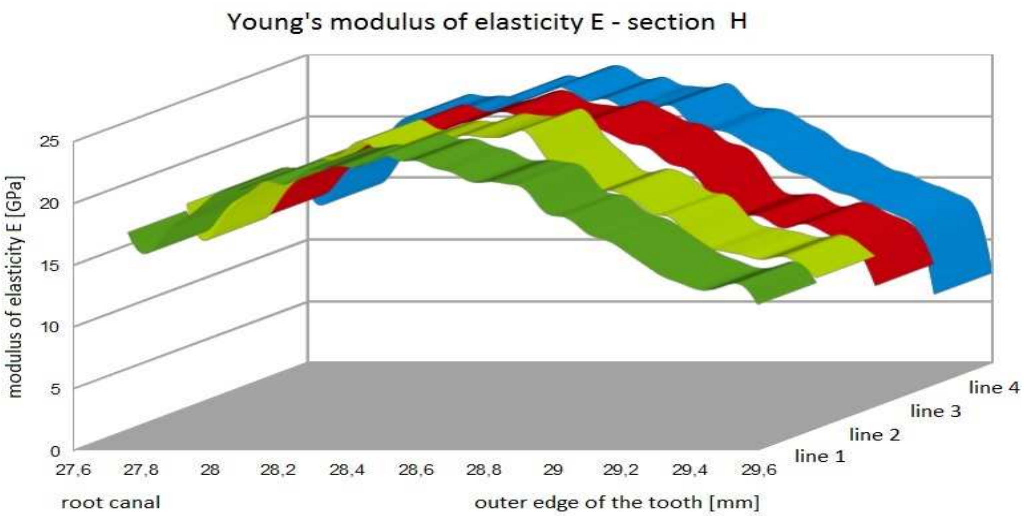

Fig. 8 – Modulus of elasticity for the side thickness at the root of the tooth - the disto-mesial direction

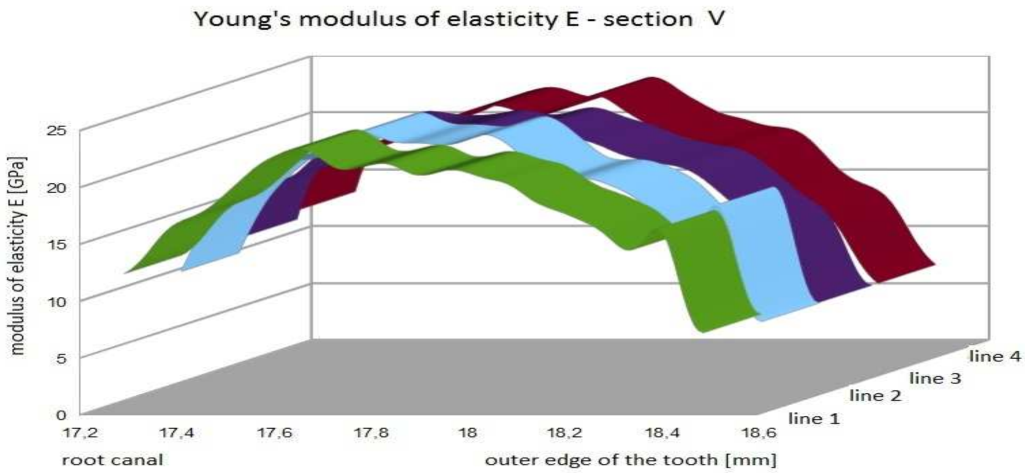

Fig. 9 – Modulus of elasticity for the side thickness at the root of the tooth - the vestibulo-oral direction

The most important conclusions:

- The dentin tubulesare orientedin directionsfrom thecement-dentin borderto the rootcanal(Fig. 5). In this orientation tubules are extended in the direction of the pulp. The transition of tubules in the tangential direction of the root canal is caused by the two rooted tooth.
- In the vestibulo-oral direction a changeoccurs in the modulus of elasticity E of the wall of the tooth;at the edge of the cement the dentin achieves a modulus of elasticity of 13 GPa, in the middle of the dentin wall 23 GPa is achieved, and at the interface between the dentin and root canal 14 GPa is achieved.
- In the disto-mesial directionthe development of the elastic modulus develops analogously to the vestibulo-oral direction. The value of the modulus of elasticity in the dentin at the edge of the cement is 14 GPa, in the middle of the dentine it is 24 GPa, and at the interface of the dentin and root canal it is 13 GPa.

Tab.1. Modulus of elasticity vestibulo-oral and disto-mesial direction

	cement-dentin junction	middle dentin	dentin near the root canal
vestibulo-oral	13 GPa	23 GPa	14 GPa
disto-mesial	14 GPa	24 GPa	13 GPa

ACKNOWLEDGEMENT

The financial support of this experiment by the Faculty of Civil Engineering, Czech Technical University in Prague (SGS project No. SGS12/117/OHK1/2T/11) is gratefully acknowledged.

REFERENCES

[1] WILLEMS G., CELISJ.P., LAMBRECHTSP., BRAEMM., VANHERLEG. Hardness and Young's modulus determined by nanoindentation technique of filler particles of dental restorative materials compared with human enamel*Journal of Biomedical Materials Research*, 1993. pp. 747–755 ISSN 1552-4965.

[2] KINNEYJ.H.,BALOOCHM., MARSHALLG.W., MARSHALLS.J.A micromechanics model of the elastic properties of human dentin Arch Oral Biol,*Archives of Oral Biology*, 1999. pp. 813–822 ISSN 0003-9969

[3] MASTHAN K.M.K. Textbook of Human Oral Embryology, Anatomy, *Physiology, Histology and Tooth Morphology*JP Medical Ltd, 2010. 275 p. ISBN 8-18-448892-0.

[4] *About teeth*[online]. [cited 2012].Available from: http://aboutteeth.com.au/about-your-teeth/the-structure-of-a-tooth/

[5] *Interaktivníembryologický atlas člověka*[online]. [cited 2011-07-27].Available from: http://www.med.muni.cz/histol/MedAtlas_2/MA_txt3-1-6-1.htm

[6] CRAIG, R.G., PEYTON, F.A. Elastic and mechanical properties of human dentin, *Journal of Dental Research*, 1958,pp. 710–718. ISSN 0022-0345

[7] TYLDESLEY W. R. The mechanical properties of human enamel and dentine,*British Dental Journal*, 1959, pp. 269–278. ISSN 0007-0610

[8] KINNEYJ.H., BALOOC M., MARSHALL G.W., MARSHALL S.J.A micromechanics model of the elastic properties of human dentine,*Archives of Oral Biology*,1959, pp. 269-278. ISSN 0003-9969

[9] PHILLIPSR.W.*Science of dental materials*,Philadelphia, W.B. Saunders Co., 1991, pp. 8-11 ISBN 9781437724189

[10] *ČasopisProgresdent*, 2008. ISSN 1211-3859

[11] GEI, M.,GENNA, F.,BIGONI, An interface model for the periodontal ligament,*Journal of Biomechanical Engineering*,2002, pp. 538-546. ISSN 0148-0731

[12] CRAIG R.G., Peyton F.A.The microhardness of enamel and dentin, *Journal of Dental Research,* 1958, pp. 661-668. ISSN 0022-0345

[13] ANGKER L., SWAIN M.V.Nanoindentation: application to dental hard tissue investigations, *Journal of Materials Research*,2006, pp. 1893–1905. ISSN 0884-2914

[14] ANGKER L., SWAINM.V.,KILPATRICKN. Micro-mechanical characterisation of the properties of primary tooth dentine.*Journal of Dental Research,* 2003, pp. 261–267. ISSN 0022-0345

[15] ANGKER L., SWAIN M. V., KILPATRICK N. Characterising the micro-mechanical behaviour of the carious dentine of primary teeth using nano-indentation, *Journal of Biomechanics,* 2005,**38(7),** pp. 1535-1542. ISSN 0021-9290

[16] KINNEY J.H., MARSHALL G.W., MARSHALL S.J. The mechanical properties of humandentin: a critical review and re-evaluation of the dental literature,*Critical Reviews in Oral Biology & Medicine*, 2003. pp. 13-29 ISSN 1045-4411

NON-DESTRUCTIVE ASSESSMENT OF TIMBER STRUCTURES

Pavel KLAPÁLEK[1], **Lenka MELZEROVÁ**[2]

***Abstract**:The purpose of this paper is to summarize and describe the currently used non-destructive assessment methods of a timber structures used in modern civil engineering.The principle of each method is shortly introduced and the reader is familiarized withtools necessary for the assessment and output parameters provided by the method.*

***Keywords**:Non-destructive tests, Modulus of Elasticity, Density, Humidity, Timber*

INTRODUCTION

The use of the non-destructive methods for assessment of timber quality has numerous benefits, mainly when used on site atthe currently standing structures where it is not possibleto remove parts of the structure and test the material in laboratory in orderto determine theexact values of the desired properties.

For the assessment of the timber properties it is important to be familiarized with the commonly used methods in order to decide which one is the bestto use in variousconditions. The topic of timber quality assessment becomes more and more important with the rise of popularity of timber structures. For instance, the reconstructions of old attics are nowadays extensively accomplished and the non-destructive methods are the only way how to determine the properties of the original timber.

There is a bunch of different methods that can be used; however, the each of them is different in its principle and suitable for a different application. The non-destructive testing of the timber can be effectively used for measurement of mechanical and physical properties such as density, strength, humidity, modulus of elasticity etc. Moreover, even determine location of the defects (knots etc.) canbe determined and locate places where the bad part of timber ends and healthy part begins.There are few cheap and fast methods, where the results are available immediately on site, but also ones that are expensive and time consuming where the results needs to be processed by the software.

---

[1]Bc.PavelKlapálek, Department of Mechanics, Faculty of Civil Engineering, CTU in Prague; Thákurova 7, 160 00, Prague, Czech Republic; pklapalek@gmail.com

[2]Ing.LenkaMelzerová, Ph.D., Department of Mechanics, Faculty of Civil Engineering, CTU in Prague; Thákurova 7, 160 00, Prague, Czech Republic; melzerov@fsv.cvut.cz

LIST OF NON-DESTRUCTIVE METHODS

2.1. VISUAL METHOD

Visual methodis a basic way to assess the quality of timber. Kind, approximate age and location of organic or inorganic defects can be relatively easily determined by a naked eye (Figure 1). Most importantly the method is used for determination of the following steps for further and more complex assessment. On the other hand there is a need for some basic knowledge of the timber and its properties.This method should be used prior to other methods of the assessment and testing.

Fig. 1Defects recognizable by visual method (http://uglyhousephotos.com)

2.2. ELECTRICAL METHOD

One of the most common and affordable ways to assess the timber quality is to exploit the electrical method. It uses the basic physical phenomenon of electrical conductivity. Using calibrated handheld devices the humidity can be measured and even the presence of the rotting can be detected(Figure 2).When the device is attached to the timber, theelectrical resistance between two electrodes is measured, and whenthe temperature and kind of investigated timber is known, the method can yield quite accurate values.The devices can be purchased for aprice in range of tens to hundreds of Euros.

Fig. 2 Representative types of humidity meters(http://www.elbez.cz)

2.3. METHOD OF ULTRASONIC WAVES

Method of ultrasonic waves is most commonly used for investigation of timber quality in civil engineering.Itexploits sound sensors to measure the spreading of ultrasonic waves through the material (Figure 3). It can be used to determine the timber properties such as density, modulus of elasticity, strength and localize the position of abnormalities (knots, cracks or other damage). The device consists of two sensors and a measuring device thatdetermines the speed of waves spreading between the sensors.With higher humidity of timber the speed decreases, while in case of a crack or any other defect the speed rises.For more detailed investigation the timber specimen must be measured at several locations. The measurement can be accomplished either parallel to fibers or perpendicular to fibers with sensors ofdifferent frequencies for a different dimensions of the timber. The first way of measurement is good for obtaining approximate properties of the timber and to gain overview of the element. The second way of measurement is good for getting detailedoverview of the properties and to localize any defect.The price of the device is in range of hundreds to thousands of Euros.

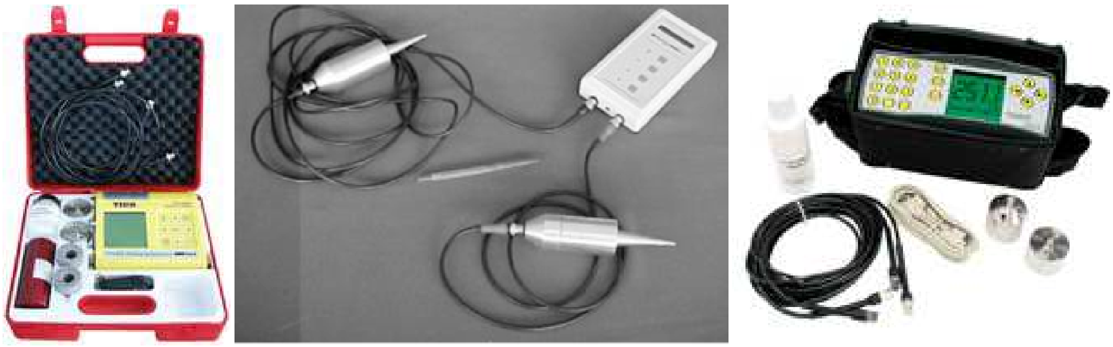

Fig. 3 Different types of devices needed for investigation by ultrasonic waves(http://tico.com)

2.4. RADIATION METHOD

Radiation method is demanding but suitable for historical timber structures. The method uses ionizing radiation and allows to "look" into the element. It is divided into the radiometry and radiography. The great advantage of this method is its non-destructive nature, but it isvery important to take certain safety measures to reduce hazards associated with exposure to radiation. The price of the device is in range of tens to few hundreds of thousands of Euros.

The radiometry utilizes the phenomenon of the passage of gamma radiation through a shielding material (Figure 4). It leads to the absorption and scattering and these data are then evaluated.

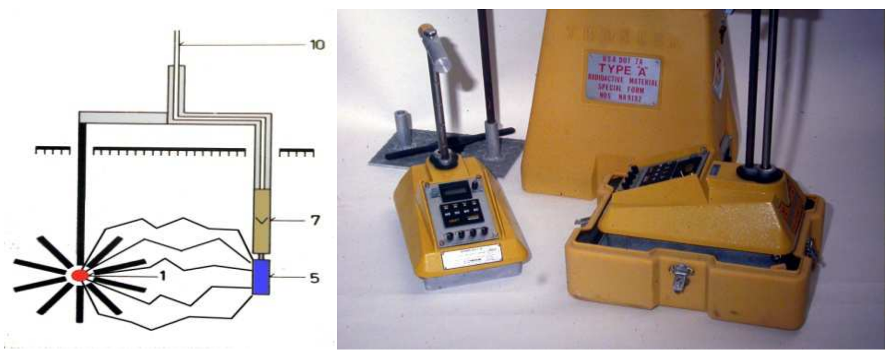

Fig. 4The principle of the method and the device for the radiometry(http://balkanplumbing.com)

The radiography then uses X-rays to create a negative image on the X-ray film or at radioscopy the X-rays passes through the magnetoscope and creates a digital image (Figure 5).

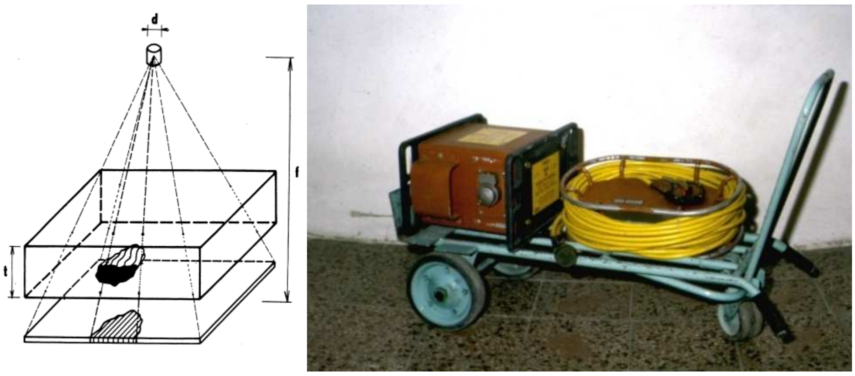

Fig. 4 The principle of the method and the device for the radiography (http://ndt-ed.org/)

2.5. METHOD OF SPIKE

Method of spike is not totally non-destructive, but the damage of an investigate specimen is minimal and it doesn't affect its mechanical properties. These are measured using a mechanical device that fires a spike with calibrated strength and measure the depth of penetration into the sample. The most ideal measurement is radial where the measured values should vary up to 10%. If measured tangentially the pin can be fired into hard annual rings and thus the measured values can vary significantly. The maximum penetration depth of the spike is 40 mm. With this measurement the density can be determinedas well as the strength and the modulus of elasticity.The most commonly used device for this test is called Pilodyn (Figure 5). The price of the device is around a few hundreds of Euros.

Fig. 5 The principle of the method of spike and necessaryequipment (http://www.gsxlslks.com, http://www.krsis.dk)

2.6. METHOD OF RESISTIVE MICRO DRILLING

Method of resistive micro drilling allows for the detection of internal defects by using deep drilling resistance micro drillequipped byresistograph (Figure 6). The results of the measurement are displayed by a diagram showing the dependence between the resistance of the drill and its penetration.This method is time consuming and is more suitable for a local analysis of properties. The price of the device is around a few hundreds of Euros.

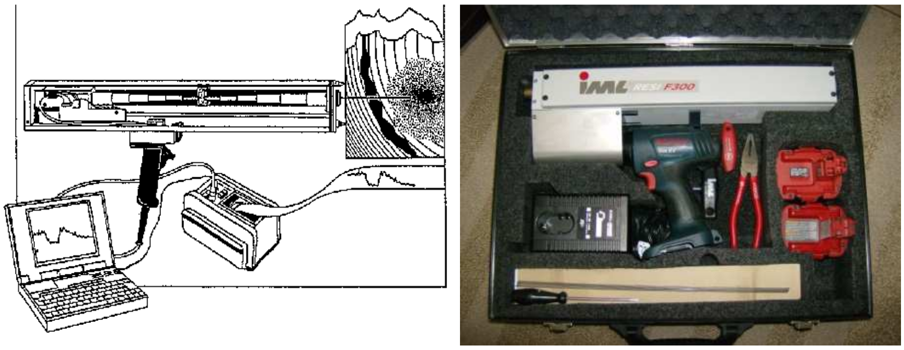

Fig. 6 The principle of the method of resistive micro drilling and necessary equipment (http://www.bam.de/)

2.7. METHOD OF RESISTIVE MICRO DRILLING

In this method, using specially adapted drill, the samples with a diameter of 4.8 mm and a minimum length of 20mmare taken from a specimen (Figure 7). Those samples are then tested in the laboratory to determine the mechanical properties (strength, modulus of elasticity, moisture). By the naked eye you can easily determine the presence of a rot, depth of penetration of the impregnation substances and others. The price of the device is around a few hundreds of Euros.

Fig. 7Specially adapted drill for extraction of samples (http://inspectapedia.com/)

2.8. PULSE METHOD

Pulse method is a dynamic method which is based on measurement of natural frequencies of the element with a set consisting of impacthammer (driver), sensors and computer that records the response of the element (Figure 8). Using the impacthammer the specimen is excited and themeasurement station subsequently records the excitation force and the response of anelement. The result is a response model consisting of frequencyresponse functions(FRF) of the tested specimen. The natural frequencies are then evaluated from FRFs and used to determine the dynamic modulus of elasticity.The price of the set is in range of hundreds to thousands of Euros.

Fig. 8: Theimpacthammer and the sensor during the measurement using the pulse method

CONCLUSION

There are many ways how to non-destructively evaluate the properties of timber and their choice depends on an expert, according to output data needed and an available equipment. Long-term experience is very important and helpful, but the basic knowledge of the available methods can help with the decision.

ACKNOWLEDGEMENT

The financial support of this experiment by the Faculty of Civil Engineering, Czech Technical University in Prague (SGS project No. 12/1117/OHK1/2T/11) is gratefully acknowledged.This outcome has been achieved with the financial support of the Ministry of Education, Youth and Sports of the Czech Republic, project No. LD12023 advanced methods for design, strengthening and evaluation of glued laminated timber.

REFERENCES

[1] BILOŠOVÁ, A.*Aplikovaný mechanik jako součást týmu konstruktérů a vývojářů: část Modální zkoušky*. vyd. 1. Ostrava, 2012.129 p. ISBN Pending

[2] EWINS, D.*ModalTesting - Theory, Practice and Application*, England:ResearchStudiesPress Ltd., 2000.400 p. ISBN 0-86380-218-4.

[3] HEŘMÁNKOVÁ, V. *BI03 - Diagnostické metody ve stavebnictví*[online].[cited2013-08-20]Brno, 2013. Availablefrom: http://www.szk.fce.vutbr.cz/vyuka/BI03/BI03%20D%C5%99evo%202013.pdf.

[4] KUKLÍK, P.and MELZEROVÁ, L. *Kompozitní materiály na bázi dřeva*. Praha: ČVUT Praha, 2011. 76p. ISBN 978-80-01-04958-7.

[5] ROSS, R.and PELLERIN, R. *Nondestructivetesting for assessing wood members in structures.* Madison: WI: U.S.Department of Agriculture, Forest Service, Forest Products Laboratory, 1994.42p.

FRACTURE PROPERTIES OF FRC WITH DIFFERENT FIBER TYPE AND CONTENT

Martin KOVÁŘ[1], **Marek FOGLAR**[2]

Abstract*:The paper presents results of a study focused on the mechanical properties of fiber reinforced concrete with different fiber type and content. Original experiments are compared to results available from the literature. Conclusions on the dependence of the fracture energy on the fiber type and content are drawn. The paper presents analytical approach to optimized force-deflection diagram of FRC beams with various fiber type and content.*

Keywords*:Fiber reinforced concrete, fracture energy, dynamic increase factor, force-deflection diagram*

1. INTRODUCTION

Fiber reinforced concrete (FRC) is because of its mechanical properties much more suitable for the use in structures subjected to higher strain rates, e.g. blast or impact loading [1]. The value of fracture energy is the decisive material characteristics for assessment of the damage of concrete structures by loadings with higher strain rates. This paper summarizes the results of the tests focused on fracture energy of fiber reinforced concrete of different strength classes, different fiber types and fiber contents subjected to different loading rates.

2. FRACTURE PROPERTIES OF FRC

2.1. METHODS OF ASSESSING THE FRACTURE ENERGY OF FRC

The fracture characteristics of FRC are usually tested on beams subjected to three-point bending or on specimens subjected to uniaxial tension. The value of the fracture energy is equal to the area under the force-deflection diagram (F-δ):

$$G_f = \frac{W}{B.H} \tag{1}$$

$$W = \int F.d\delta \tag{2}$$

[1]Ing. Martin Kovar,Department of Concrete and Masonry Structures, CTU in Prague, martin.kovar@fsv.cvut.cz

[2]Ing.MarekFoglar, Ph.D., Department of Concrete and Masonry Structures, CTU in Prague, marek.foglar@fsv.cvut.cz

where W is the area of under the force-deflection diagram and $B.H$ [m] are the cross-sectional dimensions of the crack of the specimen, F [N] is the force which loads the specimen and δ [m] is the deflection the force is causing in the middle of the span of the specimen. The area under the force-deflection diagram is taken for a limited deflection. When the loading of the specimen continues until the collapse, the value B.H is equal to the area of the concrete specimen.

The tests described in this paper were not performed according to the RILEM recommendations but according to the recommendations published in [2], the Czech national recommendation on testing of FRC. The specimens are beams, 150x150x700mm with the span of 600mm. No notch is used for the definition of the position of the macro-crack. The specimen is loaded by four-point bending and the forces divide the span into thirds. The benefit of this test arrangement is the constant value of the bending moment in the middle third of the specimen and elimination of the effect of the shear force. At the specimens without the notch, the macro-crack propagates at the weakest cross-section, i.e. the cross-section with the smallest fiber content, which is subjected to the biggest bending moment. The scatter of the results is bigger in comparison to the tests on notched specimens.

All other technical arrangements are similar to the experiments described in [3].

2.2. RESULTS OF THE EXPERIMENTS

The experiments were performed on two different strength classes of concrete and varying fiber type and content. The strength classes of concrete were chosen C30/37 and C55/67. For both types of concrete, two different materials of fibers with two different fiber contents were tested. The poly-propylene (PP) 54mm long fibers were used in dosages of 4.5 and 9 kg/m^3 (0.5% and 1%), the steel fibers were used in dosages of 40 and 80 kg/m^3 (0.5% and 1%). In total, 8 mix options were used.

Every material option was tested at three speeds of deformation to verify the dynamic increase factor and the influence of the loading rate on the fracture energy. The speeds of deformation were chosen 0.2 mm/min (approximately static loading), 2mm/min and 6 mm/min.

Tab. 1 Comparison of the fracture properties of the tested FRC

Speed of deformation υ	**C30/37, PP, ρ= 0.5%**			**C30/37, PP, ρ= 1.0%**		
	Crack opening		**Fracture energy**	**Crack opening**		**Fracture energy**
	F_{CLS}	**δ_{CLS}**		**F_{CLS}**	**δ_{CLS}**	
[mm/min]	[kN]	[mm]	[N/m]	[kN]	[mm]	[N/m]
0.2	30.6	0.09	2615	29.9	0.10	5007
2.0	31.6	0.09	2451	36.1	0.09	7405
6.0	-	-	-	36.9	0.12	6610
Speed of deformation υ	**C30/37, FE, ρ = 0.5%**			**C30/37, FE, ρ = 1.0%**		
	Crack opening		**Fracture energy**	**Crack opening**		**Fracture energy**
	F_{CLS}	**δ_{CLS}**		**F_{CLS}**	**δ_{CLS}**	
[mm/min]	[kN]	[mm]	[N/m]	[kN]	[mm]	[N/m]
0.2	28.0	0.152	6628	35.4	0.153	11467
2.0	30.5	0.130	6351	37.7	0.129	11453
6.0	31.8	0.128	6119	43.5	0.179	11667
Speed of deformation υ	**C55/67, PP, ρ = 0.5%**			**C55/67, PP, ρ = 1.0%**		
	Crack opening		**Fracture energy**	**Crack opening**		**Fracture energy**
	F_{CLS}	**δ_{CLS}**		**F_{CLS}**	**δ_{CLS}**	
[mm/min]	[kN]	[mm]	[N/m]	[kN]	[mm]	[N/m]
0.2	32.0	0.084	2100	34.4	0.117	6129
2.0	40.0	0.100	3440	37.9	0.097	8807
6.0	43.8	0.107	-	42.7	0.116	7452
Speed of deformation υ	**C55/67, FE, ρ = 0.5%**			**C55/67, FE, ρ = 1.0%**		
	Crack opening		**Fracture energy**	**Crack opening**		**Fracture energy**
	F_{CLS}	**δ_{CLS}**		**F_{CLS}**	**δ_{CLS}**	
[mm/min]	[kN]	[mm]	[N/m]	[kN]	[mm]	[N/m]
0.2	37.2	0.121	4559	37.6	0.099	7634
2.0	40.0	0.116	4899	47.8	0.120	7571
6.0	41.8	0.113	4612	49.0	0.126	7227

2.3. ANALYTICAL APPROACH TO THE DESCRIPTION OF THE FORCE-DEFLECTION DIAGRAM

The force-deflection diagrams of fiber concrete can be divided into two groups according to the material of the fibers: PP or steel fibers. Each of these groups has its own characteristic shape of the force-deflection diagram.

The typical force-deflection diagrams with emphasized characteristic points are plotted in Fig. 1 and 2.

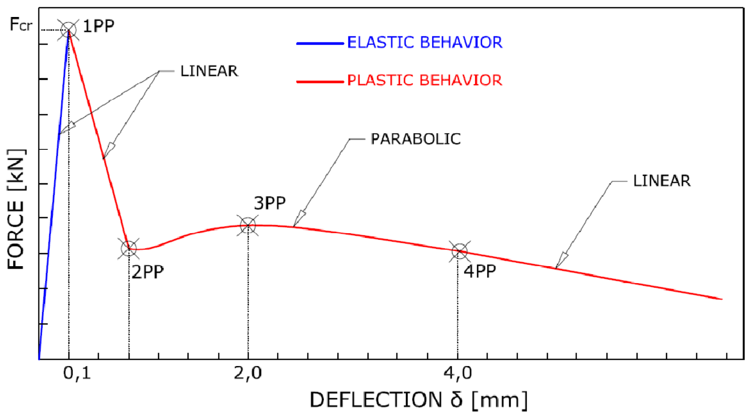

Fig. 1 Typical force-deflection diagram of a PP FRC

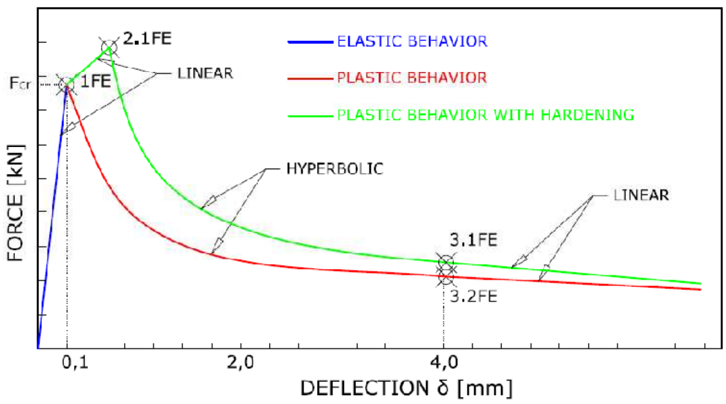

Fig. 2 Typical force-deflection diagram of a FE FRC

The behavior of FRC in bending can be characterized as linear elastic before the macro-crack appears. After the macro-crack appears, unlike at the plain concrete, the specimen performs with residual tensile resistance.

The slope of the elastic part of the force-deflection diagram is given mainly by the modulus of elasticity of concrete which is not much influenced by the volume or material of the fibers.

The value of the force at the appearance of the macro-crack depends again mainly on the tensile strength of concrete. The influence or the fibers occurs at FE fibers of higher volumes. The first phase of the force-deflection diagram can be defined as:

$$M_{cr} = 0.1F_{cr} \tag{3}$$

$$f_{ctm} = \frac{M_{cr}}{I}\frac{H}{2} = \frac{0.1F_{cr}}{BH^3}12\frac{H}{2} \tag{4}$$

$$F_{cr} = f_{ctm}\frac{BH^2}{0.6} \tag{5}$$

Where:

M_{cr} – is the critical bending moment at the appearance of the macro-crack, F_{cr} – the force at the appearance of the macro-crack, f_{ctm}– is the mean value of the tensile strength of concrete, I – is the moment of inertia of the cross-section, B and$H$ are the dimensions of the cross-section.

Higher strength classes of concrete have higher tensile strength and higher modulus of elasticity. The first macro-crack usually appeared at the deflection of 0.1mm.

The first point of the force-deflection diagram can be defined as (the point 1PP + 1FE):

$$1PP + 1FE = [0.1mm; F_{cr}] \tag{6}$$

The position of the first point gives the slope of the first part of the force-deflection diagram:

$$\mathrm{F} = 10\mathrm{F}_{\mathrm{cr}}\delta \tag{7}$$

The force-deflection diagrams of FE FRC bifurgate according to the value of the tensile stiffening.

The decreasing part of the force-deflection diagrams of FE FRC can be characterised by a hyperbola.

The force-deflection diagrams of PP FRC behave in a different way, the decrease of the tensile strength is much more significant, the point 2PP. The FE FRC with fiber volume less than 0.5% behave similarly.

The decrease is dependent on the fiber content. At the deflection of approximately 2mm, the material stiffens again, the point 3PP. This effect wears off at the deflection of 4mm, point 4PP (and 3FE). Since this point, the decreasing part of the force-deflection diagram can be considered linear.

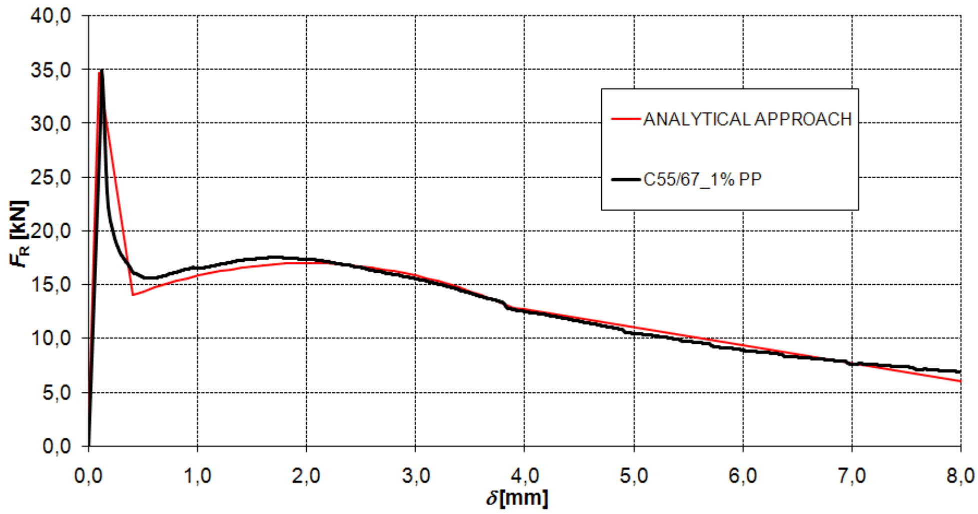

Fig. 3 Comparison of the analytical and real force-deflection diagram for PP FRC

CONCLUSION

The experiments showed great influence of the fiber type and content on the fracture energy of FRC. The fracture energy rises with the increasing fiber content.

The increase of the speed of deformation to 2mm/min caused an increase of the fracture energy. Yet, the further increase of the speed of deformation to 6 mm/min did not cause further increase of the fracture energy.

An analytical approach to the description of the force-deflection diagram was introduced.

ACKNOWLEDGEMENT

This paper was supported by the Grant Agency of the Czech Republic Grant Project No. GAČR13-30441S and the CTU project No. SGS13/077/OHK1/1T.

REFERENCES

[1] FOGLAR M., KOVAR M., Conclusions from experimental testing of blast resistance of FRC and RC bridge decks, *International Journal of Impact Engineering*, September 2013, **59**, 18-28,ISSN 0734-743X

[2] TP FC 1-1. Technicképodmínky 1: Vláknobeton - Část1 :Zkouševílváknobetonu. Praha, Českomoravskýbeton, a.s., , 34 (2007).

[3] DRAHORÁD M., FOGLAR M., VESELÝ P., SMIŘINSKÝ S., Užitídynamickéhofaktorunárůstupevnostibetonu pro zkrácenídobytrvánízkoušekvláknobetonovýchvzorků. *BETON-technologie, konstrukce, sanace*, 2012,**1**, 74-79, ISSN 1213-3116

DETERMINATION OF MICROMECHNICAL PROPERTIES OF WOOD CELL USING NANOINDENTATION

Vlastimil KRÁLÍK[1], **Václav NEŽERKA**[2], **Zdeněk PROŠEK**[3]

***Abstract**: The paper deals with the determination of nano- and microstructural, and micromechanical properties of timber. This was done by means of optical and electron microscopy, atomic force microscopy (AFM) and nanoindentation. These methods can define the parameters of individual phases within a composite, which is important for development of micromechanical models. These can be used for design and optimization of materials, such as various wood-based products. Our study provides information about the micromechanical properties of a early and late spruce cells.*

***Keywords**:* timber, mechanical properties, atomic force microscopy, nanoindentation, spruce cells

1. INTRODUCTION

Timber is one of the most popular building materials and it has been extensively used since the ancient times. Celtic people successfully built relatively lightweight structures made of timber before the 4th century BC. Nowadays its popularity is still increasing even in developed countries, because it is renewable material and its production is eco-friendly. Timber is used in civil engineering for load-bearing structures, such as floor beams, as well as for the auxiliary structures and claddings, and sometimes it is even used as a fire protection.

From the micromechanical point of view timber, or wood in general, is composed of three basic components: 1. celulose (35–55 %), 2. hemicelulose (15–35 %), and finally 3. lignin (15–30 %) [1, 2]. For the purposes of construction industry the timber produced from coniferous trees is most popular, in particular from spruce. It can be split without troubles, reaches quite high elastic deformation, it has relatively low bulk density and it can be easily glued. Therefore, it is often used for the production of wood-based composite products and glued-laminated beams, known as glulams.

[1] Ing. Vlastimil Králík, Faculty of Civil Engineering, Czech Technical University in Prague, Thákurova 7, 166 29 Prague 6 – Dejvice, Czech Republic, vlastimil.kralik@fsv.cvut.cz

[2] Ing. Václav Nežerka, Czech Technical University in Prague, Faculty of Civil Engineering, Thákurova 7, 166 29 Prague 6 – Dejvice, Czech Republic, vlastimil.kralik@fsv.cvut.cz

[3] Bc. Zdeněk Prošek; Czech Technical University in Prague, Faculty of Civil Engineering, Thákurova 7, 166 29 Prague 6 - Dejvice, Czech Republic, zdenek.prosek@fsv.cvut.cz

Mechanical properties of wood at macro-level are closely connected to the properties of wood cells at micro-level. The cell structure of wood is relatively complicated, there are several cell types and this diversity is mainly caused by the different growth and development of cells in spring (earlywood) and summer (latewood). The structure of latewood is denser because the cells are thick-walled around a cavity called lumen, and it has strengthening function while the earlywood forms a weaker layer within the annual ring and its main purpose is to transport the nutrients through big lumens. The size of cells and their walls is very limited and therefore the evaluation of mechanical properties can be done only on the micro level, for instance by means of nanoindentation.

2. EXPERIMENTAL METHODS

The investigated sample was extracted from a glulam beam composed of spruce lamellas [1]. An internal structure of the wooden cells for spring and summer growing season was monitored using AFM. It is shown in Fig. 1a and 1b. It is clearly visible that the earlywood cell is thin-walled, having the wall thickness between 2 and 3 μm and being equipped by a large lumen. The latewood cell is thick-walled and its thickness ranging between 3 and 7 μm [1, 4].

Nanoindentation tests were performed using a Hysitron Tribolab system® at the Faculty of Civil Engineering, CTU in Prague. Intrinsic elastic properties of individual cells were evaluated by statistical nanoindentation [2] at this level. The properties of lumen were tested only on the earlywood cells since the lumen of latewood cells was usually damaged as documented on the cross-sections in Fig 1a and 1b, and only the cell walls were indented on the latewood cells.

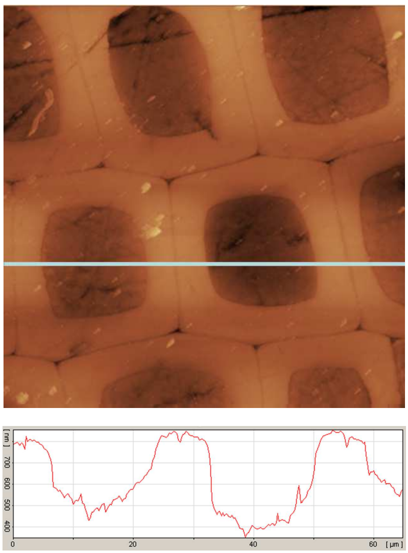

Fig. 1a AFM image of a spring wood cells 65 × 65 μm, cross section of cells

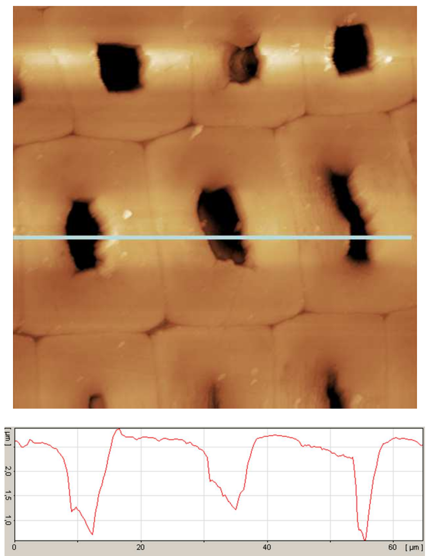

Fig. 1b AFM image of a summer wood cells 65 × 65 μm, cross section of cells

Several indents were made on both types of wooden cells at different locations of the previously polished surface of the investigated specimens. Standard load controlled test for an individual indent consisted of three segments: loading, holding at the peak and unloading. Loading and unloading of this trapezoidal loading function lasted for 5 seconds and the holding part lasted for 8 seconds. Maximum applied load was the same in both cases, equal to 400 μN. The grid of indents (4 × 5) at a single position, located by in-site imaging, is shown in Fig. 2. The indents are located in distance 3 μm to avoid their mutual influence.

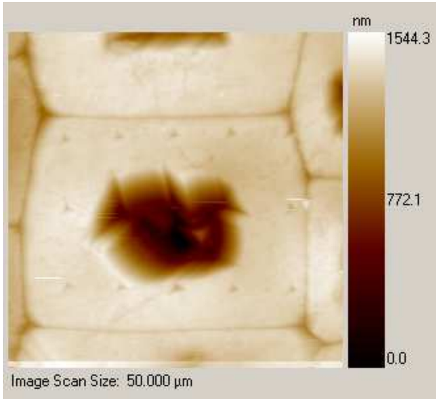

Fig. 2 Matrix of indents of summer cell wall scanned with Hysitron Tribolab®, 50 x50 μm

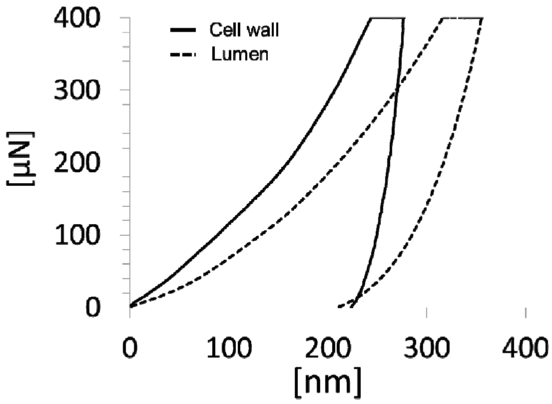

Fig. 3 Typical loading diagram of cell wall and lumen of spring wood

3. RESULTS AND DISCUSSION

The output of our measurements is the set of force displacement nanoindentation curves. These curves describe the response of the material on mechanical loading – the relationship between the loading force and penetration depth. The average penetration depth was established as 222 nm for latewood cells and 270 nm for earlywood cells. The average penetration depth in the region of lumen was 324 nm. These values are sufficient with respect to the surface roughness, but not too large to avoid interaction between phases.

Tab. 1 Average values of micromechanical parameters for wood cells

Type of wood	Position	Elastic modulus	st. dev	Hardness	st. dev
		[GPa]	[GPa]	[GPa]	[GPa]
Spring	Cell wall	10.2	0.9	0.18	0.02
	Lumen	3.1	0.1	0.13	0.01
Summer	Cell wall	12.9	1.3	0.25	0.03

Typical nanoindentation load-penetration curves representing spring wood cell wall and lumen are shown in Fig. 3. Elastic modulus and hardness was evaluated for individual indents using standard Oliver and Pharr methodology [3]. The average values and standard deviations at individual positions of the measurements are summarized in Tab. 1. Such result is in good agreement with the range of experimental values reported for spruce wood e.g. by Gindl et al. [2].

4. CONCLUSIONS

The microstructure of the wood sample was studied by AFM and it revealed different cell structures of the earlywood and latewood. Mechanical properties of individual cells were assessed by means of nanoindentation. Elastic parameters of spring and summer cell walls were obtained by means of statistical nanoindentation. The elastic modulus of latewood cell wall was established as 12.9 GPa, which is 26 % higher than the earlywood cell wall modulus, equal to 10.2 GPa.

The mechanical properties of lumen were measured only on the earlywood cells since the lumen of latewood cells was usually damaged during sample preparation. The elastic modulus of lumen was established as 3.1 GPa. The obtained results are in a good agreement with the data of other researchers, reported in open literature. Further research, focused mainly on the effect of humidity on the wood structure and mechanical properties will be done in a near future.

ACKNOWLEDGEMENT

The financial support of this experiment by the Faculty of Civil Engineering, Czech Technical University in Prague (SGS project No. 12/117/OHK1/2T/11 and 12/116/OHK1/2T/11) is gratefully acknowledged.

REFERENCES

[1] ŠLEZINGEROVÁ, J. and GANDALOVÁ, L.: *Stavba dřeva*. Brno: MZLU, 2005, 187 p. ISBN 8071576360.

[2] GINDL, W. et al. Mechanical properties of spruce wood cell walls by nanoindentation. *Applied Physics A*. 2004, **79**(8), 2069-2073. ISSN 09478396.

[3] NĚMEČEK, J., KRÁLÍK, V., VONDŘEJC, J. and NĚMEČKOVÁ, J. Identification of micromechanical properties on metal foams using nanoindentation. In: *Proceedings of the Thirteenth International Conference on Civil, Structural and Environmental Engineering Computing.* Edinburgh: Civil-Comp. Press, 2011, pp. 1-12. ISBN 978-190508845-4.

[4] OLIVER W. & PHARR G. An improved technique for determining hardness and elastic modulus using load and displacement sensing indentation experiments. *Journal of Material Research*. 1992 **7**(6), 1564-1583. ISSN 0884-2914.

NUMERICAL SIMULATION OF CRACK PROPAGATION BASED ON LINEAR ELASTIC FRACTURE MECHANICS

Karel MIKEŠ[1]

***Abstract**: In linear fracture mechanics, it is common to use the local Irwin criterion or the equivalent global Griffith criterion for decision whether the crack is propagating or not. In both cases, a quantity called the stress intensity factor can be used. In this paper, four methods are compared to calculate the stress intensity factor numerically; namely by using the stress values, the shape of a crack, nodal reactions and the global energetic method. The most accurate global energetic method is used to simulate the crack propagation in opening mode. In mixed mode, this method is compared with the frequently used maximum circumferential stress criterion.*

***Keywords**: crack propagation,stress intensity factor, maximum strain energy release rate criterion, maximum circumferential stress criterion*

1. INTRODUCTION

The description of crack propagation is one of the most important parts in linear fracture mechanic. The main questions are: Which loading value will the crack propagation begin for and which direction will the crack propagate in?

The aim of this paper is to find asuitable way how to calculate the stress intensity factor, which can be used to simulate the crack propagation in mode I. And then propose and test some criterion in mixed mode.

2. STRESS INTENSITY FACTOR CONCEPT

The stress intensity factor is aquantityused in linear fracture mechanic to describe an asymptotic stress field near the root of the crack. The values of the stress field reach infinity and declines with a square root of the distance from the crack tip.The asymptotic stress field in a state of plane stress is described in [1].

$$\sigma_x(r,\theta) = \frac{K_{\mathrm{I}}}{\sqrt{2\pi r}}\cos\frac{\theta}{2}\left(1-\sin\frac{\theta}{2}\sin\frac{3\theta}{2}\right) - \frac{K_{\mathrm{II}}}{\sqrt{2\pi r}}\sin\frac{\theta}{2}(2-\cos\frac{\theta}{2}\cos\frac{3\theta}{2}) \tag{1}$$

$$\sigma_y(r,\theta) = \frac{K_{\mathrm{I}}}{\sqrt{2\pi r}}\cos\frac{\theta}{2}\left(1+\sin\frac{\theta}{2}\sin\frac{3\theta}{2}\right) + \frac{K_{\mathrm{II}}}{\sqrt{2\pi r}}\sin\frac{\theta}{2}\cos\frac{\theta}{2}\cos\frac{3\theta}{2} \tag{2}$$

[1]KarelMikeš,Faculty of Civil Engineering, Czech TechnicalUniversity in Prague, karelmikes@gmail.com

$$\tau_{xy}(r,\theta) = \frac{K_{\mathrm{I}}}{\sqrt{2\pi r}}\sin\frac{\theta}{2}\cos\frac{\theta}{2}\cos\frac{3\theta}{2} \qquad + \frac{K_{\mathrm{II}}}{\sqrt{2\pi r}}\cos\frac{\theta}{2}\left(1-\sin\frac{\theta}{2}\sin\frac{3\theta}{2}\right) \tag{3}$$

whereK_{I} and K_{II} are the stress intensity factors in mode I and II,r is the distance from the crack tip and θ in a angle in polar coordinates.

3. CRACK PROPAGATION IN MODE I (OPENING MODE)

In mode I, the crack is only opened. Thereforewe can assume that the crack will propagate in an original direction and we have to decide only whether that the crack is propagating or not.

3.1. LOCAL IRWIN CRITERION

This concept was introduced by Irwin [2] in 1957.The stress intensity factor is used to decide about crack propagation.The propagation will begin if the value of the stress intensity factor $\mathrm{K_I}$reaches the critical value.

The rules for crack propagation according to the local Irwin criterion:

$\mathrm{K_I} < \mathrm{K_c} \Longrightarrow$	no crack propagation	*(4)*
$\mathrm{K_I} = \mathrm{K_c} \Longrightarrow$	crack is propagating	*(5)*
$\mathrm{K_I} > \mathrm{K_c} \Longrightarrow$	non-permissible situation	*(6)*

whereK_{I} is thestress intensity factor in mode I and K_{c} is a material property which is called fracture toughness$[\mathrm{Nm}^{-3/2}]$.

3.2. GLOBAL GRIFFITH CRITERION

This criterion was introduced by Griffith [3] in 1920. The propagation will begin if asufficient amount of energy is released during the propagation.

The rules for crack propagation according to theglobalGriffith criterion:

$\mathcal{G}(u,a) < G_{\mathrm{f}} \Longrightarrow$	no crack propagation	*(7)*
$\mathcal{G}(u,a) = G_{\mathrm{f}} \Longrightarrow$	crack is propagating	*(8)*
$\mathcal{G}(u,a) > G_{\mathrm{f}} \Longrightarrow$	non-permissible situation	*(9)*

whereG_{f} is a material property which is called fracture energy$[\mathrm{Nm}^{-1}]$,
$\mathcal{G}(u,a)$is a strain energy release rate which is defined as

$$\mathcal{G}(u,a) = -\frac{1}{t}\frac{\partial W_e(u,a)}{\partial a} \tag{10}$$

where$W_e(u,a)$ is a energy of elastic deformation as a function of the displacement u and the length of the crack a. $t$is a thickness of a beam.

Both criterions are equivalent and in mode I (in a state of plane stress), we can write

$$\mathcal{G}(u,a) = \frac{{K_{\mathrm{I}}}^2}{E} \qquad (11)$$

Now it is equivalent to use the stress intensity factor or the strain energy release rate.

3.3. SIMULATION IN OPENING MODE

The four methods were used to calculate the stress intensity factor or the strain energy release rate in opening mode; namely by using the stress values, the shape of a crack, nodal reactions and the global energetic method. The first three methods have a local character and manipulate with the values near theroot of the crack. The fourth method studies the change of the energy of a whole beam and calculates the strain energy release rate with using an original definition *(10)*. All these four methods were applied to the three-point bending test with geometry according to Fig.1.

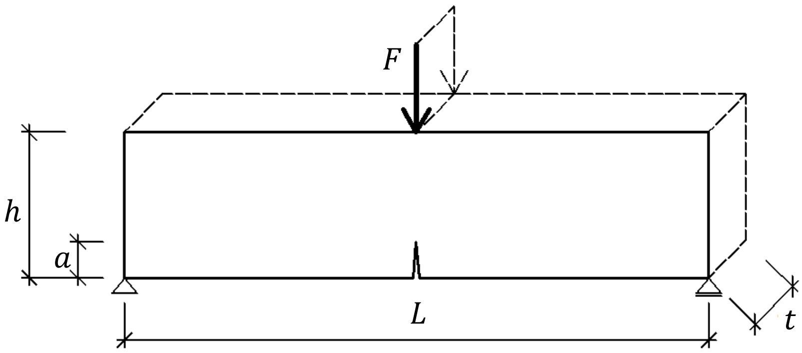

Fig.1Geometry of the three-point bending test

The comparing of the results with using the different type of the finite elementsis shown in afollowing table.

Tab. 1 Error with using the different methods and the different finite elements:

Type of finite elements: / Used method:	Linear	Quadratic	Modified quadratic
Values of stress	> 30%	10 – 30%	10 – 30%
Shape of a crack	< 10 %	2 %	1 %
Node reaction	5 – 10 %	< 5 %	< 5 %
Energetic method	5 %	2 %	0.5 %

The global energetic method with using the modified quadratic elements is the most accurate but also the most time-consuming method. If we applythis method with following geometry: high h = 0.5 m, length L = 2 m, thickness t = 0.2 m, initial length of a crack a_0 = 0.05 m, elastic modulus

E = 20 GPa, Poisson ratio ν = 0.2 and fracture toughness K_c = 4 MNm$^{-3/2}$, we obtain the Force-displacement diagram, see in Fig.2.

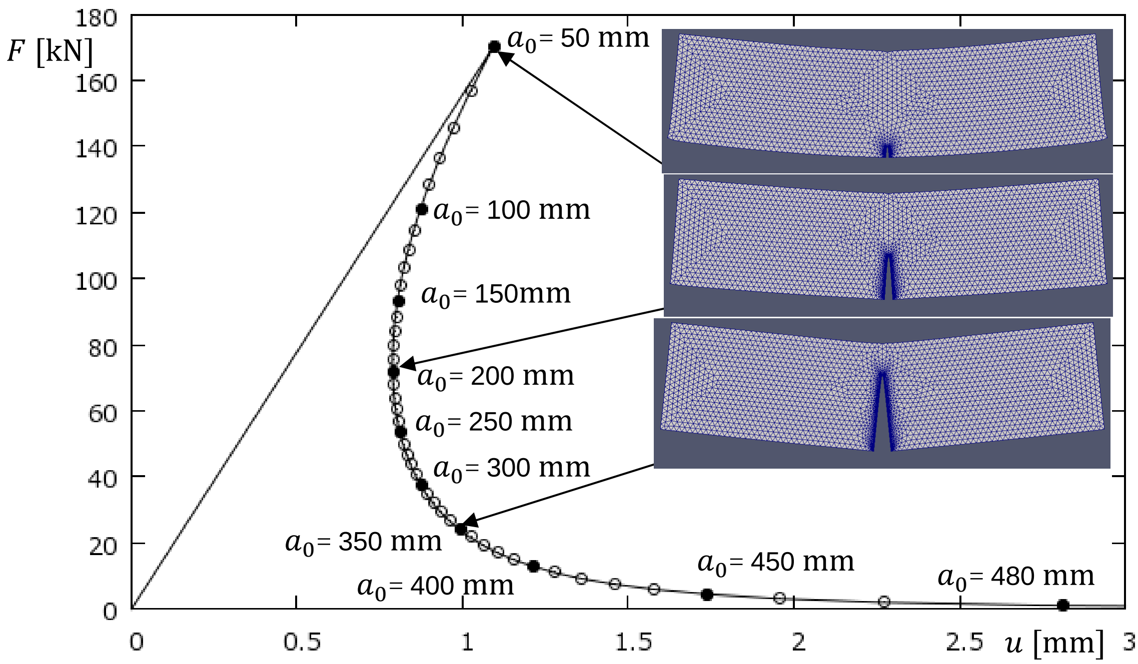

Fig.2Force-displacement diagram of the three-point bending test

4. CRACK PROPAGATION IN MIXED MODE

In opening mode in a plane there is a combination of an opening and a shear. The direction of the crack propagation has to be determined by another criterion.

4.1. MAXIMUM CIRCUMFERENTIAL STRESS CRITERION (MCSC)

This criterion determines crack propagation in the direction with the maximal circumferential stress. It is a simple idea, but there areseveral ways how to calculate the values of circumferential stress which is defined as

$$\sigma_\theta(r,\theta) = \sigma_y \cos^2\theta + \sigma_x \sin^2\theta - 2\tau_{xy}\sin\theta\cos\theta \qquad (12)$$

With using (1)-(3), we obtained:

$$\sigma_\theta(r,\theta) = \frac{K_\mathrm{I}}{\sqrt{2\pi r}}\cos^3\frac{\theta}{2} - 3\,\frac{K_\mathrm{II}}{\sqrt{2\pi r}}\cos^2\frac{\theta}{2}\sin\frac{\theta}{2} \qquad (13)$$

The first wayhow to find the maximum circumferential stress (MCSC1) isto use the values of the stress field in a number of Gauss point near the crack tip and fit a ratio $K_\mathrm{II}/K_\mathrm{I}$ with using (1)-(3). Then the maximum circumferential stress is represented by angle θ that can be found by solving following equation

$$\sin\theta + \frac{K_{\mathrm{II}}}{K_{\mathrm{I}}}(3\cos\theta - 1) = 0 \tag{14}$$

withthe following conditions

$$\theta \in (-\pi, \pi) \tag{15}$$

$$K_{\mathrm{I}} > 0 \tag{16}$$

$$K_{\mathrm{II}}\sin\frac{\theta}{2} < 0 \tag{17}$$

Anotherway how tofind the maximum circumferential stress (MCSC2) is to substitute the values of the stress field into the original definition *(12)*. Smooth with a polynomial function and find the maximum of this function.

Both ways give almost the same results, see in Fig.3.

4.2. MAXIMUM STRAIN ENERGY RELEASE RATE CRITERION (MSERRC)

This criterion determines the crack propagation in the direction with the maximal strain energy release rate which is defined in *(10)*. This maximum can be found by execution of a number of the crack extensions in the different directions. Then calculate the strain energy release rate in each direction, smooth with a polynomial function and find the maximum.

The application of this method leads to the different crack paths than with using the previous criterion MCSC,see in Fig.3.

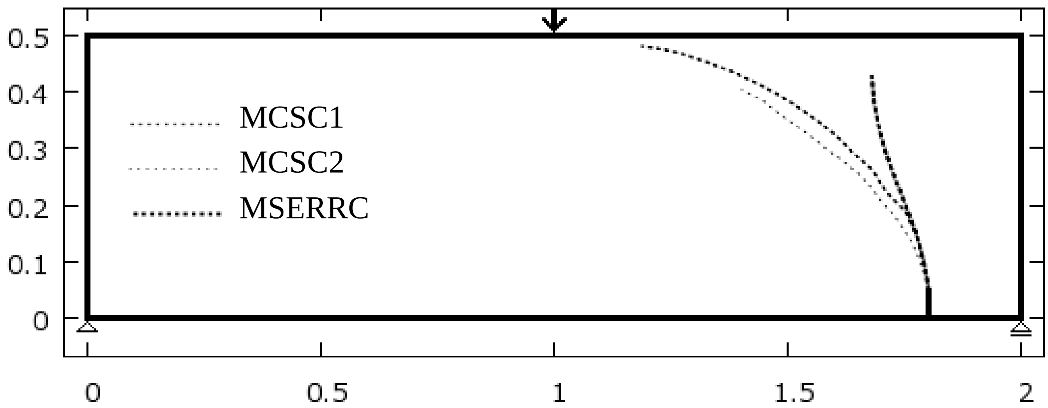

Fig.3Comparing of the different criterion in the three-point bending test

4.3. COMPARATIVE EXAMPLE

Another example is taken over from [4]. It is a rectangular panel with two holes and two initial cracks submitted to a vertical tensile. In this example both criterions lead to almost the same crack paths and results are similar to the results from [4], see in Fig.4 and 5.

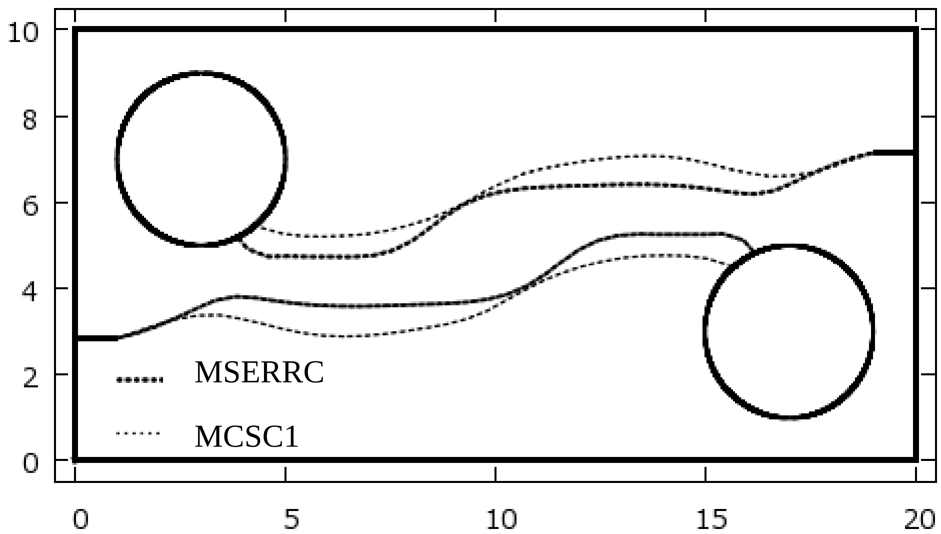

Fig.4Comparing of the different criterion in a vertical tensile test

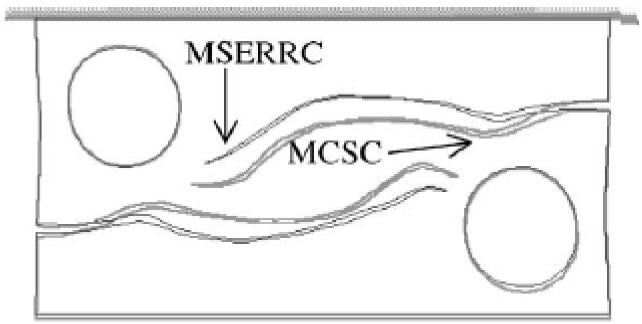

Fig.5Comparing of the different criterion in a vertical tensile test from [4]

5. CONCLUSION

With using the global energetic method, we obtained very good results in mode I. In the three-pointbending test in mixed mode, criterion based on this method leads to the different crack path then the criterions using the circumferential stress. But both criterions give the similar resultsin other examples in mixed mode.

REFERENCES

[1] JIRÁSEK, M. and ZEMAN, J. *Přetváření a porušování materiálů*. Praha: ČVUT, 2008. ISBN 978-80-01-03555-9

[2] IRWIN, G. R. Analysis of stresses and strains near the end of a crack traversing a plate. In:*Journal of Applied Mechanics*. 1957, **24**, 361-364.

[3] GRIFFITH, A. A. The phenomena of rupture and flow in solids. In:*Philosophical Transactions of the Royal Society of London*. 1921,**221**, 163-198.

[4] BOUCHARD, P. O., BAY, F. and CHASTEL. Y. Numerical modelling of crack propagation: automatic remeshing and comparison of different criteria. In:*Computer Methods in Applied Mechanics and Engineering*. 2003, **192**, 3887-3908.ISSN 0045-7825.

UNIFORM DESIGNS OF EXPERIMENTS FOR ASYMPTOTIC SAMPLING

Eva MYŠÁKOVÁ[1], Matěj LEPŠ[2]

Abstract: *The Design of Experiments creates an essential part of meta-modeling. The goal is to gain maximal information about the system with a minimal number of evaluations. For instance, to estimate a probability of failure or similarly reliability index by Monte Carlo-based algorithms, several consecutive Design of Experiments must be made to investigate properties of the failure domain. These designs are not same but are usually more or less overlapping. Therefore, at each step the goal is to create a new design in the different domain as uniform as possible but prevent duplicities among the new and the previous design.*

Keywords: *design of experiment, Latin Hypercube Sampling, space-filling, asymptotic sampling, maximin*

1. INTRODUCTION

The Design of Experiments (DoE) creates an essential part of any meta-modeling [1], experimentation [2], sensitivity [3] or reliability analyses [4]. Our work is aimed at algorithms, where several DoEs are created sequentially in overlapping domains. In other words, bounds of variables are changing during the evolution of the algorithm. Then the goal is to create a new design in the extended domain as uniform as possible but prevent duplicities among the new and the original design. Moreover, the usage of already evaluated points is preferred.

The changing of variables' bounds figures for example in reliability analysis method called asymptotic sampling, see e.g. [5]. Several Monte Carlo samplings are run with different standard deviations $\sigma > 1$ and then the required safety index β or probability of failure P_f for $\sigma = 1$ is estimated by an extrapolation. Therefore, the method enabling the usage of already evaluated points in differently distributed designs is required. In this paper we propose such a method that still ensures Latin Hypercube Sampling (LHS) property at each step of the algorithm.

[1] Bc. Eva Myšáková, Faculty of Civil Engineering, Czech Technical University in Prague, eva.mysakova@fsv.cvut.cz

[2] doc. Ing. Matěj Lepš, Ph.D., Faculty of Civil Engineering, Czech Technical University in Prague, leps@cml.fsv.cvut.cz

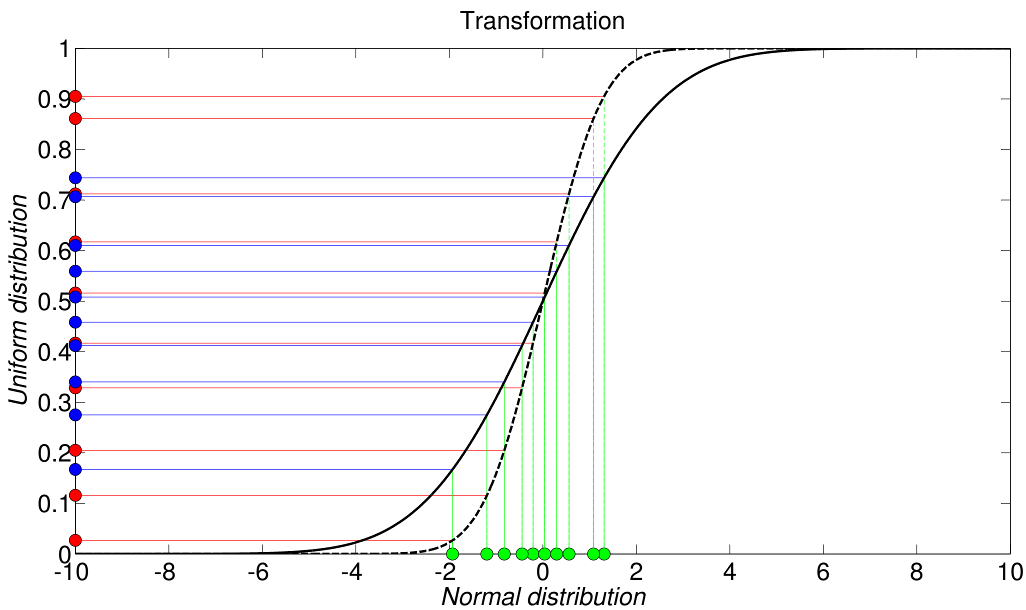

Fig. 1 Transformation of the design. The design points are transformed between individual distributions by their CDFs. Legend: Black dash line = CDF of Original distribution - normal, μ_1=0, σ_1=1; Black line = CDF of New distribution - normal, μ_1=0, σ_1=2; Red points = LHS design; Green points = design with Original distribution transformed from [0,1] LHS; Blue points = design transformed back to [0,1] by CDF of New distribution.

2. PROPOSED METHOD

In this paper we assume a simple case with two different distributions. In all examples these are normal (Gaussian) distributions with mean $\mu_1 = \mu_2 = 0$ and standard deviations $\sigma_1 = 1$ and $\sigma_2 = 2$. The next parameter we chose is the number of points in the design with the second (new) distribution - in this paper the new design has twice more points than the original design.

The problem is following: at first the initial uniformly distributed LHS design is created. This design is transformed by cumulative distribution function (CDF) of the first (original) distribution CDF_1 into the original design (certainly, the original design can by generated directly without the transformation from uniform initial design). We assume that these design points are evaluated (therefore it is desirable to use them again in the next steps). This design is then transformed back to $[0, 1]$-space by CDF_2 and here the actual problem starts. The described transformations are shown in Figure 1.

The goal is to create a new uniformly distributed LHS design in $[0, 1]$-space with $2{\cdot}np$ points, where

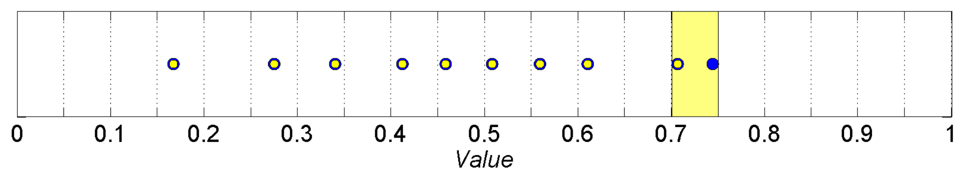

Fig. 2 Control of LHS restrictions in 1D. Legend: Blue points = design transformed back to [0,1] by CDF of New distribution; Yellow points = a "torso" (used blue points) of new LHS design.

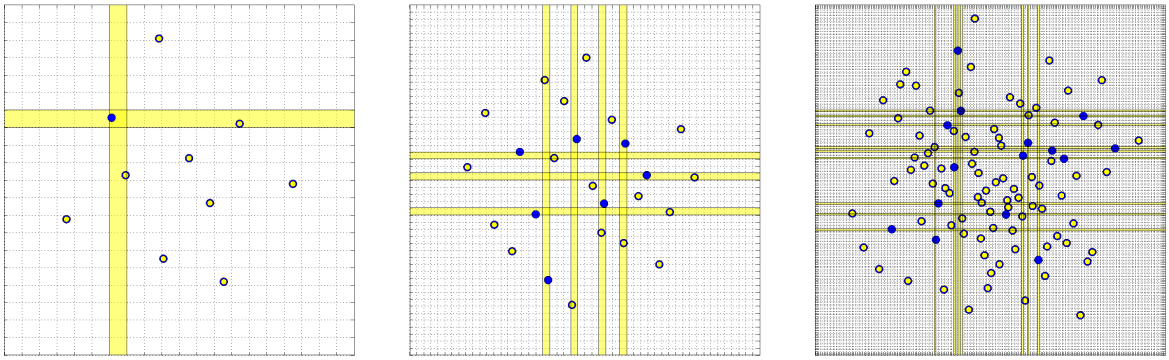

Fig. 3 Control of LHS restrictions in 2D. Legend: Blue points = design transformed back to [0,1] by CDF of New distribution; Yellow points = a "torso" (used blue points) of new LHS design.

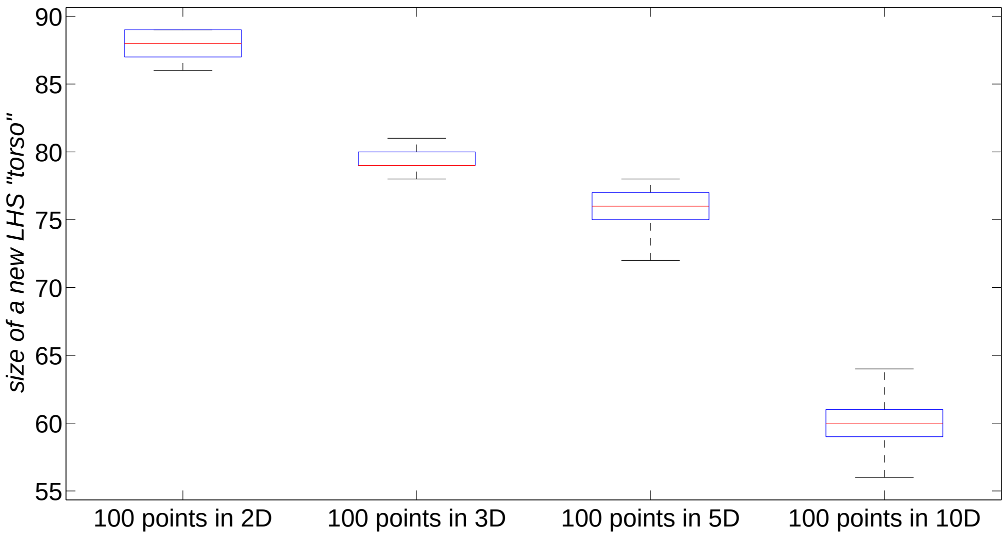

Fig. 4 Size of the "torsos" for original designs with 100 points. Statistics from 100 runs.

np is the number of points in the original design. Moreover, this design should contain as many already used points (blue points in illustrating Figures) as possible. Therefore, the following step is to control the LHS restrictions and create a "torso" of the new LHS design as shown in Figures 2, 3, 5c and 5d. The $[0, 1]$-space (each axis of multidimensional space, respectively) is divided into $2{\cdot}np$ intervals and the intervals containing more than one point are denoted as violating the LHS rules. The "torso" of the new LHS design is created by blue points so that we randomly choose a point and exclude points that share the same interval with chosen point. This is repeated until all the blue points are used in "torso" or excluded. It is obvious that different "torsos" can be created depending on the order of choosing (and excluding) the blue points. The sizes of "torsos" (number of non-colliding blue points) created from the same blue point set of 100 points are shown in Figure 4.

After the "torso" of the new LHS design is created it is necessary to complete it, i.e. to fill the unsampled columns and rows. We simply create LHS design with $(2{\cdot}np - nt)$ points, where nt is size of the "torso" (number of it's points). This auxiliary design is then distributed into vacant intervals of generated new LHS design as shown in Figure 5e.

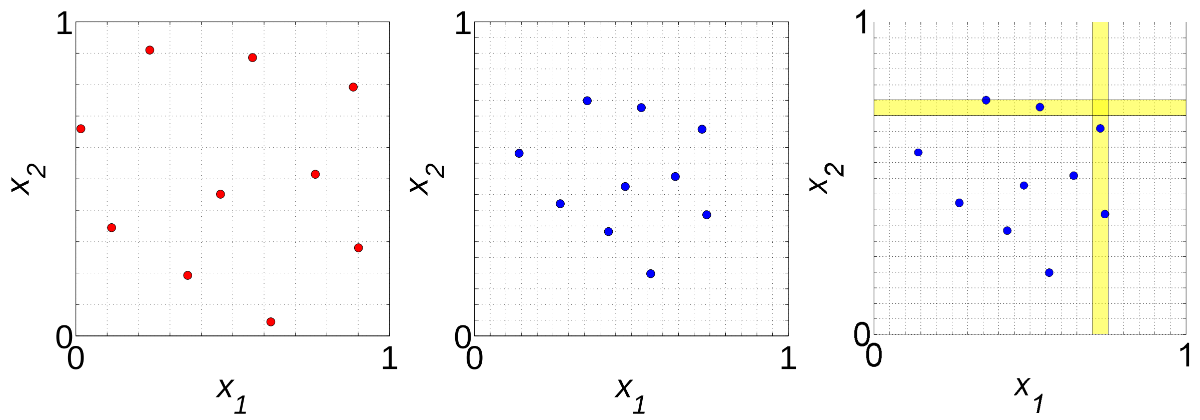

(a) An initial LHS design for transformation by CDF of Original distribution. *(b)* Design transformed back to [0,1] by CDF of New distribution. *(c)* Control of LHS restrictions.

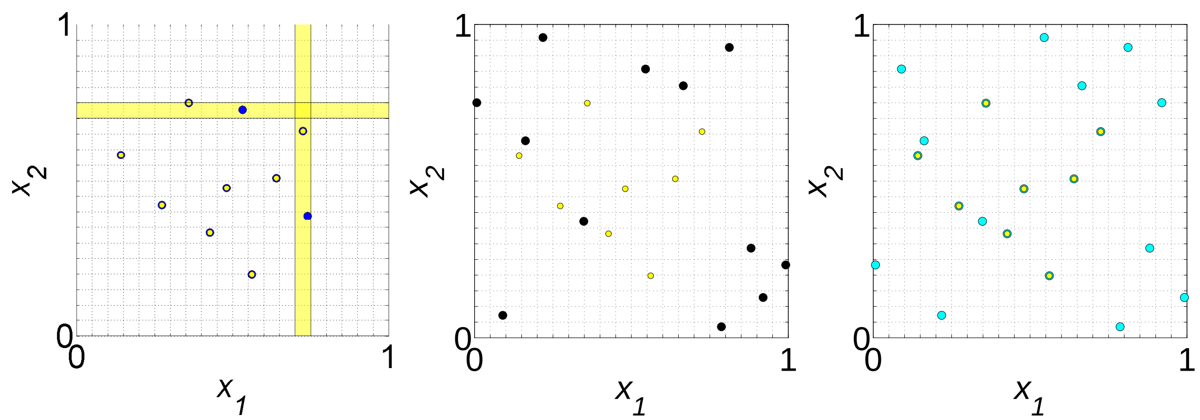

(d) Creation of a "torso" - basis of new LHS design. Points violating the LHS restrictions are not used. *(e)* New LHS - adding points on positions not occupied by points of a "torso". *(f)* Optimized new LHS design - usage of `random_Cmin_exchange` method on added points. Points of a "torso" stay in their positions.

Fig. 5 An illustration of proposed method in 2D. Legend: Red points = LHS design; Blue points = design transformed back to [0,1] by CDF of New distribution; Yellow points = a "torso" of new LHS design (used blue points); Black points = points added to the vacant positions to completing new LHS design; Cyan points = new optimized LHS design.

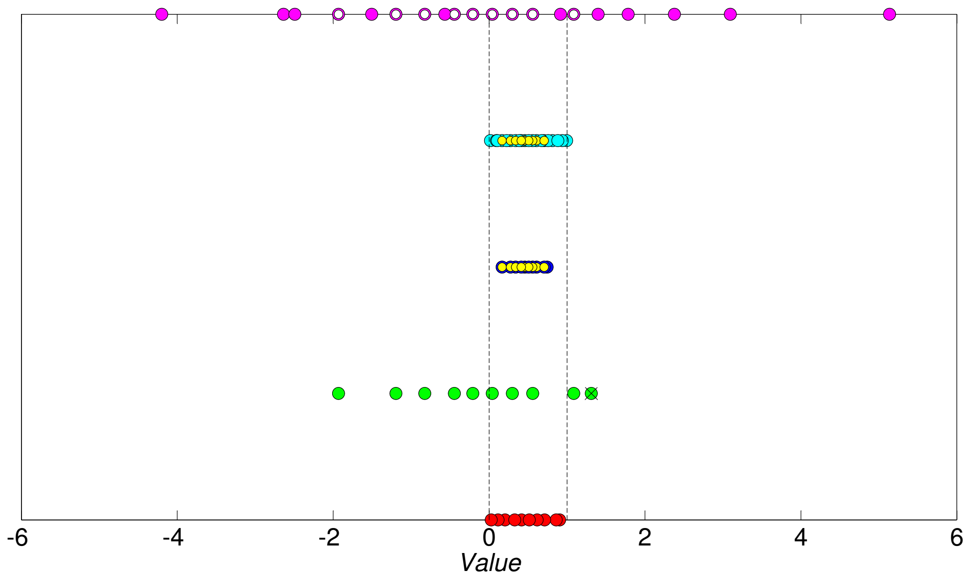

Fig. 6 The whole process in 1D. Legend: Red points = LHS design; Green points = design with Original distribution transformed from [0,1] LHS; Blue points = design transformed back to [0,1] by CDF of New distribution; Yellow points = a "torso" of new LHS design (used blue points); Cyan points = new LHS design; Magenta points = design with New distribution transformed from new [0,1] LHS; White points = points from Original distribution used in design with New distribution; Cross point = point not used in New distribution (violating LHS restrictions).

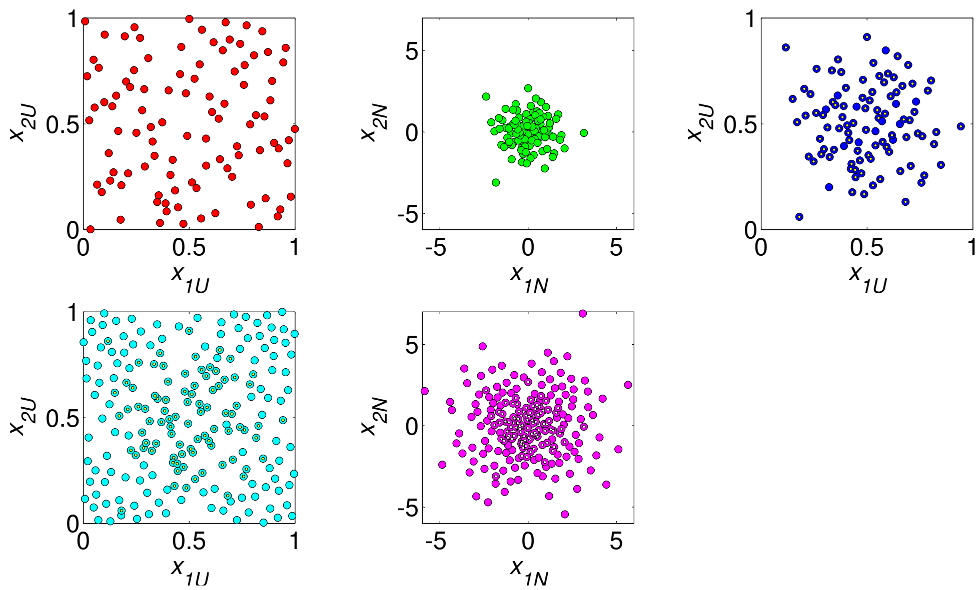

Fig. 7 The whole process in 2D. Legend: Red points = LHS design; Green points = design with Original distribution transformed from [0,1] LHS; Blue points = design transformed back to [0,1] by CDF of New distribution; Yellow points = a "torso" of new LHS design (used blue points); Cyan points = new LHS design; Magenta points = design with New distribution transformed from new [0,1] LHS; White points = points from Original distribution used in design with New distribution.

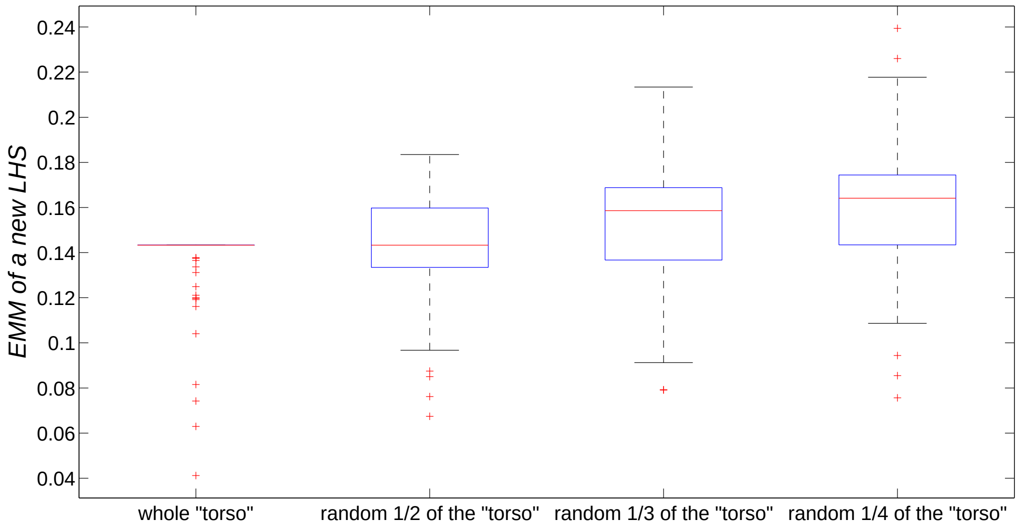

Fig. 8 The random selection of subset of the "torso". The EMM values correspond to the designs after optimization. Statistics from 100 runs.

Here the new LHS design is made. It satisfies the LHS restrictions but it does not guarantee sufficient space-filling properties. Therefore the `random_Cmin_exchange` method described in [6] and inspired by [7, 8] is used. The positions of added points are exchanged in order to destroy the close pairs of points. Note that points of the "torso" are held in their positions, only the added points can move.

Now the optimized new LHS design is done. The whole process is depicted in Figure 5. This design satisfies the LHS restrictions and contains the majority of already evaluated points. Moreover the design is optimized in terms of space-filling properties. It is ready to be transformed by the CDF_2 into the design with the second distribution as shown in Figures 6 and 7 (transformation between cyan and magenta points).

2.1. USAGE OF REMOVAL

It is obvious that usage of the whole created "torso" can limit the quality of new LHS designs. With too many points held in their positions the optimization by exchanging is not performing well enough. Figure 8 shows that random selection of the subset is not effective. At this point the usage of `removal_NEW` method [6] seems appropriate. This method removes selected number of points from the set. In each step one of the points in pair with actual minimal cross distance is removed. We tried two ways. In the first the points are removed from the "torso" - the more points are removed the more points have to be added to completing the new LHS design and the more points have the possibility of moving during the optimization. In the second way points are removed even before the creation of the "torso". Results (the Euclidian maximin distance (EMM)) of both ways for case of $100 \rightarrow 200$ points in 5D are shown in Figure 9. The EMM value is improving with decreasing number of preserved points (and therefore with increasing number of movable added points).

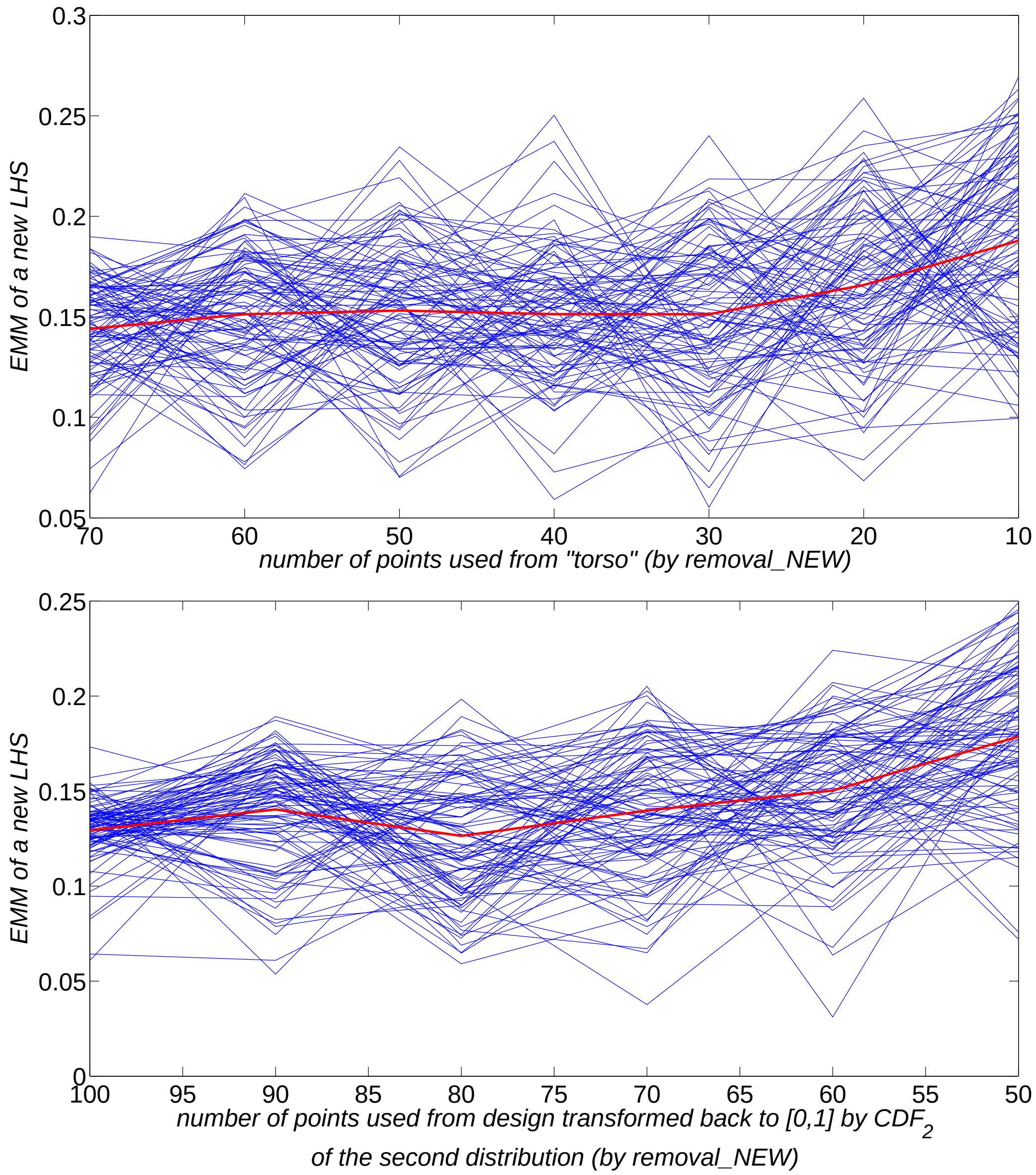

Fig. 9 Usage of `removal_NEW` *method in 5D example. Points are removed from the "torso" (top) or before creation of the "torso" (bottom). The EMM values correspond to the designs after optimization. Statistics from 100 runs.*

3. CONCLUSIONS

In this paper we present a method for creation of the designs of experiments for the cases when the bounds of variables are changed. It seems to be particularly suitable for asymptotic sampling in reliability analysis. The prime goal of the method is to create the design of experiments with new distribution such that the already evaluated points from old distribution can be used.

ACKNOWLEDGEMENT

The financial support of this contribution by the Faculty of Civil Engineering, Czech Technical University in Prague (SGS project No. SGS13/034/OHK1/1T/11) is gratefully acknowledged.

REFERENCES

[1] FORRESTER, A. and SÓBESTER, A. and KEANE, A. *Engineering Design via Surrogate Modelling: A Practical Guide.* John Wiley & Sons Ltd, 2008. ISBN 978-0-470-06068-1.

[2] MONTGOMERY, D. C. *Design and Analysis of Experiments.* Wiley, 8 edition, June 2012. ISBN: 978-1118146927

[3] SALTELLI, A. and CHAN, K. and SCOTT, E. M. *Sensitivity analysis.* NY:Wiley, New York, 2009. ISBN: 978-0470743829.

[4] BUCHER, C. *Computational Analysis of Randomness in Structural Mechanics.* Taylor & Francis, 2009. ISBN: 978-0415403542.

[5] BUCHER, C. Asymptotic sampling for high-dimensional reliability analysis. *Probabilistic Engineering Mechanics.* 2009, **24**(4), 504-510. ISSN 0266-8920.

[6] MYŠÁKOVÁ, E. and LEPŠ, M. Comparison of Space-Filling Design Strategies. In: *Engineering Mechanics 2011.* Praha: Ústav termomechaniky AV ČR, 2011, pp. 399-402. ISBN 978-80-87012-33-8.

[7] NOVÁK, D. and Lehký, D. ANN inverse analysis based on stochastic small-sample training set simulation. *Engineering Applications of Artificial Intelligence.* 2006, **19**(7), 731-740. ISSN 0952-1976.

[8] KUČEROVÁ, A. *Identification of nonlinear mechanical model parameters based on softcomputing methods.* Cachan, 2007. Ph.D. Thesis. Ecole Normale Supérieure de Cachan. Laboratoire de Mécanique et Technologie.

OPTIMUM OF TEN BAR TRUSS

Josef NOSEK[1], **Adéla POSPÍŠILOVÁ**[2]

***Abstract**: Structural-sizing optimization needs an enormous computational power. Our contribution shows possibilities of using volunteer computing for structural-sizing optimization. We use middleware BOINC (Berkley Open Infrastructure for Networks Computing). BOINC middleware was developed during the SETI@home project. Our project called CONVERTOR has more than 1000 hosts from 30 countries.*

***Keywords**: volunteer computing, BOINC, optimization, structural, CONVECTOR*

1. INTRODUCTION

Ask yourself why use volunteer computing? Because there are over 1 billion of computers in the world? This number of computers can supply more power than any other type of computing. For example the SETI@home project [1] connected more than three millions hosts (computers) and more than million users (users can have more computers) [2]. Volunteer computing (also called public resource computing) allows realizing low-cost high-performance computing project.

This paper present how to use BOINC for structural size optimization, most application of volunteer computing are based on software called BOINC [3]. The BOINC is an open source middleware based on client – server technology. The BOINC project is based at the U.C. Berkley Space Sciences Laboratory and has been funded by the National Science Foundation since its start in 2002.

2. DIFFERENCES BETWEEN VOLUNTEER COMPUTING AND GRID COMPUTING

Volunteer computing and Grid computing share the goal of better utilizing existing computing resources. However, there are few differences. Grid computing involves organizationally-owned resources: supercomputers, clusters, PCs owned and maintained by university or other organizations. All these re-sources are managed by professional employees (IT specialists). Devices are connected to high-bandwidth network links, and dedicated. There are relationships between organizations. Each of them can use or provide the resources. In contrast, volunteer computing involves an asymmetric

[1] Ing. Josef Nosek, Faculty of Civil Engineering, CTU in Prague, Thákurova 7, 166 29 Prague, Czech Republic, josef.nosek@fsv.cvut.cz

[2] Ing. Adéla Pospíšilová, Faculty of Civil Engineering, CTU in Prague, Thákurova 7, 166 29 Prague, Czech Republic, adela.pospisilova@fsv.cvut.cz

relationship between volunteers and projects. A usual project is a small or medium size academic research group with a limited computer power as well as limited budget. Most volunteers are individuals who owns (or uses) Windows (the vast majority), Linux or Mac PC. Volunteers are not computer experts and participate on the project when they are interested in and receive reward like credit, badge or screensaver. For example, representation of operating system in CONVECTOR project is in table 1. A project has no control over volunteers, cannot make deterministically prediction and cannot exclude malicious behavior.

Tab. 1 Operating system of volunteer computers

Operating system	% in sample
Windows XP	38.15
Windows 7	39.39
Windows 8	5.52
Other Windows system	16.39
Linux	0.55

3. PROJECT "CONVECTOR"

Our project called CONVECTOR have joined more than 350 volunteers and 1200 hosts from 37 countries around the world, see Fig. 1.

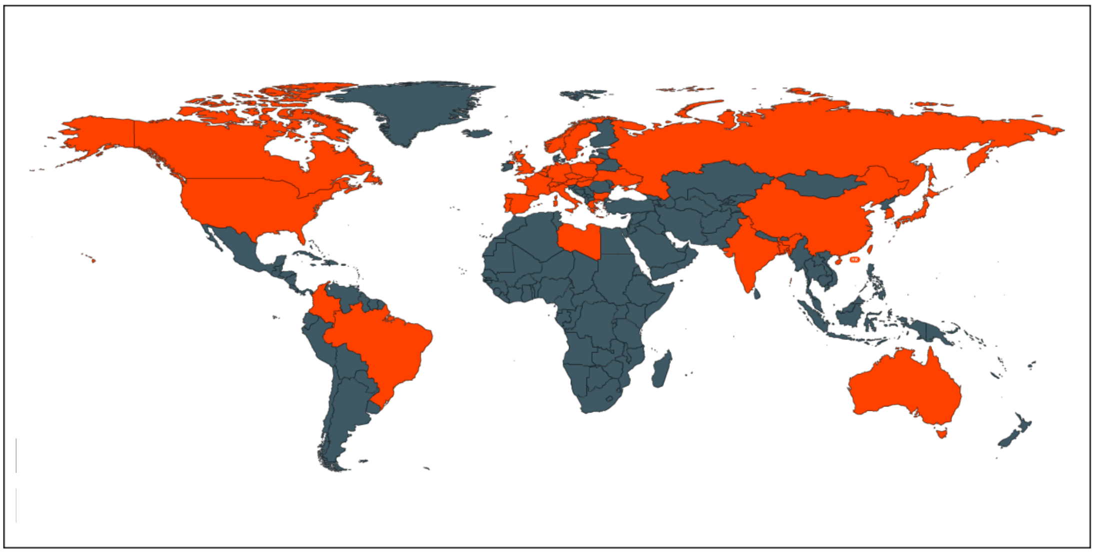

Fig. 1 Connected computers from the world[3]

[3] Figure is from the server boincstat.com

4. HOW TO BECOME A VOLUNTEER?

It is really simple. Just download and install small application (called client) and connect it to the selected project. Everything else does the client itself. Of course you can always control when the computation is allowed and how much resources can be used. If you like to try it, visit our web page convector.fsv.cvut.cz. You can do team with your friends or join to any existing team. If you have any problem or question, there exists forum where lot of people likely help you.

5. WHY WE NEED VOLUNTEER COMPUTING?

Actually we calculate the global optimum of the classical 10 bar truss optimization benchmark [4] by an enhanced enumeration method. The ten bar truss has been considered previously by many researchers and is shown in Fig. 2. In this example, truss members are individual variables. The cross-sectional areas, here design variables, are selected from the following available set of catalog values: 1.62, 1.80, 1.99, 2.13, 2.38, 2.62, 2.63, 2.88, 2.93, 3.09, 3.13, 3.38, 3.48, 3.55, 3.63, 3.84, 3.87, 3.88, 4.18, 4.22, 4.49, 4.59, 4.80, 4.87, 5.12, 5.74, 7.22, 7.97, 11.50, 13.50, 13.90. 14.20, 15.50, 16.00, 16.90, 18.80, 19.90, 22.00, 22.90, 26.50, 30.00, 33.50 [in^2]. This optimization task is defined with 42^10 possible combinations. If one takes 0.01 seconds, we need approximately 10^42 seconds. For your idea it is 10^34 years. This is a lot of time. Hence we use the enumeration enhanced with branch and bound principles [5]. In real we spend 148 176 CPU hours for solving this task. If we use one core computer it takes almost 17 years. But for out project it works for only two weeks. Now we know global optimum of this construction. It’s useful for testing optimization method.

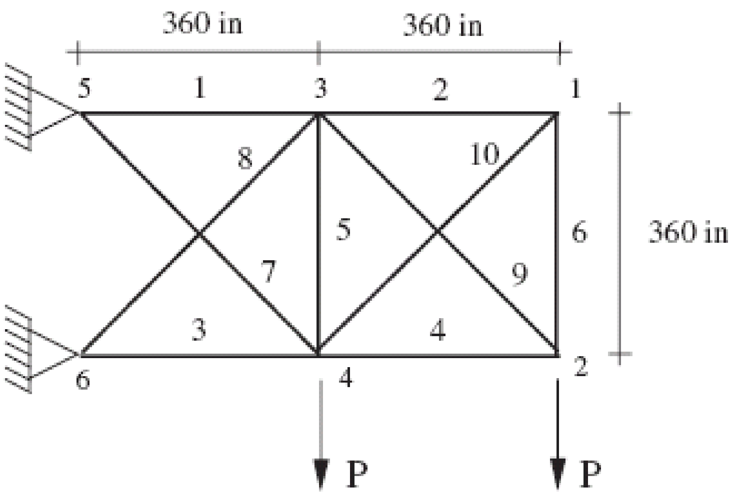

Fig. 2 The ten bar truss

6. CONCLUSION

Main goal of our project is get cheap and reliable “computing power” for solving challenging tasks. We launched project three months ago. We have solved the ten bar truss construction and we are ready for more difficult construction. Now we prepare application for 25- bar truss. We had learned a lot about volunteer computing and BOINC middleware, during last few months. We learned technical issues and social behavior of volunteer. Now we are ready to offer free computing power to other researchers and help them. We would like to improve communication with volunteer and offer him new badge as acknowledgment.

ACKNOWLEDGEMENT

The financial support of this experiment by the Faculty of Civil Engineering, Czech Technical University in Prague (SGS project No. OHK1-042/13) is gratefully acknowledged.

REFERENCES

[1] SETI@home.cz [online]. [cited 2013-09-01]. Available from: http://setiathome.berkeley.edu/.

[2] BOINCSTATS [online]. [cited 2013-09-01]. Available from: http://boincstats.com/en/stats/0/project/detail/host.

[3] BOINC [online]. [cited 2013-09-01]. Available from: http://boinc.berkeley.edu/.

[4] CAMP, C., PEZSHK, S. and CAO, G. Optimized Design of Two Dimensional Structures Using a Genetic Algorithm, *J. Struct. Eng.* 1998, vol 124. No 5. 551-559, ISSN: 0733-9445

[5] POSPIŠILOVÁ, A. and LEPŠ, M. Gobal Optima for Size Optimization Benchmarks by Branch and Bound Principles. *Acta Polytechnica,* 2012, vol 52, 74-81. ISSN 1210-2709

MATERIAL PROPERTIES OF THE CEMENT PASTE WITH FLUIDIZED FLY ASH

Tereza OTCOVSKÁ[1], Pavel PADEVĚT[2]

Abstract: *The properties of cement pastes are influenced by admixtures which can is possible add to the fresh paste. The material properties of classical fly ash are relatively good known. The fluidized fly ash is a second type of the fly ash from coal combustion. The fluidized fly ash added to cement paste change properties of the final product. The material properties of cement paste mixed with fluidized fly ash. The properties in saturated and dried condition are compared.*

***Keywords**: Cement paste, Fluidized Fly Ash, Strength in compression, Tensile strength in bending, Saturated specimen.*

1. INTRODUCTION

The use of fly ash in the construction industry is an important factor in the decision to process this waste material. A significant contribution of the fly ash has been demonstrated on the resulting concrete properties in many cases [1]. Concrete is one of the most widely used building materials and the processing of fly ash in it has a great important. The fly ash, which is produced mainly by burning coal, it is possible divided into two basic groups by way of acquisition - desulphurization. The first group contains classical fly ash, which has very favorable properties for concrete. It is possible to achieve the favorable properties suitable for concrete and also for the final concrete structure by adding fly ash into the fresh concrete.

The second type of fly ash is the fluidized fly ash. The fly ash is obtained from coal combustion in furnaces at temperatures between 1200 - 1400 °C. The filters with active lime are used to capturing fly ash. This method of obtaining is the agent of change in the chemical composition of the fly ash. The fly ash has a suitable grain size, shape and structure of the grains are different from the classical fly ash. The essential feature is a higher content of SO_3 and CaO. Higher concentrations of sulfur and lime have an adverse effect on the final properties of the concrete.

[1] Bc. Tereza Otcovská, Department of Mechanics, Faculty of Civil Engineering, Czech Technical University in Prague, tereza.otcovska@fsv.cvut.cz

[2] Ing. Pavel Padevět, Ph.D., Department of Mechanics, Faculty of Civil Engineering, Czech Technical University in Prague, pavel.padevet@fsv.cvut.cz

The determining material properties and their long-term verification can make a difference of view on this waste material and find the possibility of processing. Attention is focused to the features that affect the resistance of the material.

2. CEMENT PASTE WITH FLUIDIZED FLY ASH AND ITS PREPARATION

The preparation of cement paste with fluidized fly ash is different from the preparation of cement paste with classical fly ash. The grains of fly ash are more porous, causing a greater need for mixing water in the preparation of the cement paste. Three weight ratios between the cement and fly ash were used for the experiments. The first ratio was 70:30, 60:40 the second and the third 50:50. The first number in relations is weight's content of cement and the second one is weight's content of the fly ash in the mixture of the paste. 30 % of cement was replaced by fly ash in the first case, in the latter case 50 % compensation of the weight cement was by fly ash. The water/cement ratio (w/c), which was related to the 100 % of the amount of cement, has been left 0.4. The consistency of the cement paste with increasing amounts of fly ash in cement paste was significantly stiffer compared to cement paste with only 30 % fly ash replacement.

Fig. 1 The fracture surface after tensile bending test.

The specimens were divided for all three types of mixture into two groups: fully saturated with water and dried specimens. The preparation of the saturated specimens was in their placing in the water bath and left there until testing. The specimens were placed in the water after 3 days from manufacturing. The dried specimens were also left in the water bath after their production, but two days before testing the water were removed, two hours left in a laboratory environment, and then until the testing, dried in a temperature box at 105 °C.

The cement pastes were made for determining the compression strength, tensile strength in bending and for fracture energy. The form of prism was used for all three types of tests. Cross-sectional area was 20 × 20 mm (width and height) as it is possible to see on Fig.1. Length of specimens for bending tests was 100 mm. The specimens designed to test the compressive strength were made from the original by dividing their length into the two same parts. It was created a specimen with the length of 50 mm. The compression test was realized on the 6 solids with length 50 mm, 5 specimens were used for testing the tensile strength in bending with length 100 mm. The same elements shape was used for testing the fracture energy with notch. The number of specimens in this set was 4. Size of the notch in specimens for testing was chosen between 1/3 to 1/2 the height of the body. The notch was created in the middle of the specimen span. The distance of supports for bending test was 80 mm. The bending test has been realized in three-point bending test.

3. RESULTS OF TEST OF CEMENT PASTES

Specimens were tested at the age of one month from production. The cement paste with the classical fly ash has a high degree of maturation between 1 and 3 months of age. he focus was placed on the standard phase comparison, as in the case of concrete, during the first month.

Tab. 1 The material properties of cement pastes with the fluidized fly ash.

Relation between components (cement/fly ash)	Conditions	Compression strength (MPa)	Tensile strength in bending (MPa)	Tensile strength in bending - notch (MPa)
70/30	Dried	41.84	1.40	-
70/30	Saturated	30.08	3.95	-
60/40	Dried	29.17	2.63	2.79
60/40	Saturated	33.00	3.50	1.76
50/50	Dried	26.13	1.45	4.55
50/50	Saturated	26.94	5.09	4.25

The table 1 can be divided into two areas, the area of specimens saturated with water and the area of dried specimens. The compressive strength decreases with an increasing content of the fly ash in both cases. The compressive strengths are very high in the case of low ash content and approach to the values of the strength of a cement paste without the fly ash. The difference between the strength of saturated and dried specimens remains for the tensile strength in bending, too. The tensile strength in bending of the saturated specimens is higher than the strength of the dried elements. This trend is opposite to the case of compressive strength. The specimens with notch show increase in the tensile strength in bending for the ratio of components 50/50 against the 40 % content of the fly ash.

4. CONCLUSION

The change in the quantity of the fly ash in the cement paste causes a significant change in its material properties. The effect of saturation material is manifested also significantly. The effect of increasing the tensile bending with increasing fly ash content in the cement paste is opposite to the values of the compressive strength.

ACKNOWLEDGEMENT

This work has been supported by a project of the Faculty of Civil Engineering, Czech Technical University in Prague (SGS project No. 12/1117/OHK1/2T/11).

REFERENCES

[1] PADEVĚT, P. and LOVICHOVÁ, R. The Material Properties of Cement Paste with Fly Ash Exposed to High Temperatures, *Proceedings of 8th International Conference on Continuum Mechanics*, pp. 31-35. Rhodes, July 2013 ISBN 978-960-474-313-1.

INPUT PARAMETERS FOR MICROMECHANICAL MODELING OF WOODTISSUES

Zdeněk PROŠEK[1], Jakub ANTOŠ[2],Zuzana RÁCOVÁ[3], Vlastimil KRÁLÍK[4], Václav NEŽERKA[5]

***Abstract**:Micromechanical modeling became very popular in the last few decades because it often provides very accurate estimate of composites properties for a very low computational cost. However, it requiresa selection of a suitable homogenization scheme supplied by information about individual phases, such as their volumetric fraction and mechanical properties. The purpose of this paper is to suggest the simple micromechanical model of soft wood tissues provided the knowledge about the arrangement individual cells within the microstructure and properties of the individual phases obtained by means of nanoindentation.*

***Keywords**:micromechanical properties, wood cell, microstructure, nanoindentation, homogenization scheme*

1. INTRODUCTION

Timber, or structural wood, is one of the most popular building materials. It can be used for loadbearing structures but also for auxiliary structures or cladding. Moreover, there are plenty of wood-based products or glued laminated timber (glulam) beams on the market so that timber can be used almost for any desired application in civil engineering in low-rise structures. Wood is natural composite material, which is composed basically of three components; these are cellulose, hemicellulose and lignin. Wooden cells are arranged in parallel and therefore wood is considered as orthotropic material and its properties are usually investigated in three perpendicular directions. The mechanical properties in individual directions, i.e. perpendicular, tangential and longitudinal, often

[1]Bc. ZdeněkProšek; Czech Technical University in Prague, Faculty of Civil Engineering; Thákurova 7, 166 29 Prague 6 – Dejvice, Czech Republic, zdenek.prosek@fsv.cvut.cz

[2]Bc. JakubAntoš; Czech Technical University in Prague, Faculty of Civil Engineering; Thákurova 7, 166 29 Prague 6 – Dejvice, Czech Republic, jakub.antos@fsv.cvut.cz

[3]Ing.ZuzanaRácová, Czech Technical University in Prague, Faculty of Civil Engineering; Thákurova 7, 166 29 Prague 6 – Dejvice, Czech Republic, zuzana.racova@fsv.cvut.cz

[4]Ing.VlastimilKrálík, Czech Technical University in Prague, Faculty of Civil Engineering; Thákurova 7, 166 29 Prague 6 – Dejvice, Czech Republic, vlastimil.kralik@fsv.cvut.cz

[5]Ing.VáclavNežerka, Czech Technical University in Prague, Faculty of Civil Engineering; Thákurova 7, 166 29 Prague 6 – Dejvice, Czech Republic, vaclav.nezerka@fsv.cvut.cz

differ a lot. The mechanical properties ofwood are closely related to its microstructure, whichis unique for each species, and the difference is most apparent between coniferous and deciduous trees [1]. The aim of this paper is to summarize the homogenization strategies and micromechanical modeling used for wood tissues and to indicate how to exploit the data from the microscopy and experimental investigations, in particular AFM images and nanoindentation. The micromechanical modeling could be used in design of complicated joins with multiaxial loading and to avoid exaggerated partial safety factors leading to uneconomical design of modem timber structures. Our study was focused on spruce wood, which is most often exploited in construction industry, only in direction parallel to stem [2].

3. MICROSTRUCTURE OF WOOD AND MICROMECHANICAL PROPERTIES

Full scale modeling of wood is very complex because of growth irregularities, cracks and knots. Moreover, there is a huge difference between properties of individual tissues and this leads to complicated failure mechanisms [3]. The hygroscopicty of the material introducesother issues such as creep, shrinkage and swelling or degradation due to presence of water or increased humidity. This leads to multi-level modeling of the hierarchical microstructure, which has been tackled e.g. by Hofstetter et al. [3] or Qing and Mischnaevsky[4]. The cell walls are composed of several layers with different properties and the proper micromechanical scheme has been suggested by Quing and Mischneavsky[4]. A few authors consider the properties of cell walls constant which simplifies both, micromechanical properties and measurement of the material properties on nano-scale by nanoindentation. The cell walls are composed of four basic components – lignin, cellulose, hemicellulose and water. The microscale modeling is focused on homogenization of hexagonal cells (*tracheids*) that build up honeycomb structure with typical dimensions 20–40 μm [3] in case of softwood. The regular periodic arrangement calls for utilization of unit cell where the representative unit cell is subjected to macroscopic loading.

3. MICROSCOPY AND NANOINDENTAION MEASUREMENTS

The statistical representation of the microstructure arrangement can be obtained from the microscopy images (see Fig.1) and the results of nanoindentation (Tab. 1) find their use as input parameters describing the mechanical properties of individual phases, i.e. cell walls of early- and latewood and the weaker lumen.On the macrolevel,the microstructure of wood can be seen by a naked eye, since individual layers within annual rings, early- and latewood, differ not only in morphology of cells and their mechanical properties, but also in color (Fig. 1). The earlywoodhas lighter color, because the tracheids have bigger size lumen realties to the thickness of cell walls and therefore its density is lower. Moreover, it has been found by our measurements that the stiffness of earlywood (10.2 GPa) cell walls is lower compared to dark latewood (12.9 GPa). The purpose of the earlywood tissue is to reinforce the tree trunk while the purpose of the weaker earlywood cells is to supply the tree with water and nutrients.

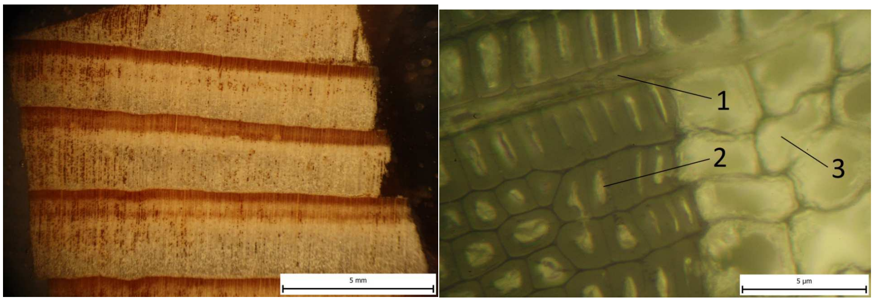

Fig. 1 Cross-section through the sample of spruce (left), microscope image of wood section (right): 1 – parenchyma cells, 2 – latewoodtracheid, 3 – earlywood tracheid.

At the micro level the structure of the tracheids can be clearly recognized (Fig. 2). There are clearly visible auxiliary cells, called parenchyma cells, which are specialized for supply of nutrients. According to our measurements using the image analyses the earlywoodtracheids had their walls approximately 2 to 3 µm thick and lumen forms a major part of the cells. The latewood tracheids in our investigative sample have significantly thicker walls, approximately 3 to 7 µm. At lower levels the microscope images clearly show distinct phases of the cells (Fig. 3) [4].The micromechanical properties of individual phases, i.e. lumen and cell walls of early- and latewood were investigated by means of nanaoindentation and the results are summarized in Tab. 1 [5].

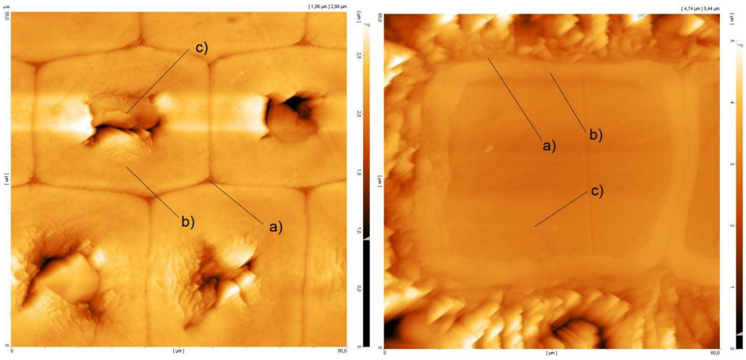

Fig. 2AFM images of tracheids: latewood cells (left) and detail of earlywood cell (right) with distinct phases: a) middle lamella, b) cell wall, c) lumen

Tab. 1 Average values of nanoindentation results

Type of wood	Position	Elastic modulus	st. dev	Hardness	st. dev
		[GPa]	[GPa]	[GPa]	[GPa]
Spring	Cell wall	10.2	0.9	0.18	0.02
	Lumen	3.1	0.1	0.13	0.01
Summer	Cell wall	12.9	1.3	0.25	0.03

The results indicate that wood is anisotropic and also inhomogeneous material from the mechanical point of view and its homogenization calls for the unit cell approach. This approach has been successfully used by Hofstetter at al. [3] who reached at relatively good agreement with the experimentally obtained data.

Numerical homogenization of the honeycomb structure was successfully used by Qing and Mishnaevsky[4].

4. CONCLUSION

The article suggested a homogenization approach for the micromechanical modeling of wood in the direction parallel to stem, based on experience of other authors in available literature and own measurements using AFM and nanoindentation. It turns out that the periodic microstructure of the early- and latewood tissues calls for utilization of unit cell approach at the micro-level. Another alternative is the utilization of numerical homogenization which could be used for the homogenization of timber at higher level where the presence of growth defects and knots cannot be omitted.

ACKNOWLEDGEMENT

The financial support of this outcome by the Faculty of Civil Engineering, Czech Technical University in Prague – SGS projects No. 12/1117/OHK1/2T/11 and SGS12/110/OHK1/2T/11 – isgratefully acknowledged.

REFERENCES

[1] ŠLEZINGEROVÁ, J. and GANDALOVÁ, L.*Stavbadřeva*. Brno: MZLU, 2002, 176 p.

[2] PROŠEK, Z. and KRÁLIK, V.Stanovenínano, mikro a makrostrukturystavebníhodřeva. In: *Proceeding of student conference NANS 2013*, Prague 2013, (In Press).

[3] HOFSTETTER, K., HELLMICH, CH. and EBERHARDSTEINER, J. Micromechanical modeling of solid-type and plate-type deformation patterns within softwood materials. A review and an improved approach, *Holzforschung*.2007, **61**, 343–351.ISSN 00183830

[4] QING, H. and MISHNAEVSKY, L. 3D multiscale micromechanical model of wood: From annual rings to microfibrils, *International Journal of Solids and Structures*. 2010, **47**, 1253–1267. ISSN 00207683

[5] EDER, M and ARNOULD, O.Experimental micromechanical characterization of wood cell walls. ln: *Wood Science and Technology*[online]. 2012-10-30 [cited 2013-06-10]. Available from: http://hal.archivesouvertes.fr/docs/00/74/70/55/PDF/Experimental_micromechnical_characterization_Eder_al.pdf

[6] FOREST PRODUCTS LABORATORY. *Wood Handbook* [online]. April, 2010. [cited 2013-07-11]Available from Forest Products Laboratory: http://www.fpl.fs.fed.us/documnts/fplgtr/fpl_gtr190.pdf

INFLUENCE OF COMPOSITION ON TENSILE AND FRACTURE PROPERTIES OF LIME-BASED MORTAR

Michal PŘINOSIL[1], **Petr KABELE**[2]

***Abstract**: Properties of lime-based mortar can be controlled by the composition of the mixture. The influencing factors are for example the ratio of types of filler with different grain size distribution, the ratio of the filler and the binder and the water ratio. Three-point bending test was performed on several sets of notched specimens with different compositions to calculate fracture energy. Using numerical simulations and data from the experiments, Young's modulus of elasticity, tensile strength and cohesive traction-separation relation were evaluated.*

***Keywords**: Mixture composition, three-point bending test, fracture energy, tensile strength.*

1. INTRODUCTION

Lime-based mortars were widely used for constructions of historical buildings. The development of cement technology reduced application of lime, but higher strength and chemical and transport properties of cement-based mortars lead to incompatibility with original masonry and lower durability. For this reason, it is necessary to recover the forgotten technology of lime. In our research, we are developing a new high performance mortar reinforced with short fibers, which should be able to accommodate high tensile strains caused by temperature and moisture induced volume changes, imposed deformations due to foundation movements or natural and artificial seismicity, etc.

As part of the project, it is necessary to design the composition of the lime-based matrix, which could be subsequently reinforced with fibers. To ensure the functionality of the fiber reinforcement, the matrix must be as homogeneous as possible. Therefore we use only fine grained aggregates. The aim of this study is to identify the effects of the mixture composition on the fracture and tensile characteristics of lime-based matrix. We are especially interested in the effect of the water ratio, the ratio between binder and filler and the ratio between several types of filler. Fracture energy was evaluated using three-point bending test with notched specimens. Tensile strength and cohesive traction-separation relation were evaluated from the experimental results using numerical simulations.

[1] Ing. Michal Přinosil, Department of Mechanics, Faculty of Civil Engineering, Czech Technical University in Prague, Thákurova 7, 166 29, Prague 6, Czech Republic, michal.prinosil@fsv.cvut.cz

[2] prof. Ing. Petr Kabele, PhD., Department of Mechanics, Faculty of Civil Engineering, Czech Technical University in Prague, Thákurova 7, 166 29, Prague 6, Czech Republic, petr.kabele@fsv.cvut.cz

2. MATERIALS

As the filler, two types of fine silica sand from Střeleč a.s. labeled ST2 (d_{max} = 0.090 mm) and STJ25 (d_{max} = 0.315 mm) were used. Hydrated air lime powder CL90 from Čertovy schody was used as the binder (matrix L). In one set (marked 13 – Tab. 1) one quarter of weight of lime was replaced by high reactive metakaolin Mefisto L05 from ČLUZ a.s. Nové Strašecí (matrix LM).

Water ratio was calculated as the proportion of the mass of water to mass of dry components (filler and binder):

$$w = \frac{m_{water}}{m_{dry}} \tag{1}$$

Finally from these components 13 mixtures with different composition were prepared. The volume proportions of individual components and water ratio are listed in Tab. 1. The mixture marked 14 was prepared and tested in 2012 [1]. The workability of fresh mixture was determined using flow table according to ČSN EN 1015-3 [2].

Tab. 1 Mixture composition

Set	Binder:Filler	ST2:STJ25	Matrix	w [-]	Flow [mm]
01	1:2	2:1	L	0.25	-
02	1:2.5	2:1	L	0.25	-
03	1:2	2:1	L	0.26	143.5
04	1:2	2:1	L	0.28	157.0
05	1:2	2:1	L	0.30	181.5
06	1:2	1:1	L	0.22	131.0
07	1:2	1:1	L	0.24	142.0
08	1:2	1:1	L	0.26	171.0
09	1:2	0:1	L	0.24	122.5
10	1:2	0:1	L	0.26	134.0
11	1:2	0:1	L	0.28	161.5
12	1:1.04	2:1	L	0.30	133.0
13	1:1.04	2:1	LM	0.30	135.5
14	1:3	2:1	L	0.25	152.0

3. TESTING SET-UP

From each mixture a set of prism beams with size 40×40×160 mm according to ČSN EN 1015-11 [3] was prepared. They were removed from the mold second day and placed in high humidity (over

85%) for 7 days. After that they were stored in laboratory conditions for approximately 200 days in order to reach full carbonation and stabilization of material characteristics [4]. Afterwards beams were divided into smaller specimens with dimensions 18×18×78 mm and in the middle a thin notch reaching 35% of height of the specimen was cut by saw. All dimensions were measured for further calculations. Reduction of specimen's size was chosen in order to achieve a less brittle post-peak response and to better capture the complete load-displacement diagram. Every set contained 10 specimens.

Three-point bending test was performed by means of the MTS Alliance RT/30 machine with controlled displacement of crosshead. The support span was 60 mm. During the test the applied force P and crosshead displacement u were continuously recorded. Moreover, the high resolution pictures of specimens above notch were captured by digital camera with macro lens for control measurement.

From measured data the initial idle branch was removed using software FitData [5] and the tail of load-displacement curve was linearly extrapolated up to P = 0 N with corresponding displacement u_0. The work W_f of external force P was calculated as:

$$W_f = \int_0^{u_0} P du \tag{2}$$

and the fracture energy G_f in ligament was calculated:

$$G_f = \frac{W_f}{A_{lig}} = \frac{W_f}{b(a - a_0)} \tag{3}$$

where A_{lig} is cross-sectional area of ligament, b is width of specimen, a is height of specimen and a_0 is depth of notch. In comparison to the RILEM recommendation [6] the effect of self-weight of specimen was neglected. Typical load-displacement diagrams (set 10) are shown in Figure 1. Calculated fracture energy G_f of all sets is shown in Figure 2.

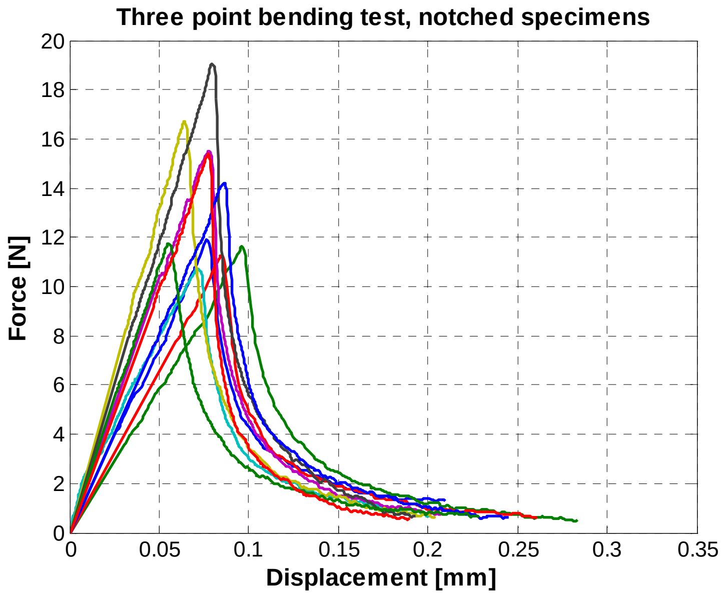

Fig. 1 Load-displacement diagrams from three-point bending test with notched specimens (set 10)

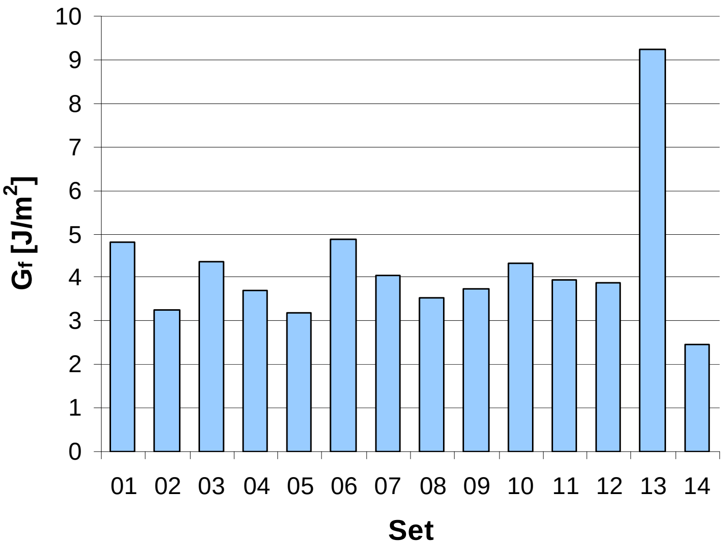

Fig. 2 Calculated fracture energy G_f

4. NUMERICAL SIMULATIONS

Young's modulus of elasticity E_m, tensile strength f_t and bilinear shape of cohesive law were determined using methodology described in [1]. The model of every set of specimens with corresponding geometry and boundary conditions was created in software Atena [7]. Young's modulus of elasticity E_m was evaluated based on comparison between initial elastic branch of load-displacement diagram from calculation with estimated modulus (1000 MPa) and average from experimental data.

Identification of tensile strength f_t and assumed bilinear shape of cohesive traction-separation law, described by three parameters δ_2, pY, pX (Figure 3), could not be done directly from experimental data.

Therefore, a kind of inverse analysis was used. Several numerical simulations with various combinations of these parameters were performed and the combination, which resulted in the best fit of the calculated load-displacement curve to the experimentally measured response, was chosen. As the criterion, square root of the sum of squares of normalized coordinates of peak of load-displacement diagram (P_{max}, u_{max}) and normalized work of external load P necessary to attain the displacement $2 \times u_{max}$ (to reduce inaccuracies of extrapolation) was used. The parameter combinations for individual simulations were determined as follows. For each parameter, a "reasonable" range was selected (Tab. 2). The bounds were constant for all parameters, except for the maximum value of tensile strength, which was varied so that the average value of fracture energy of cohesive law corresponded to the value from experiment. Rectangular statistical distribution was assumed for all parameters and their values used in the individual simulations were determined by the Latin Hypercube Sampling (LHS) method in software FREET [8]. The same permutation matrix, which determines distribution of parameters into individual simulations, was used for all sets. No correlation among the parameters was assumed.

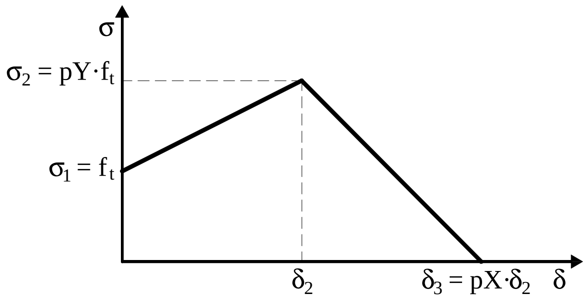

Fig. 3 Assumed bilinear shape of cohesive traction-separation law

Tab. 2 The limits of rectangular distributions of random parameters. Superscript [13] indicates set 13 with metakaolin.

	f_t [MPa]	δ_2 [mm]	pX [-]	pY [-]
Minimum	0.2 (0.5[13])	0.0001	1	0.8
Maximum	0.50÷0.85 (1.5[13])	0.0003	2	2

5. RESULTS AND DISCUSSION

Figure 4 shows the dependence of material characteristics on the water ratio with respect to the ratio of individual types of filler (the binder:filler ratio is in case same and is equal to 1:2), figure 5 shows dependence on binder:filler ratio with respect to the water ratio (ratio of individual types of filler is same) and figure 6 shows dependence on matrix type (lime, lime-metakaolin).

We can see that calculated fracture energy G_f from experiments decreases with increasing water ratio (except for water ratio 0.24 for ST2:STJ25 = 0:1), decreases with increasing ratio between filler and binder and is significantly higher for lime-metakaolin matrix than for pure lime matrix. In the case of Young's modulus of elasticity E_m and tensile strength f_t the tendencies seem to be similar, but they are not so clear. The results are consistent with the notion that a larger amount of water leads to higher porosity of the hardened mortar, which leads to a reduction of tensile strength and Young's modulus of elasticity (effective values, calculated over a larger volume of material). On the other hand, it can be expected that a larger amount of binder in the mortar leads to higher parameters, because individual grains of filler are more strongly bonded together.

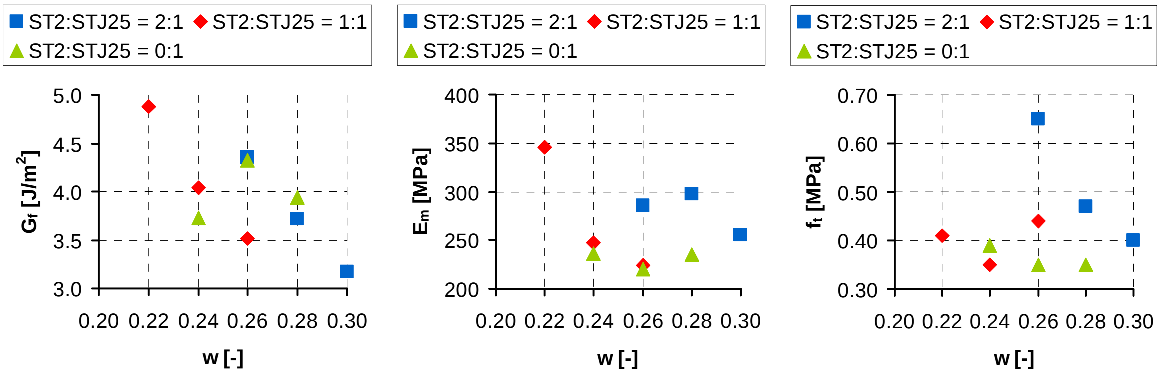

Fig. 4 The dependence of the material characteristics on the water ratio

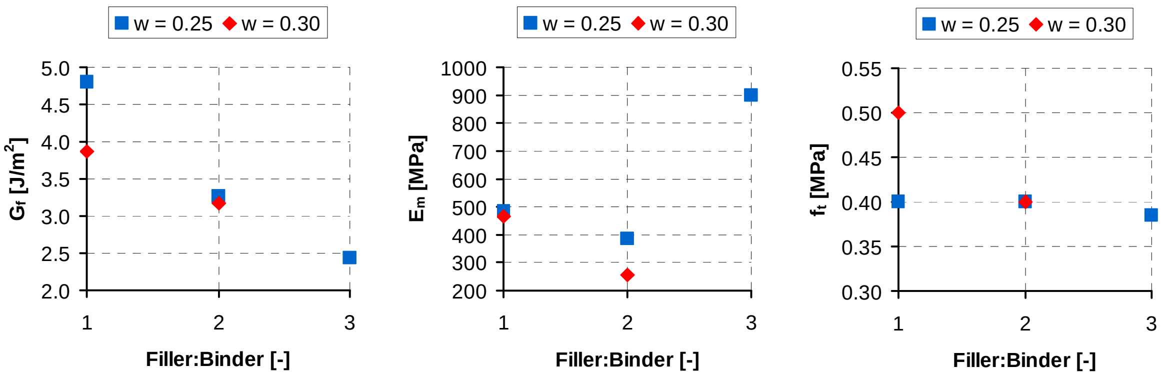

Fig. 5 The dependence of the material characteristics on the binder:filler ratio

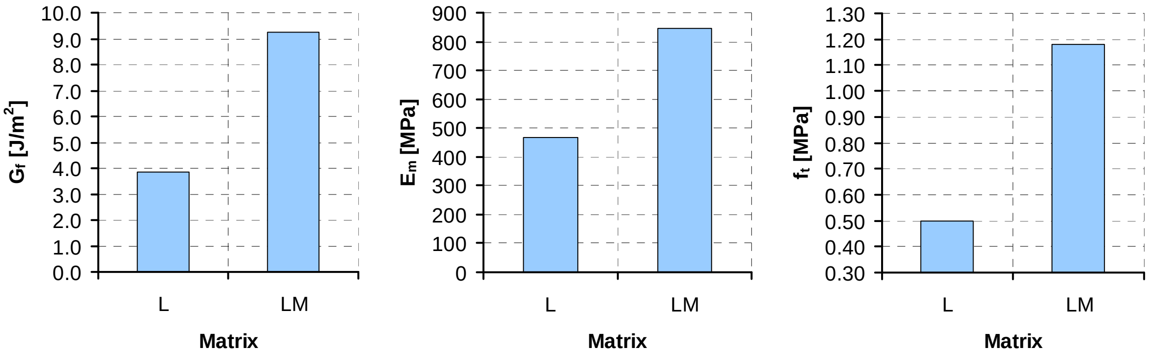

Fig. 6 The dependence of the material characteristics on matrix type (L – lime, LM - lime-metakaolin)

6. CONCLUSION

The results of this study show the dependence of tensile and fracture characteristics of lime mortar on composition of the mixture. According to the results we can conclude that larger amount of water and filler in the mixture leads to lower fracture energy, Young's modulus of elasticity and tensile strength. Replacement of a part of lime by metakaolin leads to noticeable improvement of these parameters.

It should be noted that evaluated tensile strength and cohesive law are approximate and correspond to the simulation with the best conformity with the experimental data. The accuracy depends on the number of simulations for each set (in our case it was 20). To reduce the scatter of the inaccuracy we used the same permutation matrix for all sets. This inaccuracy should be reduced also by higher number of simulations, however this method would lead to greater time requirements.

ACKNOWLEDGEMENT

Financial support of the Czech Technical University in Prague under project SGS13/034/OHK1/1T/11 is gratefully acknowledged.

REFERENCES

[1] PŘINOSIL, M., KABELE, P. Three point-bending test on notched beams. In: PLACHÝ, T. a kol, eds. *Proceedings of the Conference Nano & Macro Mechanics 2012*. Praha: ČVUT v Praze, Fakulta stavební, 2012, pp. 187-194. ISBN 978-80-01-05097-2.

[2] ČSN EN 1015-3. *Zkušební metody malt pro zdivo - Část 3: Stanovení konzistence čerstvé malty (s použitím střásacího stolku)*. Praha: Úřad pro technickou normalizaci, metrologii a státní zkušebnictví, 2000. 12 p.

[3] ČSN EN 1015-11. *Zkušební metody malt pro zdivo - Část 11: Stanovení pevnosti zatvrdlých malt v tahu za ohybu a v tlaku*. Praha: Úřad pro technickou normalizaci, metrologii a státní zkušebnictví, 2000. 16 p.

[4] IZAGUIRRE, A., LANAS, J., ALVAREZ, J.I. Effect of a polypropylene fibre on the behaviour of aerial-lime-based mortars. *Construction and Building Materials*. 2011, **25**(2), pp. 992-1000. ISSN 0950-0618.

[5] PŘINOSIL, M. *FitData: User's manual*. 2012 [online]. [cited 2013-07-22]. Available from: http://mech.fsv.cvut.cz/~prinosil/ index.php?id=FitData.

[6] RILEM Technical Committee 50 (Draft Recommendation). Determination of the fracture energy of mortar and concrete by means of three-point bend tests on notched beams. *Materials and Structures*. 1985, **18**(4), pp. 287-290. ISSN 1359-5997.

[7] ČERVENKA, V., JENDELE, L., ČERVENKA, J. ATENA *Program Documentation, Part 1: Theory*. Červenka Consulting, 2012.

[8] NOVÁK, D., et. al. *FREET Program Documentation, Part 1: Theory*. 2002.

LOCALIZATION ANALYSIS OF A DISCRETE ELEMENT PERIODIC CELL

Jan STRÁNSKÝ[1], **Milan JIRÁSEK**[2]

Abstract: *In this contribution, a strain localization measure for discrete element (DEM) cell with periodic boundary conditions is introduced. This measure is further compared with different localization criteria, namely the second order work criterion and localization (acoustic) tensor criterion. The very simple cases of uniaxial tension and shear are investigated.*

Keywords: *Localization, DEM, Periodic boundary conditions, Second order work, Localization tensor*

1. INTRODUCTION

Consider an elastic homogeneous material subjected to homogeneous deformation defined by deformation gradient $\mathbf{F}$. According to the Cauchy-Born hypothesis [1], new position $\mathbf{x}^{CB}$ of each material point $\mathbf{X}$ would be determined by relation

$$\mathbf{x}^{CB} = \mathbf{F} \cdot \mathbf{X}. \tag{1}$$

Indeed, in the elastic range, the deformed configuration of bonded (or cohesive) particle models more or less corresponds to this hypothesis. However, beyond elastic range, the inelastic processes (such as damage) in bonds occur. Firstly throughout the periodic cell, but as the deformation grows, the deformation increments might grow only in one (usually narrow) band. Such scenario is called (inelastic) strain localization [2] and is observed in materials and structures subjected to extreme loading conditions, often prior to their failure or collapse. The onset of localization might serve as an indicator of upcoming instabilities. In this contribution, the localization in a discrete element periodic cell is investigated from different points of view.

In variety of contexts (e.g. material parameters calibration or multiscale simulations), periodic cells are used [3]. Such periodic cell represents a *typical* material micro-structure under locally homogeneous

[1] Ing. Jan Stránský, Faculty of Civil Engineering, Czech Technical University in Prague, jan.stransky@fsv.cvut.cz

[2] Prof. Ing. Milan Jirásek, DrSc., Faculty of Civil Engineering, Czech Technical University in Prague, milan.jirasek@fsv.cvut.cz

deformation. In the surrounding, such cell can be virtually copied, including kinematic information about in-cell displacements and deformation gradient $\mathbf{F}$ of the cell itself, resulting in the deformation homogenity.

In the situations mentioned above, the periodic boundary conditions are usually preferable over kinematic or static boundary conditions, minimizing negative boundary effects. However, in the case of strain localization, the periodicity enforces the direction of localization, what might be non-physical. The localized inelastic strain (typically a crack) might furthermore break the assumption of microstructural representativity of the periodic cell's content. This fact is another reason why the strain localization is addressed.

Firstly, the investigated problem is described in the section 2, the new localization measure together with different localization criteria are introduced in the section 3 and simulation description and results are given in the sections 4 and 5, respectively.

2. PROBLEM DESCRIPTION

For this study, we chose a very simple model setting — random dense [4] periodic assembly of spherical particles with uniform radius r_p (see Fig. 1) and lattice-like constitutive contact model (i.e. bonds can only transmit normal forces). The contact law is elasto-damage with exponential softening in tension and elastic (with constant modulus regardless damage) in compression, see figure 1. To

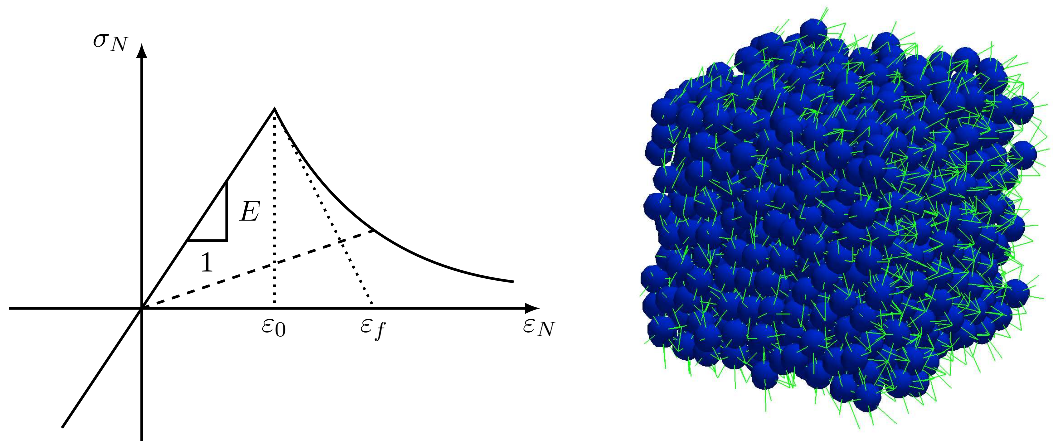

Fig. 1 Constitutive contact law (left) and periodic particle assembly (right)

guarantee linear elastic behavior around undeformed configuration, cohesive bonds are created not only between particles in touch, but also between pairs of particles, whose center distance d is less than defined value

$$d < 2I_r r_p. \tag{2}$$

I_r is so called interaction ratio and plays a role of another material parameter. The specific values of model parameters used in our tests are listed in Tab. 1. The problem quasi-static and solved by the discrete element method (DEM).

Tab. 1 Values of used parameters

Parameter	E [GPa]	ε_0 $[-]$	ε_f $[-]$	r_p $[m]$	I_r
Value	25	$1 \cdot 10^{-4}$	$5 \cdot 10^{-4}$	0.05	1.5

3. LOCALIZATION IN PERIODIC DEM CELL

3.1. LOCALIZATION MEASURE

To quantify the strain localization in fixed cubic periodic assembly, we start with relatively intuitive definition of the localization measure m_L as the sum of norms of differences between actual position $\mathbf{x}$ and ideal — in the sense of Cauchy-Born hypothesis (1) — position $\mathbf{x}^{CB}$ of particles

$$m_L = \sum_p |\mathbf{x}_p - \mathbf{x}_p^{CB}|. \tag{3}$$

$|\mathbf{v}| = \sqrt{\mathbf{v} \cdot \mathbf{v}}$ denotes Euclidean vector norm.

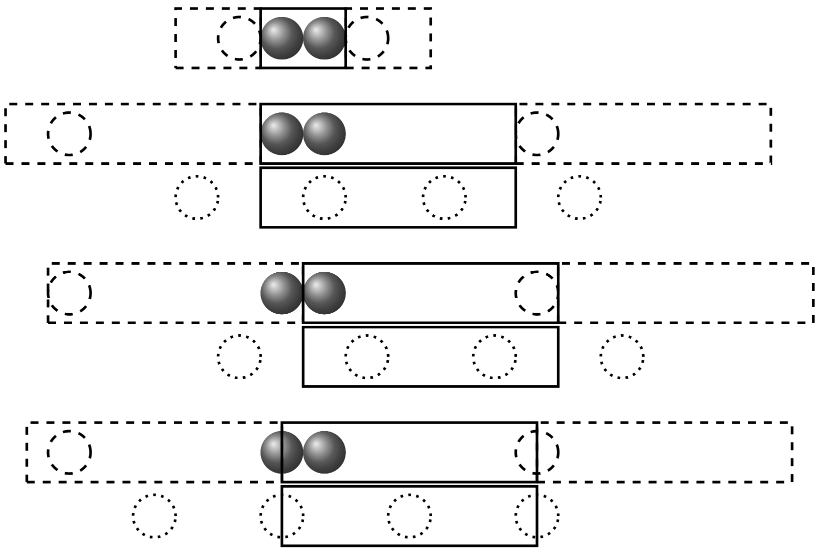

Fig. 2 Localization measure m_L for different positions of periodic cell

However, result of (3) depends on the position of periodic cell. This fact is illustrated in Fig. 2. In grey color are real particles, rectangles represent periodic cells (dashed one the periodic image), dashed circles periodic images of real particles and finally dotted circles (in second line) represents ideal position of particles. The first line is undeformed configuration, the other lines represent strained cell for different cell position.

It is clearly visible, that the sum of distances between actual and ideal positions is higher in the first case than in the second and the third one. In fact, because of the form of m_L and the extreme simplicity, its minimum (as a function of the shift) is closed interval and the second and third third line are examples of such minimum, while the first line shows non-minimal (although natural first choice) shift of the cell.

Therefore we define such shift $\mathbf{s}$ of the cell to minimize the measure m_L:

$$m_L = \sum_p |(\mathbf{x}_p + \mathbf{s}) - \mathbf{F} \cdot (\mathbf{X} + \mathbf{s})| = \sum_p |\mathbf{x}_p - \mathbf{x}_p^{CB} + (\mathbf{I} - \mathbf{F}) \cdot \mathbf{s})| \;\rightarrow\; \min. \tag{4}$$

Vector $\mathbf{s}$ is solved iteratively by standard Newton optimization

$$\mathbf{s}_{n+1} = \mathbf{s}_n - \mathbf{H}^{-1}(\mathbf{s}_n) \cdot \mathbf{g}(\mathbf{s}_n) \tag{5}$$

with $\mathbf{g}(\mathbf{s})$ and $\mathbf{H}(\mathbf{s})$ being gradient vector and Hessian second order tensor, respectively, of the measure m_L:

$$[\mathbf{g}(\mathbf{s})]_i = \frac{\partial m_L(\mathbf{s})}{\partial s_i}, \quad [\mathbf{H}(\mathbf{s})]_{ij} = \frac{\partial^2 m_L(\mathbf{s})}{\partial s_i \partial s_j} \tag{6}$$

3.2. SECOND ORDER WORK CRITERION

The second order work W_2 is related to the second order time derivative of kinetic energy. More specifically, negative second order work would lead to the increase of kinetic energy (what is typical case of bifurcation, e.g. loss of stability or crack propagation), thus $W_2 \leq 0$ is widely considered as a bifurcation condition. See e.g. [5] for more details.

The second order work of a periodic cell takes (continuous and discrete) form

$$W_2 = \int_V \delta\boldsymbol{\sigma} : \delta\boldsymbol{\varepsilon} \, \mathrm{d}V = \sum_b \delta\mathbf{l}_b \cdot \delta\mathbf{f}_b. \tag{7}$$

3.3. ACOUSTIC TENSOR CRITERION

Another localization criterion is based on tangent stiffness tensor and localization tensor. The fourth order tangent stiffness tensor is defined as

$$\mathbb{D} = \frac{\partial \boldsymbol{\sigma}}{\partial \boldsymbol{\varepsilon}}. \tag{8}$$

The criterion assumes that localization starts when the determinant of the localization tensor

$$Q = \mathbf{n} \cdot \mathbb{D} \cdot \mathbf{n} \tag{9}$$

vanishes, i.e. $\det Q = 0$. $\mathbf{n}$ is (apriori unknown) unit vector perpendicular to the direction of localized zone. See e.g. [2] for more details.

4. SIMULATIONS

The concepts described in previous sections were tested on discrete element numerical simulations using open source software YADE [6].

Although YADE (and DEM in general) solves explicitly the dynamic equation of motion, it is possible to run quasi-static simulations. To achieve this, the strain rate of the periodic cell was "small" and, more importantly, after certain number of steps the simulation was calmed to quasi-static case. By this term we mean a loop, in which until quasi-static condition was fulfilled, certain number (20 in our tests) of iteration were run normally and then linear and angular velocity of all particles were set to zero. The condition to break the loop and consider the state as quasi-static was that the relative unbalanced force $r = \overline{|\mathbf{f}_u|} \,/\, \overline{f_b} < \varepsilon$, ratio of mean unbalanced force $\overline{|\mathbf{f}_u|}$ (average norm of forces acting on particles) and mean bond normal force $\overline{f_b}$, is less than defined limit ε ($\varepsilon = 1 \cdot 10^{-6}$ in our tests). Numerical damping was introduced to help remove kinetic energy from the system.

For the tangent stiffness and the second order work, additional computation of the stresses for strains outside predefined loading path is needed. The stress is therefore evaluated in separate simulations not to devalue the original one. In all cases, the original simulation is saved, then predefined strain is applied, simulation is calmed to quasi-static case (in the same way as in the previous paragraphs), stress is evaluated using standard Love-Weber formula [7]

$$\boldsymbol{\sigma} = \frac{1}{V} \sum_b \mathbf{l}_b \otimes \mathbf{f}_b \tag{10}$$

and original simulation is reloaded.

The tangent stiffness tensor (8) was estimated using the central difference scheme

$$D_{ijkl}(\boldsymbol{\varepsilon}) \approx \frac{\sigma_{ij}(\varepsilon_{kl} + \delta) - \sigma_{ij}(\varepsilon_{kl} - \delta)}{2\delta}. \tag{11}$$

The second order work (7) was computed simply as

$$W_2(\boldsymbol{\varepsilon}, \Delta\boldsymbol{\varepsilon}) \approx \Delta\boldsymbol{\sigma} : \Delta\boldsymbol{\varepsilon} = [\boldsymbol{\sigma}(\boldsymbol{\varepsilon} + \Delta\boldsymbol{\varepsilon}) - \boldsymbol{\sigma}(\boldsymbol{\varepsilon})] : \Delta\boldsymbol{\varepsilon} \tag{12}$$

with

$$\Delta\boldsymbol{\varepsilon} = \delta \mathbf{m} \otimes \mathbf{n}, \quad |\mathbf{m}| = |\mathbf{n}| = 1 \tag{13}$$

for different directions of $\mathbf{m}$ and $\mathbf{n}$.

For both tangent stiffness (11) and second order work (13), the value $\delta = 10^{-5}$ was applied.

5. RESULTS

5.1. UNIAXIAL TENSION

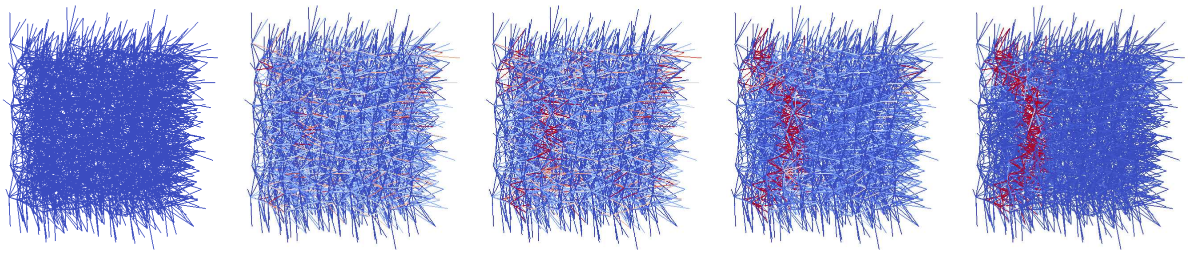

Fig. 3 Different stages of bond strains (uniaxial tension)

In the case of uniaxial tension of periodic cell, we expect the crack to develop perpendicularly to the loading direction. The numerical results meet this expectation. Different stages of bond tensile strains are shown in Fig. 3 and corresponding stress strain diagram and localization measure in Fig. 4.

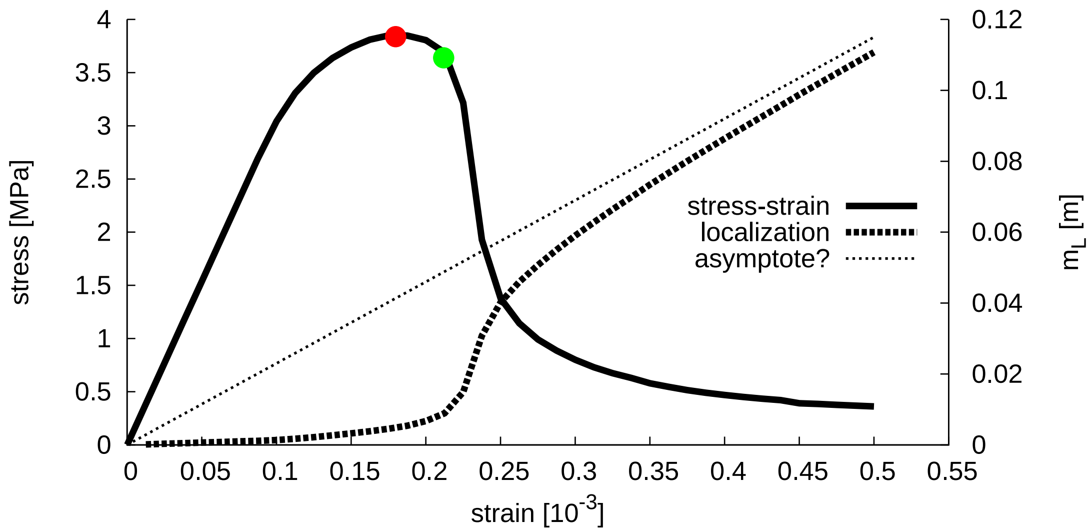

Fig. 4 Stress strain diagram and localization measure for uniaxial tension

The red point denotes the state, where the second order work vanishes, while the green point the point with non-positive determinant of localization tensor. For both criteria, the predicted bifurcation direction was approximately the loading direction. However, because of evaluation in discrete points during loading path, more than one direction fulfilled both criteria. More detailed analysis will be needed to identify exactly the point of criteria fulfillment.

Qualitatively, the localization tensor criterion seems to show better identification of the strain localization onset than the second order work criterion, which simply identifies the peak of stress-strain diagram. The localization tensor analysis also takes much less computational effort — only 12 stress computations for stiffness tensor estimation and then simple tensor calculations in comparison to much more (to sufficiently cover the stress-strain space) stress computations for the second oder work criterion.

5.2. SHEAR

Periodic cell enforces the localization band to be parallel to the cell's faces, or to cross from one corner to the other. The latter case was expected in the shear loading (prescribed one shear strain component while prescribing zero stress for all other degrees of freedom). Again, the simulation results meet our expectations. In analogy to the uniaxial tension case, the second order criterion (red dot) identifies the peak of the stress strain diagram, while localization tensor criterion seems to identify the onset of strain localization. Both criteria also predict the direction of localization approximately with the expected one (inclined 45 degrees) and more detailed analysis will be needed to find exactly the points of criteria fulfillment.

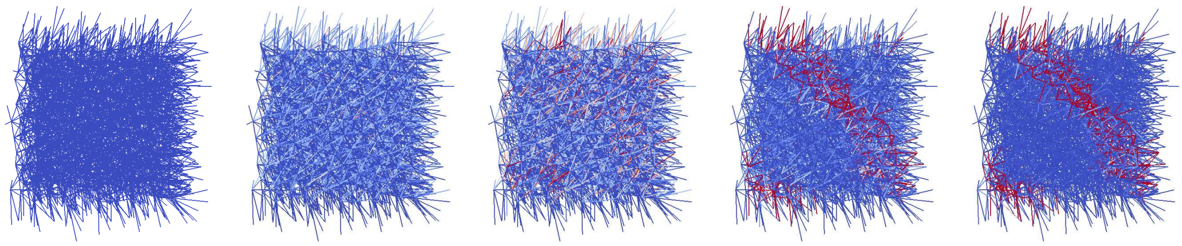

Fig. 5 Different stages of bond strains (shear)

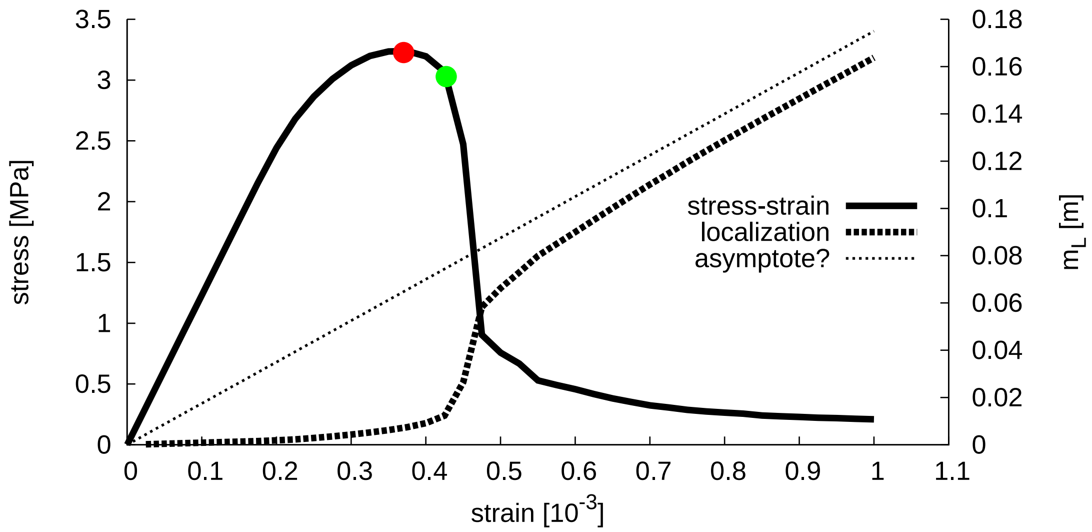

Fig. 6 Stress strain diagram and localization measure for shear

6. CONCLUSION

A new localization measure for discrete element periodic cells was introduced in this contribution. Its disadvantage might be that it is not dimensionless. From the simulation results it seems that for continuing strain increase, the measure has an asymptote, which might help in the normalization process, e.g. the values of normalized measure would be between 0 and 1 (0 for perfectly fulfilled Cauchy-Born hypothesis and 1 for fully localized — i.e. split — state).

Two bifurcation criteria (second order work and localization tensor) were investigated. For studied cases (uniaxial tension and shear), the second order work criterion tends to identify the peak of stress-strain diagram as a bifurcation point, while the localization tensor criterion seems to better identify the strain localization onset. The evaluation of the second order work criterion is computationally much more expensive than the localization tensor criterion.

Future work on this topic may focus on more detailed analysis of presented localization measure (aforementioned normalization and identification of the asymptote, different loading scenarios, non-cubic periodic cells, different sizes of periodic cells, different and non-uniformly sized particle shapes etc.), analysis on rotated periodic cells or more detailed analysis of bifurcation criteria around peak load and localization onset.

ACKNOWLEDGEMENT

The financial support of this research by the Czech Technical University in Prague (SGS project No. 13/034/OHK1/1T/11) is gratefully acknowledged.

REFERENCES

[1] FRIESECKE, F. and THEIL, F. Validity and Failure of the Cauchy-Born Hypothesis in a Two-Dimensional Mass-Spring Lattice *Journalon Nonlinear Science* 2002, **12**(5), 445-478. ISSN 0938-8974.

[2] JIRÁSEK, M. Mathematical analysis of strain localization *Revue européenne de génie civil.* 2007, **11**, 977-991.

[3] STRÁNSKÝ, J. and JIRÁSEK, M. Calibration of particle-based models using cells with periodic boundary conditions In: *II International Conference on Particle-based Methods - Fundamentals and Applications* Barcelona. ISBN 978-84-89925-69-4.

[4] TORQUATO, S. and TRUSKETT, T. M. Is Random Close Packing of Spheres Well Defined? *Physical Review Letters* 2000, **84**(10), 2064-2067.

[5] NICOT, F., HADDA, N. and DARVE, F. Second-order work analysis for granular materials using a multiscale approach. *International Journal for Numerical and Analytical Methods in Geomechanics.* [online] February 2013, [cited 2013-07-14]. 2013, Available from: doi:10.1002/nag.2175

[6] ŠMILAUER, V., CATALANO, E., CHAREYRE, B., DOROFEENKO, S., DURIEZ, J., GLADKY, A., KOZICKI, J., MODENESE, C., SCHOLTÈS, L., SIBILLE, L., STRÁNSKÝ, J., and THOENI, K. *Yade Reference Documentation, in Yade Documentation (V. Šmilauer, ed.), The Yade Project, 1st ed.* [online], 2010 [cited 2013-07-13]. Available from: http://yade-dem.org/doc/

[7] STRÁNSKÝ, J. and JIRÁSEK, M. Review on Evaluation of Equivalent Stress Tensor in the Discrete Element Method. In: *Proceedings of the 3rd Conference Nano & Macro Mechanics* Prague: CTU, 2012, pp. 245-252. ISBN 978-80-01-05205-1.

MODAL ANALYSIS AND FORCED VIBRATIONS OF A FOOTBRIDGE DUE TO RUNNING PEDESTRIANS

Vladimír ŠÁNA[1], **Michal POLÁK**[2]

***Abstract**:This paper is focused on modeling of forced vibrations of the footbridge across theOpatovickastreet. Next there are presented the results froma dynamic analysis such as determining effects of two pedestrians, who have been running synchronizedacross the pedestrian bridge. Both of the results are compared with the experiment, which have been carried out.*

***Keywords**:modal analysis, human – bridge interaction, biodynamical human body, forced vibrations*

1. SOLVED STRUCTURE

The footbridge across theOpatovickastreet is placed in the Prague near the underground station Háje. The static model of a load bearing structure is the simply supported beam with the span 25.1m. Width of the bridge deck is 6 m.The cross section is a composite structure with a reinforced concrete deck and 6 steel girders.

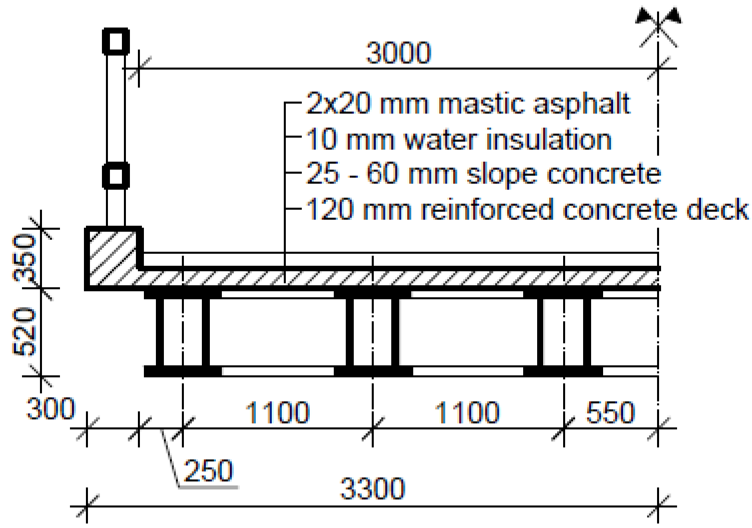

Fig.1 Cross section of the bridge structure

[1] Ing.VladimírŠána,Department of the Mechanics, Czech Technical University in the Prague, vladimir.sana@fsv.cvut.cz

[2]prof. Ing. Michal Polák, CSc , Department of the Mechanics, Czech Technical University in the Prague, polak@fsv.cvut.cz

2. THEORETICAL MODAL ANALYSIS

The purpose of a theoretical modal analysis is determination the basic dynamical characteristics of the structure. It means that we obtained natural frequencies and natural modes of vibrations. The system of the second order simultaneous differential equations in matrix form could by written as:

$$[\boldsymbol{M}]\{\ddot{\boldsymbol{w}}\}+[\boldsymbol{K}]\{\boldsymbol{w}\}=\{\boldsymbol{0}\} \qquad (1)$$

where $[\boldsymbol{M}]$ is the mass matrix and $[\boldsymbol{K}]$ is the stiffness matrix of the structure, $\{\ddot{\boldsymbol{w}}\},\{\dot{\boldsymbol{w}}\},\{\boldsymbol{w}\}$ are vectors of acceleration, velocity and displacement. Parameters for a numerical solution: bending stiffness $EI = 3.83 \cdot 10^9\, Nm^2$, continuous mass per unit length $\mu = 5.3t/m$, the span of the structure $L = 25.1m$. The bending stiffness is used for the dynamical analysis of a beam model, solved according to *MATLAB* code.

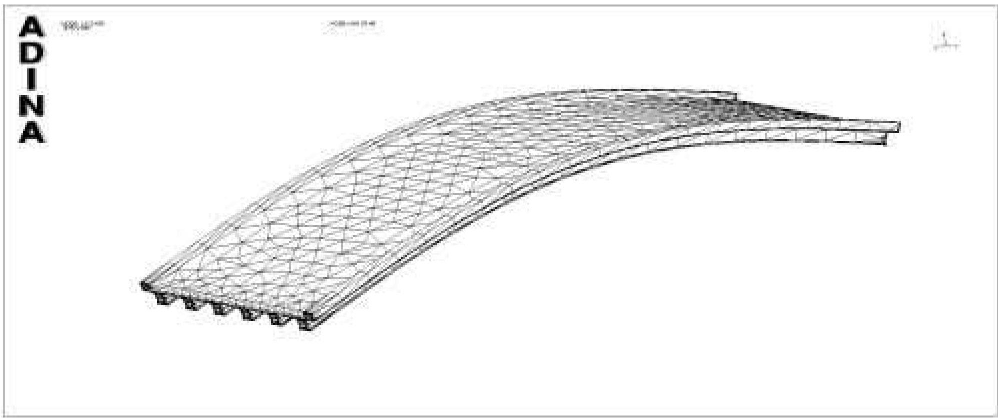

Fig.2The first natural mode of vibration

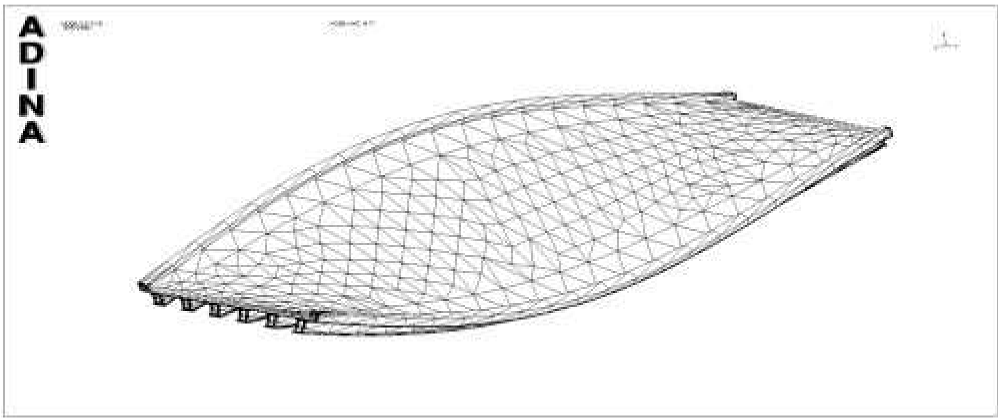

Fig.3The second natural mode of vibration

The natural frequencies were evaluated in ADINA software (developed by Dr. K. J. Bathe), where the spacecomputational model of structure was created.The space computational model was created due to determination of the bending and torsional natural shapes and frequencies of vibration. A *MATLAB* code, which is able to compute only bending frequencies and bending modes ofa vibration, was written for comparing the model. It computesthese parameters in addiction to decomposition to the natural modes of vibrations.

Tab. 1 Summary of natural frequencies

Analysis/frequency	$f_{(1)}$ [Hz]	$f_{(2)}$ [Hz]	$f_{(3)}$ [Hz]	$f_{(4)}$ [Hz]
Numerical analysis (ADINA)	2.466	5.131	9.735	13.180
Beam model *MATLAB* code	2.137	-	8.560	-
Experiment [6]	2.75	5.09	9.28	12.38

3. FORCED AND DAMPED VIBRATIONS

Forced vibrations of structures are described by second order simultaneous system of equations, which are expressed in matrix form

$$[\boldsymbol{M}]\{\ddot{\boldsymbol{w}}\}+[\boldsymbol{C}]\{\dot{\boldsymbol{w}}\}+[\boldsymbol{K}]\{\boldsymbol{w}\}=\{\boldsymbol{F}\}, \tag{2}$$

where $[\boldsymbol{M}]$ is the mass matrix, $[\boldsymbol{C}]$ is the damping matrix and $[\boldsymbol{K}]$ is the stiffness matrix of the structure, $\{\ddot{\boldsymbol{w}}\},\{\dot{\boldsymbol{w}}\},\{\boldsymbol{w}\}$ are vectors of acceleration, velocity and displacement and $\{\boldsymbol{F}\}$ is the loading vector of the forces acting in a time domain.

Note, that damping, which is considered in this paper, is estimated as Rayleigh damping, where damping matrix is expressed as linear combination of mass and stiffness matrices $[\boldsymbol{C}]=\alpha[\boldsymbol{M}]+\beta[\boldsymbol{K}]$. In according to assumption, that the first natural mode of vibration is damped least, we are able to determine coefficients of linear combination

$$\alpha=\xi_1\omega_1\ \beta=\frac{\xi_1}{\omega_1}, \tag{3}$$

where ξ_1 is the damping ratio of the first mode of vibration and ω_1 is the first circular natural frequency. The other way, how to model a structural damping is to consider hysteretic damping instead of Rayleigh damping. It means that a damping force is proportional to an elastic force and it is in the phase with the velocity of a system. For this way of damping we have to use a complex analysis.

Solution of the system of equations (2) is carried out by theNewmark'sβ integration method. This approach is suitable for the second order differential equation with constant coefficients.If we choose suitable parameters of Newmark's method it will be the unconditionally stable method.

Structural parameters for numerical solution of forced, damped vibrations: bending stiffness $EI = 3.83 \cdot 10^9\, Nm^2$, continuous mass per unit length $\mu = 5.3\, t/m$, span of the structure $L = 25.1 m$, logarithmic damping decrement (find out from experiment) $\vartheta = 0.088$. For expressing thedamping ratio we could use a relation

$$\xi = \sqrt{\frac{1}{1+\left(\frac{2\pi}{\vartheta}\right)^2}} \tag{4}$$

Coefficients of linear combination for Rayleigh damping are expressed from relations (3) and their values are $\alpha = 0.1851$ and $\beta = 0.0011$. For low damped structures should be equation (4) expressed as $\xi = \frac{\vartheta}{2\pi}$

3.1. MOVING FORCE OF A CONSTANT MAGNITUDE

The first of models, presented in this paper, to describe forced vibrations caused by pedestrians, is the force with constant magnitude in time domain, which is moving across the footbridge with a constant velocity. It is assumed, that the gravitational force of a pedestrian is increased by a dynamical increment, which express

$$F = m_p g + \frac{1}{\tau}\left(m_p \sqrt{2gh}\right) \tag{5}$$

Expression $\frac{1}{\tau}\left(m_p \sqrt{2gh}\right)$ is derived from assumption that human body during walking is acting as a mass point, which is falling free down to the desk. The velocity at the impact is $v = \sqrt{2gh}$ *(sum of kinetic and potential energy is constantduring an impact)*, quantity of motion than should be written as $p = m_p \sqrt{2gh}$. m_p is a body weight, g the gravityacceleration, τ contact time*(in numerical example it is assumed, that foot is in contact with a structure, during running, 0.25 s)*, h height of a free impact. The contact time depends on the velocity of walking, jogging or running. Time behavior of the function, describing the acting force, is the periodical rectangular impulse, which is acting for time τ.

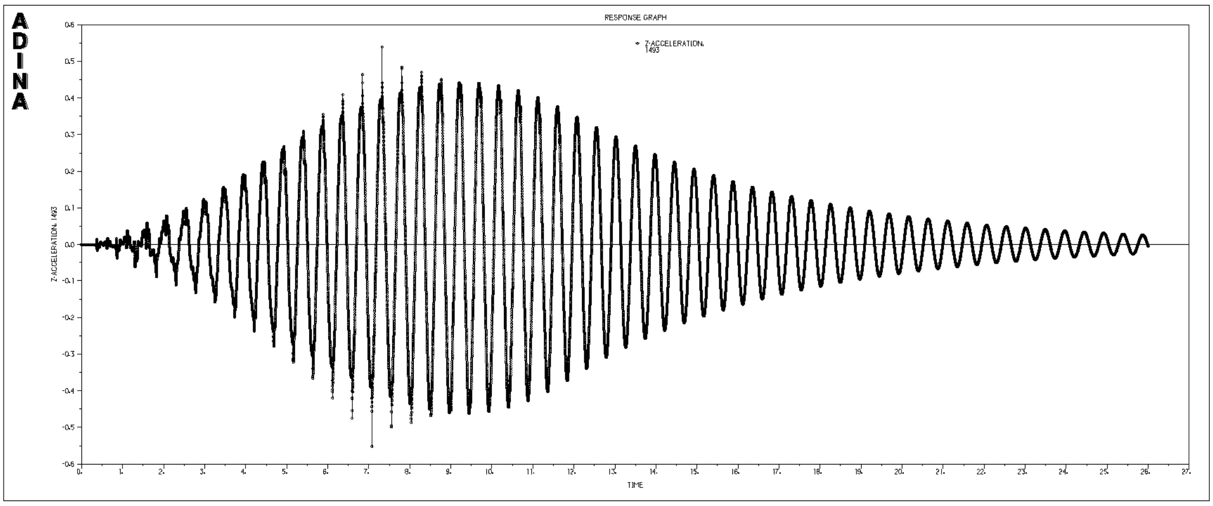

Fig.4 Acceleration of the structure in the center of the span (moving force)

3.2. HARMONICALLY CHANGING FORCE IN TIME

Harmonically changing force in a time domain is placed in the center of the span of the footbridge *(the most effective spot for influence of the vertical motion)*. Structure is modeled as a system with one degree of freedom. Equation for a harmonically changing force is

$$F_{(t)} = \alpha_1 m_p g \sin\left(2\pi f_p t\right) \tag{6}$$

α_1 is the coefficient of Fourier'sseries in [1], [2].

3.3. SIMPLE BIODYNAMICAL MODELS

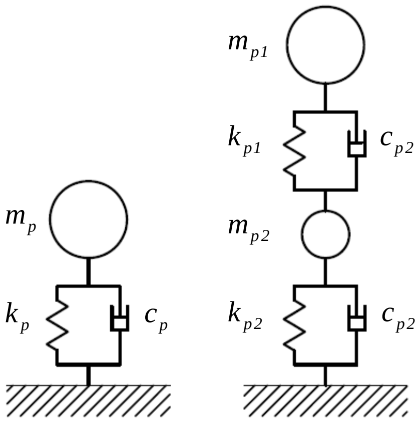

Fig. 5 Biodynamical models of a human body, at the left - SDOF system, at the right - MDOF system[7]

Biodynamical models were applied on the SDOF (single degree of freedom) system, which represents the structure of a footbridge. Harmonic force (6) was applied in the contact point between a model of the human body and the structure, therefore this is the model of a passive pedestrian.

The equations of motion for the SDOF biodynamical model of a human body and the SDOF model of the footbridge

$$\begin{bmatrix} m_p & 0 \\ 0 & m_b \end{bmatrix}\begin{Bmatrix} \ddot{w}_1 \\ \ddot{w}_2 \end{Bmatrix}+\begin{bmatrix} c_p & -c_p \\ -c_p & c_b+c_b \end{bmatrix}\begin{Bmatrix} \dot{w}_1 \\ \dot{w}_2 \end{Bmatrix}+\begin{bmatrix} k_p & -k_p \\ -k_p & k_b+k_b \end{bmatrix}\begin{Bmatrix} w_1 \\ w_2 \end{Bmatrix}=\begin{Bmatrix} 0 \\ P_{(t)} \end{Bmatrix} \tag{7}$$

The equations of motion for the 2 – DOF model of a human body and the SDOF model of the footbridge

$$\begin{bmatrix} m_{p1} & 0 & 0 \\ 0 & m_{p2} & 0 \\ 0 & 0 & m_b \end{bmatrix}\begin{Bmatrix} \ddot{w}_1 \\ \ddot{w}_2 \\ \ddot{w}_3 \end{Bmatrix}+\begin{bmatrix} c_{p1} & -c_{p1} & 0 \\ -c_{p1} & c_{p1}+c_{p2} & -c_{p2} \\ 0 & -c_{p2} & c_{p2}+c_b \end{bmatrix}\begin{Bmatrix} \dot{w}_1 \\ \dot{w}_2 \\ \dot{w}_3 \end{Bmatrix}+\begin{bmatrix} k_{p1} & -k_{p1} & 0 \\ -k_{p1} & k_{p1}+k_{p2} & -k_{p2} \\ 0 & -k_{p2} & k_{p2}+k_b \end{bmatrix}\begin{Bmatrix} w_1 \\ w_2 \\ w_3 \end{Bmatrix}=\begin{Bmatrix} 0 \\ 0 \\ P_{(t)} \end{Bmatrix} \tag{8}$$

These characteristics of biodynamical body models (one person) are used, stiffness coefficients: $k_p = 28.5$ kN/m, $k_{p1} = 62$ kN/m and $k_{p2} = 80$ kN/m. Coefficients of viscous damping: $c_p = 0.95$ kNs/m, $c_{p1} = 14.6$ kNs/m and $c_{p2} = 0.93$ kNs/m.Biodynamical parameters are presented e.g. in [7]

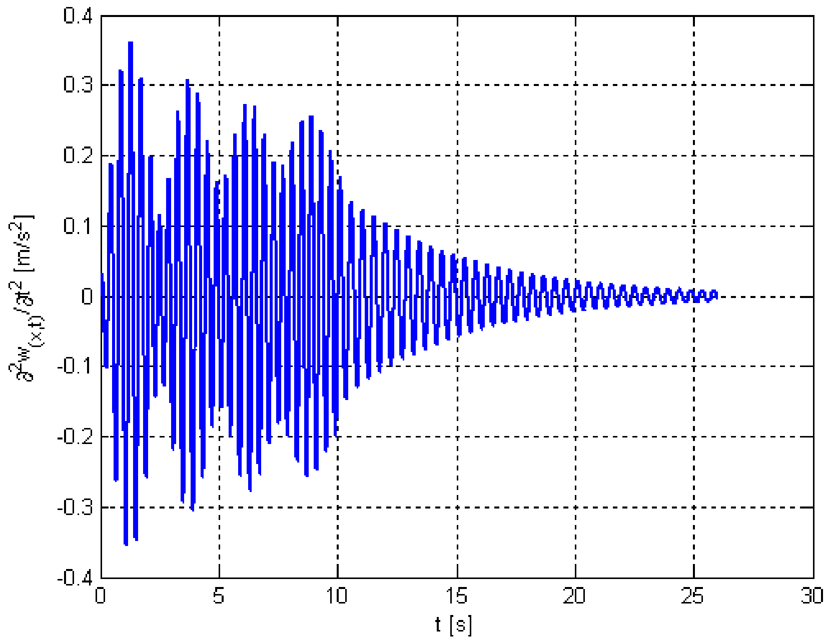

Fig. 6Acceleration of the structure in the center of the span (Biodynamical model SDOF)

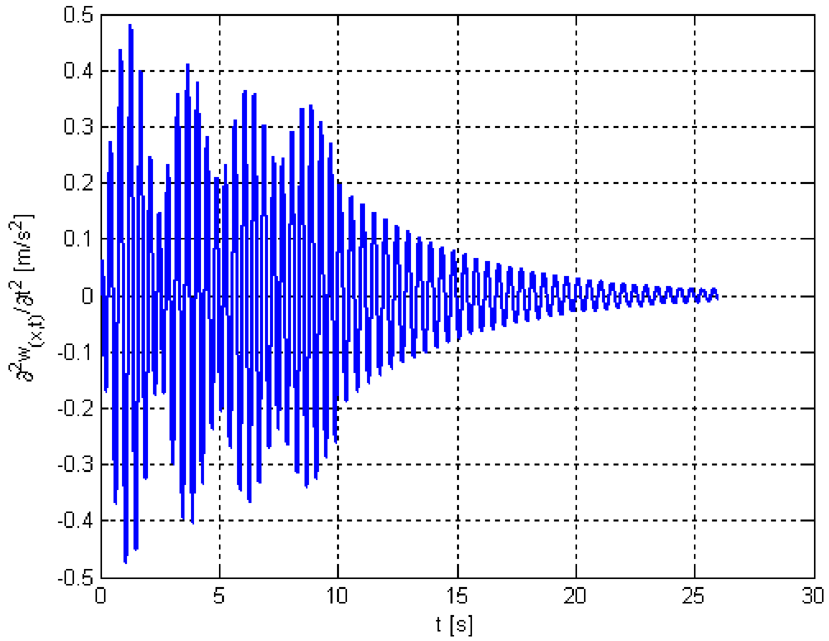

Fig. 7Acceleration of the structure in the center of the span (Biodynamical model MDOF)

Tab. 2 Summary of evaluated accelerations

Acceleration [ms^{-2}] /analysis	Moving force	Harmonic force	SDOF	MDOF	Experiment [6]
Max	0.46	0.413	0.362	0.48	0.38
Min	-0.48	-0.239	-0.354	-0.475	-0.55

The experiment was primary aimed at detection ofthe footbridge acceleration due to walking and running pedestrians. Loading models, which were considered during the experiment: synchronous walking, synchronous running, common service and vandalism.Values in Tab. 2 were measured for loading by two pedestrians, who were running synchronous with pacing frequency $f_p = 2.72$ *Hz*. Secondary, there were found out natural frequencies of vibration.

4. CONCLUSION

In this paper, there were presentedresults from the numerical dynamic analysis of the footbridge across Opatovickastreet, whichwas compared withthe experiment aimed to the modal analysis and forced vibrations. Next, possibilities in modeling of the human – structureinteraction provided by a moving force of a constant magnitude, increased by the dynamic increment, harmonic force, which acts in the center of the span and two biodynamical models,were discussed. The biodynamical models were placed in the center of the span and an excitation force wasrealized in the contact point between the human leg and the structure. This purpose leads to the model of passive pedestrian.

Numerical results were evaluated for running pedestrians with pacing frequency of runf_p *= 2.72 Hz*.

ACKNOWLEDGEMENT

This paper has been created thanks to the project (SGS 12/117/OHK1/2T/11) supported by the Czech Technical University in Prague, which is gratefully acknowledged.

REFERENCES

[1] ŽIVANOVIČ, S., PAVIČ, A. andREYNOLDS, P. Vibration Serviceability of Footbridges under Human-Induced Excitation: A Literature Review.*Journal of Sound and Vibration*, 2005. **279**(1-2), 1-74. ISSN 0022460X

[2] BACHMANN, H. and AMMANN, W. *Vibrations in structures - Induced by man and machines.* Structural engineering documents, International Association for bridge and structural engineering IABSE, Zürich, 1987.165 p. ISBN 3-85748-052-X

[3] Design of footbridges (Background document) (2008): *Human induced vibrations of steel structures.* RFS2-CT-2007-00033.

[4] NEWLAND, D. E. Pedestrian excitation of bridges – recent results.In: *Tenth international congress on sound and vibration*. 2003, published on CD

[5] STUDNIČKOVÁ, M. The effect of Pedestrian Traffic on the Dynamic Behavior of Footbridges.*ActaPolytechnica*.2004, **44**(2), 47-51. ISSN 1210-2709

[6] FANFULOVÁ, E.*Experimental analysis of dynamic response of footbridges*.Prague, 2013. Bachelor thesis. Czech Technical University in Prague. Faculty of Civil Engineering

[7] ARCHBOLD, P., KEOGH, J., CAPRANI, C. and FANNING P. A Parametric Study of Pedestrian Vertical Force Models for Dynamic Analysis of Footbridges.In: *Proceedings of Experimental Vibration Analysis for Civil Engineering Structures*, Varenna, Italy, 3-5 October 2011, pp. 339-346. ISBN 978-88-96225-39-4.

HETEROGENEOUS MATERIAL MODELING VIA DYNAMIC PACKING OF STOCHASTIC WANG TILES

David ŠEDLBAUER[1]

Abstract: *In this contribution we would like to present an algorithm for creation of Wang tiles that are used for heterogeneous cell composing. An artificially formed medium composed of two phases, solid disc particles in the matrix is considered. For clarity, set of eight Wang tiles is taken into account. Every single tile of set will be created via dynamic algorithm simultaneously. This algorithm includes both disc collisions with each other and collisions of discs with ostensible boundaries forming tile edges.Naturally there is need to fulfill boundary conditions of all tiles that come out from tilling essence and from including basic stochastic requirements. Special emphasis will be given to avoid overlapping together with required higher volume fraction.*

Keywords:*stochastic Wang tiling, dynamic model, hard discs, volume fraction*

1. INTRODUCTION

There are several approaches to the modeling of heterogeneous materials[1],[2]. One of the frequently used is a concept of periodic unit cell (PUC)[3], [4]. This concept is based on main central cell surrounded by its nine images that guarantee periodic boundary conditions, Fig 1.With these cells a final medium model is composed.

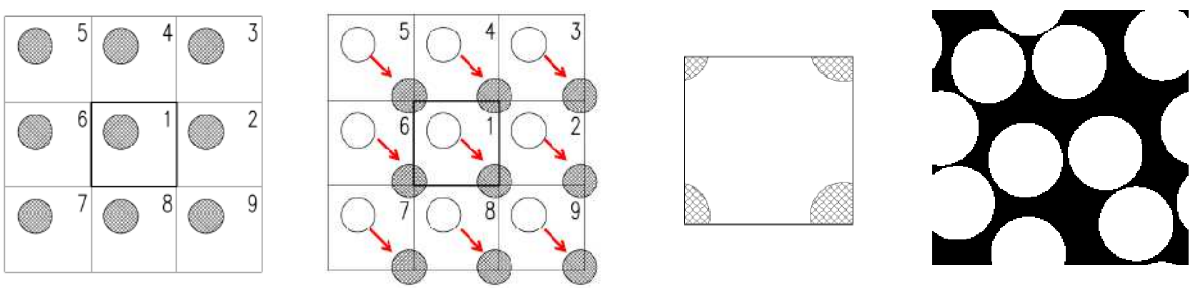

Fig. 1 PUC concept (dynamic modification) and bitmap image of PUC

However, despite the fact that each cell proved the same or similar statistic information, the final model shows a periodicity. This phenomenon is against the required heterogeneity. That is why Wang

[1]Ing. David Šedlbauer, Department of Mechanics, Faculty of Civil Engineering, CTU in Prague, david.sedlbauer@fsv.cvut.cz

tiling method for heterogeneous material modeling has been utilized.Principle of this method is to stack final material with a small set of tiles with the same features, see the following section [5], [6].

For tile generation different approaches can be used. Frequently, optimization algorithms are used with an objective function represented by statistical descriptor describing an important mechanical material property. Most of these properties depend on the distribution of solid particles in the cell. One of the problems that appear during above mentioned tile generation is undesirable overlapping. This phenomenon is usually solved using penalty functions. But these penalties could not wholly guarantee tiles without discs overlapping.

To avoid above problems, the dynamic model for tiles generation will be introduced and tested on sets with higher volume fraction.

2. WANG TILING

Arrangement of the plane with Wang tiles enables to create non-periodic bigger structures with a small set of tiles. Every single tile need not to contain all the information about structure, but the whole set have to. In 2D tiles are usually squares with edges marked by certain characters (colors, letters etc.). Tiles are jointed with edges to ensure compatibility and continuity of all edges. These tiles must not be mirrored or rotated.

In the title of the article there is stochastic Wang tiling. If we want to talk about stochastic tiling it is necessary to ensure that during the stocking there is always a choice of at least two variants, two different tiles. When considering n_h as the number of codes on horizontal edges and n_v as the number of codes on vertical edges, a full set consists of $n_h^2 \cdot n_v^2$ various tiles. For feasibility of tiling it is sufficient that the set of tiles contains one tile for each combination of the top horizontal and left vertical edges with different encodings. With the condition of above mention randomness, the minimum number of tiles is $2 \cdot n_h \cdot n_v$[7].

In the presented work two different edges of both vertical and horizontal borders are used. According to above expression, our set of Wang tiles will consist of eight elements.

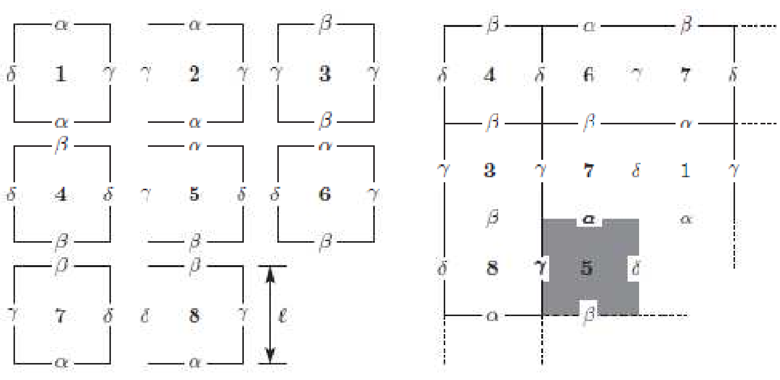

Fig. 2Wang tile set W8/2-2 with codes {α,β,γ,δ} and example of an aperiodic valid tiling [8]

3. DYNAMIC ALGORITHM

Considering the nature of practical problems of heterogeneous materials we assume that we were assigned the required volume fraction V_f and geometric parameters (radii) of solid particles *r*. A tile size should be defined early in the process. Knowledge of the tile size, required volume fraction and given disc dimensions enable us to define the total number of discs in the whole tile set. After that we can establish various volume fractions in every single tile. Based on these tiles' volume fractions we can divide a total number of discs and put its centers into tiles. We will have to pay attention to the dependence of peripheral discs and we must always check whether it is possible to stack discs with given radii into the set of tiles in compliance with given volume fraction [9].

Due to the compatibility conditions at the beginning of the algorithm each single one tile of set is divided into four marginal parts (bounds) and one central part. Width of the border area is dependent on particle radius**,** Fig 3.Therefore, at the end of process all discs belonging to the marginal regions do not interfere in the central area. If we divide each tile, so called dead space for marginal discs always occurs in corners which will affect the movement options and maximal possible number of discs within a tile.

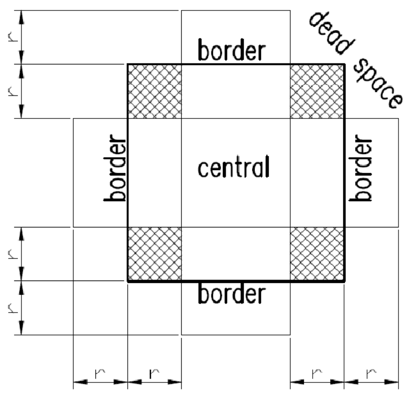

Fig. 3 Divided tile into border and central areas

Next, the number of time steps, during which whole process took place, has to be established. Then a given number of disc centers are semi-randomly thrown into the basic medium – matrix. At the beginning of the process (time step 0) disc radii have zero size. Over time, the radii increase constantly according to the final disc radii and the number of time steps. Next randomness elements in algorithm are initial velocity vectors of each disc (disc centers).

3.1. COLLISIONS

Dynamic phenomenon that occurs during the process is collision. This significantly affects parameters defining particles motion. These collisions are of two types, reflection from the tile edges and rebounds of discs. To ensure proper movement involving boundary conditions of Wang tiles, it is necessary to determine when these phenomena occur.

The earliest time of reflection depends on the current disc position and a velocity vector of each particle.This could be expressed with following equation:

$$\Delta t_e = min\{-dx_{i,ri}/vx_i\,; dx_{i,le}/vx_i\,;\ -dy_{i,lo}/vy_i\,;\ dy_{i,up}/vy_i\}, \quad (2)$$

whereΔt_e is the earliest time of reflection since the previous event or time step, $dx_{i,ri}$, $dx_{i,le}$, $dy_{i,lo}$, $dy_{i,up}$ are distances of disc centre to the borders of appropriate area (marginal, center). Velocities of the *i-th* disc in x and y directions are labeled with vx_i and vy_i respectively.

The earliest time of second type of collision, disc rebounds, can be determined as a time from certain moment until disc centers will be on the distance of their radii. We can define this time with next formulas:

$$(x_j - x_i)^2 + (y_j - y_i)^2 = (r_j + r_i)^2 \quad (3)$$

$$x_i = x_i^t + vx_i^t \cdot \Delta\, t_c, \quad y_i = y_i^t + vy_i^t \cdot \Delta\, t_c, \quad r_i = r_i^t + dr \cdot \Delta\, t_c \quad (4)(5)(6)$$

$$x_j = x_j^t + vx_j^t \cdot \Delta\, t_c, \quad y_j = y_j^t + vy_j^t \cdot \Delta\, t_c, \ r_j = r_j^t + dr \cdot \Delta\, t_c\,, \quad (7)\,(8)\,(9)$$

where$x_i,\ y_i,\ x_j,\ y_j$ arecollision disc coordinates, $x_i^t,\ y_i^t,\ x_j^t,\ y_j^t$disc coordinates $vx_i^t,\ vy_i^t,\ vx_j^t,\ vy_j^t$ disc velocities at time *t*;$r_i, r_j, r_i^t, r_j^t$are collision discs radii and at time *t* respectively. Increasing of disc radii over the time is represents variable dr and $\Delta\, t_c$ is time elapsed since time *t*. Next collision time is in this case designated as minimum of real positive roots of equation 3.

4. TESTING

For the first tests that should confirm the ability to generate Wang tiles with presented dynamic algorithm we set gradually volume fraction of whole set from 0.6 to 0.8. Another premise is that there will be only one disc in marginal area. For 8 tiles we receive 4 complete discs within tiles, Fig. 4.

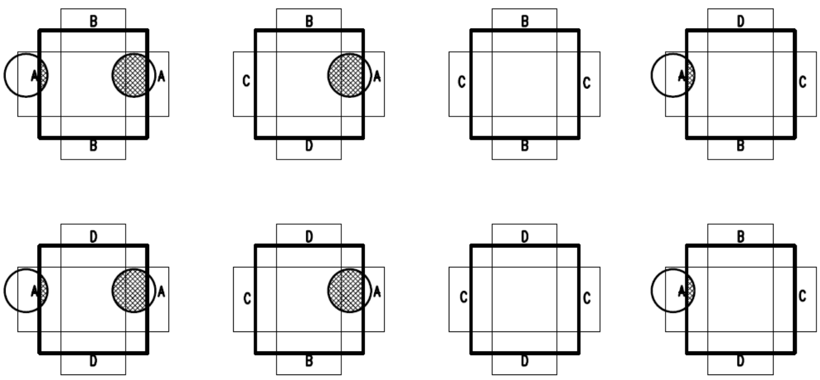

Fig. 4 Tiles with one border disc

We will also take into account that in central areas of all tiles there will be the same number of discs. If we want to make effective Wang tiling, it is desirable to have a set of tiles with a small number of discs. Considering above mentioned fact we set input parameters as follows: a radius of each tile has 25 and the size of a tile is 200 units (pixels). Number of discs in central tile areas should be set using equation 10, i.e.

$$\frac{V_f \cdot h^2}{\pi \cdot r^2} - 0{,}5 = n_c \qquad (10)$$

whereV_f is volume fraction, h is the size of one tile, r is the final radius of each disc and n_c is the number of discs in the central area. It is obvious that the above formula does not guarantee the number of discs as an integer. In this case we rounded thisnumber up to reach the required volume fraction. It would also be possible to recalculate tile sizes but to get task more difficult for generation it will still be constant.The number of time steps during which moving discs are growing was set to 50.

Main task of testing is to try dynamic algorithm for generation of tiles with referred parameters. Results can be found in the table below.

Tab. 1 Results of dynamic algorithm for Wang tiles generation

vol. frac.	*no. of cen. discs*	*retries*	success	prog. falls	overlapping
0.5	10	30	30	0	0
0.6	12	30	18	8	4
0.7	14	30	4	6	20

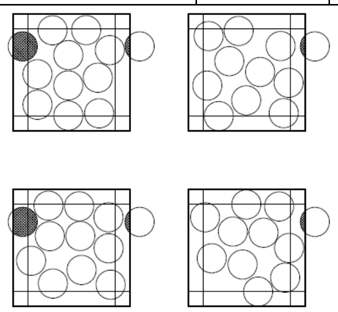

Fig. 5 successfully generated Wang tiles for volume fraction 0.5

5. CONCLUSION

In this papera dynamic algorithm for Wang tile creation was presented. Wang tiling is used to represent heterogeneous materials. This work deals with material consisting of solid discs within a matrix. Compared to PUC principles Wang tiling eliminates undesirable periodicity artifacts. Creation of these tiles is not simple task, especially if we want to have medium with higher volume fraction without overlapping of solid discs. This can be removed with dynamical phenomena such as elastic collisions of discs to each other and discs with borders during movement to final position and growing to final disc radii defined by user.

The results of testing this algorithm with one marginal disc and gradually 10, 12, 14 discs within central area of tiles seem promising. Not in all cases algorithm successfully achieved the desired properties of tiles. The setting of input parameters was sufficient for medium with 0.5 and partially with 0.6 volume fraction. The worst results were shown withthe test with 0.7 volume fraction. The algorithm was unable to stack tiles with discs because of computational complexity and numerical accuracy of the program due to some overlap appears.

In future work it is necessary to entertain an initial setup of the algorithm, especially the ratio of the tile size and the number of discs and the number of time steps. A special issue is the elimination of the dead space within tiles to allow freer disc movement.

ACKNOWLEDGEMENT

This outcome has been achieved with the financial support of the Grant Agency of the Czech Technical University in Prague, grant No. SGS13/034/OHK1/1T/11.

REFERENCES

[1] TORQUATO, S., *Random heterogeneous materials*, New York: Springer-Verlag, 2002, 701 p., ISBN 0-387-95167-9

[2] KOCHEVETS, S., BUCKMASTER, J. and JACKSON, T.L., Random propellant packs and the flames they support, Joint Propulsion Conference and Exhibit, Huntsville, 2000, AIAA 2000-3461

[3] KUMAR, N. Ch., MATOUŠ, K. and GEUBELLE, P.H., Reconstruction of periodic unit cells of multimodal random particulate composites using genetic algorithms, *Computational Materials Science*, 2008, **42**, pp. 352-367, ISSN: 0927-0256

[4] KUČEROVÁ, A., Genetic algorithm-based generation of isotropic equal-sized hard-disk microstructures, In: *The Proceedings of 4th International Conference on Advances in Structural Engineering and Mechanics*, ASEM, 2008, pp. 1583-1593, ISBN: 978-89-89693-21-5

[5] WANG, H. Proving Theorems by Pattern Recognition II. *Bell Systems Technical Journal*. 1961, **40**(2), pp. 1-41

[6] WANG, H., Games, logic and computers. *Scientific American*, 1965, **213**(5), pp. 98-106

[7] COHEN, M. F., SHADE J., HILLER S. and DEUSSEN O., Wang tiles for image and texture generation. *ACM Transactions on Graphics*, 2003, **22**(3), pp. 287-294

[8] NOVÁK, J., KUČEROVÁ, A. and ZEMAN, J. Compressing random microstructures via stochastic Wang tilings. *Physical Review E*, 2012, **86** (4), 040104 [4 pages]

[9] REINHARDT, K. Über die dichteste gitterförmige Lagerung kongruente Bereiche in der Ebene und eine besondere Art konvejer Kurven. *Abh. Math. Sem.*, Hamburg, HansischerUniversität, Hamburg, 1934, 10, pp. 216-230

MECHANICAL PROPERTIES OF MIXTURES WITH CRUSHED SLEEPERS STIFFENED BY SYNTHETIC FIBRES

Karel ŠEPS[1], **Martin LIDMILA**[2]

***Abstract**: The paper deals with utilisation of crushed concrete from railway sleepers in a mixture stiffened by synthetic fibres. The main focus of investigations is determination of mechanical-physical properties of the composite related to hardening and composition of the mixtures. The compressive strength was chosen as the representative mechanical characteristic.*

***Keywords**: crushed concrete, synthetic fibres, compressive strength*

1. INTRODUCTION

Recycling of construction waste is one of priorities of common European development. In general the priority belongs to the category sustainable development within the project Europe 2020 [1]. Positive consequences of recycling are found in several levels. Recycling tributes to a decrease of consumption of prime non-renewable resources and decrease of the amount of waste material that requires dumping.

The main idea presented in the article is utilisation of the crushed concrete from railway sleepers that is stiffened by synthetic fibres. The crushed concrete is used un-sorted in wide size ranges 0/16 and 0/1. The size grade 0/16 serves as a filler; the size grade 0/1 is engaged as a binder. Latent hydraulic properties of fine grounded concrete crush from sleepers are described in [2]. The mixture based on recycled crushed concrete and synthetic fibres can be used as a stiffening layer with properties of improved soil or for stabilisation in structural layers of railway sleeper subsoil.

Basic mechanical-physical properties were determined for the mixture, as compressive strength, bulk density and moisture of hardened mixture. Properties were determined for mixes with different composition after seven days maturing.

[1] Ing. Karel Šeps, Faculty of Civil Engineering, CTU in Prague, karel.seps@fsv.cvut.cz

[2] Ing. Martin Lidmila, Ph.D., Faculty of Civil Engineering, CTU in Prague, martin.lidmila@fsv.cvut.cz

1.1. PRODUCTION OF CRUSHED CONCRETE

The crushed concrete was made from railway sleepers type PB 2 and SB 8. The sleepers were obtained from cancelled precast plant factory siding that took place near the recycling basis of the firm Envistone. The sleepers were crushed in jaw crusher Metso Nordberg LT 105. Reinforcement and fasteners were removed by crushing shears Atlas Copco PB 2100 with span 795 mm before placing the sleeper on the feeding hopper with raft sorting machine. After separation of reinforcement a coarse loose material remained without great portion of metal components. The loose material was crushed by jaw crusher Metso Nordberg LT 105 with electromagnetic separator to take out the remaining metal parts and by belt conveyor poured in sorting machine Powerscreen 600 to sort out parts bigger than sieve size 32 [3]. 3000 kg of concrete crush was produced. With respect to anticipated dimensions of test specimens for laboratory testing a size grade 0/16 was used for elaboration of specimens.

1.2. PRODUCTION OF BINDER FROM CHRUSHED CONCRETE

Based on results of previous research [2] a hypothesis was adopted that crushed concrete from sleepers with grain size 0-125 μm can be used as binder. For that purpose concrete was crushed to size grade 0/1. Sieve grade analysis determined that within this sample is 10 – 15% of size grade 0/0,125. In this procedure binder indicated as BR 0/1 was elaborated.

2. PROPERTIES OF MIXTURES

To verify strength of the recycled concrete with binder and synthetic reinforcement four mixes were prepared. Wide size grade 0/16 was used in all mixes. The synthetic fibres were BeneSteel produced from special blend of polypropylene and polyethylene (fibres are called polymeric steel [4]). Fibres of two length were used (55 mm a 27,5 mm) in the amount 0.5% of volume. The binders were different in each mixture: blended cement CEM II/B-M(S-LL) 32,5R with dosage 130 and 260 kg/m^3 was used (specimens identified R3 and R4), binder from crushed concrete BR 0/1 with dosage 260 kg/m^3 (specimens identified R2) and mixture without binder (specimens identified R1). Water was dosed to reach consistency that can be compacted by stamping. Particular component of mixtures are summarized in Tab. 1. The mixture was prepared in a laboratory mixer with forced circulation (type FILAMOS M 80). Than the mixture was compacted in cylinder moulds (diameter 150 mm and height 120 mm). Compacting was provided by Proctor laboratory machine using methods of standard Proctor compaction test (Fig. 1). The cylinder moulds were put in laboratory and the surface was moistened. After seven days maturing the specimens were demoulded and a compression test was performed. Than samples for determination of moisture in matured mixture were gathered.

Tab. 1 Composition of mixtures

Mixture	Crushed concrete 0/16 [kg/m^3]	Fibres (55+27.5mm) [kg/m^3]	Binder [kg/m^3]	Water [kg/m^3]
R1	1650	2.73+1.82	-	79
R2	1650	2.73+1.82	260(BR 0/1)	113
R3	1650	2.73+1.82	130(CEM II)	93
R4	1650	2.73+1.82	260(CEM II)	113

Fig. 1 Mixing, production and testing of specimen

2.1. TEST RESULTS

Three specimens were made from each mixture. After seven days of maturing specimens were demoulded, measured and weighted. Than compression tests were performed. Deformation of specimens related to load was monitored during the compression tests. An example of the load – deformation curve is in Fig. 2. Compression test results of particular specimens are listed in Tab. 2. Average compression strengths were determined for each mixture recipe. Two samples were taken from each specimen after compression test and moisture of matured mixture was determined; average values are in Fig. 4. Bulk density was calculated from dimensions and weights of particular specimens. Average bulk densities are summarized in a chart (Fig. 5).

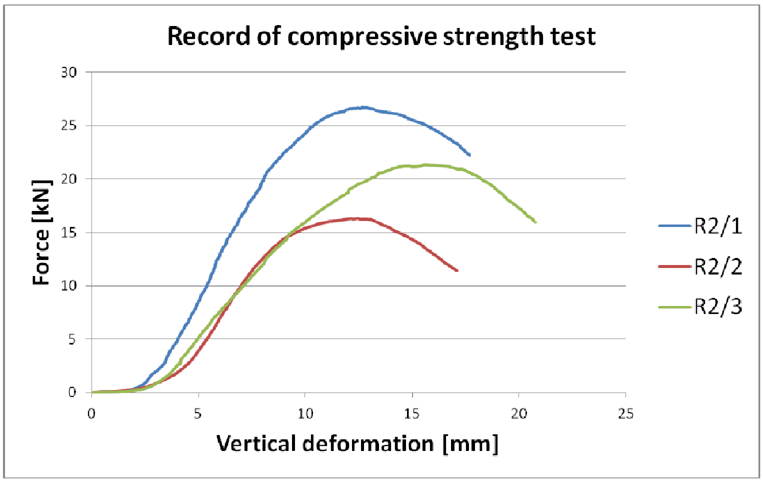

Fig. 2 Load-deformatin diagram for specimens from mixture R2

Tab. 2 Compressive strength of tested specimens after 7 days of hardening

Specimen	R1/1	R1/2	R1/3	R2/1	R2/2	R2/3
Compressive strength [MPa]	0.90	1.03	0.50	1.52	0.92	1.20
Average strength [MPa]	0.81			1.22		
Specimen	R3/1	R3/2	R3/3	R4/1	R4/2	R4/3
Compressive strength [MPa]	6.21	5.75	4.01	14.18	8.74	6.81
Average strength [MPa]	5.33			9.91		

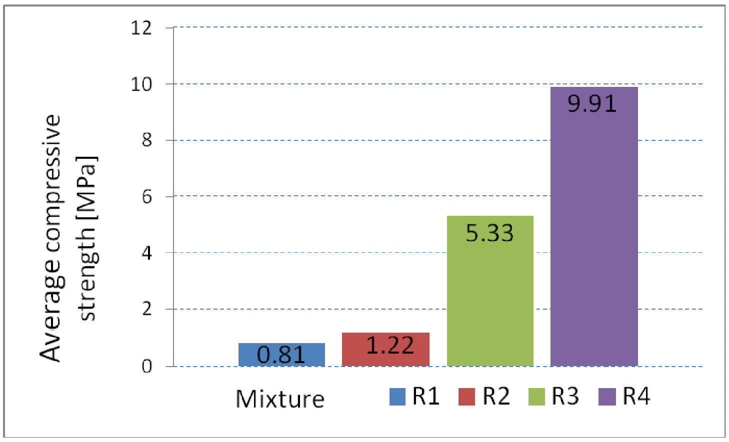

Fig. 3 Comparison of average compressive strength of mixtures

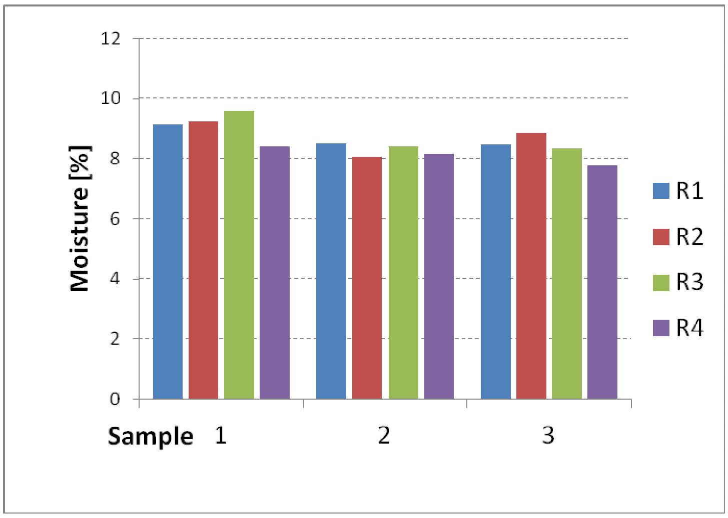

Fig. 4 Average moisture of tested specimens

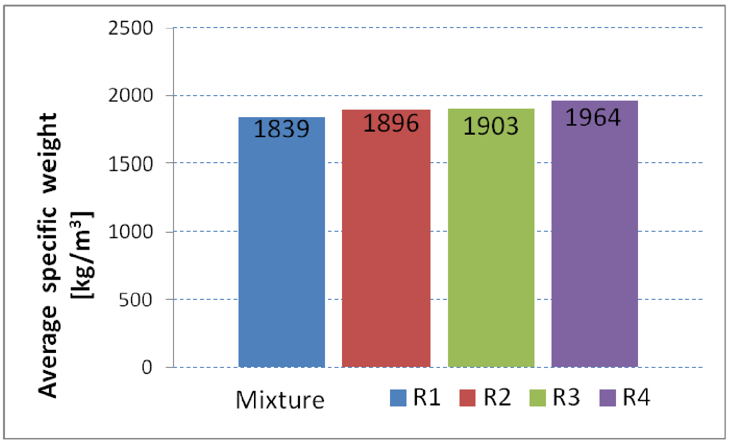

Fig. 5 Average value of specific weight of mixtures

3. CONCLUSION

The paper is concerned the first set of tests where the basic mechanical physical properties were determined only. In the next stage of investigations splitting strength will be determined and flexural strength if appropriate; a full-scale laboratory model will be elaborated where dynamic effects on the composite from crushed concrete and synthetic fibres will be measured.

ACKNOWLEDGEMENT

The experimental work was supported by project TE01020168 Centre for Effective and Sustainable Transport Infrastructure (CESTI) and SGS13/120/OHK1/2T/11.

REFERENCES

[1] *EVROPA 2020*. [cited 2013-07-08]. Available from: http://ec.europa.eu/europe2020/europe-2020-in-a-nutshell/priorities/sustainable-growth/index_cs.htm.

[2] ŠABLATURA, J. *Experimentální ověření recyklátu z betonových pražců v konstrukční vrstvě pražcového podloží*. Praha 2012. Diplomová práce. ČVUT v Praze, Fakulta stavební.

[3] ZOBAL, O., PADEVĚT, P., LIDMILA, M. and TESÁREK, P. Možnosti recyklace betonu. In: *Betonářské dny 2010*. Praha: Česká betonářská společnost ČSSI, 2010, díl 1, pp. 491-494. ISBN 978-80-87158-28-9.

[4] *BeneSteel 55*. [cited 2013-07-08]. Available from: http://www.sklocement.cz/benestcz.htm.

ORTHOTROPY IN FEM

Karel ŠOBRA[1]

***Abstract**: An overview of wood behavior is shown in this article as well as simplifying of a wood material for manual calculations and approaches which are suitable for FEM calculations. Inhomogeneous structure of wood brings many specific problems which need to be considered. Homogenization of wood is suitable for design engineers but not sufficient for research of wood at micro level.*

***Keywords**: wood, orthotropic behavior, wood material models*

1. INTRODUCTION

Wood is one of the oldest building materials. It was used mainly for the roofing in the Middle Ages. Later it began to use in floor construction. One of the oldest, well preserved wood constructions are gothic trusses. Unfortunately nowadays, not a many of trusses are saved because of many fires and other impacts (sponges, pests …).Gothic trusses are all wooden carpentry joints that means that bending elements are also made of wood. In the baroque trusses there can be the iron bending elements.

During the ages historical constructions degrades, in case of this they need to be reconstructed. During the reconstructions, which are in the Czech Republic under supervision of Monument Care Department of Ministry of Culture, originality of elements has to be protected as much as possible. In case of this, in historical trusses, damaged element is not changed as whole, but only the damaged part of an element is cut off and substituted by a new material. For this type of reconstruction contemporary joints are used. The most of contemporary joints are wooden joints [1].

2. MATERIAL

Wood is one of the oldest building materials, as mentioned above. It has many kinds of utilization. Wood can be used for construction of structure or for its parts as floor slabs, roofing etc. It can be used as floor covering, too.

Material behavior was studied on wooden beams or bars in the past [2]. Unfortunately, wood is a material, which has specific problems. Impropriate behavior is eliminated by modifying of wood.

[1] Ing. Karel Šobra, Department of Mechanics, Faculty of Civil Engineering, Czech Technical University in Prague, Thákurova 7; 166 29, Prague 6 – Dejvice; CZ, e-mail: karel.sobra@fsv.cvut.cz

Composition of wood has been modified by chemicals or composite materials are developed as other type of modification.

Wood is an organic material. That means that its composition is hugely dependent on external environment. During its growth, already, size (that means quality) of wood cells, from which wood is composed, is influenced by moisture, temperature, sunshine intensity, pollution and many more. Considering different conditions during a year, annual rings are evolved in wood composition. Annual rings are difference between springwood (darker layers at *Fig. 1*) and summerwood (brighter). It can be said that wood is hugely inhomogeneous material with a fibrous structure thanks to annual rings effect and many defects in a wood structure.

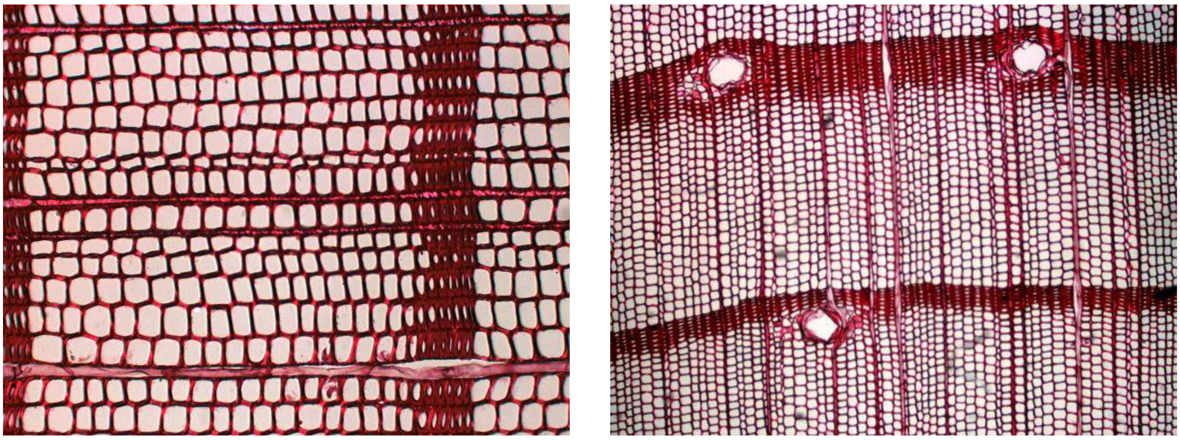

Fig. 1 Microstructure of a pine wood (Pinus Ponderosa)

2.1. ORTHOTROPIC BEHAVIOR

In spite of wood is an anisotropic material, during the calculation three axes symmetry (*Fig. 2*) is used, so wood can be considered as an orthotropic material. An axis, which has big importance, is an axis parallel with wood fibers – the longitudinal axis (L direction). Wood has another two axes of symmetry, radial and tangential. Wood elements are constructed with the main axis parallel with the longitudinal axis, because wood has the best properties along the longitudinal axis.

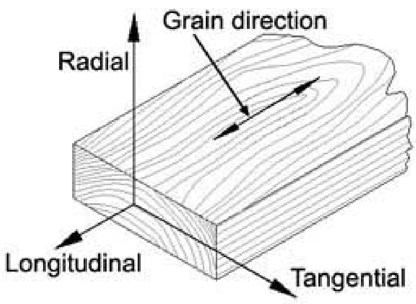

Fig. 2 Wood directions labeling

As mentioned above, wood is an orthotropic material, whose strain – stress diagram is shown at *Fig. 3*. At the diagram it is possible to see three parts. Till the limit of proportionality (σ_p) wood assigns the linear behavior. This is area of Hook's law validity with influence of orthotropy *(2)*. Wood starts to behave nonlinearly after the limit of proportionality. Development of micro cracks is in this area till macro crack is located and developed. Wood still has some bearing capacity in the nonlinear area. Strength limit (σ_s) is a point, where the bearing capacity is exhausted and a material starts to collapse.

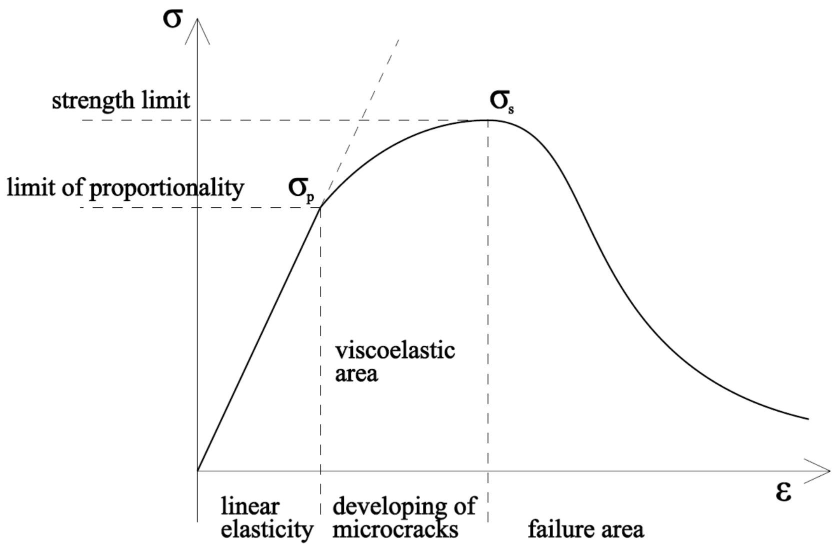

Fig. 3 Strain – stress diagram

It is necessary to get twelve material characteristics to describe a general orthotropic material – three moduli of elasticity, three moduli of elasticity in shear and six Poisson's ratios. Using the three axis symmetry and the relationship of deformation energy *(1)*, only nine material characteristics are sufficient.

$$w = \frac{1}{2}\boldsymbol{C}\sigma^2 \qquad (1)$$

Equation *(2)* describes situation, where a wood element is under loading oriented according to an axis of wood (L, T, R). In *(2)* E is modulus of elasticity, G is modulus of elasticity in shear, μ is Poisson's ratio, ε and γ are strains, σ and τ are stresses, L is a plain parallel with grain, R is a plain perpendicular to grain in the radial direction and T is a plain corresponding with the tangential direction.

$$\begin{Bmatrix} \varepsilon_L \\ \varepsilon_R \\ \varepsilon_T \\ \gamma_{RT} \\ \gamma_{LT} \\ \gamma_{LR} \end{Bmatrix} = \begin{bmatrix} \frac{1}{E_L} & -\frac{\mu_{RL}}{E_R} & -\frac{\mu_{TL}}{E_T} & 0 & 0 & 0 \\ -\frac{\mu_{LR}}{E_L} & \frac{1}{E_R} & -\frac{\mu_{TR}}{E_T} & 0 & 0 & 0 \\ -\frac{\mu_{LT}}{E_L} & -\frac{\mu_{RT}}{E_R} & \frac{1}{E_T} & 0 & 0 & 0 \\ 0 & 0 & 0 & \frac{1}{G_{RT}} & 0 & 0 \\ 0 & 0 & 0 & 0 & \frac{1}{G_{LT}} & 0 \\ 0 & 0 & 0 & 0 & 0 & \frac{1}{G_{LR}} \end{bmatrix} \begin{Bmatrix} \sigma_L \\ \sigma_R \\ \sigma_T \\ \tau_{RT} \\ \tau_{LT} \\ \tau_{LR} \end{Bmatrix} \tag{2}$$

2.2. HOMOGENIZATION OF WOOD

It is possible to see annual rings or rather curvation of wood layers in the TR plain (plain between axes T and R) at *Fig. 2*. During the manual calculation annual rings are not considered, that means certain homogenization of wood is made. This kind of homogenization is suitable only at some areas of a material, where the curvature of a material is not so important, curvature can be ignored (areas 1, 4 and 5 at *Fig. 4*). In manual calculation it is necessary to homogenize wood, because the influence of annual rings, primary cracks (for example drying cracks) and knots is not possible to consider, because calculations would be too much complicated.

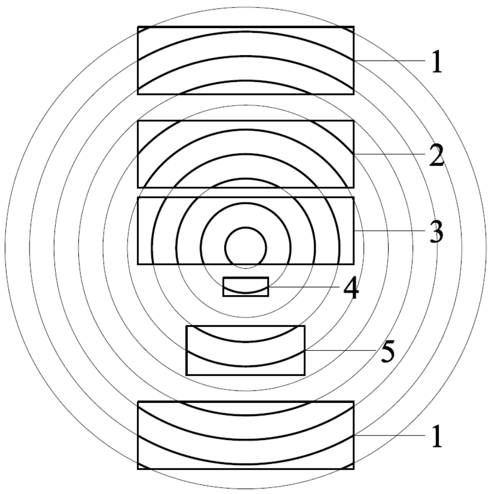

Fig. 4 Areas for homogenization of wood

Some kind of homogenization offers wood itself and its three axes symmetry. There is certain relationship between the same mechanical properties belongs to the axes. The properties in one or two perpendicular directions are much higher than properties in remaining ones. For example strength in the grain direction (parallel with grain) is much higher than strength in directions perpendicular to the grain. At the basis of this, lower properties can be considered as similar. Values of compressive strength for a pine spruce are shown in *(3)*. Values shown in *(3) – (5)* are from [3]

$$F_{c,L} : F_{c,R} : F_{c,T} = 34{,}1 : 3{,}4 : 4{,}0 \approx 10 : 1 : 1 \tag{3}$$

$$E_L : E_R : E_T = 15 : 3{,}1 : 0{,}5 \approx 30 : 6 : 1 \tag{4}$$

$$G_{LR} : G_{LT} : G_{RT} = 573 : 474 : 53 \approx 10{,}8 : 8{,}9 : 1 \tag{5}$$

Formulas *(3) – (5)* are useful for homogenization, too. It is complicated to determine all twelve material characteristics. Symmetry reduces necessary number of mechanical characteristics to nine. Properties only in one direction are often determinate in practice and formulas shown above help to recalculate properties in remaining ones. In equations *(3) – (5)* F_c is compressive strength.

This type of homogenization is useful for numerical modeling too. If it is possible to use an orthotropic material model in any kind of the FEM solver, still there is necessity to full stiffness matrix or compliance matrix with adequate number of mechanical characteristics (often only few of them are known).

3. MATERIAL STUDIES

Nowadays, there is aim to describe wood material as much as possible. In case of this there are studies which can describe wood using modern computational technique and many complicated material models. For example in [4] there are shown simulations of grain behavior in knots surrounding using the fluid analysis. Setting and development of cracks in the areas (for example diminished by drying crack) is the same as in areas where sharp skew angle (higher concentration of stress) is solved using these models. Such areas cannot be described using the homogenized material.

Authors of [5] describe, that there are many approaches how to create material model of wood. Microstructure of wood can be modeled at a cell (or mesoscale) level using cellular models, at a microscale (cell walls) level using laminate and multiscale models. Another approach describes wood using fracture mechanics-based models or using models which combine micromechanical and continuum mechanical-lattice models. Constitutive model of wood is described in [6].

3.1. MICROMECHANICAL MODELS

The difference between the mechanical properties of longitudinal and other two directions can be explained by the cell shape in the cross-section plane. Cells of wood are hexagonal, but condition during the growth of cells causes their irregularity. On the mesoscale wood is a cellular solid. Mechanical and physical properties of cellular solids are dependent on the cell material and cell shapes. Idealization of the shape of the hexagonal honeycomb cell is shown at *Fig. 5*.

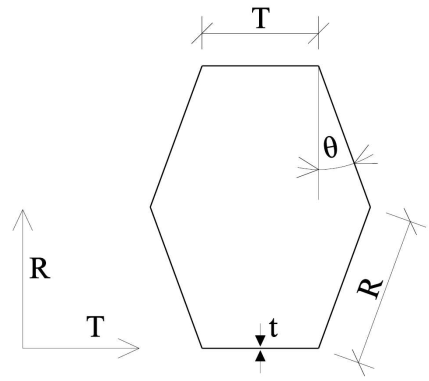

Fig. 5 Honeycomb shape of wood cells

Relative density of honeycomb cells is important for micromechanical models. The relative density of cells is calculated as a ratio between densities of the cellular structure ρ and the solid cell walls ρ_s *(6)*. Mechanical properties of cells can be solved using the classical beam theory, where the cell walls are considered as beams.

$$\frac{\rho}{\rho_s} = \frac{t}{R}\frac{2R+T}{2(T+R\sin\theta)\cos\theta} \tag{6}$$

Cell walls can be considered as a kind of multilayer composite according *Fig. 6* in multiscale models. Number of layers, angle of microfibers and different composition of layers influences behavior of wood cells. For example a lower angle of microfibril induces a lower axial shrinkage and a higher angle induces a higher shrinkage.

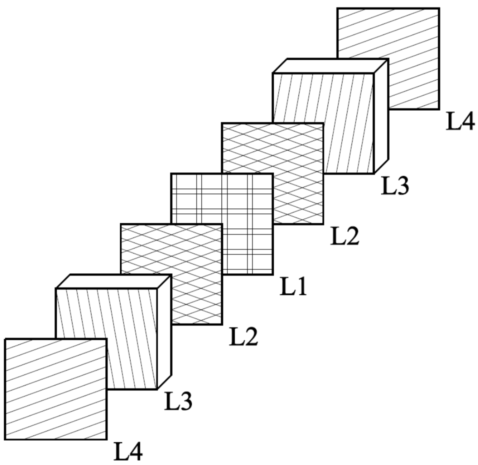

Fig. 6 Composition of cell wall using multilayer approach

Despite the numerical difficulty of micromechanical models it was established relationship between parameters of the wood microstructure and the mechanical behavior of wood, including the influence of moisture.

3.2. WOOD FAILURE

In [5] it is noted that the wood cells close to the fracture surface can absorb a great amount of energy before breaking. The fracture toughness of wood is closely related to the structure in L3 layer in *Fig 6.* Spiral structure of fibrils in this layer induces a different form of buckling failure in tension, which causes a high energy absorption during fracture. Twisting angle of 15° between fibers in spiral structure provides optimal trade between stiffness and toughness.

The material is described using the typical beam elements connected with the spring elements in lattice models. For example the structure of a material can be described by blocks of an infinity lattice structure where the horizontal elements are made from beam elements and the spring elements are used for diagonal elements. In lattice models the damage and crack growth are represented as breaking of beams or other elements in a material structure. Contribution of broken elements to the stiffness matrix is removed during the calculation. The lattice structure with different properties can be used for each direction.

3.3. CONSTITUTIVE MODEL

Many studies describe nonlinearity of wood, some approaches was shown above. But homogenized orthotropy of wood can be described using the constitutive model as well. For formulas describing the constitutive model some assumptions are made: wood is an idealized 3D, homogeneous, orthotropic material. Wood is a homogeneous continuum and there are no growth defects in the wood, and the grain is oriented straight and parallel to the long axis of an element.

Many types of material behavior provide a constitutive model. Bilinear, elastoplastic and more behaviors can be described only be changing same parameters *(7)*.

$$E_n = \left(\alpha E_{n-1} + \beta E_0\right)\left(\frac{\sigma_y}{\sigma_{n-1}}\right)^{\gamma} \tag{7}$$

Where E_n is the current modulus of elasticity, E_{n-1} is the modulus of elasticity in the previous step and E_0 is the initial modulus of elasticity, σ_y is the yield stress and σ_{n-1} is the yield stress in the previous step, constant parameters α, β and γ are defined by user at the beginning of calculation. Formula *(7)* is suitable for a bilinear model, when $\alpha = 0$ and $\gamma = 0$. This approach is most suitable for nonlinear FEM codes. It can be used for both 2D and 3D problems.

4. CONCLUSION

Wood is one of the oldest engineering materials. It is a fibrous, porous, inhomogeneous, anisotropic material. Its properties are influenced by many factors and exhibit a very wide range of variability during the time, moisture, temperature and loading. An orthotropic behavior of wood is shortly presented herein as well as approaches which are usable for calculation or homogenization of a wood structure.

There are many ways how to describe behavior of wood. Some of them are very sophisticated and thanks to this, time intensive for calculation. This type of material models is not appropriate for design engineers. On the other hand these models are necessary for academic studies and provide better understanding of wood as a material or wooden elements which helps to extend knowledge of design engineers and improve design approaches of wooden elements or constructions. The second type of models, homogenized one, is much simple but ignores a lot of conditions, which influence behavior of wood.

For design engineers it is not necessary to have detailed data from complex analyses of wooden element, because design approaches consider many disadvantageous conditions in few design parameters.

Unfortunately, the material model made according to [6] still does not work properly. Due to this, implementation to the FEM solver developed at the Department is delayed.

ACKNOWLEDGEMENT

Data presented in this paper were set with the financial support by Czech Technical University in Prague (SGS project No. 13/034/OHK1/1T/11).

REFERENCES

[1] GERNER, M. *Carpentry joints*. 1st ed. Prague: Grada, 2003, 220 p. ISBN 80-247-0076-X.
[2] BODIG, J. and JAYNE B. A. *Mechanics of wood and wood composites*. Reprint ed. Malabar, Fla.: Krieger Pub., 1993, 712 p. ISBN 08-946-4777-6.
[3] POŽGAJ, A. et al. *Structure of wood properties*. Bratislava: Príroda, 1997, 488 p. ISBN 80-07-00960-4.
[4] GUINDOS, P. and GUAITA M. A three-dimensional wood material model to simulate the behavior of wood with any type of knot at the macro-scale. In: *Wood Science and Technology* [online]. [cited 2013-07-10]. Available from: http://link.springer.com/10.1007/s00226-012-0517-4.
[5] MISHNAEVSKY, L. Jr. and QUIN, H. Micromechanical modelling of mechanical behaviour and strength of wood: State-of-the-art review. In: *Computational Material Science* [online]. [cited 2013-07-10]. Available from: http://www.sciencedirect.com/science/article/pii/S0927025608001882.
[6] TABIEI, A. and WU, J. Three-dimensional nonlinear orthotropic finite element material model for wood. In: *Composite Structures* [online]. [cited 2013-07-10]. Available from: http://www.sciencedirect.com/science/article/pii/S0263822300000891.

DEPENDENCE OF THE MECHANICAL PROPERTIES OF CEMENT-BASED COMPOSITES ON PVA CONTENT

Jaroslav TOPIČ[1], Pavel TESÁREK[2], Tomáš PLACHÝ[3], Václav NEŽERKA[4]

***Abstract**: The aim of the article is to present the results of non-destructive testing of cement-based composite with the addition of polyvinyl alcohol (PVA). The composite was enriched by PVA in form of polymer solution in various concentrations. Individual samples differed in the PVA content and the tested parameters are compared with a reference sample without any PVA additions. The main purpose of our work was to determine the material parameters of PVA enriched cement-based composites on nano- and macro-level.*

***Keywords**: composite, cement, polyvinyl alcohol, non-destructive testing*

1. INTRODUCTION

Due to extensive use of concrete in civil engineering there is a tendency for a perpetual improvement of the material. This is accomplished mainly by means of additives and admixtures with the positive impact on the final product, in particular on its utility properties. Among others, polymers are very popular. First attempts to modify the concrete using polymers date back to 1950. Nowadays, polymers are very commonly used admixture to concrete or Portland cement. Most often, the polymers are added into fresh concrete in form of polymer solution during mixing. Typical representative is PVA, which has been exploited and its influence investigated in the presented paper.

It has been reported that the additions of PVA have a positive influence on concrete in terms of freeze resistance, capillary absorption and fracture-mechanical properties [1]. According to other few studies also the compressive strength of PVA enhanced samples was also increased. On the other hand, the Young's modulus is reduced with the PVA additions and the workability of the fresh concrete is poorer.

[1] Bc. Jaroslav Topič; Czech Technical University in Prague, Faculty of Civil Engineering; Thákurova 7, 166 29 Prague 6 – Dejvice, Czech Republic, jaroslav.topic@fsv.cvut.cz

[2] Ing. Pavel Tesárek, Ph.D., Czech Technical University in Prague, Faculty of Civil Engineering; Thákurova 7, 166 29 Prague 6 – Dejvice, Czech Republic, tesarek@fsv.cvut.cz

[3] Ing. Tomáš Plachý, Ph.D., Czech Technical University in Prague, Faculty of Civil Engineering; Thákurova 7, 166 29 Prague 6 – Dejvice, Czech Republic, tomas.plachy@fsv.cvut.cz

[4] Ing. Václav Nežerka, Czech Technical University in Prague, Faculty of Civil Engineering; Thákurova 7, 166 29 Prague 6 – Dejvice, Czech Republic, vaclav.nezerka@fsv.cvut.cz

The properties of hardened composite are strongly influenced by the amount of the added PVA into the mix and the main goal of this paper is to define an optimum amount of PVA in the cement-based composites for their best performance while keeping the drawbacks at a satisfactory level.

2. MATERIALS AND SAMPLES

The samples were made of Portland cement CEM I 42.5 produced in Radotín. PVA was added into the fresh paste in form of water solution in concentration of 16 % (brand name Sloviol) having the molar mass equal to 67 g/mol.

There were prepared five sets of samples, each represented by three prismatic specimens having the standard dimensions 40 × 40 × 160 mm and five 50 mm high cylindrical specimens with the diameter 30 mm. The reference set, denoted “A”, was composed only of cement and water, without any additions of PVA. Samples denoted “B” to “E” contained PVA in different amount, see Tab. 1.

The needed amount of cement, water and PVA solution was determined before the production of samples, the water and PVA solution were mixed in the required ratio in order to satisfy the water to cement ratio equal to 0.35 and PVA to cement ratio equal to 1.4, 2.8, 4.0, and 5.6. Cement was continuously added into the PVA solution diluted by the mixing water during stirring of the fresh paste in order to produce a homogeneous mix. The prepared samples were placed into casts, from which the specimens were removed after 2 days of hardening. Consequently, the specimens were placed into water having the temperature of 20°C to ensure the same conditions during hardening. After 28 days of curing the specimens were removed from water a kept in a laboratory at the temperature of 22°C and relative humidity 50 %.

Tab. 1 Composition of tested cement-PVA samples

Set	Cement [g]	w/c = 0.35		PVA [wt. % of cement]
		Water [g]	Solution of PVA [g]	
A	1000	350	0	0.0
B	1000	263	88	1.4
C	1000	175	175	2.8
D	1000	100	250	4.0
E	1000	0	350	5.6

3. EXPERIMENTAL METHODS AND RESULTS

Shrinkage of the material was monitored during the first 7 days of curing. Furthermore, the weight development and dynamic Young’s (E) and shear (G) moduli were also monitored and these values were evaluated on the wet samples during the first 28 days of curing. Last measurements were performed 35 days from the production of the samples and it was accomplished on dry samples.

Dynamic Young's and shear moduli were determined using the impulse method on the prismatic specimens (40 × 40 × 160 mm). The basic principle of the method is excitation of the investigated specimen by a measured force and measurement of the specimen response. When the natural frequencies are evaluated the elastic moduli can be calculated. The moduli can be evaluated from higher natural frequencies and using different boundary conditions or impact location. The measurement was accomplished by Brüel & Kjaer device, type 3560-B-120. The bulk density of the PVA augmented specimens was, as expected, lower, compared to the reference sample. It is obvious from Fig. 1 that the density is reduced by the additions of PVA. Quite significant reduction can be observed even on the paste containing the lowest amount of PVA. Quite interestingly, another significant reduction appeared between the sets "D" and "E".

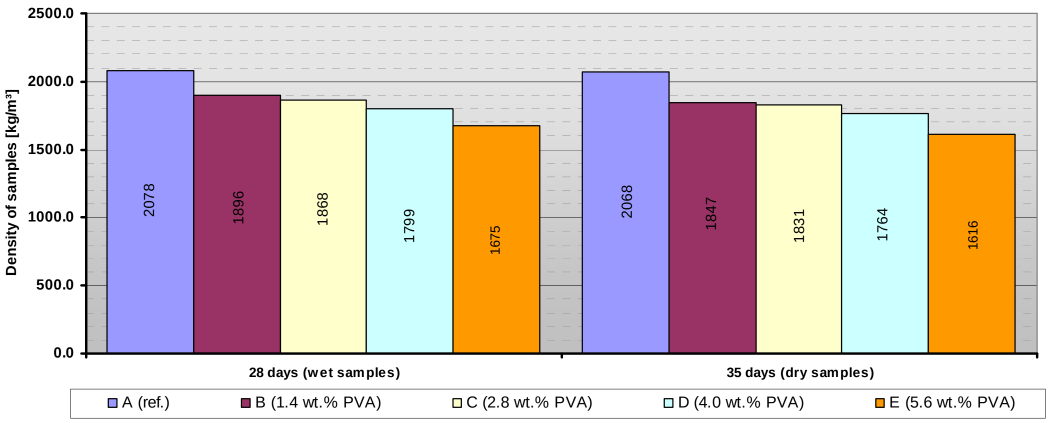

Fig. 1: Bulk density of the tested samples

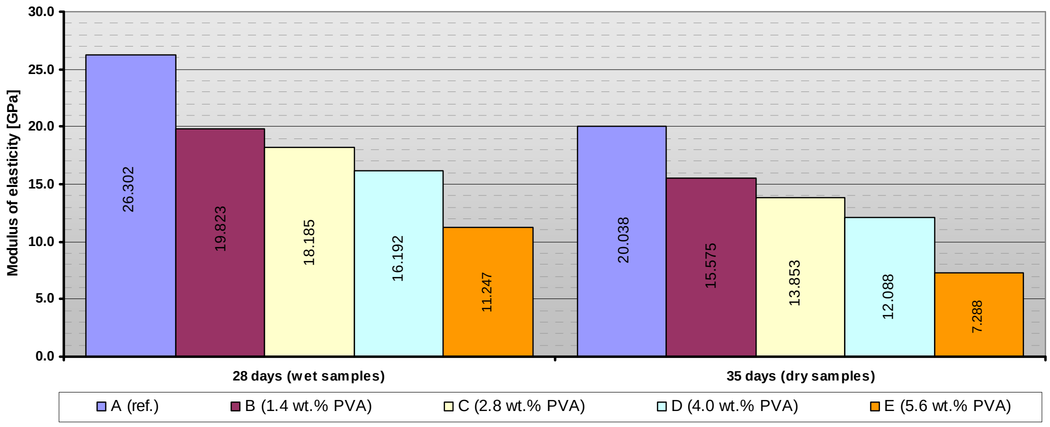

Fig. 2: Dependence of the dynamic Young's modulus on PVA content

It is obvious from Fig. 2 that the stiffness (dynamic Young's modulus) decreases with the additions of PVA, the content equal only to 1.4 % of mass contributed to the reduction by 25 %. There is a linear relationship between the content of PVA and the stiffness of cement paste for the sets "B" to "D", however, as in case of bulk density, there is more significant drop between the sets "D" and "E". The development of shear modulus follows the same trends (Fig. 3).

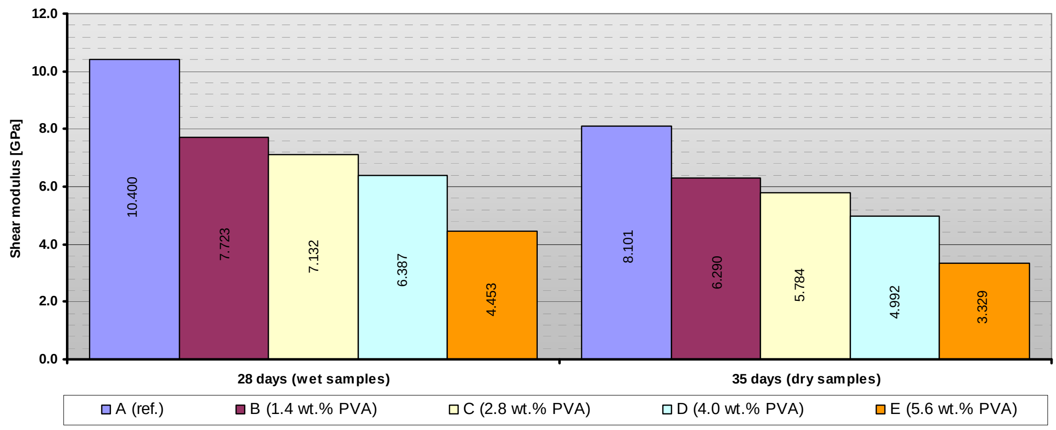

Fig. 3: Dependence of the shear modulus on PVA content

4. CONCLUSION

The results of our measurement indicate that the presence of PVA significantly influences the properties of cement pastes and it is valid even for a little concentrations (1.4 wt. %). It is mainly caused by an increase of pore size and content within the hardened paste with the amount of PVA added. Significant difference, observed between samples "D" and "E", was caused by poor workability of the fresh paste and complicated casting. It was not possible to completely remove cavities (bubbles) from the fresh mortar, when the PVA concentration exceeded 5.6 %. Therefore, it is not suitable to add more than 4 % as an additive into cement-based composites.

ACKNOWLEDGEMENT

The financial support of this experiment by the Faculty of Civil Engineering, Czech Technical University in Prague – SGS project No. 12/1117/OHK1/2T/11 is gratefully acknowledged.

REFERENCES

[1] BENSTED, J. and BARNES, P. *Structure and Performance of Cements*. London, Spon Press, 2002, pp. 57-99. ISBN 0-203-47778-2.

[2] ZONGJIN LI. *Advanced Concrete Technology*. New Jersey, John Wiley & Sons, Inc., 2011, pp. 281-292. ISBN 978-0-470-43743-8.

[3] SINGH, N. B. and RAI, S. Effect of polyvinyl alcohol on the hydration of cement with rice husk ash. *Cement and Concrete Research* . 2001, **31**, 239-243. ISSN 0008-8846.

[4] MORTAL, R., ORANGE, G., BOMAL, Y., GODARD, P. Reinforcement of hydrated portland cement with high molecular mass water-soluble polymers. *J Mater Sci* . 2007, **42,** 4858-4869. ISSN 0022-2461.

[5] MOJUMDAR, S. C. and RAKI, L. Preparation and properties of calcium silicate hydrate-poly (vinyl alcohol) nanocomposite materials. *Journal of Thermal Analysis and Calorimetry*, 2005, **82**, 89-95. ISSN 1418-2874.

CHANGES OF THE DYNAMIC MODULUS OF ELASTICITY IN DEPENDENCE ON THE NUMBER OF THE FREEZE-THAW CYCLES

Richard ŤOUPEK[1], Tomáš PLACHÝ[2], Michal POLÁK[3], Pavel TESÁREK[4]

Abstract: *The paper presents the determination of the modulus of elasticity on gypsum samples using the non-destructive impulse excitation method. The great advantage of non-destructive testing, compared to destructive, is that still the same sample is tested and it excludes various negative effects. The paper presents the development of modulus of elasticity on gypsum samples according to the number of freeze-thaw cycles. For cyclic loading, the samples were saturated with water at 20 °C and tested in 8-hour cycles. Samples were removed from the water bath and placed in a freezer with a temperature lower than -20 °C and after 8 hours they were placed again in the water bath for a period of eight hours. The difference from 'dry' frost resistance was that the samples of hardened plaster were exposed to "wet" frost resistance, i.e. to the extreme load of the samples with the external climatic conditions.*

Keywords: *Gypsum, modulus of elasticity, impulse excitation method, freeze-thaw cycles*

1. INTRODUCTION

The resistance to the external climatic conditions is one of the most important properties of the building materials, which are used for building envelopes. The porous building materials, which will be used in an exterior, have to be frost resistant, resp. resistant to freeze-thaw cycles. Several studies [1, 2] of the gypsum use in exteriors were done abroad and also some research teams studied materials, which are available in the Czech Republic. They determined e.g. the frost resistance experimentally according to the methodology for plasters, because such methodology for gypsum does not exist [3], and the resistance to the external climatic conditions for samples freely stored in exterior [4].

[1] Ing. Richard Ťoupek, Department of Mechanics, Faculty of Civil Engineering, Czech Technical University in Prague, Czech Republic, plachy@fsv.cvut.cz

[2] Ing. Tomáš Plachý, Ph.D., Department of Mechanics, Faculty of Civil Engineering, Czech Technical University in Prague, Czech Republic, plachy @fsv.cvut.cz

[3] prof. Ing. Michal Polák, CSc., Department of Mechanics, Faculty of Civil Engineering, Czech Technical University in Prague, Czech Republic, polak@fsv.cvut.cz

[4] Ing. Pavel Tesárek, Ph.D., Department of Mechanics, Faculty of Civil Engineering, Czech Technical University in Prague, Czech Republic, tesarek @fsv.cvut.cz

2. LOADING OF THE SPECIMENS

For the purpose of these tests, the grey gypsum produced by the company Gypstrend (CZ) was chosen. The specimens were made with the water/gypsum ratio 0.71. The dimensions of the specimens were 40 × 40 × 160 mm. The tests started at the age of the specimens 28 days. The wet variant of the freeze-thaw cycles was used for the determination of the sample resistance. Before starting the tests, the samples were placed to the water bath of the temperature 20 °C. The samples were in the bath for four hours till the full water saturation. The saturation was verified by weighting of the samples, the weight of the samples stopped changing after 4 hours. The freeze-thaw cycle is composed from two phases, during the first one the water saturated sample was placed to the freezer with the temperature - minus 20 °C at minimum and it was in the freezer for 8 hours. After 8 hours, the sample was put to the water bath of the temperature 20 °C for another 8 hours.

3. IMPULSE EXCITATION METHOD

The Impulse Excitation Method (IEM) was chosen to determine the dynamic Young's modulus because of its non-destructive character. The sample was supported in the fundamental longitudinal nodal position in the middle of its span. The acceleration transducer was placed at the center of one end surface of the sample. The opposite end surface of the sample was struck perpendicular to the surface by the impact hammer. The waveforms of the excitation force and the acceleration were recorded and transformed using the Fast Fourier Transform (FFT) to the frequency domain. The Frequency Response Function (FRF) was evaluated from these signals using the vibration analyzer and the program PULSE 14.0. The test was repeated four more times for each sample and the averaged function FRF was saved. From an averaged FRF, the fundamental resonant frequency was determined for each sample. The mass and dimensions of the sample were measured, the FRF was evaluated and the dynamic Young's modulus E_{dl} was determined using the relation

$$E_{dl} = \frac{4lmf_l^2}{bt} \tag{1}$$

where: E_{dl} is the dynamic modulus of elasticity [Pa], f_{l} is the fundamental longitudinal resonant frequency [Hz], b is the width of the sample [m], t is the height of the sample [m], l is the length of the sample [m], m is the mass of the sample [kg].

4. RESULTS

The main goal of this experiment was the determination of changes of the modulus of elasticity in dependence on the number of freeze-thaw cycles using the impulse excitation method. Therefore, the values of modulus of elasticity of gypsum samples for three different conditions were measured at first (Table 1): samples with natural moisture content, water saturated samples, frozen samples.

Tab. 1 Experimental results – modulus of elasticity [GPa] at the beginning of testing

Samples/ conditions	Dry samples with natural moisture content	Water saturated sample	Frozen water saturated sample
1	5.31	3.53	9.71
2	5.41	3.61	9.60
3	5.32	3.50	9.32
4	5.05	3.34	8.94
5	5.19	3.40	8.65
6	5.20	3.35	9.59

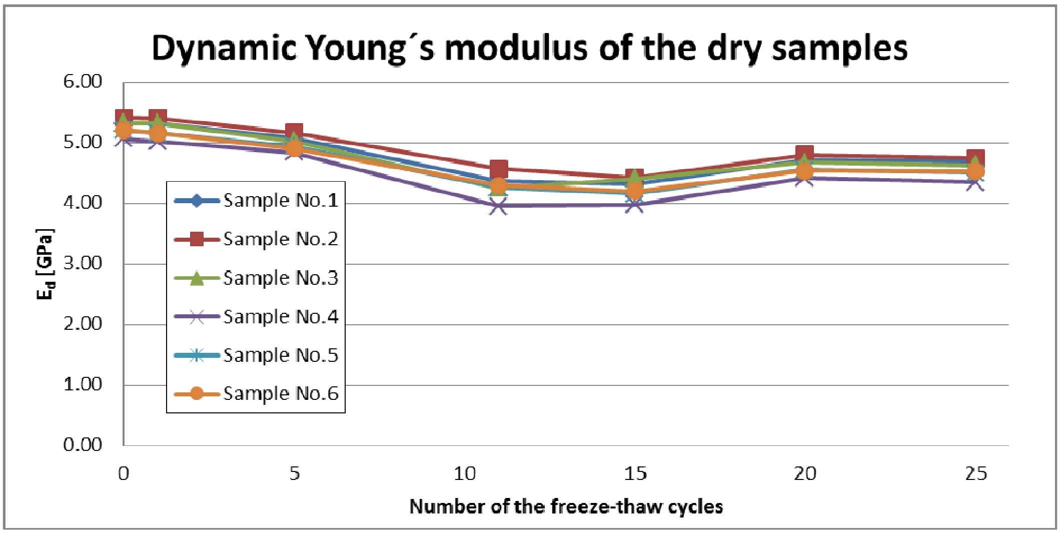

Fig. 2 Dynamic modulus of elasticity of the gypsum samples with natural water content.

The reason, why to determine these characteristics, was the thorough survey of samples behavior before starting the measurement, resp. after the first freeze phase of the freeze-thaw cycle. Especially, we are interested in the influence of water content to the monitored characteristics in the form of liquid and also ice. There can be seen in Tab. 1 that dynamic modulus of elasticity of the frozen samples is approximately two times higher than for the dry samples. The values of the dynamic modulus of elasticity of the dry samples and the water saturated samples correspond well with our previous measurements [5]. The changes of the modulus of elasticity of the gypsum samples are shown in Fig. 1. The character of these changes is very similar for all six samples. The modulus of elasticity decreased about 13 % after the 25 freeze-thaw cycles. The values of modulus of elasticity for water saturated samples decreased only about 8 %.

5. CONCLUSION

From the obtained experimental data it results that after 25 freeze-thaw cycles no significant changes – decrease of moduli of elasticity – have occurred on gypsum samples. The decrease is only about 13 %. The gypsum durability in extreme conditions was verified by this experiment and not only during wet freezing and thawing but also during drying. This is the worst combination of conditions which has the significant influence on mechanical properties deterioration of the building materials. The decrease of stiffness 13 % is probably caused by the solubility of gypsum in water [4] during cyclic drying and soaking. In analogous experiments, but only with freeze-thaw cycling without drying and soaking phases, on different kind of gypsum, the gypsum mechanical properties have not decreased, the compression strength was determined so it was destructive testing [3]. The disadvantage of these destructive experiments was that the mechanical properties were determined on different samples. During our experiments, this influence was eliminated but the comparison with destructive testing will be done in our future research.

ACKNOWLEDGEMENT

This work has been supported by the Technology Agency of the Czech Republic – Competence Centers under No. TE01020168 Centre for Effective and Sustainable Transport Infrastructure (CESTI) and Czech Technical University in Prague under the project No. SGS12/117/OHK1/2T/11.

REFERENCES

[1] ZDRAVKOV, B., PELOVSKI, Y. Extruded building materials from FGD gypsum. *Journal of Environmental Protection and Ecology*. 2006, **1**, 129 – 136. ISSN 1311-5065

[2] ZHAO, Feng-qing, et al. Water resistant block from desulfurization gypsum. *Construction and Building Materials.* 2012, **27**, 531-533. ISSN 0950-0618

[3] ROVNANÍKOVÁ, P. Study of gypsum frost-resistance. (In Czech), *Zpravodaj STOP*. **8**(2), 2006, pp. 14-20.

[4] ČERNÝ, R., et al., *Properties of modified gypsum*, (In Czech), CERM, 2010.

[5] PLACHÝ, T., et al. Nondestructive Determination of Young's Modulus of Gypsum Specimens Using Impulse Excitation Method. In: *Proceeding of the 48th International scientific Conference of Experimental stress Analyses.* 2010, pp. 339-344. ISBN: 978-80-244-2533-7.

[6] ZOBAL, O., PADEVĚT, P. Properties of the Concrete from the Orlik Dam after 50 Years in Operation, In: *Proceedings of the 50th Annual Conference on Experimental Stress Analysis*. 2012, pp. 555-558. ISBN 978-80-01-05060-6.

[7] MELZEROVÁ, L., KUKLÍK, P. Non-destructive Tests of Modulus of Elasticity for the GLT Beam, In: *Proceedings of the 50th Annual Conference on Experimental Stress Analysis.* 2012, pp. 271-276. ISBN 978-80-01-05060-6.

[8] PAPÁN, D., Experimental measurements of paraseismic effects due to traffic. In: *Proceedings of the 20th European Regional Earthquake Engineering Seminar: Seismic assessment and upgrading of existing structures*, Institute Universitaire Kurtz Bosch, Sion, Switzerland, 2001, pp. 144-145.

[9] BENČÁT, J., PAPÁN, D., Experimental dynamic analysis of Ružín railway bridges. In: *Proceedings of the 22nd Danubia-Adria Symposium on Experimental Methods in Solid Mechanics, DAS 2005*, Parma, Italy, 2005, pp. 253-254, ISBN 9781604235739

REAL CROWD BEHAVIOR ON THE GRANDSTANDS

Ing. Bc. Martin Verner[1]

Abstract*: The aim of this paper is to approach the issue of active sports crowd on grandstands. Active crowd raises vibration on the grandstands. Design represents one of the ways to describe this crowd and then determines the time required for the synchronization. This article serves as a basis for the design of experiments on real sports grandstands.*

Keywords*: single-storey grandstand, multi-storey grandstand, synchronize of crowds, sense of rhythm*

1. INTRODUCTION

Sports stadiums have long been not only serve for sports games. Currently, the trend is to use their maximum capacity for other activities. The most common unsportsmanlike activities include organizing music concerts. Architects are trying to make the most of sporting or musical spectators had a clear view of the course / stage while events were to place as close as possible. Stadiums can be divided by many criteria. Stadiums can be divided into stadiums with single-storey grandstand and multi-storey grandstand.

2. TYPES OF GRANDSTANDS

When, the stadium has only one floor, the spectators in the most remote places had very poor visibility on the field. The largest single-storey, and concurrently the largest stadium, is in the United States. His name is Michigan Stadium. Its capacity is 109,901 viewers (maximum visit was in November 2011 114,804 viewers). The downside is that spectators in the last series look at the field from a distance of approximately 100 m. With the distance the acoustics of the stadium is exacerbated, so it is bad usable for music concerts. The biggest problem of the single-storey stadiums are their floor area that these stadiums are marginalizing to edge of the residential agglomerations with more space than in urban centres- [1].

So that the spectators would be as close as possible to the playing surface and also the largest possible number of spectators would come at the grandstand, the stadiums are built with the multi-storey grandstand. These stadiums occupy much smaller floor area than the single-storey stadiums; therefore they are the appropriate type in densely populated places. The world largest multi-storey

[1] Departments of Mechanical, Faculty of Civil Engineering, Czech Technical University, martin.verner@fsv.cvut.cz

stadium is located in North Korea. It is called Rungrodo May Day stadium and has a capacity of 150,000 spectators. Architects are trying that the stands situated above have no support coming from the stands below. Supporting the above raised grandstands would build from the bottom of the grandstands, and they would worsen the view of the spectators on the bottom of the stands. It is the attempt to compress the overall height of the floors stands. These two efforts lead to the fact that most of the grandstands are from the static point of view - subtle cantilever beam. Subtle cantilever beams have lower natural frequency of oscillation than the lower grandstands, which are supported at both ends of the stands. [1]

2.1 REGISTERED EXAMPLES OF GRANDSTAND VIBRATION

The first registered case in which fans vibrate a grandstand by moving is from 1900. The case became in the Scottish city of Glasgow. It was played at the stadium of Glasgow Rangers, who had a wooden grandstand with a capacity of 80,000 spectators. It was a single-storey stadium. The international football match was played between the teams of Scotland and England. In the 50th minute, the English had a chance to score a goal. The spectators stood up from the seats to see better and then sat down again. The spectators move caused the vibration of the grandstand which ultimately led to its collapse. During the accident twenty-six people died and over five hundred were injured-[2].

In 2010, the spectators felt vibration in Nuremberg, Germany. It was played the Bundesliga match between teams 1 FC Nuremberg - Borussia Dortmund. Guest fans began to support their team by rhythmic jumping in the grandstand. This jumping caused vibration of the structure. Vibrations of the grandstand were not so intense to collapse the grandstand but caused panic of the fans who were under the grandstand-[3].

In 1999, the Millennium Stadium in Cardiff in Wales was officially opened. At the opening, the stadium had the largest cantilever grandstands in the world. The stadium is used for the needs of Welsh rugby and football national team, sometimes it is used for the music concerts. During the first musical concert spectators felt the vibrations of the grandstands. These vibrations cannot cause collapse of the grandstands but they have a bad effect on the human body. It could easily happen that the vibrations cause panic on the grandstand located under the vibrating grandstand. Therefore, the owner of the stadium decided to reinforce the grandstands by using 52 supporting pillars. These columns are collapsible and are used only during the organization of musical productions because they worsen visibility at the bottom of the grandstand and also reduce the capacity of the stadium itself-[2].

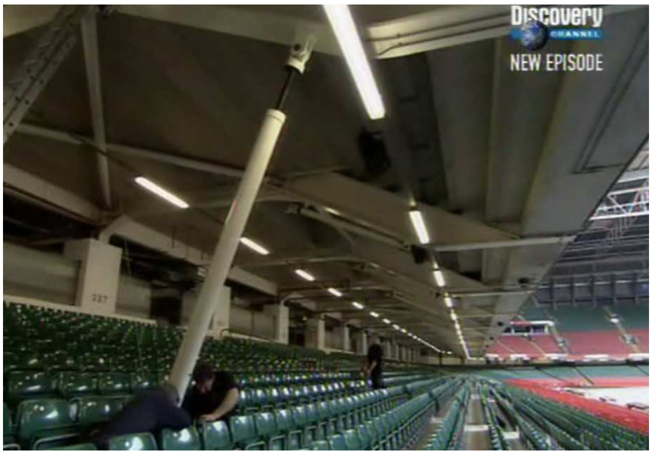

Fig. 2 Installed supports at the Millennium Stadium in Cardiff [2]

3. CAUSES OF VIBRATION

The last 20 years we have seen a change in behaviour of spectators during a sporting match. The spectators are not only sitting in their seats and passively watching the match but they are active in cheering on of their team. For example in the Czech Republic since the World Championships in ice hockey, 2004, fans have invited each other to jumping around the all stadium by shouting: "Who does not jump is not Bohemia". This jumping usually does not last long and on the grandstand causes minimal vibrations.

So that the spectators cause vibrations of grandstands, they must be numerous and they must be synchronous. If the bigger group of spectators starts jumping, everybody jumps with different frequencies, these frequencies cancel each other out and grandstand is vibrated at least but when the group is synchronized it represents the greatest risk for grandstand. Generally, the steel construction vibrates easier than concrete ones.

4. SYNCHRONIZATION OF ACROWD

As it was already mentioned, the greatest risk for the grandstand construction is a synchronized crowd. The question is how to describe this crowd and to determine the probability of its occurrence. The best the probability of synchronization crowd describes by using conditional probabilities. Condition represents an occurrence of the element that makes easier of crowd synchronization.

4.1 CONDITIONS TO ACCELERATE SYNCHRONIZATION

Alone crowd needs a long time to synchronize. Examples include walking people. Two walkers go longer behind or next to each other, so after some time they harmonize their steps and then walk with the same frequency of steps. On the grandstand, harmonization is faster when the crowd has got a management. Music concerts, during which drums are played, are the best for crowd management. The drummer adds rhythm to the whole stadium, according to active spectators who copy it to be synchronized. During a sports match there is a group of people with drum and they are between the active spectators. Drummer gives a fairly accurate pummelling rhythm that others follow.

Another way to synchronize the spectators is their embrace. A certain group of people grabbing around his shoulders and they start to jump. By grabbing around their shoulders they perceive rhythm of group faster than if they are jumping alone. This embrace is most common at concerts, and mostly there is no risk, because the spectators embrace mainly on slower songs where they do not jump. Frequent embrace is also at sporting matches, where one of lines of spectators embraces and eventually jumps up and down or left and right. This jumping is very intense and can cause vibrations of grandstand.

Probability of occurrence a drummer at concerts is about 99%. The probability that at sports match will be present man with a drum varies according to the sport match. For example, at some sports matches the drummers are prohibited. At football matches the presence of drummer is with the probability of about 85%. It is my long-term monitoring of sporting matches in the country.

4.2 PREREQUISITES TO SYNCHRONIZE OF CROWDS

The parameters that describe the ability of the crowd to be synchronized are very difficult to determine. The most important parameter is the determination of the composition of the spectators. For monitoring the ability to synchronize of crowds we need to know the four basic parameters: group size, the ratio of male / female, age structure and ethnic composition of the group. Input parameters will be acquired on the basis of long-term monitoring of the behaviour of sports fans in the grandstands. These four parameters serve as a basis for determining the fifth parameter which is the musical talents of individual in the jumping´s crowds. If an individual has an ear for music he synchronizes better with the frequency of drumming than an individual who has a no ear for music. If the whole crowd is musically gifted, synchronization of the crowd realizes almost immediately. This parameter cannot be detected by just watching. It can be obtained by examination of individual subjects (medical examination) or based on a probability curve, which shows how they are represented in the population of individuals with a musical ear. For example, a young black woman has a better ear for music than white-old man.

5. CALCULATION

There will be data obtained by monitoring from the attendance of sport matches. After every sport match there will be done individual data processing. For each measurement there is required: the group size and the maximum time required for the synchronization. After the calculation, the resulting values are recorded in the histogram, wherein the horizontal axis shows the time required for synchronization and the vertical axis indicates the size of the group. The calculation parameters are listed in section 4.2. Based on the monitored parameters, probability distribution of ear for music and the probability distribution describing the maximum height of the jump will be added to specific person. Sense of rhythm will be described by time that is required to synchronize the different groups of people. These parameters help us to generate a randomly parameter for a specific person. Subsequently, by using linear regression it will be estimated the average spectator from group. This viewer will serve as a reference for synchronization of other spectators.

The actual stabilization is carried out on the formula (1)

$$u(t) = u_{ref} - u * exp\text{-}(60/t) \tag{1}$$

5.1 CALCULATION PROCEDURE

Input parameters – Tab.1.

Tab. 1 Example- input parameters

Size group		**4 person**		
number of person	1. person	2. person	3. person	4. person
sex	female	male	male	male
nationally	paleface	paleface	paleface	paleface
age	32	25	24	45

Subsequently, the data (Tab. 1) is assigned to a given probability of density distribution of ear for music and probability distribution that specifies the maximum height of the jump. It generates a particular parameter for a given person. Examples of distribution functions-Fig. 2.

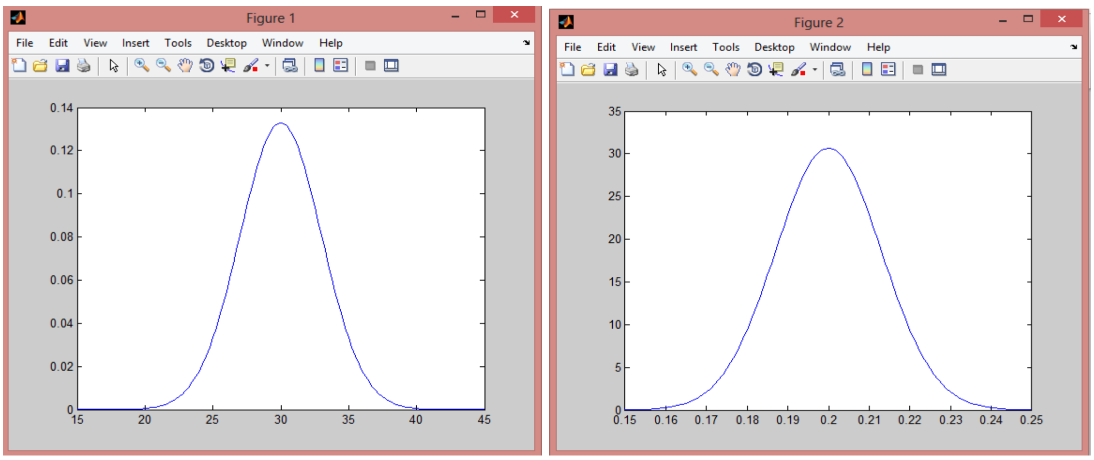

Fig. 2 Parameters for white men 20 year aged. The time required for synchronization (left), jump height (right)

Tab. 2 Example - Assigning data

Size group		4 person		
number of person	1. person	2. person	3. person	4. person
sex	female	male	male	male
nationally	paleface	paleface	paleface	paleface
age	32	25	24	45
time to synchronize	29.40s	24.21s	23.87s	33.78s
jump height	0.254m	0.354m	0.357m	0.311m

The result is that the group is synchronized by synchronizing the last person in the group. Specifically, in our case the group is synchronized after 33.78s and jump height will be 0.354 m.

6. CONCLUSION

The aim is to introduce the model, especially its input parameters that most accurately to describe the crowd on the grandstand. The idea of this model is that a group synchronizes after sometime around the reference person. The synchronization is described by equation (1). Input data are obtained from experiments and long-term observation.

REFERENCES

[1] List of stadiums by capacity. In: *Wikipedia: the free encyclopedia* [online]. San Francisco (CA): Wikimedia Foundation, 2001 [cited 2013-07-13]. Available from: http://en.wikipedia.org/wiki/List_of_stadiums_by_capacity

[2] DISCOVERY CHANNEL. *Megastructures Built From Disaster: Stadiums*. USA, 2008.

[3] PECK, Brooks. *Nurnberg's shaking stadium is by design, not cause for terror*. [online]. [cited 2013-07-13]. Available from: http://sports.yahoo.com/soccer/blog/dirty-tackle/post/Nurnberg-s-shaking-stadium-is-by-design-not-cau?urn=sow-294442

DEVELOPMENT OF HYDRATION HEAT AND MODEL MIXTURES WITH FLY ASH

Ondřej ZOBAL[1], Zdeněk BITTNAR[2], Vít ŠMILAUER[3]

Abstract: *Higher level of fly ash used into cement/concrete is still, from many aspects, a topical issue in construction industry. Tens of years ago, significant part of cement into concrete mixtures for massive constructions started to be substituted for fly ash already. The reason was that this substitution significantly decreases the values of the hydration heat. This paper deals with experimental verification of the hydration heat development in cement pastes with various fly ashes and various degrees of cement substitution. Subsequently a model was created based on the experiments. The model allows working with different input parameters and predicting of behaviour of constructions (materials), with regard to the hydration heat development, thus technological design can be optimised.*

Keywords: *hydration heat, fly ash, cement, simulation*

1. INTRODUCTION

Substitution of clinker for fly ash for decrease of the hydration heat has been applied for many years, mainly in massive constructions. Examples are the Hungry Horse Dam completed in the USA in 1948, where up to 35% of Portland cement was substituted for fly ash [1], or construction of the Orlík Dam in the Czech Republic in 1956 to 1961, where almost 30 % of cement was substituted. Executed analysis of concrete from the body of the Orlík Dam shows that concrete of very high quality is being concerned [2]. However, use of quantity of fly ash as a substitution for clinker brings some problems too, particularly delay of the beginning of setting and slow increase of initial strength or higher carbonation and also high variability of fly ash [3] are concerned. This paper describes measurements of the hydration heat with the aim to find out reactivity of fly ashes with subsequent calibration of models for concrete embedment of massive constructions.

[1]Ing.OndřejZobal,Faculty of Civil Engineering, Czech Technical University, ondrej.zobal@fsv.cvut.cz

[2]Prof. Ing. ZdeněkBittnar, CSc., Faculty of Civil Engineering, Czech Technical University, bittnar@fsv.cvut.cz

[3]Doc. Ing. VítŠmilauer, Ph.D., Faculty of Civil Engineering, Czech Technical University, smilauer@cml.fsv.cvut.cz

2. MEASURING HYDRATION HEAT

Composition of cement pastes for the experiment was as follows. Substitute of cement for fly ash was 25 and 55 % of the weight. The water cement ratio of all pastes was constant and its value was 0.5. The water cement ratio was chosen as a compromise between working properties of individual mixtures. The sample No. 1 is a standard mortar recipe; the reference sample of a pure cement paste is No. 2. The used cement: CEM I 42.5R Mokrá. Tab. 1 summarizes measured values of the hydration heat for 3, 7, 18 days of hydration. The most significant effect of fly ashes on reaction kinetics occurs within 72 hours.

Tab. 1 Values of the hydration heat for various mixtures of cement and fly ash at 3, 7 and 18 days.

Mixture	Q_3 [J/g_{binder}]	Q_7 [J/g_{binder}]	$Q_{max(18)}$ [J/g_{binder}]
1 - CEM I 42.5 R Mok (30) + sand (15)	230	294	334
2 - CEM I 42.5 R Mok (30)	**258**	**322**	**357**
3 - CEM I 42.5 R Mok (22.5) + EPc (7.5)	263	330	381
4 - CEM I 42.5 R Mok (22.5) + EME ET (7.5)	261	330	376
5 - CEM I 42.5 R Mok (22.5) + ETu 3. section (7.5)	286	361	407
6 - CEM I 42.5 R Mok (13.5) + EPc (16.5)	294	365	433
7 - CEM I 42.5 R Mok (13.5) + EME ET (16.5)	287	360	421
8 - CEM I 42.5 R Mok (13.5) + ETu 3. section (16.5)	315	408	490

3. CALIBRATION OF THE AFINNE MODEL

Affine model provides thermal flow for any type of binder including the admixtures of fly ash. The model used is a four-parameter model with B1, B2, $\alpha\infty$, η parameters according to equations (1) and (2), where $Q_{h,pot}$ is the potential hydration heat of the binder in J/g and α is the degree of hydration (reaction).

$$\tilde{A}_{25} = B_1\left(\frac{B_2}{\alpha_\infty}+\alpha\right)(\alpha_\infty-\alpha)\exp\left(-\bar{\eta}\frac{\alpha}{\alpha_\infty}\right) \qquad \frac{1}{Q_{h,pot}}\frac{\partial Q_h}{\partial t}=\frac{\partial\alpha}{\partial t}=\tilde{A}_{25}\exp\left[\frac{E_a}{R}\left(\frac{1}{T_{25}}-\frac{1}{T}\right)\right] \quad \textit{(1), (2)}$$

Fig. 1 shows the calibrated curve of the affine model with experimental data on a pure paste.

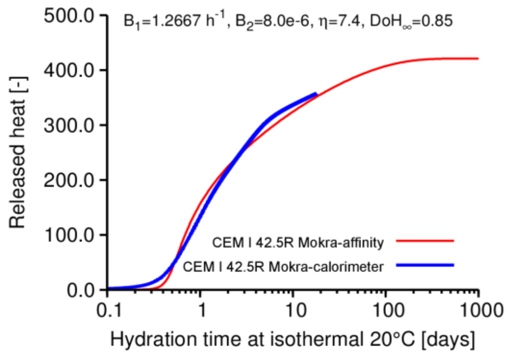

Fig. 1 The development of hydration heat during isothermal 20 ° C cement CEM I 42.5R Mokrá (blue - calorimeter; red - model)

4. SIMULATION

Based on the calibrated affine model, 60 simulations of temperature development during concrete embedment of the items of various thicknesses were carried out. The quantity of substituted cement was 25 and 55 % and the value of water cement ratio was 0.5. We considered these four variables:

- Quantity of the binder 300 and 400 kg/m^3 of concrete,
- Binder with Q_{pot} 500, 383, 254 J/g. These values successively comply with CEM I, 25% and 55% of clinker substitution,
- Thickness of concrete items 0.5; 1.0; 1.5; 2 and 4 meters,
- Concrete embedment in summer or winter. Initial temperature of concrete in summer 20°C, in winter 10°C. Ambient air temperature in summer 25°C, winter 5°C.

The results of the simulations are mentioned in Tables 2 and 3; maximum temperatures reached are concerned in particular. The temperature of concrete of 94.6°C (400 kg/m^3, CEM I, 4 m, summer) is reached in the least favourable combination.

Tab. 2 Summary of values

Thickness of concrete items	maximal temperature [°C] - summer					
	cement in mixture - 300 kg/m^3			cement in mixture - 400 kg/m^3		
	Q_{pot} [J/g binder]			Q_{pot} [J/g binder]		
	254	383	500	254	383	500
0.5 m	34.633	42.021	49.682	39.358	50.434	62.370
1.0 m	37.577	47.466	57.694	43.905	58.690	74.402
1.5 m	39.638	51.075	62.791	46.969	63.921	81.590
2.0 m	41.192	53.677	66.331	49.208	67.544	86.271
4.0 m	44.921	59.466	73.619	54.323	74.943	94.639

Tab. 3 Summary of values

Thickness of concrete items	maximal temperature [°C] - winter					
	cement in mixture - 300 kg/m^3			cement in mixture - 400 kg/m^3		
	Q_{pot} [J/g binder]			Q_{pot} [J/g binder]		
	254	383	500	254	383	500
0.5 m	15.548	21.210	27.209	19.160	27.801	37.438
1.0 m	21.163	29.628	38.589	26.558	39.472	53.685
1.5 m	24.642	34.902	45.656	31.192	46.708	63.426
2.0 m	27.071	38.583	50.526	34.433	51.685	69.894
4.0 m	32.388	46.488	60.540	41.462	61.870	81.935

Fig. 2 shows the temperature field at maximum temperature of concrete with CEM I. Thickness of the unit of 1 m, cement content of 400 kg/m^3, substitution of 0 and 55% of cement for fly ash and summer season are considered. On the left, there is the mixture only with CEM I and on the right, there is the mixture with 55% of clinker substituted for fly ash. Maximum temperatures are 74.7 and 43.9°C.

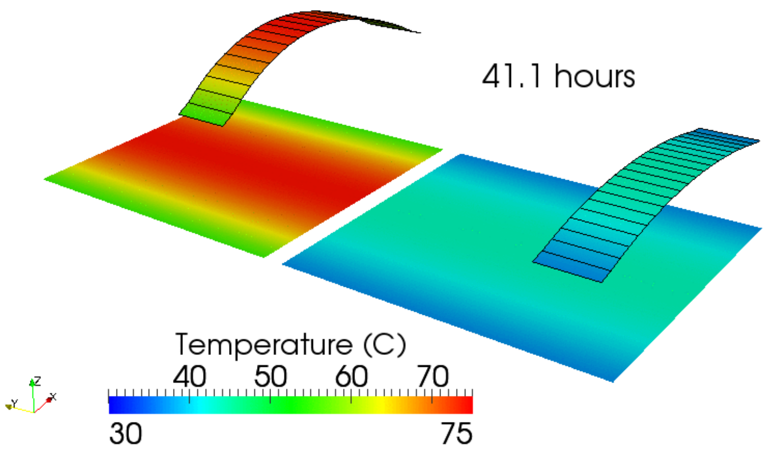

Fig. 2: The temperature of the element with a thickness of 1 m during concreting in the summer after 41.1 hours - left concrete with CEM I, the right to pay 55% of clinker ash.

5. CONCLUSION

Calorimetry proved relatively insignificant “filler effect” of increased reaction space for heterogeneous nucleation. This allowed simplification of simulations with the temperature development of concrete construction. In the least favourable combination, the temperature of concrete of 94.6°C (400 kg/m^3, CEM I, 4 m, summer) is reached. Such high temperatures are hazardous for delayed formation of ettringite. The time of reaching maximum temperatures varies between 29-217 hours. We can roughly state that the temperature increase by a half occurs in case of 50 % substitution of clinker for fly ash. The simulations mentioned show that resulting temperatures can be significantly influenced using substitution of clinker for fly ash. These measurements and simulations should help support our long-term aim, which is more application of fly ash in construction industry, particularly as an active component into cement and concrete, which is prevented by mistrust of professionals as well as legislation in the Czech Republic.

ACKNOWLEDGEMENT

The financial support of this experiment by the Faculty of Civil Engineering, Czech Technical University in Prague (project FR-TI3/757) is gratefully acknowledged.

REFERENCES

[1] BERG, W. et al. *Příručka – Popílek v betonu – základy výroby a použití*. ČEZ Energetické produkty, s.r.o., 2013, 167 p. ISBN 978-80-260-4226-6.

[2] ZOBAL, O., PADEVĚT, P., ŠMILAUER, V., KOPECKÝ, L. and BITTNAR, Z. Experimental analysis of material and mechanical properties of the concrete dam Orlík after 50 years. In: *19.Betonářské dny 2012*. Praha: ČBS , 2012, pp. 248-253. ISBN 978-80-87158-32-6

[3] NEVILLE, A., M. *Properties of concrete*. 2009. New York. 661p. ISBN 0-582-23070-5

WANG TILE SETS AND SCHUR COMPLEMENT IN EVALUATION OF MICROSTRUCTURAL FIELDS

Lukáš ZRŮBEK[1], Jaroslav KRUIS[2], Jan NOVÁK[3], Anna KUČEROVÁ[4]

Abstract: *This contribution addresses the method of Wang tilings used to reproduce fluctuating stresses, strains and displacements in random materials subject to uniform strain excitation. Using small sets of Wang tiles allows to avoid an abrupt evaluation of fluctuating fields in large macro-scopic domain and synthesize them by means of stochastic tiling algorithm instead. Assuming each tile discretized by the same regular finite element mesh, all admissible micro-scale problems can be obtained effectively by the Schur complement method.*

Keywords: *microstructure, Wang tilings, stress field synthesis, Schur complement method*

1. INTRODUCTION

In this paper we draw our attention in high performance analysis of micro-scopic fluctuation fields in random particulate composites subject to uniform strain excitation that can be used as microstructure-sensitive enrichment functions in Partition of Unity [1] and Hybrid Finite Element methods [2, 3]. The proposed technique rests on the method of Wang tilings, used to synthesize random, statistically consistent, microstructural patterns of open planar domains. A synthesized domain is composed of tiles, statistical volume elements [4] that are gathered in sets. All distinct tiles together must involve a complete morphological information of the target texture. If so, the set corresponds to representative volume element.

In addition, and contrary to a purely microstructural information synthesized to date [5], the sought enrichment fields are nonlocal. In other words, the neighbours in a certain distance from each individual

[1] Ing. Lukáš Zrůbek, Department of Mechanics, Faculty of Civil Engineering, Czech Technical University in Prague, lukas.zrubek@fsv.cvut.cz

[2] Doc. Ing. Jaroslav Kruis, Ph.D., Department of Mechanics, Faculty of Civil Engineering, Czech Technical University in Prague, jk@cml.fsv.cvut.cz

[3] Ing. Jan Novák, Ph.D., Department of Mechanics, Faculty of Civil Engineering, Czech Technical University in Prague and Institute of Structural Mechanics, Faculty of Civil Engineering, Brno University of Technology, novakj@cml.fsv.cvut.cz

[4] Ing. Anna Kučerová, Ph.D., Department of Mechanics, Faculty of Civil Engineering, Czech Technical University in Prague, anicka@cml.fsv.cvut.cz

tile are responsible for the fields inside the tile, and must be therefore taken into account. It yields, thousands of micro-scale problems, square tilings of optional neighbourhood extent $m \times m$ (Tabs. 2 & 3), with imposed periodic boundary conditions have to be solved. Recently, structured discretizations arising from raster image representations of microstructures have been resolved by Moulinec-Suquet Fast Fourier Transform based algorithm [6]. However, strongly heterogeneous materials with a significant contrast in material parameters of individual phases, e.g. high porosity foams or fibre reinforced plastics, have caused serious convergence difficulty, thereby, turning our attention to conventional finite element method (FEM).

2. WANG TILES, SETS AND TILINGS

The method of Wang tilings, introduced by Hao Wang [7], can be viewed as a planar domino game or a jigsaw puzzle. This study proceeds from the recent observation [5] that the Wang tile sets represent a generalization to the periodic unit cell concept (PUC), common in multiscale simulations. However, contrary to the PUC framework, the appealing feature of tilings consist of the ability to reproduce non-periodic microstructural patterns. A brief specification of Wang tilings follows.

A single Wang *tile* can be referred to as a piece of square four-sided domino (tetromino). Tiles are not allowed to rotate when brought together with other pieces through congruent edges (green, red, yellow triangular sub-regions in figure Fig. 1(b)). This means, that two tiles with identical sequence of edges, mutually rotated by $k\pi/4$ are considered as different, Fig. 1(b, c). In practical applications, the triangular edge regions are concentrated to edges (Fig. 1(d)) denoted either by colors [8], alphabetical codes [5] or enumerated by integers [9, 10].

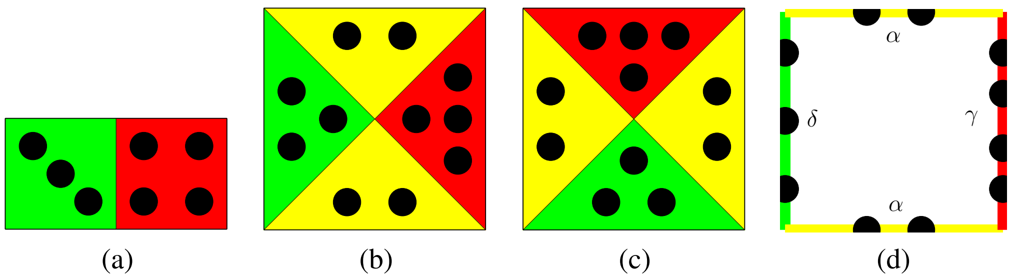

Fig. 1 a) Ancient domino piece, b) Wang tile with three different codes on four edges, c) another Wang tile obtained by rotating tile (b) by $\pi/4$ clockwise, d) tile (b) with edge regions concentrated to edges.

A collection of unique tiles that enable to cover up open planar domains aperiodically is called *tile set*, Fig. 2(a). It is referred to as $Wn^t/n_1^c - n_2^c$, where W stands for "Wang" initial, n^t is the number of tiles in the set and n_i^c denotes the number of edge codes in ith spatial direction. The number of edge codes n^c in the ith spatial direction can be chosen arbitrarily, however, the number of tiles n^t, Tab. 1, must satisfy,

$$n^t = n^{NW}\sqrt{n^{cs}}, \qquad (1)$$

where n^{cs} is the number of tiles in the so called complete set

$$n^{cs} = (n_1^c n_2^c)^2, \tag{2}$$

and $n^{NW} \in \{2, \dots, \sqrt{n^{cs}}\}$ stands for the optional number of tiles with an identical arrangement of northwestern (NW) edge codes (α, γ adjacent to shaded tile $t = 5$ in Fig. 2(a)). The complete set of n^{cs} tiles is obtained by permuting the chosen codes c_i, see [5, 11] for further details.

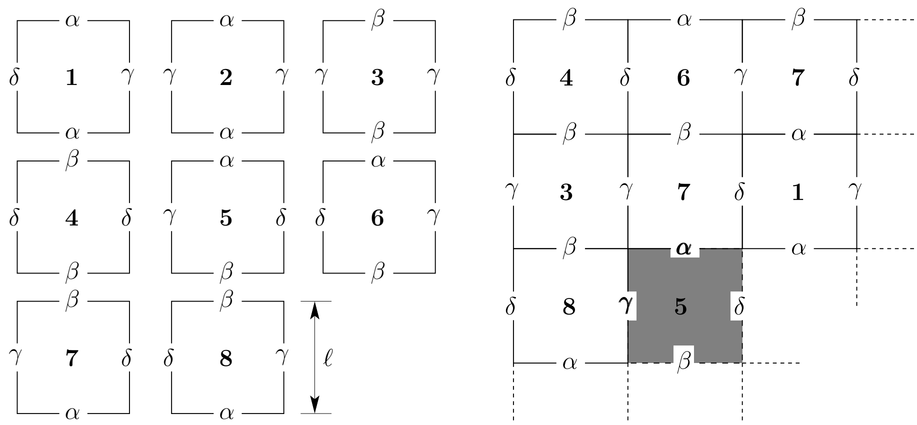

(a) (b)

Fig. 2 a) Wang tile set W8/2-2, b) example of valid tiling.

A *tiling* is the assembly of multiple copies of tiles from the set, Fig. 2(b). If there are no missing tiles in the tiling lattice and a morphological information across congruent edges is compatible everywhere we say the tiling is *valid* (so called ground state, see [10]). Since, invalid tilings are meaningless from the viewpoint of microstructure synthesis, the abbreviation *tiling* is used instead of the valid tiling [5].

Tab. 1 Number of tiles in Wang tile sets with respect to n_i^c, n^{cs} and n^{NW}.

n_i^c		n^{cs}	n^{NW}	n^t	Tile set
n_1^c	n_2^c				
2	2	16	2	8	W8/2-2
3	3	81	2	18	W18/3-3
4	4	256	2	32	W32/4-4
5	5	625	2	50	W50/5-5
...	...				

When tiling a domain, we use stochastic Cohen-Shade-Hiller-Deussen (CSHD) algorithm [12]. The tiles are successively placed one by one, so that the edge codes of newly placed tiles must comply with those of their neighbours placed previously. The index of a new tile to be placed is selected randomly but to keep the procedure random, there must be always at least two of such tiles associated with each north-western edge-code combination. Aperiodicity of resulting tilings is thus guaranteed when assuming that the random generator never returns a periodic sequence of numbers (see [12] for further details).

3. TILES WITH STRESS FLUCTUATION PATTERNS

Contrary to the synthesis of purely microstructural data, as reported e.g. in [5], the subject of this contribution is more difficult as it aims at synthesis of non-local field patterns. In what follows, we limit our exposition to stress fluctuations σ^*_{ij} due to the uniform strain excitation E. Regarding the non-local character of stresses, we do not last with the same number of tiles as it is normally used for microstructural data, see eg. [13]. The distribution of all components σ^*_{ij} in each tile depends, at least, on their distribution in adjacent tiles.

To simplify the exposition, let us assume the highlighted tiles $t = 1$ in Fig. 3(a). The stresses in each of the tiles are the functions of the interior microstructure and stress distribution in eight tiles placed around. It yields that, despite the fact that all tiles "one" have identical microstructure, the σ^*_{ij} components will differ for distinct combinations of surrounding tiles. It is also obvious that those differences will be further pronounced by decreasing the ratio of the tile edge dimension ℓ, Fig. 2(a), and characteristic microstructural length(s) given by disk diameters and/or typical distances among the disks in Fig. 4(b).

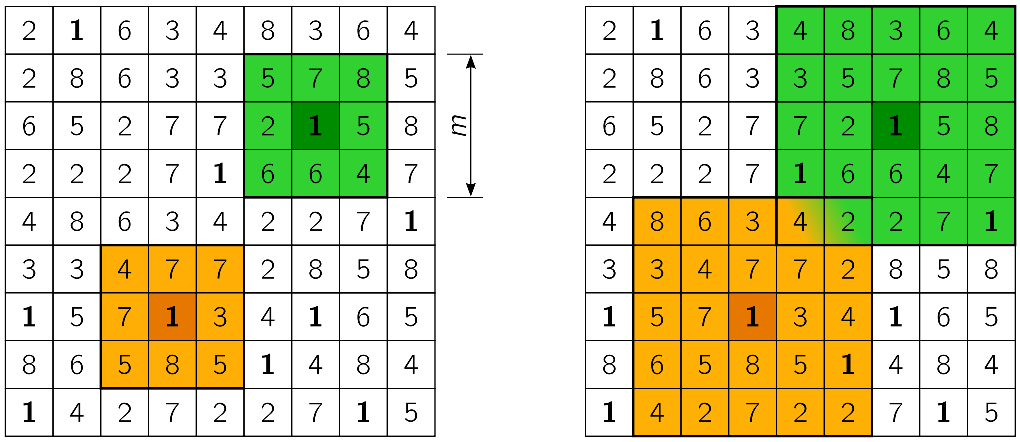

(a) (b)

Fig. 3 Tiling map with highlighted neighbours of the first tile from $W8/2-2$, a) nearest, adjacent neighbours, b) first and second layer of neighbour tiles.

In order to eliminate the traction jumps in a synthesized enrichment function, larger neighbourhoods should be considered, see Fig. 3. A particular number of distinct stress pattern patches in all tiles $1, \ldots, n^t$, with respect to the particular extent of neighbours $m \times m$ is given by disjunctive colligation of admissible patches in each tile, see Tab. 2,

$$n^{\mathrm{comb}}_{m\times m} = n^t \cdot (2n^c_i)^{2(m-1)} \cdot (n^{NW})^{(m-1)^2}. \tag{3}$$

Tab. 2 Number of tilings to be solved in order to obtain all possible combinations of stress patterns for tiles $t \in 1, \ldots, n^t$.

Tile set	No. of all possible tilings $\mathcal{O}_{m\times m}$ for increasing extent $m \times m$					
	1×1	3×3	5×5	7×7	9×9	11×11
W8/2-2	$8.0 \cdot 10^{0}$	$3.3 \cdot 10^{4}$	$3.4 \cdot 10^{10}$	$9.2 \cdot 10^{18}$	$6.3 \cdot 10^{29}$	$1.1 \cdot 10^{43}$
W18/3-3	$1.8 \cdot 10^{1}$	$3.7 \cdot 10^{5}$	$2.0 \cdot 10^{12}$	$2.7 \cdot 10^{21}$	$9.4 \cdot 10^{32}$	$8.3 \cdot 10^{46}$
W32/4-4	$3.2 \cdot 10^{1}$	$2.1 \cdot 10^{6}$	$3.5 \cdot 10^{13}$	$1.5 \cdot 10^{23}$	$1.7 \cdot 10^{35}$	$4.7 \cdot 10^{49}$
W50/5-5	$5.0 \cdot 10^{1}$	$8.0 \cdot 10^{6}$	$3.3 \cdot 10^{14}$	$3.4 \cdot 10^{24}$	$9.2 \cdot 10^{36}$	$6.3 \cdot 10^{51}$

4. DESIGNING TILE SET MORPHOLOGY

As mentioned above, to create open domain tilings of self-equilibrated stress fluctuations (balanced traction fluctuations in the tiling lattice), it is necessary to store a number of copies of each tile $t \in \{1, \ldots, n^t\}$. This is given by all possible combinations of tiles that can arise around each tile t, when preserving the edge matching rules, Tabs. 2 & 3. An example of the genesis of two distinct copies of tile $t = 1$, embedded in the smallest neighbourhood $m = 3$, is represented by the flowcharts in Fig. 4.

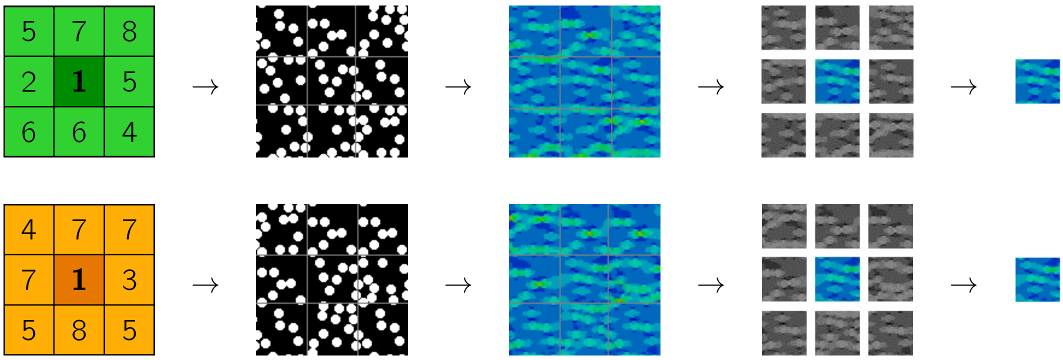

Fig. 4 Stress patch flowchart, a) map of two distinct tilings $\mathcal{O}_{m\times m} = \mathcal{O}_{3\times 3}$, b) microstructure of tilings $\mathcal{O}_{3\times 3}$, c) stress fluctuations σ_x^* in $\mathcal{O}_{3\times 3}$, d) $\mathcal{O}_{3\times 3}$ decomposition, e) distinct stress fluctuation patterns (patches) in tile $t = 1$ as functions of different neighbourhoods.

Having all the $\mathcal{O}_{m\times m}$ at hand, we solve $n^{\text{comb}}_{m\times m}$ of periodic boundary value problems where $\mathcal{O}_{m\times m}$ are the subject to uniform strain loadcases as in classical homogenization framework. In two dimensions, we set the loading strain vector component successively to one, while the remaining two equal to zero. Despite the domain $\mathcal{O}_{m\times m}$ is not periodic on external boundary, the periodic boundary conditions are acceptable considering the very local character of stress fluctuations and their negligible action to the solution in the central tile [14]. For example, instead of eight tiles (recall that $n^t = 8$ for $W8/2-2$) necessary to reconstruct either microstructural or stress patterns according to the methodology reported in [11], this number increases to $32,768$ when using the proposed strategy, see the first row of Tab. 3.

Tab. 3 No. of combinations of tiles with respect to neighbours placed in cardinal-i and ordinal-ij directions and for $m = 3$.

Tile set	Cardinal i-th and ordinal ij-th directions									No. combinations
	n^t	N	S	E	W	NW	NE	SW	SE	$n^{comb}_{3\times3}$
W8/2-2	8	4	4	4	4	2	2	2	2	$32,768$
W18/3-3	18	6	6	6	6	2	2	2	2	$373,248$
W32/4-4	32	8	8	8	8	2	2	2	2	$2,097,152$
W50/5-5	50	10	10	10	10	2	2	2	2	$8,000,000$

5. EVALUATION OF STRESS FLUCTUATION PATTERNS IN TILES

5.1. MOULINEC-SUQUET FFT BASED SOLVER

The above mentioned periodic boundary conditions allow us to use the solution to elastic fields by means of the fast Fourier transform (FFT) based Moulinec-Suquet solver [6]. It is characterised by a well-known Lippman-Schwinger type integral equation. The periodic kernel of the integral formulation admits a compact closed-form expression in the Fourier space, so that its action to sought stresses can be effectively evaluated by FFT algorithms [15]. Although the computational overhead of this numerical strategy is imperceptible, it has several demerits as Gibbs effects, problems with infinite contrast of phases to cite a few.

5.2. SCHUR COMPLEMENT METHOD

Assuming now the situation when each tile is discretized by the finite element method. It has to be emphasized that all tiles of the same type are discretized by identical finite element mesh. Optionally, each pixel is a single element. A conventional approach of solving the full system would be thus extremely demanding. In order to speed up the computation, the Schur complement method can be used. For each type of tile, the Schur complement is evaluated. It means, all DOFs defined inside the tile are eliminated out to the edges, therefore, the tile is represented by its boundary DOFs only. Now, the tile resembles a generalized finite element or a subdomain in the domain decomposition methods. For simplicity, we illustrate the complexity on the following example. Let each tile be covered by an FE discretization of 200×200 finite elements, i.e. $\ell = 200$ px, yielding approximately $40,000$ nodes per tile. However, the Schur complement method reduces the nodes to boundaries, resulting the total number of nodes to 800. The smallest admissible tiling $\mathcal{O}_{3\times3}$ is composed of 9 tiles and contains 360×10^3 nodes, which must be solved by conventional approach. Contrary, the Schur complement method requires approximately 5×10^3 nodes.

The Schur complement method, also known as the substructuring method [16, 17], is based on a special ordering of DOFs. The DOFs defined in the internal nodes are ordered at first and the DOFs defined on the boundary are ordered as last. With respect to this ordering of unknowns, the system of equations defined on a single tile can be written in the form

$$\begin{pmatrix} \boldsymbol{K}_{ii} & \boldsymbol{K}_{ib} \\ \boldsymbol{K}_{bi} & \boldsymbol{K}_{bb} \end{pmatrix} \begin{pmatrix} \boldsymbol{d}_i \\ \boldsymbol{d}_b \end{pmatrix} = \begin{pmatrix} \boldsymbol{f}_i \\ \boldsymbol{f}_b \end{pmatrix}, \tag{4}$$

where $\boldsymbol{d}_i$ stands for the vector of internal unknowns, and $\boldsymbol{d}_b$ represents its external (boundary) counterpart. By analogy, $\boldsymbol{f}_i$ and $\boldsymbol{f}_b$, respectively, are associated with the part of the right hand side vector connected to tile interior and edges. Symbols $\boldsymbol{K}_{ii}, \boldsymbol{K}_{ib}, \boldsymbol{K}_{bi}, \boldsymbol{K}_{bb}$ are the appropriate matrices. If the matrix $\boldsymbol{K}_{ii}$ is non-singular, it further follows from Eq. 4, that the vector $\boldsymbol{d}_i$ can be recast as

$$\boldsymbol{d}_i = \boldsymbol{K}_{ii}^{-1}(\boldsymbol{f}_i - \boldsymbol{K}_{ib}\boldsymbol{d}_b), \tag{5}$$

and the original system of equations, Eq. 4, reduces to

$$(\boldsymbol{K}_{bb} - \boldsymbol{K}_{bi}\boldsymbol{K}_{ii}^{-1}\boldsymbol{K}_{ib})\boldsymbol{d}_b = \boldsymbol{f}_b - \boldsymbol{K}_{bi}\boldsymbol{K}_{ii}^{-1}\boldsymbol{f}_i. \tag{6}$$

Notice, that the above system of equations contains only the unknowns defined in the boundary nodes.

The Schur complement matrix $\boldsymbol{K}_{bb} - \boldsymbol{K}_{bi}\boldsymbol{K}_{ii}^{-1}\boldsymbol{K}_{ib}$ is the stiffness matrix of a tile and it resembles the stiffness matrix of a generalized element. In other words, for the tiling with 9 tiles, the problem of the mechanical field synthesis is assembled similarly to a problem with 9 finite elements.

5.3. PARALLELIZATION

Specific properties of the Wang tilings lead to implementation in parallel environment which results in substantial speedup with respect to other methods.

The beginning of the proces is devoted to the elimination of the internal DOFs on tiles. It means, the Schur complement matrices $\boldsymbol{K}_{bb} - \boldsymbol{K}_{bi}\boldsymbol{K}_{ii}^{-1}\boldsymbol{K}_{ib}$ are evaluated for each tile $1, \ldots, n^t$. Only small number of processors is used in this step, preferably the same number as number of tiles in set (e.g. 8 for set $W8/2-2$). After the all Schur complements are computed, all of them are sent to remaining cluster processors which will be used for the evaluation of mechanical fields in central tiles of $m \times m$ tilings. While relatively small number of processors is used for the Schur complements (e.g. eight), the number of processors allocated for the following step is assumed to be much larger, e.g. hundreds or thousands. Implementation of this broadcast is crucial. It will be studied whether computation of the Schur complements on all processors is not faster then the broadcasting.

Second step of the computation will be devoted to the calculation of the mechanical fields. As mentioned above, the number of all tilings is known in advance. Each processor is assumed to be loaded by $n^{\mathrm{comb}}_{m\times m}/n_{\mathrm{CPU}}$ tasks, where n_{CPU} denotes the number of processors. Regarding the Schur complements of $1, \ldots, n^t$ are known, this step is performed only by means of the appropriate Schur complement matrices and the boundary solutions.

6. INITIAL OUTCOMES

So far very simple numerical experiments have been executed to compare computational time needed by the FFT based solver and the Schur complement method. In the performed tests we changed a few variables to get an overview of how their variation affect the computational time.

The first of the variables is the ratio of elastic moduli of composite phases. Its influence on the time required for the calculation is shown in the Fig. 5(a), where capital 'S' is for the Schur complement method and capital 'F' denotes the FFT based solver. Lowercase 's' or 'b' stands for small (26px) or large (78px) tiles and numbers 4, 6 or 8 correspond to required accuracy 10^{-4}, 10^{-6} or 10^{-8}, respectively. Increasing the ratio increases slightly the computational overhead of the Schur complement method over the FFT method. The presented results confirm that the high contrast in material stiffnesses leads to enormous computational time needed by FFT based solvers and the Schur complement method becomes faster.

The second variable we change during the experiments is the required accuracy of results. The dependence of time on the required accuracy is shown in Fig. 5(b), where the key is almost the same as in Fig. 5(a) but here the numbers 2, 10, 100 and 1000 indicate the ratio of elastic modulus of phases. One can notice that computational time is almost not affected by required accuracy in the case of the Schur complement method, while it is significantly increased for the FFT based method.

The third altered variable is the size of solved domains, i.e. the discretization density of employed tiles. We used only two sizes, namely small tiles with the edge lenght of 26px and large tiles with $\ell = 78$px. As it turned out, the solved domain size significantly affects the time required to solve the Schur complements on individual tiles, because the number of DOF's of tiles increases quadratically. Nevertheless, Schur complements need to be solved only once at a preprocessing phase and further calculations are affected only with a linear increase of DOF's on the tile boundary.

7. CONCLUSIONS

The results show that by using the Schur complement method we can count with high or even infinite elastic stiffness ratios (in the case of porous materials), which is not possible using the FFT based solver. Furthermore, we are able to achieve high accuracy of calculations in a reasonable time compared to well posed FFT solutions.

ACKNOWLEDGEMENT

This work was supported by the Czech Science Foundation, through projects No. 13–24027S (L. Z., A. K.), P105/12/0331 (J. N.) and GACR 13–18652S (J. K.). In addition, we would like to thank the

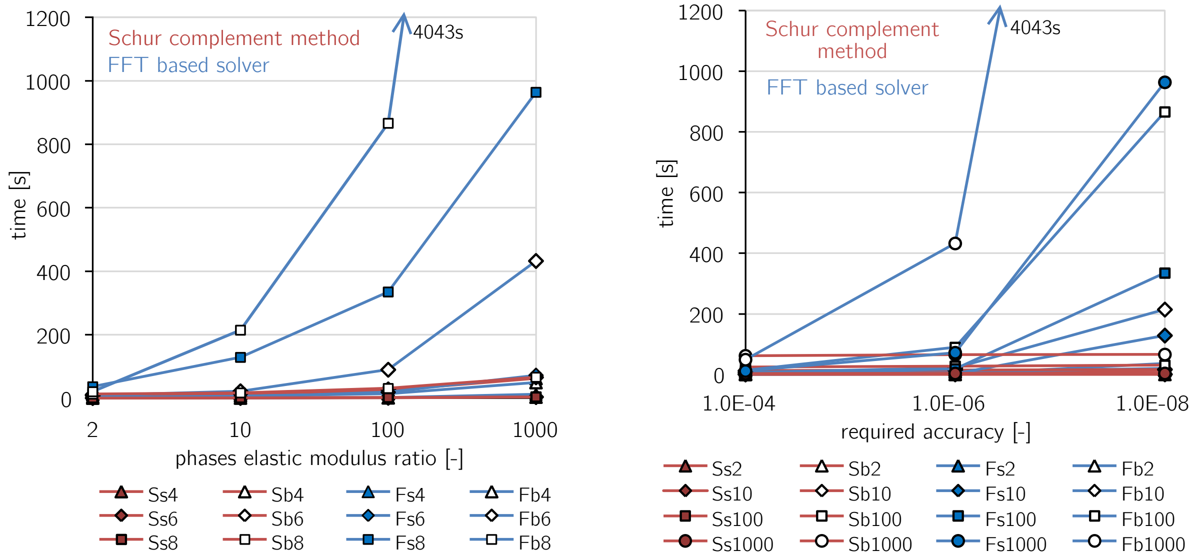

Fig. 5 a) Dependence of computational time on contrast ratio of elastic moduli, b) dependence of computational time on prescribed accuracy.

European Social Fund endowment under Grant No. CZ.1.07/2.3.00/30.0005 (J. N.) of Brno University of Technology (Support for the creation of excellent interdisciplinary research teams at Brno University of Technology).

REFERENCES

[1] MELENK J.M. and BABUŠKA I. The partition of unity finite element method: Basic theory and applications, *Computer Methods in Applied Mechanics and Engineering,* 1996, **139**(1), 289-314. ISSN 0045-7825.

[2] TEIXEIRA de FREITAS J.A. Formulation of elastostatic hybrid-Trefftz stress elements, *Computer Methods in Applied Mechanics and Engineering,* 1998, **153**(1), 127-151. ISSN 0045-7825.

[3] NOVÁK J., KACZMARCZYK Ł., GRASSL P., ZEMAN J. and PEARCE Ch.J. A micromechanics-enhanced finite element formulation for modelling heterogeneous materials, *Computer Methods in Applied Mechanics and Engineering,* 2012, **201**, 53-64. ISSN 0045-7825.

[4] FULWOOD D.T., NIEZGODA S.R., ADAMS B.L. and KALIDINDI S.R. Microstructure sensitive design for performance optimization, *Progress in Materials Science,* 2010, **55**(6), 477-562. ISSN 0079-6425.

[5] NOVÁK J., KUČEROVÁ. A. and ZEMAN J. Compressing Random Microstructures via Stochastic Wang Tilings, *Physical Review E,* 2012, **86**(4), 040104. Available from: http://arxiv.org/abs/1206.0933.

[6] MOULINEC H. and SUQUET P. A fast numerical method for computing the linear and nonlinear mechanical properties of composites, *Comptes rendus de l'Académie des sciences. Série II, Mécanique, physique, chimie, astronomie,* 1994, **318**(11), 1417-1423.

[7] WANG H. Proving theorems by pattern recognition–II, *Bell Systems Technical Journal,* 1961, **40**, 1-41. ISSN 0005-8580.

[8] WANG H. Games, logic and computers, *Scientific American,* 1965, **213**(5), 98-106.

[9] CULIK K. An aperiodic set of 13 Wang tiles, *Discrete Mathematics,* 1996, **160**(1), 245-251. ISSN 0012-365X.

[10] ARISTOFF D. and RADIN C. First order phase transition in a model of quasicrystals, *Journal of Physics A: Mathematical and Theoretical,* 2011, **44**(25), 255001.

[11] NOVÁK J., KUČEROVÁ. A. and ZEMAN J. Microstructural enrichment functions based on stochastic Wang tilings, *Modelling and Simulation in Materials Science and Engineering,* 2013, **21**(2), 025014. Available from: http://arxiv.org/abs/1110.4183.

[12] COHEN M.F., SHADE J., HILLER S. and DEUSSEN O. Wang tiles for image and texture generation, *ACM Transactions on Graphics, Citeseer,* 2003, **22**(3), 287-294. 255001. ISSN 0730-0301.

[13] ZRŮBEK L., KUČEROVÁ. A. and NOVÁK J. Complex microstructural enrichment functions based on extended Wang tile sets, *Proceedings of the* 3^{rd} *Conference Nano & Macro Mechanics: NMM2012,* 2012, 263-270. ISBN 978-80-01-05097-2.

[14] TERADA K., HORI M., KYOYA T. and KIKUCHI N. Simulation of the multi-scale convergence in computational homogenization approaches, *International Journal of Solids and Structures,* 2000, **37**(16), 2285-2311.

[15] FRIGO M. and JOHNSON S.G. The Design and Implementation of FFTW3, *Proceedings of the IEEE,* 2005, **93**(2), 216-231.

[16] KRUIS J. Domain Decomposition Methods on Parallel Computers, *Progress in Engineering Computational Technology,* 2004, 299-322. ISBN 1-874672-22-9.

[17] MEDEK O., KRUIS J., TVRDÍK P. and BITTNAR Z. Static Load Balancing Applied to Schur Complement Method, *Computers & structures ,* 2007, **85**(9), 489-498. ISSN 0045-7949.